Optimisation of Electrolytically-gated Thin Film Transistors made from Printed Nanosheet Networks

A DISSERTATION PRESENTED BY

DÓMHNALL Ó SÚILLEABHÁIN

TO

THE DEPARTMENT OF PHYSICS

IN PARTIAL FULFILLMENT OF THE REQUIREMENTS

FOR THE DEGREE OF

DOCTOR OF PHILOSOPHY

IN THE SUBJECT OF

PHYSICS

TRINITY COLLEGE DUBLIN

DUBLIN, IRELAND

JANUARY 2022

Declaration

I declare that this thesis has not been submitted as an exercise for a degree at this or any other university and it is entirely my own work.

I agree to deposit this thesis in the University's open access institutional repository or allow the library to do so on my behalf, subject to Irish Copyright Legislation and Trinity College Library conditions of use and acknowledgement.

Elements of this work that have been carried out jointly with others or by collaborators have been duly acknowledged in the text wherever included.

_____

Dómhnall Ó Súilleabháin

Optimisation of Electrolytically-gated Thin Film Transistors made from Printed Nanosheet Networks

Abstract

Networks of two-dimensional nanosheets show great potential in a wide variety of different applications, with particular focus on the area of printed electronics. One of the main issues facing such nanosheet network transistors is the fact that their performance is limited by the resistance between nanosheets, and are therefore unable to reach the same levels as their single crystal equivalents. This issue is compounded by the fact that what exactly contributes to the electrical behaviour of these networks is not yet known. This work aims to investigate some potential avenues of improving the performance of electrolytically gated nanosheet network transistors while illuminating the inner workings of such networks.

One of the benefits of using liquid-phase exfoliated nanomaterials is that different materials can easily be combined into composite inks in controlled proportions, allowing for control over the resulting network's properties. Increasing amounts of graphene were added to WS_2 dispersions in order to spray composite films with different volume fractions of graphene with a view to improving the transistor performance. The addition of the graphene to the WS_2 follows percolation theory, with a percolation threshold where the graphene volume fraction $\varphi = 0.08$. For pure WS_2 devices where $\varphi = 0$, the device mobility was 0.1 $cm^2\ V^{-1}\ s^{-1}$ and the on:off current ratio was $\approx 10^4$, whereas for graphene devices the mobility was 0.35 $cm^2\ V^{-1}\ s^{-1}$ and the on:off current ratio was 1.3. Hence although the device mobility improved with the addition of graphene, this came with a corresponding drop in the on:off current ratio. Since the on:off ratio worsened significantly faster than the other device properties improved, this is unlikely to be a feasible route to future device optimisation. However, this was able to provide some insight into the workings of the nanosheet network, with the network conductivity, mobility, and carrier density all following percolation scaling.

While all-printed nanosheet network transistors have been demonstrated, the switch from solid metal electrodes to porous graphene electrodes must be investigated to

ensure that such devices are performing optimally. In particular, the effect of the change in gate electrode must be investigated since the high capacitances associated with electrolyte gating run the risk of having the gate electrode affect the device performance. WSe_2 transistors were fabricated with printed graphene gate electrodes of different volumes, ranging from 10^{-4} mm^{-3} to 1 mm^{-3}. Below the threshold of gate volume = 10 × channel volume the gate geometry began to negatively impact the device performance since the gate capacitance was dominating the overall device capacitance, with the device mobility reaching values as low as 2×10^{-4} cm^2 V^{-1} s^{-1}. Above this threshold the device mobility remained constant with respect to gate volume at a value of $\approx 10^{-2}$ cm^2 V^{-1} s^{-1}. Fortunately, the porous nature of a nanosheet gate electrode means that increasing the gate thickness will be sufficient to ensure that the resulting device is unaffected by the gate capacitance, thereby avoiding the need to have very large area gate electrodes.

A major stumbling block in the optimisation of nanosheet network devices is the lack of in-depth understanding of the inner workings of the networks themselves. While these networks are by no means a complete unknown, obtaining more insight into these networks should help facilitate further improvements applied to nanosheet networks. Liquid cascade centrifugation was used to size-select WS_2 and $MoSe_2$ dispersions into multiple inks of different mean nanosheet size ranging between 37 nm and 488 nm, which were then sprayed into transistors. This allowed the changes in dry conductivity, wet conductivity, and mobility to be measured against nanosheet length. It was found that the dry conductivity increases with increasing nanosheet size, while the wet conductivity and mobility decrease with increasing nanosheet size. The same analysis was then performed on the device mobilities which found that for majority carriers (e.g. electrons in WS_2) the trend with increasing nanosheet size was in the opposite direction to the minority carriers. This demonstrated clearly that the carrier density of the nanosheet networks was what determined the direction of the trend with increasing nanosheet size. This also enabled an estimation for the mean nanosheet length that gave the optimal device results. For WS_2, the maximum mobility value was μ_e 4.96 $\times 10^{-2}$ cm^2 V^{-1} s^{-1} at $<L>$ = 69 nm. For $MoSe_2$, the maximum mobility value was μ_e 1.07 $\times 10^{-2}$ cm^2 V^{-1} s^{-1} at $<L>$ = 80 nm. Crucially, this data was also used to test a model relating the network properties to the properties of individual nanosheets, which was found to be able to successfully predict both the increasing and decreasing trends

with nanosheet size in each case. While the model is in need of refinement, this will be a useful tool for determining the optimum nanosheet size for future nanosheet network transistors.

Contents

List of Publications

1. Ó Súilleabháin, D., Vega-Mayoral, V., Kelly, A.G., Harvey, A. and Coleman, J.N., 2019. Percolation effects in electrolytically gated WS2/graphene nano: nano composites. ACS applied materials & interfaces, 11(8), pp.8545-8555. Basis for Chapter 5.

2. Biccai, S., Boland, C.S., O'Driscoll, D.P., Harvey, A., Gabbett, C., Ó Súilleabháin, D., Griffin, A.J., Li, Z., Young, R.J. and Coleman, J.N., 2019. Negative gauge factor piezoresistive composites based on polymers filled with MoS2 nanosheets. ACS nano, 13(6), pp.6845-6855.

3. Ó Súilleabháin, D., Kelly, A.G., Tian, R., Gabbett, C., Horvath, D. and Coleman, J.N., 2020. Effect of the Gate Volume on the Performance of Printed Nanosheet Network-Based Transistors. ACS Applied Electronic Materials, 2(7), pp.2164-2170. Basis for Chapter 6.

4. Garcia, J.R., Ó Súilleabháin, D., Kaur, H. and Coleman, J.N., 2021. A Simple Model Relating Gauge Factor to Filler Loading in Nanocomposite Strain Sensors. ACS Applied Nano Materials, 4(3), pp.2876-2886.

5. Kelly, A.G., Ó Súilleabháin, D., Gabbett, C. and Coleman, J.N., 2021. The electrical conductivity of solution-processed nanosheet networks. Nature Reviews Materials, pp.1-18.

Listing of figures

To my friends and family, this couldn't have been done without you.

Acknowledgments

I would like to start as so many others have by thanking Johnny for giving me the opportunity to work alongside so many excellent people. When I was but a young, innocent undergrad student doing my final year project in the Coleman group I was regaled with stories from the other postgrads about the joys and horrors that came with the PhD life, both by the rest of Johnny's group and by the man himself. As it turned out, the stories were all true. Luckily for me, I was able to do my fourth year undergrad project in this group and so I knew going in what kind of ~~mad~~ interesting people were waiting for me once I officially joined Johnny's group. The fact that Johnny himself is able to not only keep so many of us on track but manage to keep up our spirits and our enthusiasm for research is especially admirable, even if said encouragement sometimes took a liquid form. The fact that I only got 'fired' the one time still astounds me. I would also like to thank the staff in CRANN and the School of Physics for their help along the way: Ciara, Marie, Eva, Catherine, and Karl.

To the Coleman group, it has been one hell of a journey, and you've made the last four years an amazing experience. Special thanks have to go to Adam, who has tirelessly put up with my questions and complaints for a full four years, displaying an endless patience that I don't think I could ever match, and who has taught me all I know. From his advice on experiments to his seemingly endless store of scientific knowledge, it's hard to imagine getting through my PhD without him. Thanks to Victor for showing me the ropes, and reassuring me that 3pm was *not* too early to visit the pub. Thanks to Cian for all his help in the labs and his sterling advice on the nature of hope. To Yash, it's been a joy to work alongside you for the last four years, and we definitely upped the standards for the glühwein, no matter what some people might say.

To the rest of my fellow Colepeople, past and present, you've made my time in the group one that I won't ever forget. Conor, Seb, Andrew, Dave, Sonia, JB, Dan, Aideen, Tian, Kev, Harneet, Bharathi, Jose, James, Mark, Shixin, Dominik, Luke, Eoin, Jack,

Alina, Oran, and Emmet, there are almost too many of ye to list! You're an amazing group and I'm proud to have stood among you for a time.
Thanks to all the rest of my fellow PhD students in the School of Physics for their good craic on those Friday nights in the Before Times, back when I could still remember what the bottom half of your faces looked like. Thanks to Cansu especially for letting me raid her stash of coffee non-stop for the last two years.
Thanks to my parents, for supporting me through the last four years and putting up with me as I resolutely ignored your hints about moving out. One day I'll get a real job. To my non-physics friends, thank you for all the fun times and for learning quickly not to ask too many questions about what it is that I actually do.

If I never have to hear the word "Temescal" again, it will still be too soon.

If we knew what we were doing, it would not be called research, would it?

Unknown, commonly attributed to Albert Einstein

1

Introduction

The past 100 years have seen one of the greatest technological explosions in human history, leading to changes that would have been almost unimaginable at the start of the 20^{th} century. Not least of these was the development of the transistor, which ushered in the beginning of the information age we find ourselves in today. Following the successful isolation of graphene monolayers and the subsequent explosion in nanomaterial research, the beginning of the 21^{st} century has the potential to spearhead a similar rise in scientific knowledge. Although the current study of 2D materials is less than two decades old, it already shows great promise due to the breadth of potential applications from optoelectronics to energy storage to composites. This has coincided with a surge of research into additive manufacturing and printed electronics, which boasts such things as printed, nanomaterial-based sensors[1] and capacitors.[2] While such devices may not be in the same league as silicon-based ones, this is by no means a disaster for the field due to the emergence of such concepts as the Internet of Things, which would require large amounts of cheap, low-performance devices.[3,4] This is also the kind of field that best suits the electrolytically-gated transistors that are the focus of this thesis.

The current status of electrolytically gated devices is that while the proof of concept has been successfully demonstrated,[5] the performance of these devices still leaves a considerable amount to be desired. This is in addition to the fact that up until this

point the nanosheet networks themselves have largely been treated as a black box, and any route to optimising their performance will require a degree of knowledge as to their internal workings. With this in mind, the central hypothesis of this work can be considered to be as follows:

"How do we improve both our understanding and the performance of these nanosheet network devices?"

With this in mind, the aim of this work is to explore various avenues of optimising printed nanosheet network devices with the ultimate goal of making them viable for commercial, Internet-of-Things applications. While this endpoint is beyond the scope of this thesis, it is hoped that the results in this work will be a useful stepping stone on the road to achieving it.

Thesis Outline

Two-dimensional materials represent one of the most widely researched fields in modern science, with roughly 5% of all scientific publications nowadays being based on or in nanoscience. While the history of nanomaterials is an extensive one, ranging back to approximately 900BC when carbon nanotubes were unintentionally used to reinforce Damascus steel swords,[6] it was esteemed physicist Richard Feynman who laid the foundations for what would become the modern era of nanoscience with his famous talk: "There is Plenty of Room at the Bottom".[7] While scientists like Micheal Faraday had worked with nanoparticle dispersions even before this,[8] Feynman's lecture would soon be followed by the discovery of materials like C_{60} and carbon nanotubes.[9,10] However the discovery that truly set off the current gold rush of nanomaterials research is undoubtedly that of monolayer graphene in 2004,[11] demonstrating to the world the potential that lies within 2D materials. The properties of such 2D materials and the techniques used to fabricate them form the basis of Chapter 2.

After the synthesis of large quantities of nanosheets was achieved, the next step was to deposit them to form networks made up of trillions of individual flakes, and it is these networks and the devices made from them that will form the backbone of this thesis. Nanosheet networks have already shown great potential in batteries[12] and com-

posite[13] applications, and it is no surprise that they also show great potential in printed optoelectronics, showing properties that rival those of silicon and nanotube networks.[14] The specific focus of this thesis is on transistors derived from such printed nanosheet networks, and the formation and properties of these networks will be discussed in Chapters 3, as well as a brief overview of the current state of printed transistors. The techniques used to create and characterise these printed nanosheet network devices will be discussed in Chapter 4.

One major problem facing 2D material based transistors is the disparity between the properties shown by individual nanosheets versus those shown by a large network of nanosheets, since the junctions between adjacent sheets also contribute adverse effects to the network properties. In practise, this means that a network transistor will perform worse than the properties of the 2D materials that make up said network would suggest. One potential method of overcoming these effects is discussed in Chapter 5, where small amounts of highly conductive graphene flakes are added to a less conductive, semiconducting network to improve the performance of the overall device. The addition of graphene below the percolation threshold could improve the network mobility without adversely other aspects of the device performance. This also adds sorely needed insight into the inner workings of the network itself as the amount of graphene is increased.

Although fully printed electrolytically gated transistors have been demonstrated,[5] there is still a considerable amount of work necessary to ensure that such devices are operating at their optimum. In particular, any side effects that arise from switching from a metal electrode gated device to a printed nanosheet network gated one must be investigated, as the newly porous nature of the gate electrode must be considered when analysing such devices. The effects of the changes in the gate electrode are investigated in Chapter 6 By varying the volume of printed graphene gate electrode, it is expected that the properties of the device can be tuned to achieve the best performance, and to establish a benchmark for future work in all-printed transistors.

While it is increasingly clear that there exists a large gap between the properties of individual nanosheets and their networks that is due to the inter-nanosheet junctions,

pinning down the precise impact of these junctions has not yet been accomplished. Research into the inter-network transport properties and the effect that network morphology has on printed films is still in its infancy, and quantitative studies on these factors is limited. By using liquid cascade centrifugation to prepare devices out of inks of different mean nanosheet length, a means to investigate the inner workings of these networks can be developed. This was carried out in Chapter 7.

To conclude this work, a final evaluation of the main findings will be presented, alongside a discussion of potential ways to expand on the main results in the development of electrochemical transistors. It is hoped that the work presented here will be a building block in the field of nanosheet network based optoelectronic devices, and will provide useful information to future researchers. In particular it is hoped that the findings in this thesis will provide the foundations for producing optimised nanosheet network transistors by outlining the various investigations performed here and the outcomes that arose as a result.

A learning experience is one of those things that says, "You know that thing you just did? Don't do that."

Douglas Adams

2

2D Materials & Exfoliation

2.1 Two-Dimensional Materials

The first demonstration of free-standing monolayer graphene by Andre Geim and Konstantin Novoselov[11] changed the world of materials science forever. While knowledge of the existence of layered crystals had been around for decades if not centuries,[15,16,17] it had previously been theorised that single layers would be fundamentally unstable due to thermal fluctuations tearing the monolayer apart.[18,19] However, it was discovered that the surface of graphene is not atomically flat, but is instead slightly rippled, thus enabling it to survive as free-standing monolayers.[20,21] Since then scientists have rushed to unearth the potential behind these layered materials, with over one billion euro invested into graphene and related 2D materials by the EU alone.[22]

On a more general level, these two-dimensional materials are defined as those with one length dimension of between 1 and 100 nanometers, while the other two dimensions exceed 100 nanometers.[23] This also allows us to model these materials as a 2D electron gas where the electrons are free to move on an infinite plane, but are kept from moving freely in the third dimension by quantum confinement effects. The layered nature of these nanomaterials arises from the properties of the bulk crystal, with the covalent bonds within each layer being much stronger than the van der Waals bonds between

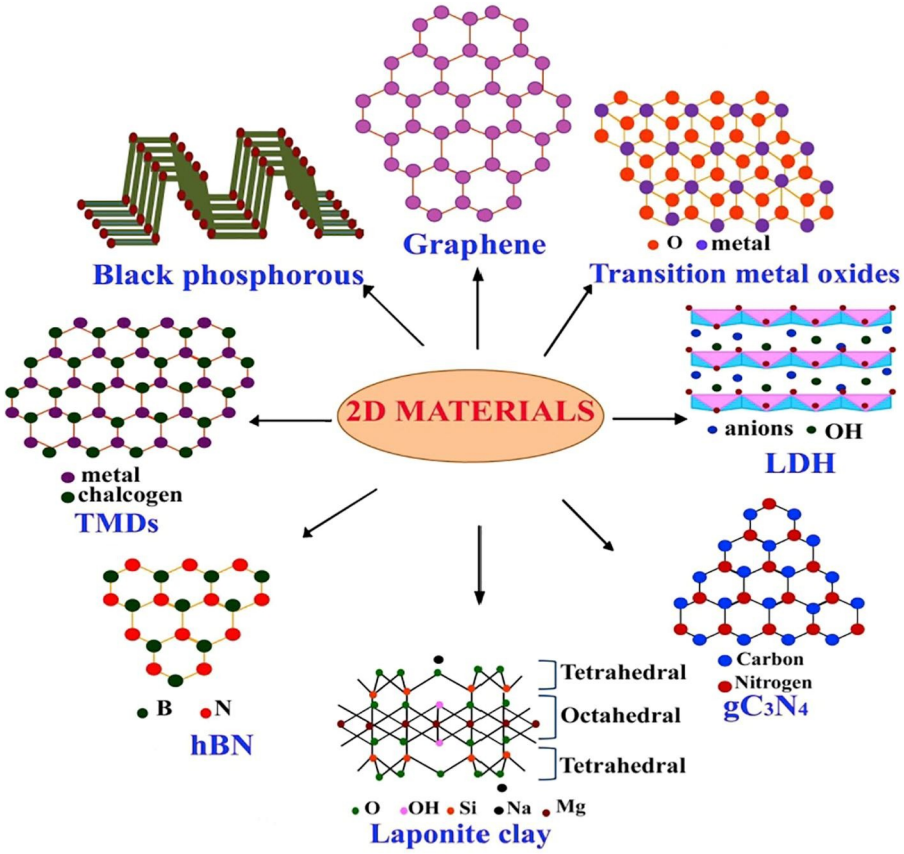

Figure 2.1: Some of the many types of 2D materials. Image adapted from Ref.[27]

adjacent layers. This means that if enough energy is applied it is possible to delaminate single layers from the larger crystal. It also means that the properties of the nanomaterials are going to be different from the properties of the bulk crystals since the electrons are now confined to a 2D plane. In the case of graphene, researchers soon found that the properties quickly diverged from that of bulk graphite, showing room temperature carrier mobilities far above that of the bulk crystal,[11] as well as remarkable optical,[24] thermal,[25] and mechanical properties.[26]

While graphene might be the most famous member of the 2D material family, there are many different types of 2D material and there are a wide variety of properties displayed by these materials.[28,23] Some of these can be seen in Figure 2.1, with the most well known including one-atom thick structures like hexagonal boron nitride (hBN), single-element monolayers like black phosphorus (BP), and transition metal dichalcogenides (TMDs) like WS_2 and MoS_2, to list but a few. In recent years these ranks have also been bolstered by two other families of 2D material: MXenes and perovskites, both

of which have generated increasing amounts of research interest.[29,30]

The sheer variety of 2D materials on display is also reflected by their properties, and many options can be found for metallic, semimetallic, semiconducting, and insulating nanosheets. The amount of available materials has sparked a lot of application-focused interest because this means that entire devices can be constructed entirely out of these 2D materials, and the choice of materials means that there are vast numbers of combinations available with different strengths coming with each one.

Now that graphene and other two-dimensional materials had been demonstrated to the world, the next step was finding ways to produce them in large enough quantities so that their remarkable properties could be fully explored. The scotch tape method used by Geim and Novoselov in their famous paper,[11] while very good at producing high quality monolayers, is unsuitable for any applications that require large amounts of material. It is therefore necessary to look to other exfoliation methods if we want to investigate the potential behind these materials. This chapter will focus primarily on the nanomaterials used in this work, with a particular emphasis on their electrical properties, before moving on to look at how these materials can be synthesised.

2.1.1 Conducting Nanosheets

As the catalyst for the current wave of 2D material-based research, it is no surprise that graphene had the most excitement surrounding it. This is not unearned, as even before 2004 the idea of a graphitic monolayer had been floating around the academic world. In the 1800s graphite was first shown to be layered,[16] and later on the first insights into what the properties of graphene would be came when PR Wallace predicted semi-metallic behaviour and a linear dispersion relation. This is particularly significant as it in turn implies that the effective mass of the charge carriers in graphene is zero.[15] It wasn't until 2004 that graphene began to be more than just a useful theoretical concept, when Geim and Novoselov used micromechanical exfoliation to successfully isolate single layers of graphene on SiO_2, each monolayer estimated to be only 3.5Å thick.[11] It didn't take long for researchers to flock to graphene as news of its remarkable electrical and mechanical properties became known.

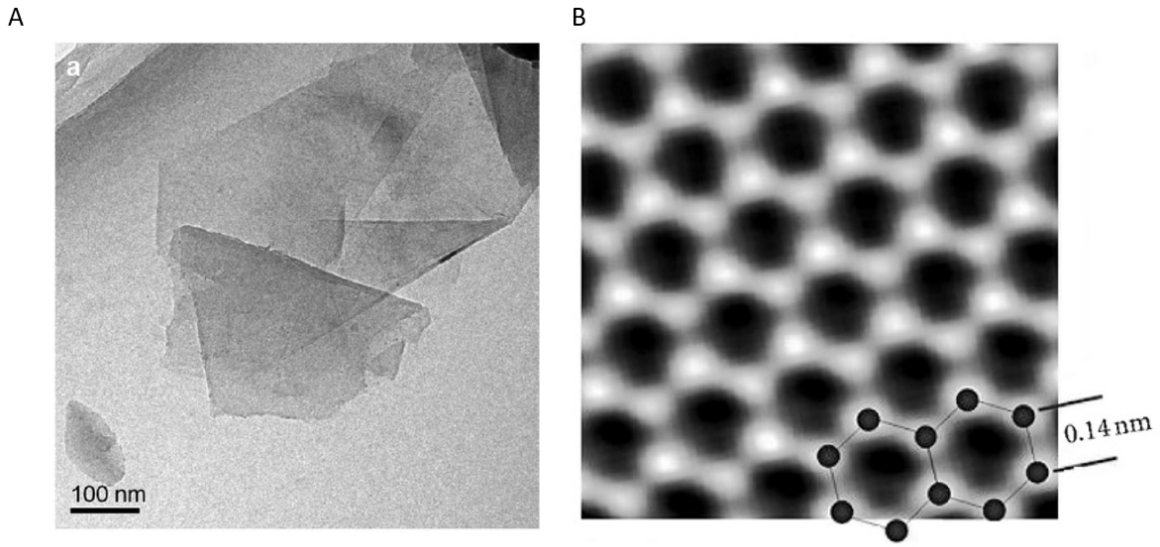

Figure 2.2: (A) TEM image of graphene nanosheets, taken from Ref[31]. (B) High-resolution TEM image of a graphitic monolayer showing the atomic structure of graphene, taken from ref[32]

A single graphene flake can be seen in Figure 2.2(A), showing its layered nature, but in order to understand the properties of graphene it is crucial to first investigate its structure. Graphene forms a hexagonal structure where each individual carbon atom is covalently bonded to three other atoms in the xy-plane, as can be seen in Figure 2.2(B), with each graphene layer being approximately 3.5Å thick. Each carbon-carbon bond is an *sp2* hybridised bond consisting of the $2s$, $2px$, and $2py$ atomic orbitals, leaving the $2pz$ orbitals standing perpendicular to the basal plane of the graphene sheet.

These in-plane carbon-carbon bonds are the reason behind the mechanical properties of graphene, being very resistant to any kind of dislocation due to the significant energy cost associated with replacing even a single carbon atom with a non-carbon atom. However, these bonds do not contribute to the conductivity of the nanosheet. Instead the remaining $2pz$ orbitals will each covalently bond to their neighbouring atom's $2pz$ orbital, where each contributes one electron to form a half filled π-band.[33,34] This π band is the source of graphene's valence electrons.[35] Graphene's ability to resist deformation and lattice impurities also has massive implications when considering its electrical properties, specifically when it comes to electron scattering. In general it is known that the resistivity of a material is heavily influenced by impurities and scattering defects, broadly considered under the umbrella of the mean free path of a charge

carrier as it passes through a material. Graphene's ability to resist such impurities and defects allows charge carriers to travel massive distances (>1μm) without interruption, a phenomenon known as ballistic conduction.[11,36] In real systems this is harder to achieve, due to the presence of external sources of scattering centres that exist near the graphene monolayer. These will be able to affect charge transport within the graphene and reduce the mean free path of the charge carriers. Similar to other 2D materials, graphene is particularly vulnerable to negative influence from external sources such as surface roughness, or effects from materials in contact with the nanosheets.[33] Indeed, the mobility of charge carriers in graphene has been found to be largely independent of temperature, leaving defect scattering and external scattering sources as the main factors limiting the performance of graphene devices.[37]

While graphene is by far the most famous of the conducting 2D materials, it is by no means the only one. As more and more 2D materials are successfully synthesised the number of available conducting nanosheets has grown similarly. One particularly noteworthy class of conducting nanosheets are MXenes, a family of layered ternary carbides and nitrides that have the general formula $M_{n+1}X_nT_x$, where M is a transition metal, X can be carbon or nitrogen, T is either -O, -OH, or -F, and n can be 1,2, or 3.[29] These nanomaterials are formed from their bulk precursor materials classified as MAX phase layered ceramic crystals (the A here being a group IIIA or IVA element). Unlike graphene and TMDs, the interlayer bonds are not van der Waals bonds and are too strong for the standard mechanical exfoliation methods utilised by Geim and Novoselov to work well. While it is theoretically possible to exfoliate MXenes in this way, the yield tends to be too low to be practical for applications. Instead, strong etchants such as HF must be used to remove the interlayer metal atoms (the 'A' components), allowing the remaining material to be exfoliated into 2D sheets. Computational analysis of MXenes suggests that they are broadly split between metallic and semiconducting behaviour, meaning that they can fill a wide variety of roles within the sphere of printed electronics.[38]

2.1.2 Semiconducting Nanosheets

Similar to graphene, the layered nature of transition metal dichalcogenides (TMDs) has been known to the scientific world for quite some time. MoS_2 for example was described as a layered crystal in the 1920s,[39]and the same discovery followed for many other TMDs in the decades following this.[40]In 1963, Frindt *et al.*[41] managed to exfoliate few-layer flakes of MoS_2 using the scotch tape method, and were quickly able to characterise the differences in electronic behaviour as the layer number decreased[42]. Work on Li-ion exfoliated MoS_2 has likewise taken place since the 1980s,[43] with the work of Joensen *et al.* managing to exfoliate single layers of MoS_2 in solution.[44] It was therefore no surprise that the new wave of nanomaterial research sparked by graphene would include TMDs, with particular focus on their remarkable properties as the crystals were scaled down to the monolayer. Indeed, their potential for 2D material research was raised by Novoselov in his 2005 paper.[45] Further investigation into single layers of TMDs was done in 2007 by Li *et al.*,[46] where they determined that the monolayer form of MoS_2 was a direct bandgap semiconductor, in contrast to bulk MoS_2's indirect bandgap. This was then confirmed experimentally in 2010 by Mak *et al.*[47]

TMDs are a family of inorganic layered crystals with a stoichiometry of MX_2, where M is a transition metal and X is a chalcogen atom, namely sulfur, selenium or tellurium. This means that the TMD family is a very extensive one, displaying metallic,[48] semimetallic,[49] semiconducting,[47], or insulating[50] behaviours depending on the material. This allows researchers to select a desired TMD based on the intended application.

A monolayer of a TMD consists of a hexagonal lattice of transition metal atoms bounded above and below by a hexagonal lattice of chalcogen atoms, giving the form X-M-X. The various possible permutations of M and X atoms are highlighted in Figure 2.3 The chalcogen atoms are offset from the transition metal atoms as can be seen in Figure 2.3(B) and (C). Each monolayer is roughly 7Å thick,[51,52]and the individual layers bond together via van der Waals interactions to form the bulk crystals. As with graphene, the bond strength is anisotropic with the van der Waals bonds being much weaker than the mostly covalent bonding within each layer.[50] They were therefore a

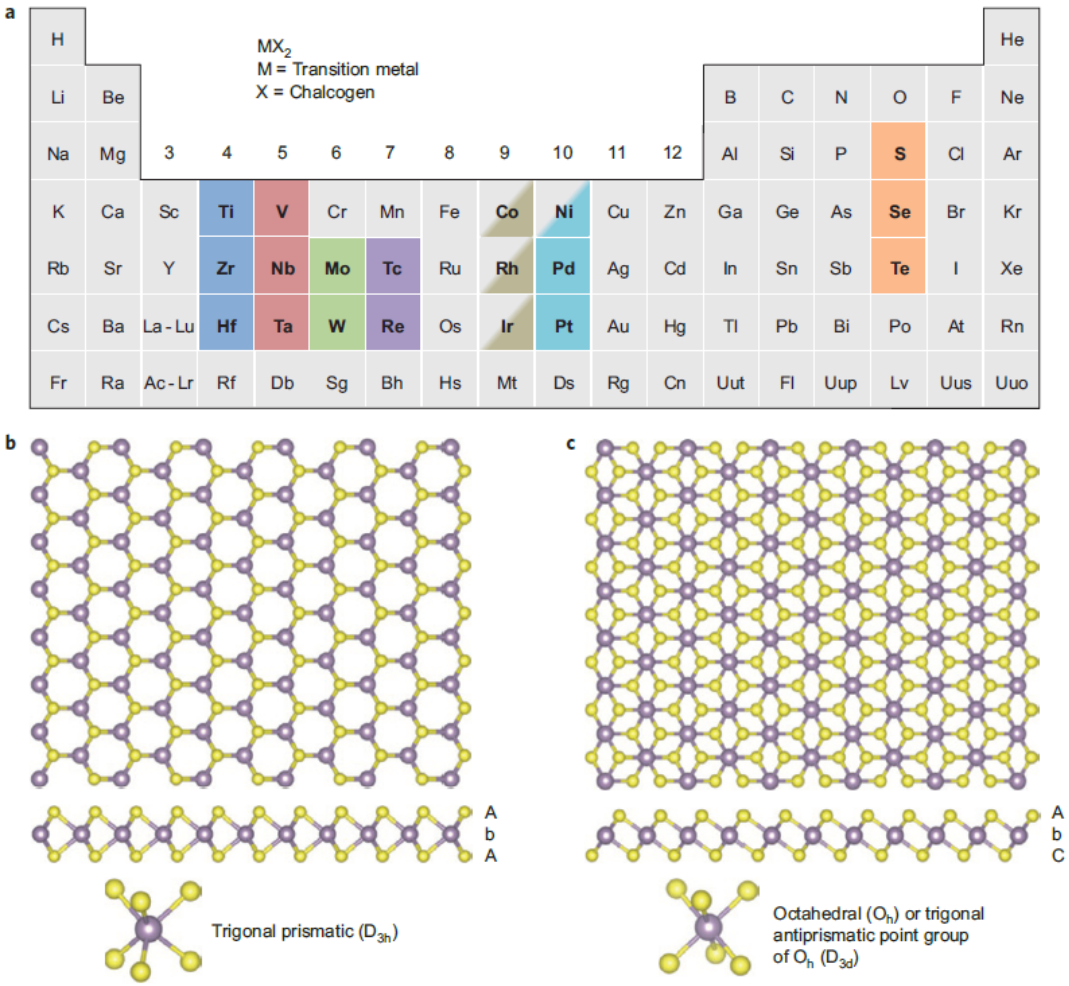

Figure 2.3: The variety of transition metal dichalcogenides, as well as the structure of individual layers and the polymorphs they can take on. Adapted from Ref.[50]

natural extension of the graphene gold rush, with a similar focus on exploring every aspect of the TMD nanosheets, ranging from their optoelectronic properties[53,54,55] to their use in mechanical applications.[56,57]

The chemistry of a given transition metal is primarily dictated by the number and energy level of the outermost *d*-orbital electrons, and it is the choice of transition metal that determines the band structure and therefore the properties of the resulting TMD. The strong interactions between the *s* and *p* orbitals in the metal-chalcogen bonds results in two large energy bands referred to as the bonding and anti-bonding bands, which lie far below and far above the Fermi level respectively. Between these bands lie the energy states corresponding to the transition metal's *d*-orbitals, and it is these *d*-orbital states that determine the properties of the TMD. For example, Group V TMDs have a half-full *d*-band which results in them displaying either metallic or

semimetallic behaviour, with the Fermi level lying within one of the *d*-orbital bands. Group VI TMDs on the other hand typically have filled *d*-bands which results in the Fermi level lying between *d*-orbital states, in turn leading to the material displaying either semiconducting or insulating behaviour. In general, the choice of chalcogen atom has very little effect on the properties of the TMD compared to the transition metal atom, but in general the higher the atomic number of the chalcogen atoms the smaller the bandgap of the resulting TMD.[50,58,33] A narrowing of the bandgap has been experimentally observed in molybdenum-based TMDs as the size of the chalcogen atom increases, from 1.9eV for MoS_2 to 1.1eV for $MoTe_2$.[51,59]

Another property of these materials that must be considered when dealing with them is the crystalline phase of the sheets. TMDs can crystallise in a variety of polymorphs, i.e. different arrangements of the M and X atoms within each monolayer, as well as different polytypes, i.e. the different arrangements of successive monolayers. In a given TMD, each transition metal atom can be coordinated with the surrounding chalcogen atoms to give either a trigonal primsatic (2H) or octahedral (1T) geometry, which can be seen in Figure 2.3(B) and (C) respectively. The numbers in 2H and 1T refer to the number of X-M-X units within the unit cell. When these monolayers are stacked, the geometry changes in turn, with the most common of the resulting polymorphs being 1T, 2H, and 3R, referring to trigonal, hexagonal and rhombohedral coordination. Each different type of TMD will have its own thermodynamically preferred phase, and in the case of Group VI transition metals this geometry is the 2H trigonal prismatic phase.[50]

One of the properties of Group VI TMDs that sparked a considerable amount of interest is the fact that the bandgap of the materials change as the bulk crystal is exfoliated down to a monolayer. We can look at the band structures of MoS_2 as calculated via density functional theory and chart the changes as the number of layers decreases as seen in Figure 2.4.[60] For bulk MoS_2, the valence band maximum is located at the Γ point and the conduction band minimum is located halfway along the Γ-K symmetry line, at the Λ point.[61] There is also a direct-bandgap transition located at the K point. The Γ point has significant contributions from the chalcogen p_z and

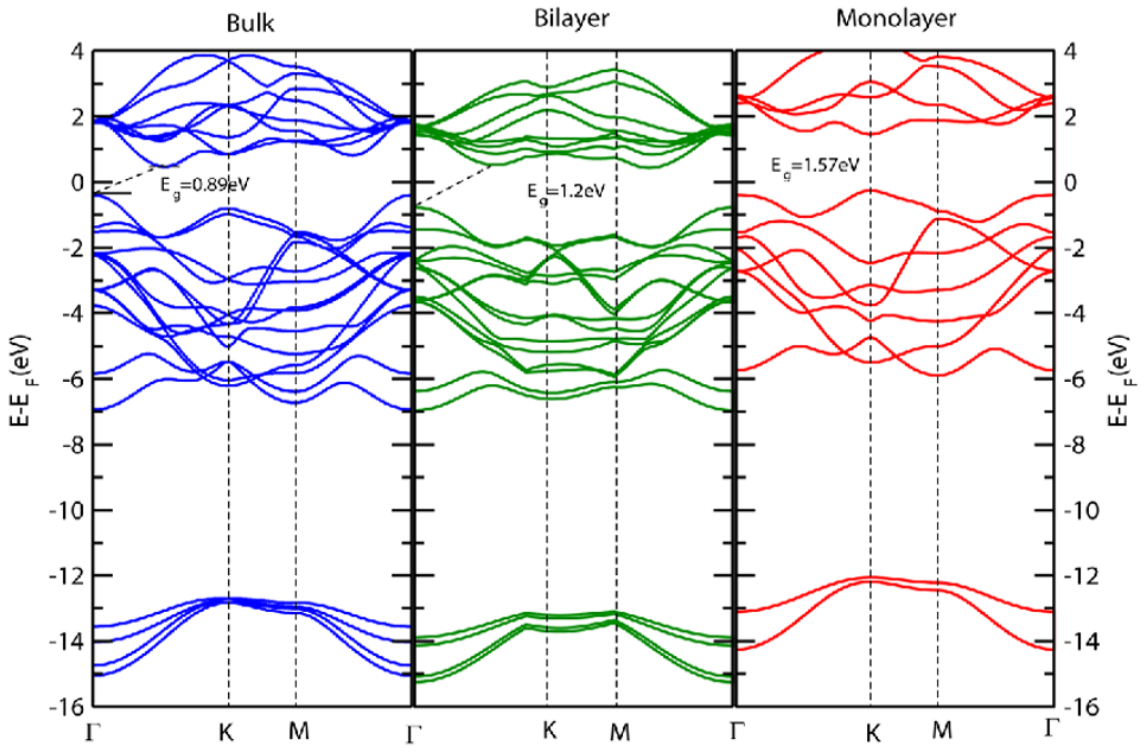

Figure 2.4: The band structure of MoS_2 as a function of layer number. Adapted from Ref.[60]

metal d_{z^2} orbitals, and the out-of-plane nature of these orbitals results in there being a significant amount of interlayer interactions contributing to the Γ point. Removing these interactions by reducing the number of layers causes the valence band height to decrease and the conduction band height to increase as quantum confinement effects take hold.[47,50,62] The K band on the other hand is largely unaffected by the decreasing layer number. The main contributions to the K-point are in plane d-orbitals that are strongly localised to the metal atom sites. Since these metal atoms are sandwiched between two chalcogen atoms, this means that there are minimal interlayer effects at the K point.[61,47] As the layer number decreases, the Γ-Λ energy gap finally becomes greater than the K point gap and the MoS_2 transitions to a direct gap semiconductor. This happens when it is reduced to a single monolayer. This can be experimentally confirmed by looking at the photoluminescence (PL) spectra of monolayer MoS_2 compared to bulk or even bilayer MoS_2, which shows an increase in the PL quantum efficiency of 10^4 from bulk to monolayer, and 10^2 from bilayer to monolayer.[47] This photoluminescence is also primarily located in the visible light spectrum, ranging from ~670nm for MoS_2[61] to ~400nm for WS_2[63].

Although the surface atoms in TMDs are reported to have an absence of dangling bonds,[64] this unfortunately does not translate to having the kind of high electron mean free path that graphene exhibits. Instead, the factors that limit electron transport in TMDs are generally missing chalcogen atoms or anti-site substitutions (in which a metal atom occupies what should be a chalcogen site)[65], with the dominant form of defect depending on the method in which the nanosheets were produced. TMDs are also known to be very sensitive to external sources of scattering, as well as effects from the contact metals, the properties of the substrate, and molecules adsorbed onto the nanosheet surface.[33] For these reasons, the mobility of TMD nanosheets tend to be much lower than those of graphene, but the presence of the modest energy bandgap ensures that TMDs will have a place in the wider 2D device sphere regardless. Theoretical calculations indicate that the mobility limit for MoS_2 is ~400 $cm^2V^{-1}s^{-1}$, and values reaching this point have been achieved on a SiO_2 substrate.[66,67] Although mobilities of ~700 $cm^2V^{-1}s^{-1}$ have been achieved using an ALD-made Al_2O_3 substrate[68] it seems unlikely that any further increases in TMD mobility will follow in future. Besides, there is still a lot of work to be done if mass-produced TMD-based devices are to meet the benchmark set by these devices, so future work will be optimising on bringing devices made in other ways.

Other notable kinds of semiconducting nanosheets include perovskites, a family of ceramics with the general formula ABX_3, where A and B are cations and X is an anion (usually oxygen). These materials have attracted a lot of scientific attention in recent years due to their high dielectric constants, ferroelectric properties and high-temperature superconductivity.[69] Because of the enormous number of potential perovskites, it is no surprise that there are many semiconducting variants among them.[30] Some metal halide hybrid perovskites such as $CsPbBr_3$ have been synthesised in platelet form and demonstrate high-lifetime photoluminescence. This has led to their use as the active material in solar cells, photodetectors,[70] and transistors.[71]

2.1.3 Insulating Nanosheets

Insulating nanosheets represent the final key component needed in order for functional electronic devices to be made entirely of 2D materials, since they are a critical part of any electronics fabrication process. The most famous of this group is hexagonal boron nitride (hBN), which consists of one-atom thick layers of boron and nitrogen in a similar structure to that of graphene. Indeed hBN was first exfoliated by Geim and Novoselov in their 2005 follow up paper in the same way as they had exfoliated graphene.[45] The two materials both consist of one-atom thick layers arranged in a hexagonal lattice structure, and this is why hBN displays many of the same physical properties as graphene, such as good thermal conductivity, mechanical strength, and robustness against defects and impurities. Unlike in graphene where the bonds within each layer are fully covalent, the inter-atom bonds in hBN are affected by the different electronegativity of the boron and nitrogen atoms, and hence each individual B=N bond has a polar component to it.[72,73] This is in contrast to graphene, in which the intralayer bonds have no polar character. This has a profound effect on the band structure of hBN, producing a bandgap of between 5.5 and 6eV.[74] The reason for the range of values for the bandgap shown in the literature is due to the tendency of individual sheets of hBN to slip and slide into more favourable conditions.[75]

Given its nickname of 'white graphene', it comes as no surprise that hBN is of considerable interest to materials scientists as a potential building block for heterostructure devices. With its excellent stability and physical robustness, it is ideal for use in stacked device structures and other heterostructures.[76] For example it was found that by placing a monolayer of graphene on top of a layer of boron nitride, the atomically flat plane of the hBN nanosheets smoothes out the wrinkles in the graphene monolayer while simultaneously stabilising it against destruction by thermal vibrations.[77,78] Most importantly, the hBN layers are also able to screen any external scattering sources that would normally limit the mobility of the graphene nanosheet, resulting in a measured mobility of 10^5 $cm^2V^{-1}s^{-1}$ for the graphene sheet.[79,80] It is also proposed that hBN layers can be used to encapsulate more atmosphere sensitive species of 2D material such as black phosphorus, although so far this has not been a 100% successful method.[81]

Another use is as the insulating component of devices such as capacitors and transistors. Since hBN can be easily exfoliated in much the same way as graphene, it can likewise be incorporated into a functional ink for printing. However, attempts to use hBN as the dielectric layer in thin film transistors (TFTs) have proven ineffective, with the hBN network layer instead screening out much of the gating effects so that only the semiconducting nanosheets closest to the dielectric experience the effects of the gate voltage. This leads to poor switching behaviour, which in turn limits the potential applications of this material.[5]

2.2 Exfoliation

Now that these monumental discoveries had been made, the next step was finding ways to consistently synthesise these materials. The initial discovery of graphene, and many other subsequent 2D materials, were mainly achieved using micromechanical cleavage.[11,47,82,45] This involves using adhesive tape to delaminate small numbers of layers from the bulk crystal, with further peeling steps producing thinner and thinner sheets until finally monolayers of the material can be isolated. These are then generally transferred to suitable substrates for characterisation. This method is good for producing thin and high quality flakes, but the amount of time and effort that goes into producing even a single such flake makes it unsuitable for wide scale industrial applications, which tend to require much higher yield processes.

The methods for producing high quality 2D materials can be broadly separated into two categories: bottom-up and top-down. Broadly speaking, bottom-up methods involve growing 2D materials on a desired substrate using elemental precursors, whereas top-down methods involve starting from a bulk layered crystal or powder and breaking it down into smaller and thinner layers. A schematic of this can be seen in Figure 2.5. As is unfortunately so often the case in science, no one method is inherently superior to any other method, since each one comes with its own set of advantages and drawbacks. As a result researchers tend to choose a suitable method based on what applications they have in mind for the material.

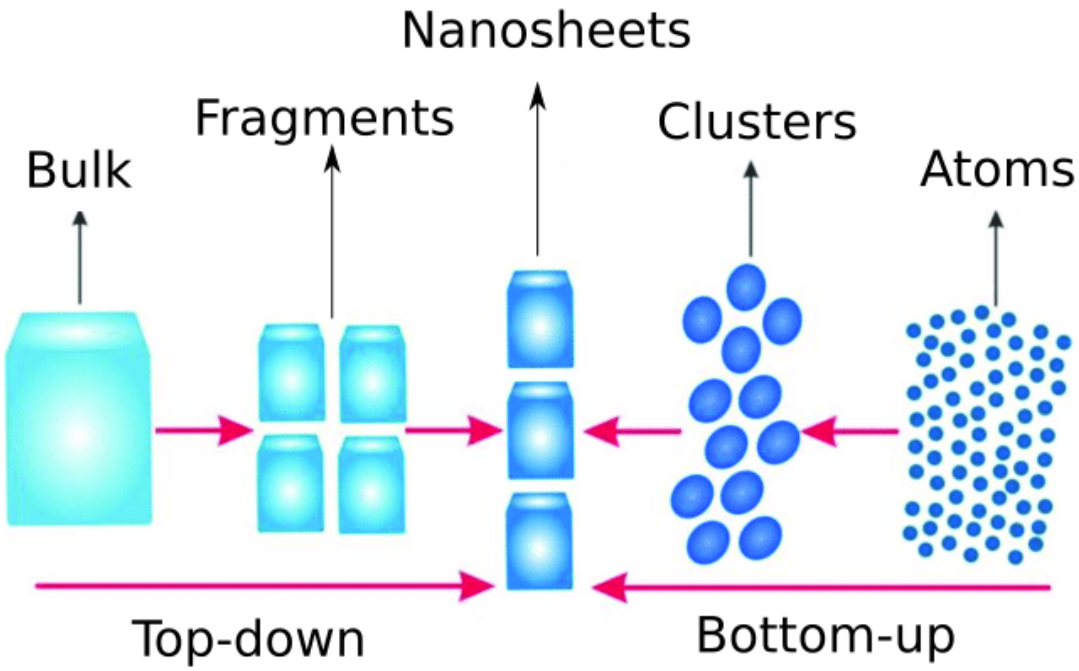

Figure 2.5: The two categories of nanomaterial synthesis. Adapted from Ref.[83]

The most well known bottom-up synthesis method is chemical vapour deposition (CVD), and in many ways it is a good representative of the strengths and weaknesses of bottom-up synthesis. CVD involves using a high temperature furnace to react one precursor in the vapour phase with a second precursor in solid phase,[84] for example reacting a thin film of molybdenum with vapour phase sulfur to produce MoS_2.[85] This method is capable of producing high quality single crystals on centimeter length scales, making it an ideal candidate for producing the kind of films needed for high end optoelectronic applications.[86] It also has the added bonus of being easy to integrate into the preexisting technological infrastructure used by the semiconductor industry. The main drawback of this method is the conditions required for CVD to take place. The synthesis environment also requires extreme conditions and expensive substrates, making them less than ideal for low-cost, low-complexity applications such as the ones aimed for in this thesis.[87] In addition, applications which require large amounts of mass tend to require scalability, which CVD techniques are unsuited for.

Top-down synthesis is more commonly called exfoliation, and its use in materials science dates as far back as the first investigations MoS_2 in the 1960s.[41] The original top-down method is the aforementioned micromechanical exfoliation, commonly known as the 'scotch tape' method. This method is however unsuited to any kind of large-scale application due to the time required to exfoliate single nanosheets, so researchers needed to develop other ways of exfoliating nanomaterials. These methods needed to be capable of producing large quantities of exfoliated material with few defects, with a view to mass-producing these nanosheets for applications.

Liquid based techniques quickly became one of the more appealing 2D material production avenues, following on from similar techniques used in carbon nanotube (CNT) production.[88] The advantage of this kind of method is that once the nanomaterials are dispersed in a liquid solution, they can be very easily processed into functional inks and deposited using a variety of techniques.[5,89,90] They can also be very easily and extensively characterised, since optical spectroscopic techniques can analyse the entirety of a liquid phase dispersion simultaneously, providing information on billions of nanosheets at once.[91]

The oldest of these techniques is intercalation, in which the bulk crystal is introduced to a chemical solution which allows molecules to be drawn between the layers, thereby vastly lowering the energy required to exfoliate each layer from the bulk crystal.[43,44,92,93,94] In some cases, the energy gap is reduced far enough that even as small a perturbation as simply stirring the resulting dispersion is enough to cause the layers to separate.[95] This dates back to when graphene oxide was first synthesised by chemically modifying graphite sheets to make it more hydrophilic. This drew water molecules in between the graphene sheets, widening the interlayer gap. Evolved forms of this technique can now be used to synthesise graphene oxide nanosheets of up to 50 μm in length.[96] These nanosheets could be stabilised with ionic or charge-neutral surfactants which adsorb to the basal planes of the nanosheets, preventing reaggregation. Similar methods exist to fabricate TMD nanosheets via intercalation. Lithium ions can be adsorbed between the TMD layers, which can then be reacted with water to produce hydrogen gas, widening the interlayer gap. Due to the fact that intercalation-produced nanosheets are subjected to less sonication time than LPE nanosheets, the lateral size and thus the aspect ratio of these nanosheets tend to be larger than those produced via sonication only.[94,96]

Unfortunately, in both of these cases the intercalation comes with a price. In the case of graphene, the severe amount of functionalisation needed to set the conditions for intercalation causes the resulting nanosheets to be insulating, a far cry from the magnificent properties of pristine graphene. While it is possible to chemically remove these unwanted functional groups and obtain reduced graphene oxide, the basal plane of these nanosheets will be left with a high concentration of defects and vacancies, making them unsuited to device-based applications. The TMDs are also affected by the process. In the case of MoS_2 intercalation, lithium and metals like it will donate electrons to the nanosheets during the process. When more than 0.29 electrons per MoS_2 formula unit is injected into the material, the process causes the *d*-band of the TMD to be filled completely. This results in the metallic 1T phase becoming more thermodynamically stable than the semiconducting 2H phase, and therefore the MoS_2 transitions from the 2H phase to the 1T phase.[43,97,98] Work continues on reversing or

avoiding this drawback, such as the work of Lin *et al.* in 2018,[99] which avoided filling the MoS2 d-orbitals by using much larger intercalation ions than the traditional Li-based intercalation. Since fewer of these intercalants are used per MoS_2 formula unit, fewer unwanted electrons are introduced to the nanosheets compared to standard Li intercalation. This allows the exfoliation of large, thin nanosheets which still remain in their semiconducting phase.

Finally, there is the fact that the intercalation process inevitably leaves behind waste products in the exfoliating solvent, which runs the risk of leaving waste products in any films fabricated from these inks and can require careful washing steps to remove. While this is by no means a deal-breaker, it adds an extra bit of complexity to the process which should be avoided if possible. Given the recent advances in electrochemical exfoliation of 2D materials,[99,100] it is quite likely that this will become the ideal method for high-performance LPE nanosheets.

2.2.1 Liquid Phase Exfoliation

Liquid phase exfoliation (LPE) was the method used during this work to exfoliate 2D materials. It is a simple, cheap and versatile method of producing 2D nanosheets from the bulk crystal, and these sheets can then be easily processed further into printable inks. Developed independently by Hernandez *et al.*[101] and Blake *et al.*[102] in 2008, it quickly proved to be very effective at exfoliating nanomaterials, capable of producing 2D flakes out of many layered crystals including novel materials like MoO_2[103]or everyday items like talcum powder.[104] The versatility of LPE can be seen most clearly in Figure 2.6, which shows a series of dispersions grouped by type. From left to right we see graphene, black phosphorus (BP), hBN; TMDs, transition metal oxides such as MoO_3; and transition metal hydroxides such as $CoOH_2$. In its most basic form LPE is a three-step process.[105] The first is dispersion, in which the bulk powder is immersed in a chosen solvent. The solvent must be chosen carefully so as to facilitate the exfoliation process, with different solvents being better or worse suited to the task. The second step is exfoliation, in which the bulk crystal is reduced to nanosheets in suspension. The exfoliation arises from acoustic cavitation effects, in which the ultrasonic waves

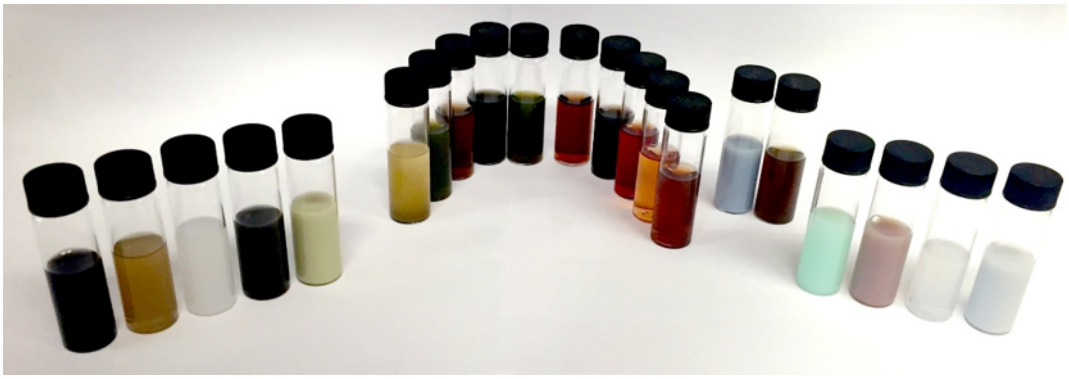

Figure 2.6: Some of the many materials that can be exfoliated using LPE, loosely grouped by type. From left to right: Group 1 is graphene, black phosphorous, hBN, TiB_2, GaS; Group 2 is TMDs; Group 3 is transition metal oxides; Group 4 is transition metal hydroxides. Image unpublished at time of writing, used with permission.

cause a series of microscopic bubbles to form within the solvent. These bubbles then collapse in on themselves within a few tens of microseconds,[106] creating a shockwave capable of overcoming the interlayer van der Waals forces. The third step is stabilisation, in which the nanosheets are prevented from clumping together and reaggregating once the exfoliation process ends.

It is important to note that the exfoliation process is also accompanied by a fragmentation process, in which scissions form along the nanosheet basal planes.[107,108] This reduces the lateral dimensions alongside the exfoliation process.The fragmentation process had previously been described as 'tearing' induced by either flake-container collisions or microjets that form during sonication, but while this description is useful it is incomplete, and by exploring how the fragmentation occurs it is hoped that it will lead to further optimisation of the LPE process.

Until very recently, the precise mechanism behind LPE was only known in the vaguest terms, and aside from the fact that cavitation-induced shear forces were what caused the formation of nanosheets the fundamentals of the process were largely unclear. In 2020, Li *et al.* investigated the process in detail by performing LPE on a single flake of graphite, and characterised the flake at various stages during the exfoliation process.[107] A schematic of the three main sub-processes taking place within the main exfoliation process is shown in Figure 2.7.

After sonicating the flake for five seconds it was found that the flake had ruptured

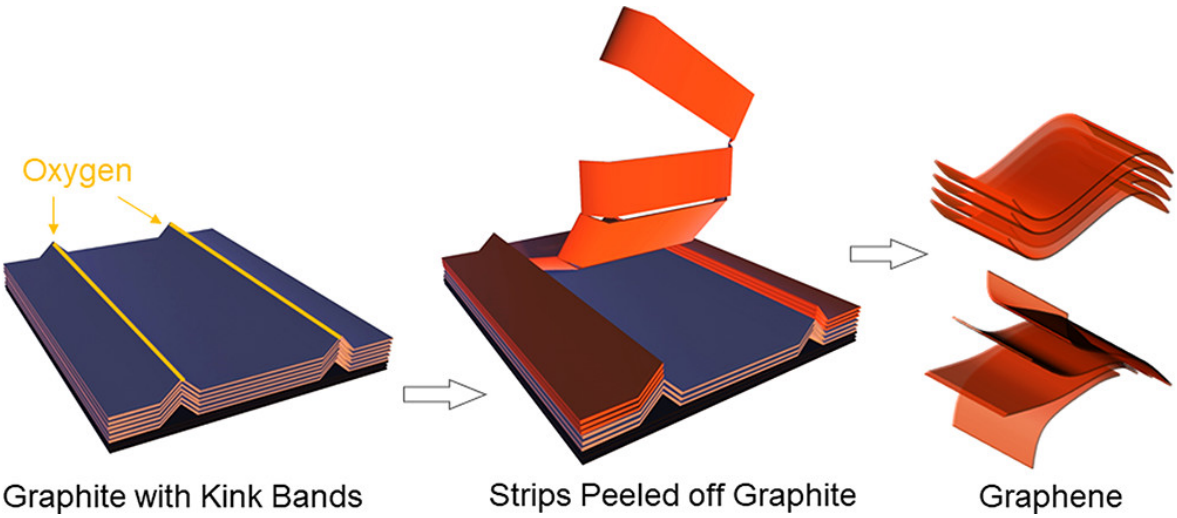

Figure 2.7: The three stages of nanosheet exfoliation via ultrasonciation: (A) kink band formation, (B) peeling off of graphite strips, (C) exfoliation. Adapted from Li *et al.*[107]

into two, with the fragmentation taking place both along existing defects and along newly formed kink bands. These kink bands, as seen in Figure 2.7(A), are areas where the flake had buckled along the z-axis, and were observed to form along crystallographic axes with formation being favoured along the zigzag axis. It had been suggested by previous works[109,110] that the tips of these buckles, i.e. where the carbon lattice becomes discontinuous, can be functionalised by oxygen atoms and therefore further weaken the flake along the kink band. Energy-dispersive X-ray spectroscopy (EDX) data confirms that the exposed edges of the flakes are much more oxygen-rich than the surrounding area. These kink bands were also observed forming in the absence of surfactants and impurities, suggesting that this is a physical process rather than a purely chemical one.

Once these kink bands form, they act as weak points in the graphite flake. The places where the curved bands peak leads to an increase in chemical reactivity at those points, which in turn leads to an increase in the amount of stacking faults in that part of the flake. This enables any graphite thin strips located between two such kink bands to peel off and enter into dispersion as seen in Figure 2.7(B), in a manner analogous to how carbon nanotubes can be unzipped to form graphitic flakes.[111] These strips are not yet thin enough to count as 2D materials, as measurements of the strips that peel away from the main flake show thicknesses approximating a few hundred nanometers.

This is where the final fragmentation process takes over, in which the thin graphite

strips are fully exfoliated into nanosheets as in Figure 2.7(C). The energy input from the sonication process is utilised both to create new flake edges (fragmentation) and new basal plane surfaces (exfoliation), where the lengths, widths and thicknesses of the resulting flakes can be expressed in terms of the surface energies of the edge and basal planes as follows[112]

$$\frac{\sqrt{L \cdot W}}{Nt} = \frac{2aE_E}{E_S} \tag{2.1}$$

Here L, W are the nanosheet length and width, N is the number of layers, t is the monolayer thickness, a is a constant, and E_E and E_S are the edge and basal plane surface energies respectively. Since E_E and E_S are material specific, and assuming as Backes *et al.* do that the constant a is independent of nanosheet thickness, it follows from this that the dimensions of the final flakes are primarily determined by the intrinsic qualities of the 2D material in question[113]. This suggests that the impact of the exfoliation solvent is primarily related to the rate of exfoliation, and indeed Li *et al.*[107] found that the above equation held across varying solvents, exfoliation times, and sonication methods.

As well as being able to easily produce nanosheets from a wide variety of starting materials, the LPE produced flakes were found to be almost completely defect free and unfunctionalised.[114] This was demonstrated in the case of LPE produced graphene by analysing the Raman spectra of the newly exfoliated flakes. These showed a strong and clearly defined G-band signal at 1580cm^{-1} which is characteristic of sp^2-hybridised carbon, whereas the $1350\,\text{cm}^{-1}$ D-peak associated with defects decreased as the nanosheet size increased. This suggested that the D-peak was due to the nanosheet edges, and that the sheets were free of basal plane defects.[115,116] However, other research groups have shown that LPE produced nanosheets do show basal plane defects for longer sonication times,[108] suggesting that the LPE process requires some degree of optimisation in order to minimise the appearance of defects. Longer sonication times in particular seem to be linked to a higher chance of basal plane defects, which will have unwanted and negative effects on the electronic properties of the flakes.

2.3 Stabilisation

Once the exfoliation process is completed and the sheets are in suspension, it becomes necessary to keep them from reaggregating before the dispersion can be put to use. There are a few different techniques, with solvent and surfactant stabilisation being the two most relevant to this discussion. Stabilisation using polymers is also a well-used technique, but will not be explored in as much detail.

2.3.1 Solvent Stabilisation

When choosing a suitable solvent for exfoliation, one must take into account both the properties of the solvent and how it interacts with the nanosheets. The ideal solvents for exfoliation are those that match the surface energy of the nanosheets as closely as possible, so that the energy cost of exfoliation and stabilisation of the subsequent dispersion is as low as possible. This rule of thumb follows on from similar investigations into exfoliation of CNT dispersions.[117] Figuring out precisely which solvents will match well with what materials requires a mix of solubility theory and statistical thermodynamics.[118]

To determine if a given solute:solution combination will work, the free energy of mixing must be determined.

$$\Delta G_{mix} = \Delta H_{mix} - T\Delta S_{mix} \tag{2.2}$$

where G_{mix}, H_{mix}, and S_{mix} are the Gibbs free energy, enthalpy and entropy of mixing respectively. The free energy indicates the amount of usable energy within the system that is available to do work. Mixing is thermodynamically favourable if $\Delta G_{mix} < 0$.

When dealing with a combination of rigid 2D flakes and a solvent, the enthalpy term is going to be the one that has the biggest impact on whether the flakes will be dispersed, since the rigidity of the flakes causes the entropy term to be much smaller than the enthalpy one.[119,94,120] It can be derived that the ΔH_{mix} term depends on the

Flory-Huggins interaction parameter χ as follows[121]

$$\Delta H_{mix} = \chi\varphi(1-\varphi)\frac{kT}{\nu_0} \tag{2.3}$$

where φ is the volume fraction of solute and ν_0 is the volume of a single particle. Given that ΔG_{mix} must be negative for favourable mixing, it follows that χ must be minimised. For negative values of χ, the solvent-solute interactions dominate and the nanosheets will be stabilised by the solvent. On the other hand, if χ is positive then the solute-solute interactions will take over leading to the nanosheets aggregating and crashing out of any dispersion. Utilising Hildebrand's 1936 solubility parameter δ, χ can be broken down further into the following[122]

$$\chi = \frac{\nu_0}{kT}(\delta_i - \delta_j)^2 \tag{2.4}$$

where δ_i is defined as the square root of the cohesive energy density for material i. It can be seen that matching the solubility parameters should lead to the most stable dispersions, although this equation is less accurate when taking polar solvents into account.

In 1967, Hansen modified the above formula to account for this discrepancy by dividing the solubility parameter δ into three separate components: dispersive, polar, and hydrogen bonding[123]

$$\delta^2 = \delta_D^2 + \delta_P^2 + \delta_H^2 \tag{2.5}$$

For a given polar solvent-solute mixture, the values of these three components for the solvent should be as close as possible to that of the respective solute in order to form a stable dispersion. Note that although the above equations suggest that it is not possible for χ to be negative, this does not account for the entropy of mixing which will always slightly skew the overall thermodynamics in favour of a stable dispersion when considering rigid 2D nanosheets.[94,120] It also needs to be remarked that the Flory-Higgins model upon which these equations are based relies upon certain assumptions to be true, for example the assumptions that the solvent and solute particles are the

same size and that χ is independent of the volume fraction of solute, which cannot be reliably assumed to be the case for nanosheet:solvent dispersions. Despite these limitations, the model is a useful tool to estimate the suitability of a given solvent for dispersing nanosheets.

Solvent stabilisation remains a very common way to make stable nanosheet dispersions, since it needs no additives or other chemical processes to be stable. This is particularly relevant when dealing with dispersions made for printing applications, since the presence of additives is almost always detrimental to the properties of a printed film. Solvent stabilised dispersions have also been observed to protect the nanosheets against oxidation by way of a solvation shell around the sheets, such as in the case of black phosphorus exfoliated in N-methyl-2-pyrrolidone (NMP).[124] This allows 2D materials that would otherwise be unstable in ambient conditions to be fabricated. It is also possible to exfoliate in a mixture of solvents, such as when 2D materials were exfoliated in a co-solvent mix of water and ethanol.[125,126,127] By tuning the relative amounts of each of the component solvents, the rheological properties of the solvent can be tuned to provide the best possible exfoliation environment.

As much as solvent stabilisation can be very useful, it isn't without its drawbacks. The solvents that are most suited to exfoliation tend to be high boiling point solvents such as NMP or N-Cyclohexyl-2-pyrrolidone (CHP), which are very difficult to remove after exfoliation. In addition these solvents are generally very toxic, and attempts to replace these solvents with less poisonous ones led to a reduction in the final yield.[128] Unfortunately the problems with these solvents are known to go beyond their toxicity. Exposure to the powerful ultrasonic waves involved in tip sonication has been shown to cause NMP to polymerise, which in turn leads to a considerable reduction in both the quality and the yield of CNT dispersions.[129,130]

While co-solvent dispersions have many advantages, they do not have the ability to fully replace the more traditional solvents like NMP. Direct comparisons between co-solvent dispersions and NMP dispersions reveal that both the total nanosheet yield and the percentage of monolayers were lower for the co-solvent dispersion.[131,132] Long term stability is also an issue with such dispersions, since co-solvents are very sensitive

to both temperature changes and differential evaporation rates. This means that the values of the surface energy γ, and thus the ability of the solvent to stabilise the nanosheets can change drastically.[127,133]

2.3.2 Surfactant Stabilisation

In contrast to using solvents, surfactant stabilisation generally requires much less fine tuning when preparing to exfoliate 2D nanomaterials[134,135]. By adding surfactants to a dispersion of precursor powder in water, the surfactant molecules adsorb to the surface of the nanosheets as they are exfoliated and then protect the dispersion against reaggregation via either electrostatic or steric repulsion, depending on the choice of surfactant. Anionic, cationic, zwitterionic, and non-ionic surfactants can all be used this way.[136,137]For the purposes of this discussion we will focus on the amphiphilic surfactant sodium cholate (SC).[138]

Sodium cholate dissociates in water to give a sodium cation and a cholate anion, after which the hydrophilic head of the surfactant remains in the water, while the hydrophobic tail adsorbs to the nanosheet basal plane. The charge disparity between the head and tail groups results in the formation of an electric double layer (EDL) around each nanosheet. Under the right conditions, this electrostatic repulsion is able to overcome the intersheet van der Waals attraction and keep the nanosheets from reaggregating.[87,139]

There has been a lot of theoretical work done to determine exactly what these conditions are, with independent studies looking into this in the 1940s by Derjaguin and Landau[140] and later on by Verwey and Overbeek[141] , from which was derived the DVLO theory of stabilisation. It predicts that for two spherical charged particles interacting in a liquid, the potential energy V of the system is as follows

$$V = \frac{\varepsilon_0 \varepsilon_r \, r^2 \, \zeta^2}{D} e^{-\kappa D} - \frac{Ar}{12D} \tag{2.6}$$

Here ε_0 and ε_r are the permittivities of free space and the liquid respectively, r is the particle radius, ζ is the zeta potential of the dispersion, D is the inter-particle distance,

κ^{-1} is the Debye screening length of the EDL, and A is the Hamaker constant.[142] The zeta potential indicates the size of the potential barrier from the repulsive force between two particles, and is key when considering the stability of nanoparticles in dispersion. The preferred values of the zeta potential are either >30mV or <-30mV, which will result in the particles in dispersion being electrostatically repelled. If the magnitude of the zeta potential is too low, this can result in the nanoparticles aggregating and crashing out of dispersion.[143]

One of the advantages of using surfactant stabilisation is that it allows for exfoliation in what would otherwise be non-ideal solvents like water, avoiding the need for toxic, difficult to remove solvents. Surfactants themselves are almost universally non-toxic, making them much better suited to environmentally friendly dispersions. Since surfactants are known to adhere to nanosheet surfaces very quickly after delamination, they tend to give smaller and thinner nanosheets compared to an equivalent solvent stabilised dispersion.[144] This means that a researcher can choose between solvent and surfactant based stabilisation in order to obtain a desired nanosheet size. If larger, thicker sheets are required, solvent stabilisation can be preferable, whereas if smaller thinner sheets are preferred then the optimal stabilisation route would be surfactants, assuming that both methods are otherwise equally viable, i.e. that atmospheric degradation and surfactant-induced doping are not a concern. Finally since a wide variety of potential surfactants are available, they can be selected based on the desired impact on the resulting nanosheets. Chosen surfactants can be positively, negatively, or neutrally charged as desired. As can be seen in Figure 2.8, the choice of surfactant is largely based on the desired effect on the nanosheets, since it will not affect the final concentration of the dispersion.[135]

Using surfactants does come with some drawbacks, the first being that the surfactants are quite difficult to remove from the nanosheet surfaces after exfoliation. A film created from surfactant-stabilised nanosheets will require lengthy annealing steps to ensure that the surfactants decompose and are removed from the film. Given that surfactant stabilisation frequently takes place in aqueous environments, this limits the variety of 2D materials that can be exfoliated in this manner, since some species of

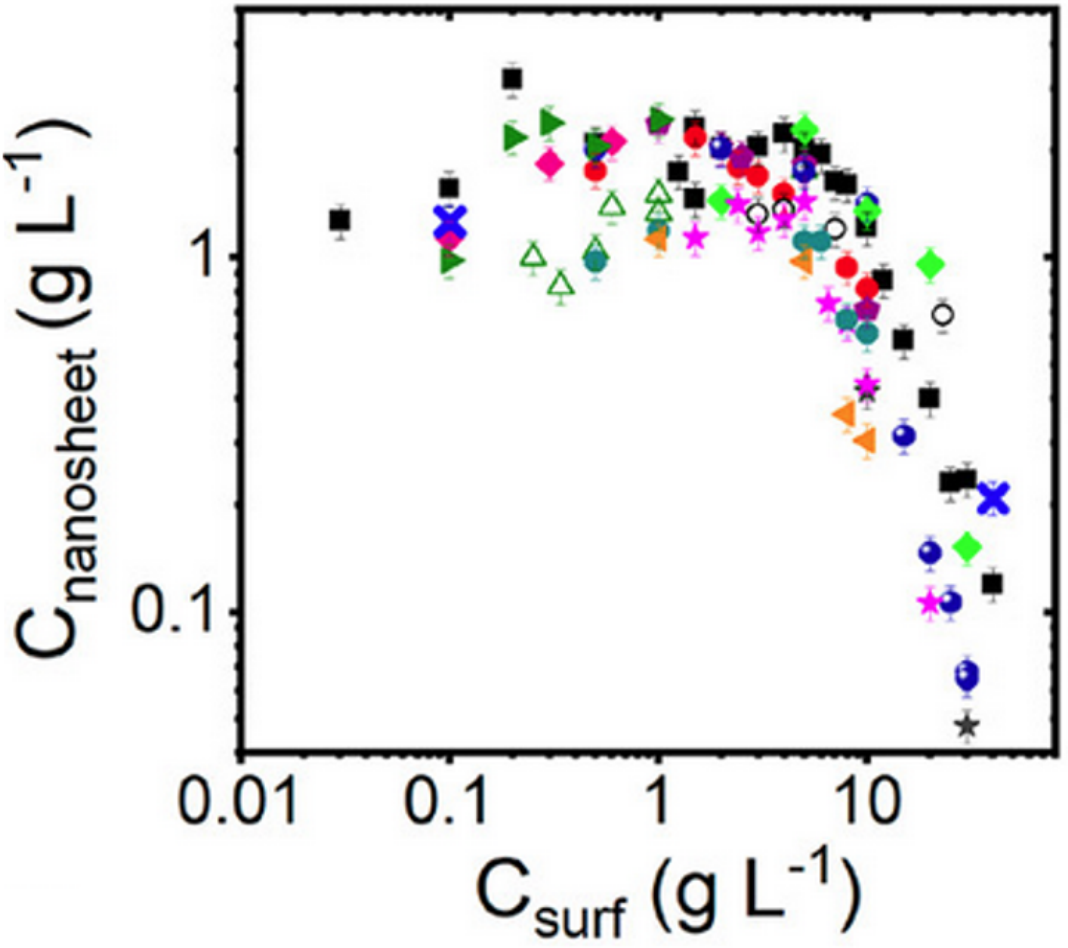

Figure 2.8: A plot of nanosheet concentration versus surfactant concentration for a range of different surfactants. Each different symbol represents a different surfactant. Image taken from Ref.[135]

nanosheet will degrade rapidly in such environments.

2.3.3 Polymer Stabilisation

Polymer stabilisation is relatively unexplored compared to solvent or surfactant exfoliation, and follows a very similar mechanism. One head of the polymer adsorbs onto the nanosheet basal plane while the rest of the many loops and tails of the polymer extends into the solvent. Here the repulsion mechanism is steric. When two nanosheets come close, the adsorbed polymers become restricted and the number of potential chain confirmations falls, causing an increase in free energy. This energetic cost associated with two nanosheets coming together means that it acts as a repulsive force.[134,145]

It is also possible to directly exfoliate in a polymer 'solvent', so to speak, without the need for an aqueous environment as is needed for surfactant stabilisation. This allows a significant degree of fine control over the viscosity of the exfoliation environment, in addition to facilitating the fabrication of composites. They can also be very useful for printing, given that they can both act as ink binders and assist in the printing process. This can prove very useful, such as when WS_2 exfoliated in aqueous poly (vinyl alcohol) PVA was shown to retain most of its monolayer optoelectronic properties even after the dispersion was deposited into a film, a process which normally results in a good degree of reaggregation.[146] The presence of the polymer molecules acts as a shield isolating one nanosheet from another, dampening the normal interlayer interactions.

As is typical of these methods though, polymer stabilisation is not free from drawbacks. Polymers are extremely difficult to remove from the nanosheet surfaces, which can in turn lead to changes in the nanosheet properties by way of doping. This is not in and of itself a drawback since targeted doping can be extremely useful, but not if pristine undoped nanosheets are desired.[4] Since polymer stabilisation is one of the least explored methods, there is a lot of potential for improvement in this area, and it's definitely a possibility that some of these drawbacks will be mitigated in the years to come.

2.4 Size Selection

An inescapable property of LPE-produced nanosheet dispersions is that they are polydisperse, the flakes displaying a wide range of both lengths and thicknesses.[112] The energy inputted into the system during LPE is not evenly distributed, which results in some parts of the starting crystals being exfoliated more than others. Some chunks of the parent crystal are not fully delaminated, resulting in large, thick sheets. Other flakes are fragmented severely, resulting in smaller, thinner flakes. This is a problem when considering the potential applications for LPE dispersions. Some like mechanical reinforcement in composites require large nanosheets, whereas others like catalysis require smaller nanosheets.[147,148] Printed electronics applications especially need to consider

the nanosheet thicknesses, since for TMDs the bandgap will be thickness dependent.

There are two main techniques used in order to obtain a more tightly controlled range of nanosheet sizes, namely density-gradient ultracentrifugation (DGU) and liquid cascade centrifugation (LCC). DGU methods rely on the subtle differences in buoyancy between nanosheets of different thicknesses, adapted from its initial use to sort CNT dispersions.[149,150] The nanomaterials are placed into a centrifuge tube containing a density graded medium (DGM), allowing nanosheets of different densities to settle under centrifugation at different points within the tube. They can then be extracted and redispersed to give dispersions with varying thicknesses. This technique is constrained both by low final yields and the presence of residual DGM in the dispersions, which adds an unwanted component when considering applications for the dispersions.

Liquid cascade centrifugation is a sedimentation based separation technique relying on the different sedimentation rates of nanosheets of different masses. This process occurs normally under gravity, and by centrifuging this process is sped up as the force is increased. The sedimentation rates are given by the Svedberg equation

$$s = \frac{m(1-\rho v)}{f} \tag{2.7}$$

where s is the sedimentation coefficient, m is the nanosheet mass, ρ is the solvent density, v is the volume in solution occupied by a single gram of nanomaterial, and f is the frictional coefficient. For 2D materials, the frictional coefficient depends on the length and thickness of the nanosheets and on the viscosity of the solvent. In general, larger nanomaterials experience more friction and will have higher f values.[151]

By performing successive size selections on a dispersion at several different speeds, the dispersion can be separated out into multiple ones with different mean lengths and thicknesses. Figure 2.9 shows how this is done, first by centrifuging at a low rpm to remove all of the unexfoliated material, then taking the supernatant and centrifuging that at a higher rpm. The resulting sediment will give a dispersion containing large, thick nanosheets. Trapping between two higher rpms can give smaller and thinner nanosheets, although with a lower mass yield. Notably, the dispersions will become

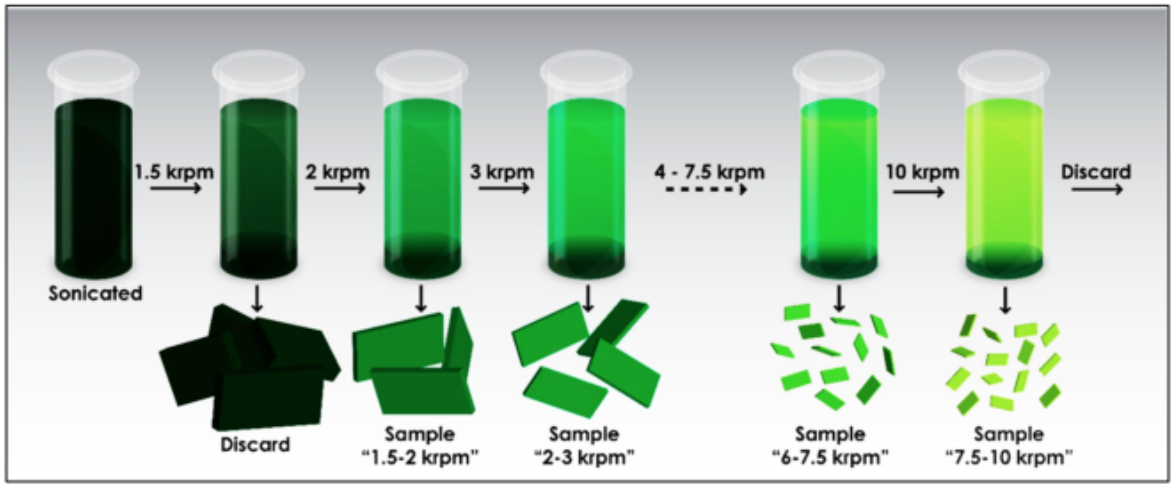

Figure 2.9: Liquid cascade centrifugation, showing the different size-selected Image from Ref[152].

more and more monolayer enriched after each successive centrifugation. This technique allows for a certain size of nanosheet length to be easily trapped between two fixed speeds. While this method is very simple and can reproducibly produce dispersions with a given mean nanosheet length, there are still some challenges left to be overcome. The dispersions produced are still polydisperse, and depending on the chosen trapping speeds can have quite broad distributions of nanosheet sizes. Lastly, any monolayers isolated via LCC tend to be very small. Since LCC sorts nanosheets by mass, and LPE dispersions have a well defined relationship between nanosheet length and thickness, it seems that this is an unavoidable drawback.[112]

We are stuck with technology when what we really want is just stuff that works.

Douglas Adams

3

Networks & Printed Electronics

While the field of printed electronics predates the modern surge in 2D materials, there is little doubt that these two fields were a match made in heaven. The ease with which liquid phase dispersions can be produced and the variety of the nanomaterials that can be made this way mean that all of the basic building blocks of optoelectronic devices are easily available for fabrication. Indeed, in the last few years a wide variety of devices have been made solely out of printed nanomaterials.[153,154,155] This has coincided with the printing technologies themselves becoming more and more advanced, with improved resolution and new fabrication techniques. Given the timescales that scientific progress tends to operate on, it is quite likely that the potential of this field has yet to be fully realised and that new and improved ways of printing devices will arise in the years to come.

Even so, printing electronic devices has become an extremely lucrative field, with some estimating that the printed electronic materials market is forecast to grow from $35.7 billion in 2019 to $363.1 billion by 2030,[156] with the sub-market of flexible printed electronics estimated to reach $6.9 billion by 2031.[157] The sheer potential of these devices is clearly not something that can be ignored, even if the field is still in its youth. This can be seen more clearly when one considers that the money invested into silicon devices at a similar stage in their development was of an equivalent level, and yet it took decades for silicon devices to reach their current stage. These printed

nanosheet devices include but are not limited to strain sensors,[57] gas sensors,[158,159] solar cells,[160,161] super-capacitors,[162,153] and transistors.[163,5,164]

3.1 Preparing Functional Inks

Although at first glance it might seem straightforward to prepare a suitable ink for printing a liquid phase exfoliated nanomaterial, the reality is somewhat more complicated. As discussed in Chapter 2, some solvents are better at stabilising LPE dispersions, but these solvents more often than not tend to be unsuited for printing purposes due to high boiling points and toxicity.[87] Getting the properties of the ink right is critical for many of the printing methods discussed in this chapter to work properly, not to mention the impact that ink rheology has on the formation of the final printed films.[134] Malkin and Isayev[165] state that if printing results are to be properly reproducible, then the rheology of the inks must be both tightly controlled and within a particular range when it comes to properties like the ink viscosity and surface energy. The precise range needed will vary based on the nanomaterial, printing method, and surface energy of the substrate.[166,167]

The requirements of the inks are also going to be different depending on the deposition method in question, with some methods coming with much stricter requirements than others. Drop casting, for example, can be done with most inks without needing to alter the properties of the ink, whereas inkjet printing can only be done with strict control over the ink rheology.[166] This is further complicated by the fact that some inks contain substances other than just the solvent and the desired nanomaterial. Materials that are unstable against aggregation in aqueous environments require additives to be stable, which will in turn affect the rheology of the ink and the way in which it will be printed. This also means that an extra annealing step will need to be performed to remove the additives from the final film. Not to mention the fact that different nanomaterials will affect the ink properties in different ways, with the shape and spatial arrangement having significant effects.[168] Dispersions containing a higher concentration of nanoparticles will be more viscous,[169] and high aspect ratio nanoparticles such

as platelets will have higher viscosities than an equivalent concentration of spherical nanoparticles.[170] This will also have an impact on what printing methods are best suited to printing a given ink, since different printing methods will require different ink viscosities.[134]

As no one solvent offers the desired properties for both exfoliation and printing, we employed a solvent exchange process in this work. Here, we chose to exfoliate in a solvent suited to stabilising nanosheets in order to obtain a higher yield of nanosheets, which were then transferred into a solvent better suited for printing.[171,5] NMP for example, while ideal for exfoliating nanosheets, has a high boiling point and is highly toxic and for these reasons is known to be very hard to remove from printed films after the fact. Although adding an annealing step is an option, this in turn limits the potential substrates that can be used. In particular, PET begins to burn at temperatures above 110 °C. Surfactant-based exfoliation methods suffer from similar drawbacks, since the surfactants must be removed from the printed films in order to prevent them from interfering with the network properties. This can be done via annealing or by washing the films, both of which add additional and unwanted complexities and restrictions to the fabrication process.

3.2 Deposition Techniques

It should come as no surprise that there are a good number of different printing methods, and as is the case with the exfoliation techniques discussed in Chapter 2, the decision of which printing technique to use is largely up to the researchers involved, with different techniques having different advantages and drawbacks. Some printing methods like spray coating are suited to making large numbers of devices in parallel, others like drop casting are employed to making devices when there is a limited quantity of material available. Hence the choice of method is going to be primarily dictated by the amount of material available, the qualities of the ink, and the end-goal for the resulting devices.

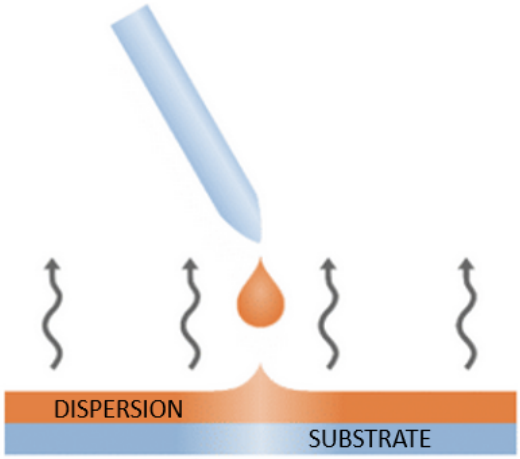

Figure 3.1: Schematic of a drop casted film. Image adapted from Ref.[176]

3.2.1 Drop Casting & Spin Coating

Drop casting is by far the simplest method of depositing nanomaterials onto a substrate. It involves pipetting the nanomaterial ink onto a chosen substrate, which can be rigid or flexible, at room temperature or heated.[172,173,174,175] A simple schematic of the drop casting process can be seen in Figure 3.1(A). The dispersion (orange) is pipetted onto the substrate and allowed to settle. The solvent then evaporates from the substrate to form a thin film, which is typically annealed to ensure that any residual solvent is removed. This technique's simplicity also applies to the inks it can be used on, since it doesn't require the ink to fit any particular parameters and can instead dropcast most dispersions as received. This is due to the fact that the key parameter for drop casting isn't the properties of the ink but instead involves controlling the morphology of the dispersed nanomaterials. To that end the key interactions are those between the solvent and the substrate.[177] In the ideal printing case, the surface energy of the ink and of the substrate will be as close as possible. A good match between these surface energies will determine the contact angle of each drop as well as causing the diameter of each droplet to be fixed, known as contact-line pinning.[178]

Drop casting is also a very material-efficient process since almost none of the drop casted nanomaterials will be wasted, making it suited for fabricating thin films out of a limited supply of material. A key strength of this method is that it is well suited to

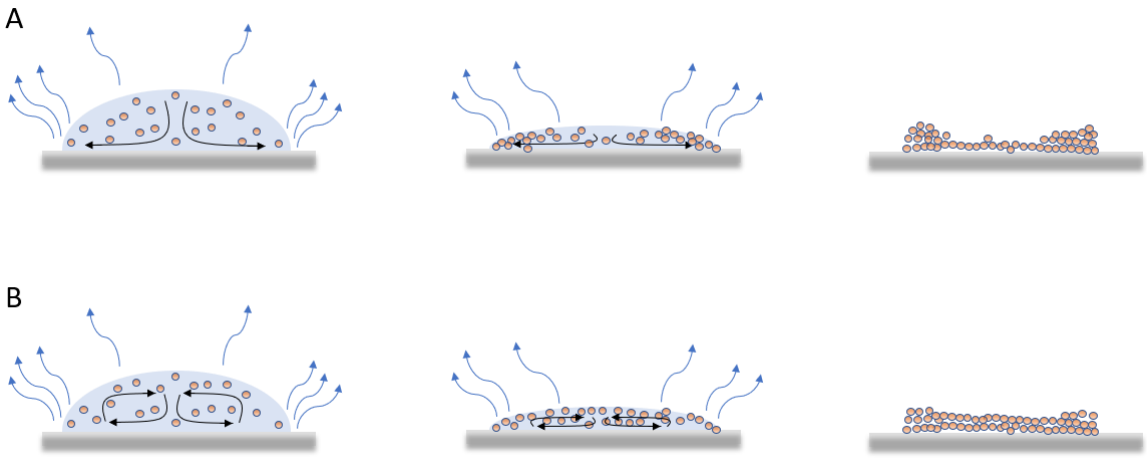

Figure 3.2: (A) The drying process in an average droplet of a nanomaterial ink. As the solvent evaporates, more material builds up at the droplet edges. (B) The drying process in a droplet with a recirculating flow. This results in a more even deposition of material.

fabricating vertical heterostructures, since it is trivial to deposit a second nanomaterial on top of a dried film of the first nanomaterial, provided steps are taken to avoid redispersion of the initial layer. These steps can involve using different solvents or binders to stabilise each layer such that each layer is stabilised using a solvent that is not suited to stabilising the layers below and above it. For example, Withers *et al.* used successive drop casting steps to fabricate heterostructures based on several different kinds of nanosheet, including graphene, hBN, and TMDs.[90]

Unfortunately, this comes at a cost, namely that the quality of the resulting film is generally quite poor. Because the films are formed by evaporating the solvent, the resulting film is affected significantly by drying effects. These are known to lead to inhomogeneities and non-uniform thickness profiles,in turn negatively impacting the electrical properties of the film. In particular, the "coffee-ring" effect arises out of the most likely way that the ink droplet dries on the substrate. After the droplet is deposited, the edges of the droplets are subject to higher evaporation rates than the centre as a result of the droplet edges having a higher surface area to volume ratio. Since the edges of the droplet are pinned in place by solvent-substrate interactions, this causes a flow of solvent and material outwards from the centre of the droplet, replenishing lost solvent. As evaporation continues, this results in much more of the dispersed material being deposited around the edges of the droplet rather than being

evenly distributed throughout the area of the drop.[179,180] This results in an uneven ring with little to no material being deposited in the centre of the droplet.[181,182] An example of this can be seen in Figure 3.2(A).

While it is not impossible to turn coffee-ring formation to one's advantage,[183] the lack of fine control over the film uniformity makes it much more ideal to find a way of avoiding this effect,[184,185] and indeed doing so in one way or another is a requirement for making consistently homogeneous films.

One solution to this problem is to modify the starting ink in order to introduce a recirculating Marangoni flow to the drying process. This is a phenomenon in which rather than a purely outward radial flow which moves material to the droplet edges, a recirculating flow is induced within the droplet which will move material inwards as more solvent evaporates. This results in the dispersed material being evenly distributed throughout the droplet area, as shown in Figure 3.2(B). While there are many ways to induce a Marangoni flow, including via surfactants, heating, or suitably concentrated inks,[186,180,187] an ideal way of doing so is via co-solvent inks. Differences in the evaporation rates between the two solvents causes a surface tension gradient to form within the droplet, in turn driving the Marangoni flow and resulting in a much more uniform film.

While there are other techniques that have managed to reduce the impact of the coffee-ring effect, for example by drop casting the films in a solvent-saturated environment to slow down the rate of evaporation or to sonicate the film as it is drying,[188,189] they aren't able to fully address the lack of fine control over the features of the final film. For these reasons drop-casting is best suited for making films that don't require this level of control over the homogeneity and other features, such as films for fuel cell and energy storage applications.[190,191]

Spin coating is a natural evolution of drop casting, given that it can essentially involves the same process except the dispersion is dropcast onto a spinning substrate. This technique has been used in the wider semiconductor industry for decades, meaning there are considerable advantages in fabricating nanomaterial thin films using this method since it guarantees a degree of compatibility with existing infrastructure. To

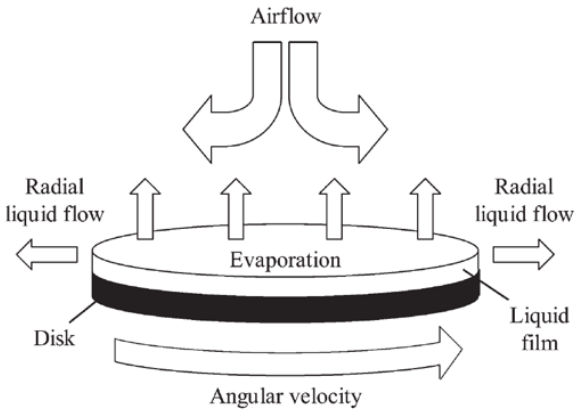

Figure 3.3: Schematic of a spin coating setup. Image taken from Ref.[192]

form a spin coated film a nanosheet dispersion is dropcast onto a substrate, which is then accelerated to a high angular velocity, typically between 1 and 10 krpm depending on the ink in question.[193,194] This is shown in Figure 3.3, which also notes some of the processes taking place throughout the spin coating procedure. The centrifugal force spreads the droplet across the entire area of the substrate while simultaneously prompting rapid evaporation of the solvent, with any excess liquid being ejected from the film by the same force. This results in a thin, uniform film, although the precise nature varies significantly with both the properties of the ink and interactions between the substrate and the various components of the ink.[192] For instance Wang *et al.*[195] found that, assuming a very fast angular velocity, the final film thickness is independent of the initial film thickness and inversely dependent on the square root of the ink viscosity and ink density. In particular, the angular velocity of the substrate has a significant effect on the film thickness, with the film thickness showing an inverse dependence on the angular velocity.[196,195]

Like drop casting, the ink must be tailored with regard to the substrate, in this case to ensure that the film will be uniform.[197] The main way of accomplishing this is to ensure that the solvent preferentially wets the substrate, thus driving the nanomaterial to the surface of the fluid layer and forming more homogeneous films. The payoff that comes with the large number of factors to consider is a lot of control over the final film, both in terms of the film's thickness and the resulting morphology. The thickness can

be reproducibly adjusted between microns and a few nanometers as needed,[198] even down to the level of single nanosheets such as in the case when Yang *et al.* fabricated single-sheet films of black phosphorus on gold electrodes.[199]

Spin coating is therefore an excellent method when tight control over the film structure, thickness, and homogeneity are needed. As is unfortunately inevitable however, the benefits of spin coating come with some unavoidable disadvantages. In order to apply an even coating to the substrate the nanosheet ink must be at a high concentration,[105] and after the spinning stage a substantial amount of the ink will be lost, increasing the amount of material required to make a film even further. Furthermore, it is again restricted by the lack of patterning ability, and it is for this reason that other methods were used during these projects.

3.2.2 Spray Coating

Similar to spin coating, spray coating is both a conceptually simple and widely used printing technique. First introduced in the late 18th century, the concept has evolved over the years with the quintessential aerosol spray can being developed in 1941. Considering that this technique quickly found a home in the manufacturing sector for depositing large quantities of polymers,[201] it was only a matter of time before it was used to deposit nanomaterials, such as carbon nanotubes or LPE nanosheets.[202,102]

Spray coating works by gravity-feeding an ink into a nozzle and atomising it so that the resulting aerosol is deposited on the desired substrate, as shown in Figure 3.4. The atomisation can be achieved in a variety of ways ranging from compressed gas backpressure, electrospray, or ultrasonic waves,[203,204,205] but for the purposes of this work we will be focusing on atomisation using pressurised nitrogen gas. When the ink and the gas meet, the shear forces arising at the ink reservoir-nozzle interface turns the ink into micron-sized droplets, which the carrier gas then transports to the substrate.

The spray coating process requires quite a bit of optimisation to achieve an even spray deposition, since there are a significant number of factors that need to be considered when depositing a film in this manner. These include the carrier gas pressure, the distance between the spray gun and the substrate, the ink viscosity, the size of the

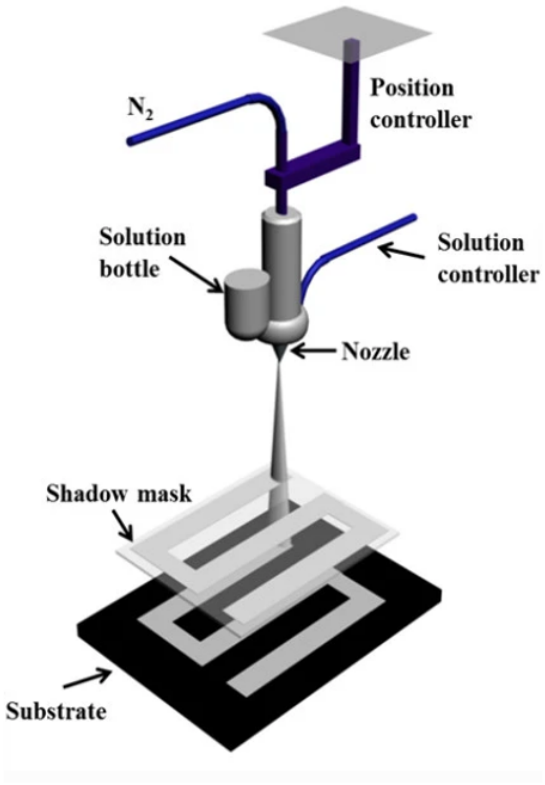

Figure 3.4: Schematic of an aerosol spraying setup using shadow masks. Taken from Ref.[200]

spray nozzle, and the mean size of the particles being sprayed. For instance, if the spray gun is too close to the substrate then the gas will blow away unevaporated droplets resulting in a significant loss of material. If it is too far away from the substrate then the droplets will evaporate before they reach the surface, resulting in poor network formation and lower quality films. Of these factors, the most important to control is the carrier gas pressure, since this parameter will control the droplet size.[206,207] Higher backpressures lead to smaller drop sizes, which evaporate faster and have been observed to improve network uniformity.[208,209] In particular, smaller droplets are less susceptible to the coffee-ring effect as the solvent will evaporate too quickly for a significant amount of radial solvent flow to take place within the droplet.[208] This also serves to highlight the benefits of using a low-boiling point solvent such as isopropanol and of spraying onto a heated substrate, both of which will further increase the rate of solvent evaporation.[206] This can be expedited by heating the substrate during the spraying process, further increasing evaporation rates.[210]

A key advantage of spray coating is that it can easily spray hybrid inks, i.e. inks

with multiple active components such as the 2D:2D composite inks which will feature in Chapter 5. The composite inks can have different viscosity η and surface energy γ, meaning that the spraying parameters could need to be altered when moving from one composite loading level to another in order to ensure that the network remains consistent. The main downside to spraying is the lack of resolution, which often forces the use of shadow masks to define the limits of the sprayed area. Hence, while the simplicity of the spray coating technique makes it ideal for scalable processes and the fabrication of large quantities of devices where the feature size is relatively large,[209] any fabrication process which needs high resolution will need to use a more precise technique.

3.2.3 Inkjet Printing

Inkjet printing has been the subject of a lot of attention in the field of additive manufacturing. It is a relatively low-cost, versatile, non-contact deposition technique which makes it ideal for controlled deposition of nanomaterial inks. Unlike spray coating, inkjet printing also allows for much tighter control over the deposition area, and doesn't require the use of shadow masks to define the printing resolution. This, combined with the almost zero loss of material involved, makes inkjet printing an ideal technique for fabricating devices out of 2D materials.

Inkjet printers come in two types, continuous inkjet printers and drop on demand (DoD) printers. Continuous inkjet printers have a constant stream of droplets being deposited onto the substrate until an electrostatic charge is applied, which redirects the droplets into a waste reservoir. This technique was later refined into the DoD method, which was much more accurate and came with increased control over the patterning of the final films.

While it is not the only type of DoD printer, for the purposes of this work we will be focusing specifically on piezoelectric inkjet printers. These are preferentially used for printed electronics applications since thermal inkjet printers are made specifically to print aqueous inks, whereas piezoelectric printheads can print in multiple different solvents.[211,87] Within the printhead, each nozzle contains a small ink reservoir and a

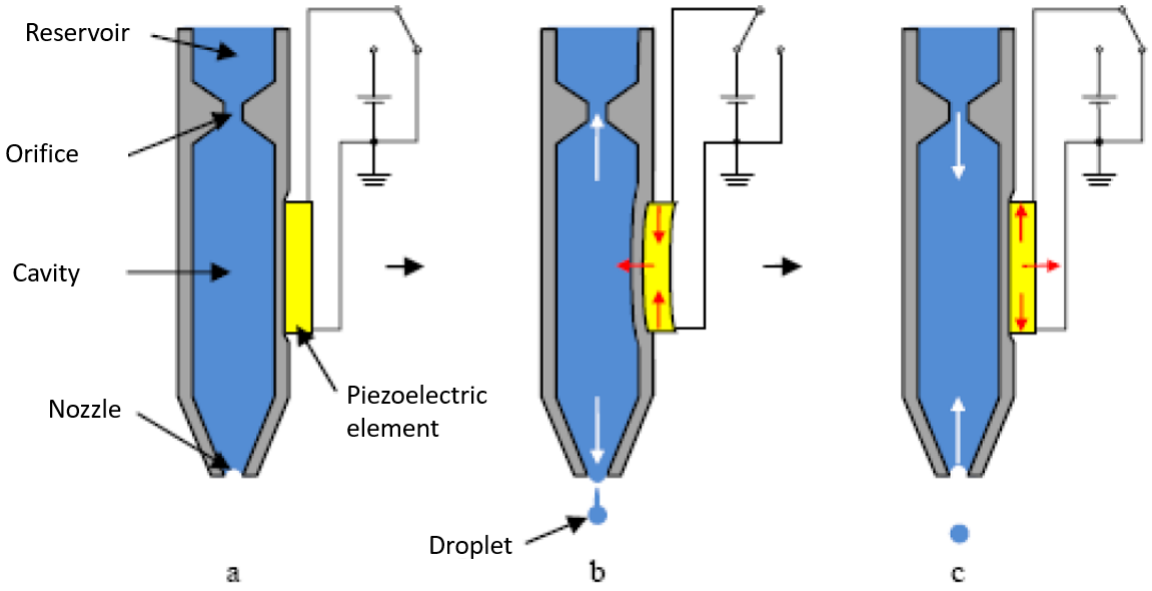

Figure 3.5: Operating principle of a piezoelectric inkjet printhead. (A) The printhead in its default state. (B) A voltage is applied to the PZT causing it to push a droplet from the nozzle. (C) The voltage is removed and the PZT returns to normal, drawing more ink from the reservoir. Image adapted from Ref.[212]

piezoelectric element, typically lead zirconium titanate (PZT). During the fabrication process, the crystal is melted and then cooled in the presence of a strong electric field, aligning all of the internal dipoles in one direction. This means that when an external electric field is applied to the element, it induces mechanical deformation within the PZT crystal.[182] The structure of a piezoelectric printhead can be seen in Figure 3.5(A), where the PZT crystal is in its equilibrium position. When an electric field is applied to the PZT in Figure 3.5(B), the resulting deformation causes the PZT crystal to protrude into the ink chamber. This pushes a droplet through the nozzle, after which the electric field is removed, causing the PZT element to return to its default state. This draws more ink from the main ink reservoir into the printhead chamber, as shown in Figure 3.5(C). The electric field waveform that drives the PZT deformation will depend on the properties of the ink, in particular on the energy needed to break off a single droplet.

This is the key advantage of piezoelectric printers. Since the mechanism behind the printing does not depend on any particular property of the ink, it allows for a wide variety of solvents and ink binders to be printed simply by varying the waveform. More importantly, it does not affect the properties of the ink in any way. Unlike in thermal inkjet printers where the deposition process requires vaporisation of the ink,

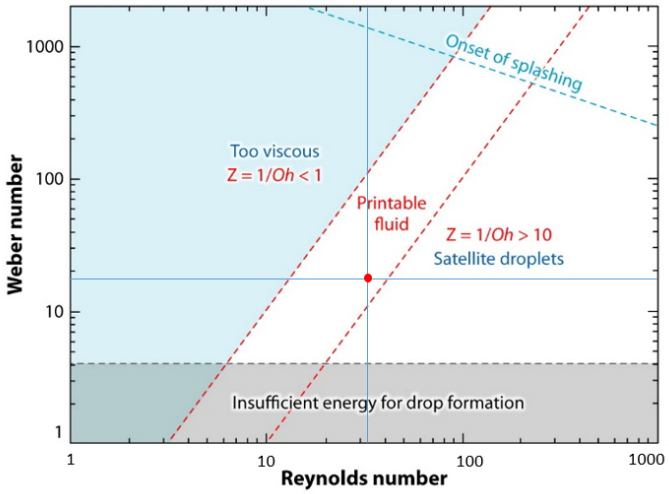

Figure 3.6: The values for Reynolds and Weber numbers where inkjet printing is possible. The red dot represents an estimate for the Reynolds and Weber numbers of isopropanol, assuming a nozzle diameter of 20 µm and droplet velocity of 5 m/s. Image adapted from Ref.[211]

piezoelectric printers do not affect the properties of the ink at any stage. This also allows the inkjet printing of both composite inks[213] and co-solvent inks.[214]

The properties of the ink must be tightly controlled in order to successfully use it for inkjet printing. These properties are best characterised by the dimensionless Weber and Reynolds numbers, which take into account the surface tension, viscosity, and inertial forces. The Weber number is the ratio between the fluid's inertia and surface energy

$$We = \frac{\rho a v^2}{\gamma} \tag{3.1}$$

where ρ is the ink density, a is the droplet diameter, v is the droplet velocity, and γ is the surface energy. Similarly, the Reynolds number compares the inertial and viscous forces

$$Re = \frac{\rho a v}{\eta} \tag{3.2}$$

where η is the ink viscosity. Since both of these numbers rely on the droplet velocity, the inverse Ohnesorge number was introduced to remove this dependence

$$Z = (Ohn)^{-1} = \frac{Re}{\sqrt{We}} = \frac{\sqrt{\rho \gamma a}}{\eta} \tag{3.3}$$

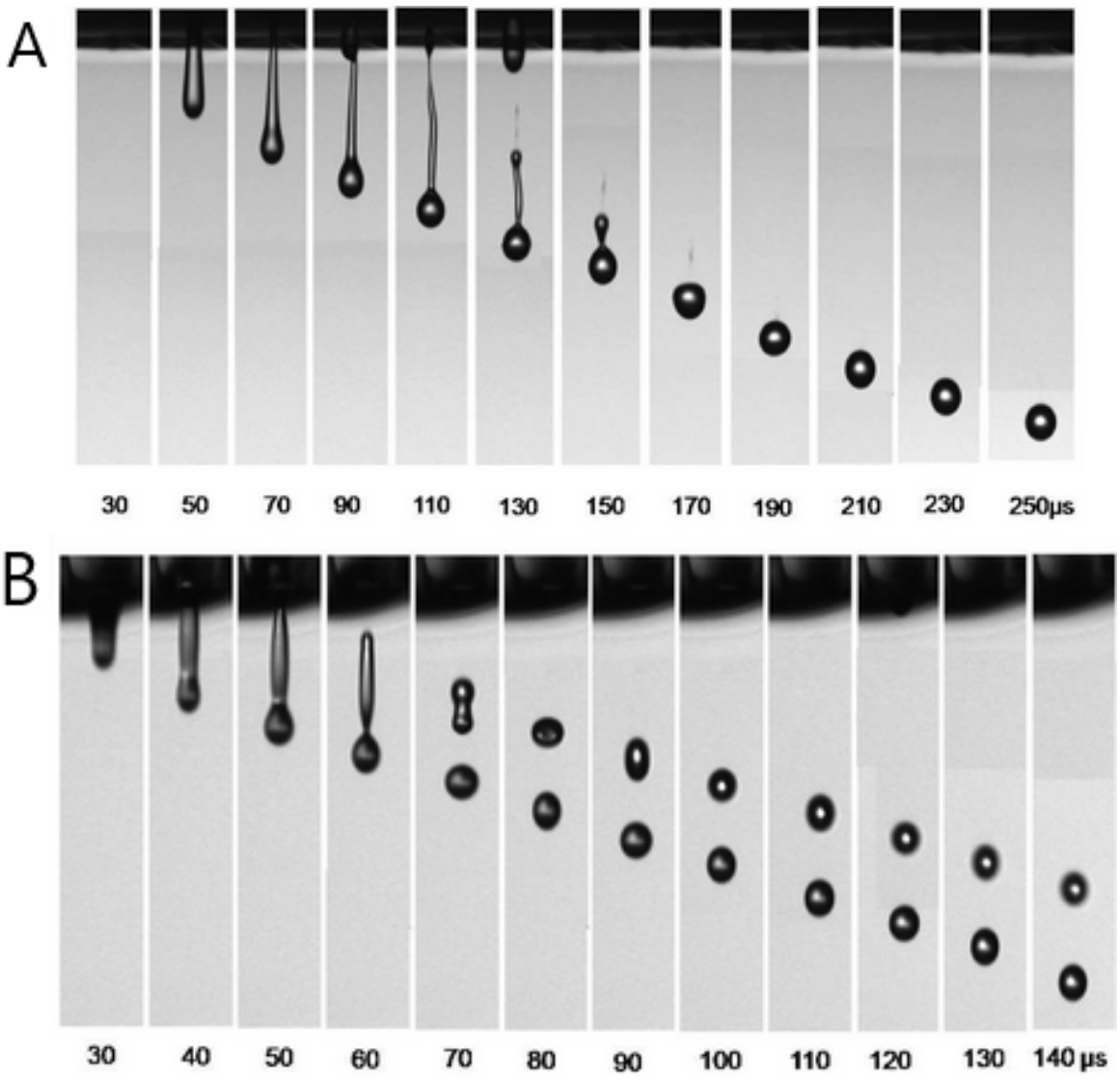

Figure 3.7: Time lapses of droplets ejected from a piezoelectric printhead for (A) an ink with a suitable Z value and (B) an ink with $Z > 10$. Images adapted from Ref.[216]

This is a measure of how printable the ink is. The initial calculations by Derby *et al.* gave the optimal values for Z as between 1 and 10,[215,211] although a more recent experimental study from Jang *et al.* give the ideal printing values as between 4 and 14.[216]

A representation of this can be seen in Figure 3.6, showing a graph of We against Re. This shows the regions for which printing is possible, and the consequences of attempting to print with an ink outside of this printable zone. If $Z < 1$, the viscous forces are too strong amd the ink will be unable to form droplets in response to the PZT deformation. If $Z > 10$, multiple droplets will be ejected from the printhead

leading to the formation of satellite droplets which will splatter onto the substrate and lead to a severe decrease in the printing resolution by potentially forming contacts between adjacent features. It can also negatively affect the final film uniformity, since the satellite droplets will not be deposited evenly across the entire film. Figure 3.6 also shows an estimation for Re and We for isopropanol, which was the base solvent for the inks used in this work. This was calculated using the physical parameters provided by Ref[217], which gives $\eta = 2.4 \times 10^{-3}$ Pas, $\rho = 781.2$ kg m^{-3} and $\gamma = 0.023$ N m^{-1}. This estimate also assumed a droplet size of 20 μm and a printing velocity of 5 $m\ s^{-1}$, which are consistent with the inkjet printer used during this work. As a result, this gave estimates for Re and We of 32.6 and 16.98 respectively, shown as a red dot in Figure 3.6. Additionally, this gives a value for Z of 7.9, which lies within the acceptable range for inkjet printing.

The impact of the Z number can be most clearly seen in Figures 3.7(A) and 3.7(B), showing the difference between a good and bad ink for printing. As the PZT crystal moves, the resulting pressure wave causes a jet of ink to emerge. Inertial forces will cause the bulk of this jet to snap off to form the main droplet, with a tail of ink forming behind it. If the surface energy and viscosity are suitably balanced, this tail will be drawn back into the main droplet as seen in Figure 3.7(A). If the Z number for the ink lies outside the optimal range, then the tail will break away from the main droplet and collapse into one or more satellite droplets as seen in Figure 3.7(B). These will impact the substrate near the main droplet, which is particularly a problem for high resolution printing. These unwanted droplets can significantly blur the edges of printed films, leading to potential shorting between adjacent conducting films. It should be noted that the Z number is not a hard and fast rule, since nanomaterial inks with Z as high as 36 have successfully been printed.[218] Torrisi *et al.* successfully printed a graphene ink with $Z \approx 24$, showing that it is possible to print 2D material based inks without the need to strictly adhere to the Z guidelines.[163] Nonetheless this remains a useful metric to determine how suited a given ink is for printing, since high-Z printable inks are the exception rather than the rule.

Inkjet printed films are also quite susceptible to the coffee-ring effect, as discussed

in a previous section.[180,219] While many of the same techniques apply with regard to avoiding or mitigating the effect, additional care must be taken to ensure that the Z number of the ink remains within acceptable parameters. Co-solvent inks have been successfully used to inkjet print nanomaterial films,[220] and due to the level of control that this method offers over the final viscosity and surface energy of the ink[221] this is an ideal method for simultaneously tuning Z and dealing with the coffee-ring effect. This also avoids the use of binders in the ink, which can potentially negatively impact the performance of the printed device.

3.3 Printed Nanosheet Networks

The properties of printed nanosheet networks have some critical differences from a more conventional CVD-grown film. Assuming that the nanosheets are randomly aligned, this means that there will be a significant portion of the film that is taken up by empty space, generally estimated to be roughly 50% of the total volume of the film for aerosol sprayed networks.[5] In addition, since the film consists of discrete nanosheets rather than a homogeneous block of material, the inter-sheet interactions will play a significant part in determining the properties of the film.[222,223,224] A nanosheet-nanosheet junction in which the two sheets are lying on top of one another, i.e. a basal plane-basal plane junction, will have a much smaller junction resistance than an basal plane-edge interaction, even if the two sheets in these scenarios are otherwise identical.[14] This means that in addition to considering the homogeneity of a printed nanosheet network, it is critical to have some control over its morphology.[99,225,172]

However, the morphology is only one aspect of nanosheet networks that is relatively unknown. Is it also clear that the electrical behaviour of these nanosheet networks needs to be investigated in order to discover what factors contribute to it and the transport processes taking place within these 2D systems. Much of what occurs within nanosheet networks is largely unknown, and gaining some understanding of what takes place within said networks can inform future decisions on the formation and applications of nanosheet devices. In addition, it is known that the junction resistance is a limiting

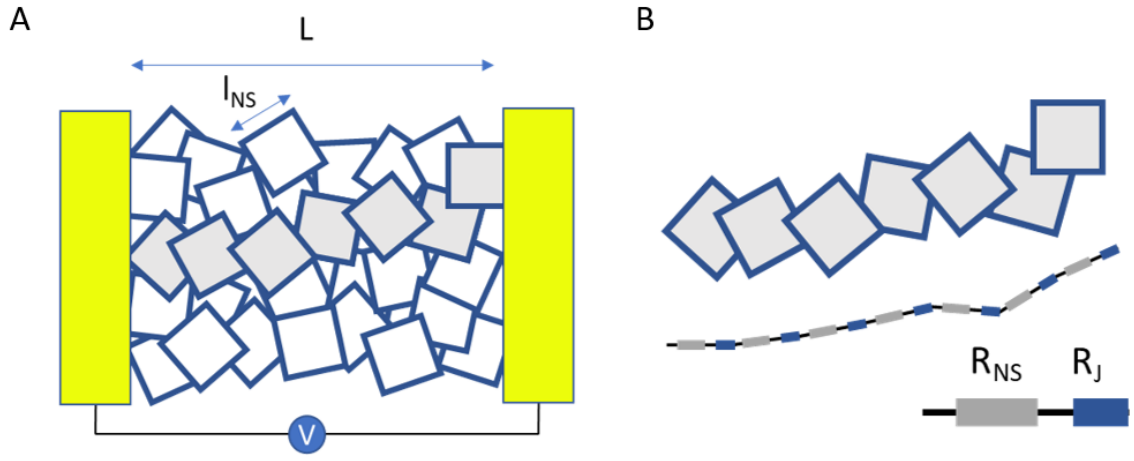

Figure 3.9: (A) Schematic of a nanosheet network. The nanosheets are randomly arranged between two electrodes a distance L apart. (B) Schematic of a single conductive pathway within the network. The fundamental unit of such a pathway is one nanosheet and one junction.

factor in such networks,[5,89,226] meaning that determining a method of estimating the value of the junction resistances is key.

It is possible to derive a model to describe the electrical behaviour of a model nanoparticle system, although it must be noted that this model is still in development and has not yet been published. The derivation presented here is the work of my supervisor, Prof. Coleman, and is derived here prior to its use in analysing the data presented in Chapter 7. By considering that the particles are randomly spread between two electrodes a distance L apart, and that the nanoparticles themselves have length l_{NS}. This scenario is illustrated in Figure 3.9(A).

When a voltage V is applied and a conductive path is formed between the electrodes, the current must pass through a series of both nanosheets and inter-sheet junctions, which can be modelled as resistors in series with respective resistances of R_{NS} and R_J. One such conductive pathway is shown in Figure 3.9(B), and it is proposed by Garrett *et al.*[227] that for a nanotube bundle the network impedance is equivalent to that of one junction and one nanotube in series. We make a similar approximation here, stating that the network resistance can be determined by considering one single conductive pathway through the network. This pathway can be represented by an equal number of nanosheets and junctions, and the most basic unit within the conductive path will

consist of one nanosheet and one junction. The minimum number N of such units within a given conductive path is given by

$$N = \frac{L}{d_{NS} + d_J} \tag{3.4}$$

where d_{NS} is the average distance travelled by an electron within a nanosheet before jumping, and d_J is the average distance travelled by an electron during the jump from sheet to sheet. Hence, the voltage drop across one nanosheet-junction unit is $V_p = V/N = V(d_{NS} + d_J)/L$. This can in turn be separated into the nanosheet and junction voltage drops

$$V_J = \frac{R_J}{R_J + R_{NS}} V\frac{d_{NS} + d_J}{L}, \quad V_{NS} = \frac{R_{NS}}{R_J + R_{NS}} V\frac{d_{NS} + d_J}{L} \tag{3.5}$$

From here, it is possible to express other properties of the network in terms of the nanosheet and junction resistances. From the definition of the network mobility $\mu_{Net} = v_d/E_A$ where $v_d = L/\tau_{Net}$ is the drift velocity and E_A is the applied electrical field across the network such that $E_A = V/L$, it follows that

$$\tau_{Net} = \frac{L}{\mu_{Net}\, E_A} = \frac{L^2}{\mu_{Net}\, V} \tag{3.6}$$

where τ_{Net} is the time taken for an electron to pass through the entire network from one electrode to the other. τ_{Net} can also be expressed in terms of the times taken for an electron to cross N nanosheet-junction units $N(\tau_{NS} + \tau_J)$, from which follows

$$\tau_{Net} \approx \frac{L}{d_{NS} + d_J} (\tau_{NS} + \tau_J) \tag{3.7}$$

where τ_{NS} and τ_J are the times taken to cross a single nanosheet and a single junction respectively. These times can also be independently calculated. For τ_{NS}, the same method as for Equation 3.6 can be applied, which gives

$$\tau_{NS} = \frac{d_{NS}^2}{\mu_{NS}\, V_{NS}} \tag{3.8}$$

By substituting in the value for V_{NS} obtained in Equation 3.5 this becomes

$$\tau_{NS} = \frac{d_{NS}^2}{\mu_{NS}} \frac{R_J + R_{NS}}{R_{NS}} \frac{L}{(d_{NS} + d_J)V} \tag{3.9}$$

A value for τ_J can be found by considering that the current through a resistor is defined as the rate at which charge carriers pass through the resistor, i.e. $I = dQ/dt$. Since in this case the charge being considered is that of a single electron and the time associated with this jump is τ_J, this gives

$$\tau_J = \frac{e}{I_J} = \frac{eR_J}{V_J} \tag{3.10}$$

Once again the voltage drop across the junction found in 3.5 can be substituted into this equation to obtain

$$\tau_J = e(R_J + R_{NS}) \frac{L}{(d_{NS} + d_J)V} \tag{3.11}$$

Hence, combining this equation with Equation 3.6 allows the network mobility to be expressed solely in terms of the properties of the nanosheets and junctions

$$\frac{L^2}{\mu_{Net}\, V} \approx \frac{L}{(d_{NS} + d_J)V} \left(\frac{d_{NS}^2}{\mu_{NS}} \frac{R_{NS} + R_J}{R_{NS}} \frac{L}{(d_{NS} + d_J)V} + \frac{eL\ (R_{NS} + R_J)}{(d_{NS} + d_J)V} \right) \tag{3.12}$$

By rearranging to isolate the network mobility term we arrive at

$$\frac{1}{\mu_{Net}} \approx \frac{R_{NS} + R_J}{(d_{NS} + d_J)^2} \left(\frac{d_{NS}^2}{\mu_{NS} R_{NS}} + e \right) \tag{3.13}$$

By inverting both sides and grouping related terms, the network mobility can be expressed as

$$\mu_{Net} \approx \frac{(d_{NS} + d_J)^2}{d_{NS}^2} \left(\frac{1}{1 + \frac{R_J}{R_{NS}}} \right) \mu_{NS} \left(\frac{1}{1 + \frac{e\mu_{NS} R_{NS}}{d_{NS}^2}} \right) \tag{3.14}$$

We assume that the distance between adjacent nanosheets is significantly smaller than the mean length of the sheet, and hence $d_{NS} + d_J \approx d_{NS}$. Therefore

$$\mu_{Net} \approx \frac{\mu_{NS}}{\left(1 + \frac{R_J}{R_{NS}}\right) \left[1 + \frac{e\mu_{NS} R_{NS}}{d_{NS}^2}\right]} \tag{3.15}$$

By assuming a classical model, Ohm's law can be used to give $R_{NS} = d_{NS}/\sigma_{NS}A_{NS}$ and $\sigma_{NS} = n_{NS}e\mu_{NS}$ where σ_{NS} is the nanosheet conductivity, A_{NS} is the cross-sectional area, and n_{NS} is the nanosheet charge carrier density. Combining these gives $R_{NS} = d_{NS}/(A_{NS}n_{NS}\mu_{NS}e)$. It is also important to consider the network porosity P and how that impacts the network carrier density, which for the full network we hypothesise to be described by $n_{Net} = n_{NS}(1-P)$.[225] By combining these two points and taking

$$\sigma_{Net} = n_{Net}e\mu_{Net}$$

this gives an equation to describe the conductivity of a nanosheet network

$$\sigma_{Net} \approx \frac{\sigma_{NS}(1-P)}{\left(1+\frac{R_J}{R_{NS}}\right)\left(1+\frac{d_{NS}/A_{NS}}{n_{NS}d_{NS}^2}\right)} \tag{3.16}$$

We treat the nanosheets as approximately square, such that the cross-sectional area term can be rewritten as $A_{NS} = l_{NS}t_{NS}$ where t_{NS} is the nanosheet thickness. We also relate the d_{NS} term by considering the stacking arrangement of the nanosheets. In a film where the nanosheets are expected to be aligned completely randomly such as an aerosol sprayed film, the value of d_{NS} could theoretically range from almost zero (where the electron enters the sheet and then almost immediately leaves) to almost l_{NS} (where the electron travels almost the full length of the nanosheet before leaving). Hence on average, a given electron would be expected to travel a distance $d_{NS} = l_{NS}/2$ through a nanosheet before travelling to the next one.

Hence, Equation 3.16 becomes

$$\sigma_{Net} \approx \frac{\sigma_{NS}(1-P)}{\left(1+\frac{R_J}{R_{NS}}\right)\left(1+\frac{2}{t_{NS}n_{NS}l_{NS}^2}\right)} \tag{3.17}$$

The next step is to express as many variables as possible in terms of intrinsic properties, by rewriting $R_{NS} = d_{NS}/(A_{NS}\sigma_{NS}) = 1/(2t_{NS}\sigma_{NS})$ and $\sigma_{NS} = n_{NS}e\mu_{NS}$. Finally, since the nanosheets here are a product of liquid phase exfoliation, the thickness of the sheets can be assumed to have a consistent relation to the nanosheet length over the whole range

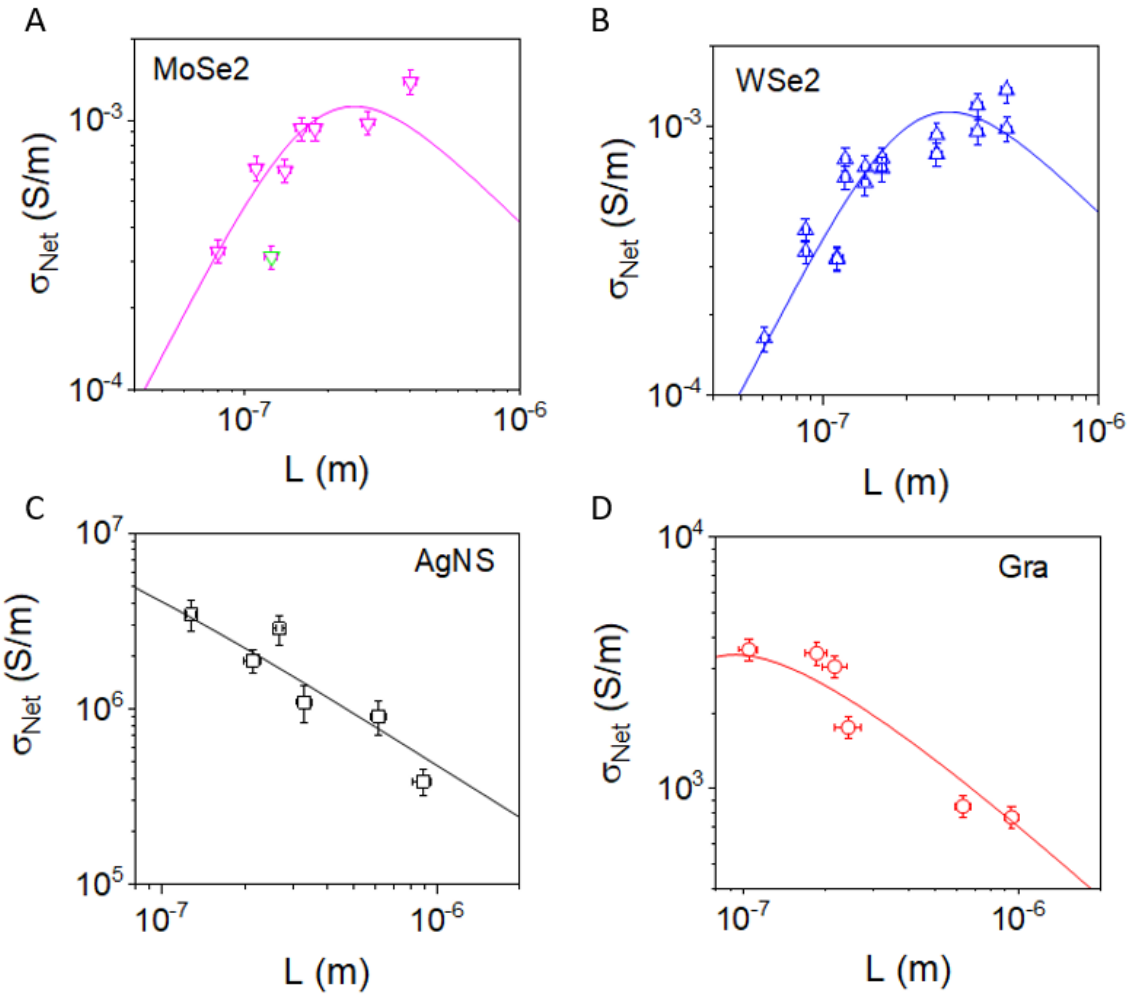

Figure 3.10: Network conductivity against mean nanosheet length for (A) $MoSe_2$, (B) WSe_2, (C) silver nanosheets, and (D) graphene. The solid lines are fits to Equation 3.19. Data is unpublished at time of writing, used with permission.

of different flake sizes,[112] allowing t to be replaced with l/k where k is the nanosheet aspect ratio. This gives

$$\mu_{Net} \approx \frac{\mu_{NS}}{\left(1 + 2R_J n_{NS} e \mu_{NS} l_{NS}/k\right)\left(1 + \frac{2k}{n_{NS} l_{NS}^3}\right)} \tag{3.18}$$

for the network mobility, and

$$\sigma_{Net} \approx \frac{\sigma_{NS}(1-P)}{\left(1 + 2R_J n_{NS} e \mu_{NS} l_{NS}/k\right)\left(1 + \frac{2k}{n_{NS} l_{NS}^3}\right)} \tag{3.19}$$

for the network conductivity. In order to test this model, it was applied by Dr Cian

Gabbett to printed networks of multiple different materials. (NB: this data has not yet been published) Networks of $MoSe_2$, WSe_2, silver nanosheets (AgNS), and graphene were fabricated for a variety of mean nanosheet lengths, with the resulting conductivity trends shown in Figure 3.9. It can be seen that both of the TMD-based networks in Figure 3.9(A) and (B) show an increase in the network conductivity with increasing <L>. This is what would be intuitively expected from a network in which the junction resistance is the limiting factor, since a network of larger nanosheets should have fewer junctions than an equally sizes network of smaller nanosheets, as has been observed in nanotube-based transistors.[228] Indeed, the model predicted by Equation 3.19, represented by the solid lines in Figure 3.9(A) and (B), fits the recorded data.

In contrast, the AgNS and graphene networks shown in Figure 3.9(C) and (D) do not follow this reasoning. Instead, both networks counter-intuitively show decreasing network conductivity as the flake length increases. However, as is shown by the solid lines representing fits to Equation 3.19, this behaviour is also accounted for by the model. This non-intuitive behaviour for more conductive materials arises Therefore it can be seen that the model is able to account for and explain both the intuitive and non-intuitive behaviours of differently sized nanosheets.

While this model shows promise, it must be noted that it is still in its early stages of development. The basis of the derivation for Equation 3.19 considers only a single conductive pathway through a nanosheet network, whereas in reality it is expected that there would be many such pathways in parallel, each likely to have a different number of conducting units within it. It also does not account for the inherently polydisperse nature of LPE-exfoliated dispersions. Despite this, the predictions made can be used to provide information the network properties. In this thesis this model will be used to obtain estimates for the junction resistance R_J by varying the values of the mean nanosheet length l_{NS}.

3.4 Printed Transistors

If any single invention can be said to have shaped the modern world, the transistor is it. The first working transistor was developed by William Shockley, John Bardeen, and Walter Brattain at Bell Labs in the aftermath of the Second World War, although patents for theoretical devices operating under the same principle had existed since 1925. This device consisted of a germanium diode contacted with gold electrodes and was about the size of a fist, a stark contrast to modern day transistors, which are roughly 10 nm in size. The famous Moore's Law predicted a doubling in the number of components on a computer chip every 2 years,[229] although in order to match that trend modern silicon-based microprocessors require high-cost fabrication techniques and industrial scale processes. In this regard printed devices are very unlikely to be able to compete with silicon, especially when taking into account the billions of dollars that have already been invested into silicon development and infrastructure. Instead, printed 2D material devices will act to compliment existing silicon devices by filling in a niche that silicon is unsuited to, namely easily fabricated low cost, low performance devices.[3]

The basic idea behind a transistor is a three electrode device, where the current flowing between two probes is controlled via a voltage applied to the third electrode. Although the original transistor was a bipolar junction transistor, a second type known as the metal-oxide-semiconductor field effect transistor (MOSFET) was developed in 1959 and quickly became the dominant type of transistor. It is estimated that 10^{22} such devices have been fabricated since the 1960s,[230] with modern individual microprocessors containing between 30 billion[231] and 1 trillion MOSFETs.[232] The MOSFET is ideal for digital electronics since it consumes very little power and can readily be fabricated from (doped) silicon and its oxides, in turn allowing them to very easily be mass produced. Although the devices used in this thesis are electrochemical transistors and not conventional MOSFETs, the fundamental equations that describe their behaviour are applicable to the electrolytically gated devices. Rather than having a dielectric layer between the channel and gate electrodes, the electrochemical devices

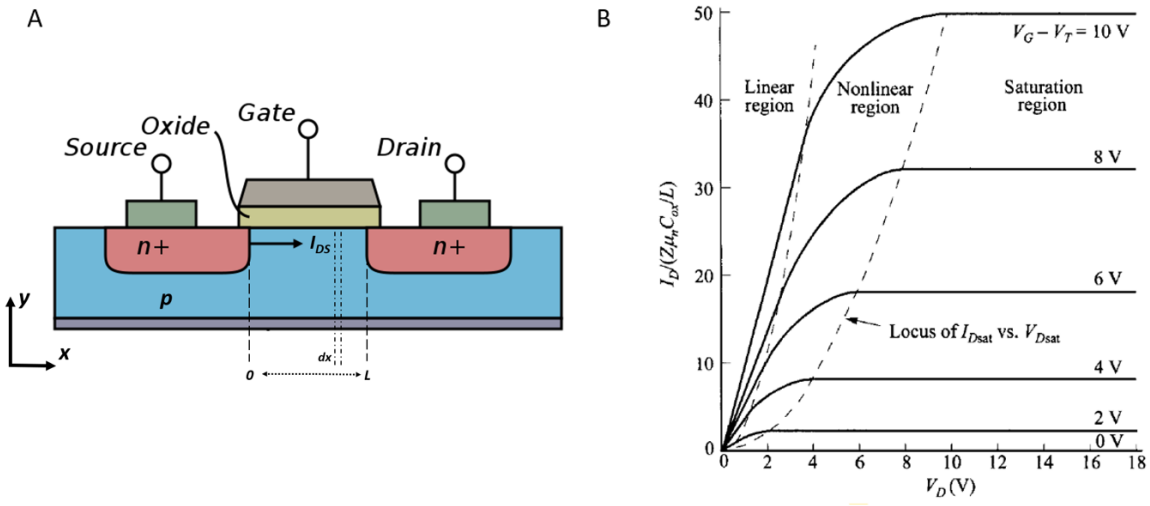

Figure 3.11: (A) Cross-section of a basic MOSFET, showing the small vertical slice to be considered in the MOSFET equation derivation. Image adapted from Ref.[233] (B) I_{DS} against V_{DS} for a variety of values of V_{GS}. Image taken from Ref.[234]

used here have a liquid electrolyte as a separator. This will be discussed in more detail in a later section.

The basic MOSFET structure consists of two doped regions on top of an oppositely doped semiconductor substrate such that the two doped regions act as the source and drain terminals, as seen in Figure 3.11(A). An oxide layer is deposited on the substrate, and the gate electrode is deposited on top. When a voltage is applied to the gate electrode, charge carriers are drawn from the substrate to the oxide-semiconductor interface, which eventually results in the formation of a thin layer of highly doped semiconductor. Since the conductivity scales with carrier density this results in a significant increase in the current flowing from source to drain.

It is important therefore to derive an equation relating the source-drain current (I_{DS}) to the gate-source voltage (V_{GS}), with the source-drain voltage (V_{DS}) also needing to be taken into account. The relative strength of V_{DS} compared to V_{GS} dictates the overall performance of the transistor, with three main regimes: where $V_{DS} << V_{GS}$, where $V_{DS} \approx V_{GS}$, and where $V_{DS} \geq V_{GS}^2$. This is shown in Figure 3.11(B). As a result, the graph of I_{DS} compared to V_{DS} will contain a region where I_{DS} is linear against V_{DS}, a region where I_{DS} begins to level off, and a region where I_{DS} is constant with increasing V_{DS}.

As is often the case with physical systems, when modelling MOSFET behaviour some assumptions and approximations must be established. First, that the metal-oxide-semiconductor section behaves like an ideal capacitor, with no current flowing through the gate electrode and no inhomogeneities in the electric field at the oxide-semiconductor interface. It is also necessary to assume that the carrier mobility is constant throughout the semiconductor channel, that the field-induced doping is the same across the entirety of the oxide-semiconductor interface, and therefore that there is no charge carrier diffusion to be considered. The analysis also assumes that the electric field due to the gate voltage is much larger than the electric field due to the voltage between the source and drain electrodes, leading to what is known as the gradual channel approximation where the voltage profile changes linearly across the channel.[234]

When the gate voltage is increased above a certain threshold voltage (V_T), charge carriers are drawn to the channel-oxide interface. The areal charge density Q can be expressed as

$$Q = -C_{ox}(V_G - V_T) \tag{3.20}$$

where C_{ox} is the areal capacitance of the oxide-channel interface and V_G is the gate voltage. Note that the negative sign indicates that the charge carriers in this instance are negative. When a voltage is then applied across the channel from source to drain, the voltage V_{cb} with respect to distance along the x-axis from the source electrode at each point can be given as

$$Q(x) = -en_s(x) = -C_{ox}(V_G - V_{cb}(x) - V_T) \tag{3.21}$$

where e is the charge on a single electron and n_s is the sheet density of charge carriers in cm^{-2}. This is illustrated in Figure 3.11(A). The conductivity of the channel at any given point x can be expressed as

$$\sigma = en(y)\mu_n(y) \tag{3.22}$$

where $n(y)$ is the charge density in cm^{-3} and $\mu_n(y)$ is the electron mobility, which is

assumed to be constant throughout the channel. Note that the contribution to the conductivity from the positive charge carriers has been neglected since in this instance $n_{e-} >> n_{b+}$. Using Ohm's law, an expression for the channel conductance, g, can be derived

$$g = \frac{W}{L}\int_0^y \sigma(y)\,\mathrm{d}y = \frac{W\mu_n}{L}\int_0^y en(y)\,\mathrm{d}y \tag{3.23}$$

where W and L are the channel width and length respectively. Since the integral on the right hand side is equivalent to the total charge per unit area in the channel, this can be rewritten as

$$g(x) = \frac{W\mu_n}{L}|Q(x)| \tag{3.24}$$

This is related to the resistance of an infinitesimally small segment of the channel $\mathrm{d}x$ as follows

$$\mathrm{d}R = \frac{\mathrm{d}y}{L\,g(x)} = \frac{1}{W\mu_n}\frac{\mathrm{d}x}{|Q(x)|} \tag{3.25}$$

with the accompanying voltage difference being equal to

$$\mathrm{d}V = I_{DS}\,\mathrm{d}R = \frac{I_{DS}}{W\mu_n}\frac{\mathrm{d}x}{|Q(x)|} \tag{3.26}$$

By integrating Eqn. 3.26 from $x = 0$ to $x = L$ while substituting in Eqn. 3.21, and using the fact that $V_{cb,x=0} = 0$ and $V_{cb,x=L} = V_{DS}$, it follows that

$$\int_0^{V_{DS}} |Q(x)|\,\mathrm{d}V = \int_0^{V_{DS}} C_{ox}(V_G - V_{cb}(x) - V_T)\,\mathrm{d}V = \int_0^L \frac{I_{DS}}{W\mu_n}\,\mathrm{d}x \tag{3.27}$$

Since the current I_{DS} is constant and the voltages V_T and V_G do not change with respect to V, this simplifies to

$$I_{DS} = \frac{WC_{ox}}{L}\mu_n V_{DS}\left(V_G - V_T - \frac{V_{DS}}{2}\right) \tag{3.28}$$

For the linear transistor regime where $V_{DS} << V_G$, the contribution from the $V_{DS}/2$ factor can be ignored, hence

$$I_{DS} = \frac{WC_{ox}}{L}\mu_n V_{DS}\,(V_G - V_T) \tag{3.29}$$

In the case of an electrolytically gated porous nanosheet network transistor, this equation must be modified to account for the porosity of the nanosheet films. Since the liquid electrolyte permeates the entire volume of the transistor, the gating effect is equally applied to the entire volume of the channel. This means that rather than affecting only a quasi-2D area of the channel near the oxide-semiconductor interface, the gating will affect the entire 3D volume of the channel. This allows the areal capacitance C_{ox} to be rewritten as $C_V t$, where C_V is the volumetric capacitance of the channel and t is the channel thickness.

When analysing an I_{DS} against V_G transfer curve the section of the curve that is analysed to give the device mobility is the linear section of the curve (see Figure 3.11(B)). The slope of this line is the device transconductance g_m, defined as follows

$$g_m = \frac{\delta I_{DS}}{\delta V_G} = \frac{WtC_V}{L}\mu V_{DS} \tag{3.30}$$

Since the volumetric capacitance of these devices is heavily dependent on nanosheet size and thickness,[235] it is more useful to use $C_V\mu$ as the figure of merit for such devices, since all other parameters are known prior to any measurements being performed.

3.4.1 Electrochemical Transistors

The key difference between the standard MOSFET device structure and an electrochemical transistor is the separator between the channel and the gate electrode. In a MOSFET, this is a dielectric layer, whereas in an electrochemical device, this is an electrolyte. For the purposes of this thesis the separator is an ionic liquid, a salt that is liquid at room temperature.[236] The liquid nature of the separator is key to this work and others involving porous semiconductor channels, since it enables the separator to form an interface with the entirety of the exposed surface area of a porous nanosheet network, while a solid dielectric would only be able to contact the topmost nanosheets.[5] In the case of a dielectric layer this would severely limit the ability of the transistor to switch to an ON state since the sheets further away from the dielectric layer will not experience as strong of an electric field from the gate electrode, resulting in poor

switching behaviour. In contrast, an ionic liquid device avoids this issue by gating the internal volume of the channel via electrochemical doping rather than via the effect of an electric field. Unfortunately this comes with a tradeoff when considering the OFF state, which tends to have higher currents than the OFF states of dielectric-based devices since the electrolyte will increase the conductivity of the semiconductor.

This change from a dielectric separator to an electrolyte one also allows electrochemical devices to reach much higher capacitances (~µF cm^{-2}) than their solid state dielectric counterparts (~nF cm^{-2}), which means that such devices are better able to overcome the adverse effects of any defects present in the semiconductor.[237] The liquid electrolyte helps the charge carriers overcome the junction resistance, thus improving the device performance.

When a voltage is applied to the gate electrode in an electrochemical transistor, the gate:electrolyte interface acts like a capacitor, drawing ions from within the ionic liquid to the interface.[238] This results in the formation of an electrical double layer (EDL) at the interface, which consists of a closely packed layer of ions very close to the interface and a second, more diffuse layer of ions in the liquid near the interface.[239,240,241,242] This in turn causes a charge imbalance within the liquid as a whole. In order to balance the charges within the device, oppositely charged ions within the liquid are then driven into the channel, forming a second EDL at the channel:electrolyte interface. This in turn draws more charge carriers from the source and drain electrodes into the channel in order to balance out the charges at the channel:electrolyte interface.[243] The two EDLs can be thought of as a pair of dielectric parallel plane capacitors in series with an equivalent thickness of a few nanometers, resulting in high areal capacitances on the order of a few µF cm^{-2}.

As the voltage at the gate electrode is increased, the concentration of ions at the channel:liquid interface increases, thus increasing the carrier concentration within the channel. This what leads to the increase in the channel conductivity.[237] In the EDL, the potential of the outer layer of ions will be partially screened by the inner layer of ions, which results in the outer layer being much more weakly bound to the gate surface. The speed at which the ions can form the EDL in response to an input electric

field at the gate electrode is what determines the switching speed of the transistor, which is typically on the order of a few ms.

Due to the nature of the ionic liquid, there are two key factors that must be considered before operating an electrochemical transistor. The first is the presence of water within the system. If water molecules are present as the gate voltage is cycled, this can lead to major hysteresis within the device's transfer voltage-current curve,[244,245] as well as potentially introducing unwanted contaminants into the electrolyte. While the exact reason for this is unknown, the most likely culprit is electrolysis of water.[246] Removing the water by annealing the ionic liquid under vacuum is an ideal method for removing trace amounts dissolved within the liquid.

The second factor that must be considered is the electrochemical window of the ionic liquid. This is the voltage range for which the ionic liquid remains stable as the gate voltage is cycled and does not undergo either reduction or oxidation reactions.[247,248] This is also affected by the water content of the ionic liquid, with the electrochemical window of the liquid decreasing with increasing presence of dissolved water.[249,250]

Note that although the electrochemical window described in the literature for the ionic liquid used throughout this work, 1-ethyl-3-methylimidazolium bis (trifluoromethylsulfonyl) imide (EMIm-TFSI), is -2.07 V to +2.12 V,[248,251] this work uses a different method to prepare the liquid. While Ref[248] removes dissolved water vapour by bubbling dry N_2 through the liquid, this work used a two-step annealing process involving heating the liquid under high vacuum ($<10^{-4}$ mbar) for >12 hours. This removes more water from the liquid and thus widens the electrochemical window more than was accomplished in Ref.[248]

Electrochemical nanosheet network transistors also tend to have higher transconductances than their dielectric-based counterparts owing to the high ionic conductivities of the ionic liquids.[252] Both organic and nanosheet-based electrochemical devices can easily reach transconductances on the order of 1 mS,[5] which is comparable to high-performance solid-state devices such as ZnO.[252,253] Rivnay *et al.* note that for organic transistors, electrochemical devices show a factor of ~10^3 higher conductances than equivalent field-effect devices for low frequency operation (<1 kHz), but begin to

suffer from reduced performance at lower frequencies than equivalent dielectric-based devices.[238]

3.4.2 A Review of Printed Thin-Film Transistors

While the field of 2D-material based printed electronics still has a long road ahead of it, they are not the only class of material being investigated for their potential. Indeed there are several other types of printed devices that are also being developed to the point where they can also act as a competitor to silicon based devices. In practice however, due to the time and resources already invested into silicon devices, it is much more likely that printed electronics will find its own niche in an area which silicon is not suited to. This section will give a brief overview of the current status of the various avenues of materials research and what the advantages and disadvantages are of each.

Organic Semiconductor Networks

In many ways organic semiconductors were the pioneers of printed electronics research, with the first printed organic field effect transistors (OFETs) being produced in the mid 1980s.[254] Since then the field has expanded massively, taking advantage of the readily available amount of potential materials to explore the diverse requirements for printed thin-film transistors. A wide range of organic materials, typically polymers, are currently being investigated for their potential switching behaviour. These include materials like P3HT, which is capable of producing organic thin film transistors (OTFTs) with p-type mobilities of 20 $cm^2V^{-1}s^{-1}$.[255] Crucially, organic electrochemical transistors (OECTs) are capable of producing high transconductance values on the order of 1 mS since they are able to gate the entire volume of the device,[238,243] similar to porous nanosheet network devices. OECTs are also capable of reliably producing on:off current ratios of 10^6, which is a point in their favour for low-power digital electronics. Unfortunately, organic semiconductor materials tend to have lower mobilities than their silicon and metal-based competitors,[256,257] which is a major hindrance when considering their potential applications. There is also a lack of high-mobility n-type organic materials, which limits their potential use in CMOS applications.[258]

The wide variety of potential organic materials also acts as a drawback when considering the amount of time and resources needed to investigate the properties of each one correctly. In addition, the large size of the individual polymer molecules leads to further complications when considering that there are many charge transport processes, including both inter- and intra-molecular processes, that are still not fully understood. The impact of molecular or crystalline defects and trap states on the electronic performance is yet to be completely investigated. Since these defects can lead to a high amount of inter-device variance, this is a serious issue for large scale fabrication and integrated circuits.

The final hurdle in the path of OFETs is the lack of ambient stability that comes with most organic semiconductors.[259] Both water and oxygen have been shown to induce degradation in organic polymers,[260] meaning that some sort of encapsulation will be necessary for their use in long-lasting devices, although this doesn't prevent their use in one-off sensor devices. This, plus the fact that OFETs are easily manufactured using printing technologies[175] means that they have considerable potential for future applications.

Carbon Nanotube Networks

Carbon nanotubes (CNTs) very quickly became a material of interest when it came to printed transistors. Semiconducting single-walled CNTs display near-ballistic electron transport and have direct bandgaps in the range of 0.7 to 1 eV, which makes them ideal for applications, particularly in optoelectronics.[261] CNT-based FETs are now capable of outperforming silicon transistors and display both high on:off current ratios and high mobilities, although in the case of ultra-short channel devices the presence of ballistic transport makes carrier mobility a poor estimate of device quality.[262] While inkjet printed CNT networks are not capable of that level of performance, they can still reach mobilities of 20 $\mathrm{cm}^2\ \mathrm{V}^{-1}\ \mathrm{s}^{-1}$.[263]

One issue with CNT production is separation of metallic CNTs from semiconducting ones during the synthesis process, which has hampered CNT production since the beginning. For TFT applications it is important that the CNT network does not con-

tain metallic elements in order for the transistor to display proper switching behaviour. Failing to properly remove all of the metallic elements will adversely affect the on:off ratio, although it will also increase the channel conductivity. While techniques do exist to purify CNT samples to the levels required for transistors, such as density gradient centrifugation[264] and the use of specific solvents to remove one type of nanotube[265], these have issues with scalability and with processing large volumes of material, generally producing large amounts of chemical waste.[266] Unfortunately the impact of this is that despite their high performance, scalability remains a major roadblock for printed CNT transistors.

MXenes

The use of MXenes in printed electronics largely differs from that of the other avenues of research listed here, since most MXenes display metallic rather than semiconducting behaviour. FOr this reason they have found a lot of use in devices as printed contacts rather than the active material itself.[267] The fact that the work function of MXenes can be tuned during the fabrication stage also adds to their utility and allows them to be tailored to match the electronic characteristics of the other materials in a device.[268] In addition, semiconducting MXenes are predicted to exist,[269] and can be synthesised by modification of existing metallic MXenes,[270,271]. These tend to be low-bandgap semiconductors with bandgaps between 0.24 and 1.8 eV, suggesting a considerable potential in optoelectronics. However, the majority of focus given to MXenes and their use in transistors is on their potential as electrical contacts, and experimental realisation of a printed MXene-based transistor has not yet been realised.

Hybrid Perovskites

Hybrid perovskites are another aspect of materials science research that has recently gained much popularity. They have been shown to display considerable promise in optoelectronic applications, with particular focus on solar cells and other photovoltaic devices.[30,272] While traditionally perovskites has referred to fully inorganic materials such as $CaTiO_3$, the recent research interest has primarily been into organic/inorganic

hybrid perovskites. One of the most widely studied hybrid perovskites is Methylammonium Lead Iodide ($MAPbI_3$), which has been successfully used to make inkjet printed solar cell devices.[273] Unfortunately the demanding nature of inkjet printing can require the addition of unwanted additives to ensure that the perovskite ink prints properly at room temperature. This will likely add multiple additional cleaning steps to any fabrication process. Other options are to modify the hybrid perovskites themselves via the addition of chlorine,[274] although this still adds to the complexity of the printing process, as well as potentially requiring additional steps afterwards to remove unwanted chemicals from the final printed film.

There has also been considerable research into the potential of metal halide hybrid perovskites (such as the previously mentioned $MAPbI_3$) as the active material in printed transistors. This is mainly due to the extremely high theoretical carrier mobility predicted for these materials, ranging up to ~800 $cm^2\ V^{-1}\ s^{-1}$, as well as the potential for light-emitting transistors.[275] As is typically the case real world perovskite devices are unable to reach this threshold, achieving mobilities between the orders of 10^{-2} and $10^2\ cm^2\ V^{-1}\ s^{-1}$ depending on the material and method of fabrication.[275] It should be noted that the highest mobility value was an outlier with the high mobility achieved via slow, vapour assisted growth of the pervoskite layer, something that is impractical for large scale production.[276] At time of writing inkjet printed hybrid perovskite-based transistors have not yet been demonstrated, although the capability to do so is present.

Thus far the main issues that need to be overcome for printed hybrid perovskite TFTs are environmental stability and the toxic chemicals required to produce them. Lead halide perovskites are particularly problematic in this regard, since the high toxicity of lead is somewhat unavoidable when dealing with them. Efforts to replace lead with the less toxic tin have also run into issues due to the high vulnerability of tin to oxygen, and the fact that the majority of previous research into these materials has been performed on lead halide perovskites, thus necessitating more research to find a suitable replacement. Finally, $MAPbI_3$ itself is known to suffer from poor thermal stability and begins to break down at temperatures above 85 °CC.[277]

Layered Crystal Networks

The field of nanosheet network-based printed electronics has exploded in the past decade once the issues with synthesising material and producing nanosheet inks were worked out. Researchers have successfully printed a range of devices, from gas sensors[158], strain sensors[57], and photodetectors.[278]

Printed nanosheet transistors are the subject of more and more research as time goes by, ever since they were first demonstrated by Torrisi *et al.* in 2012.[163] This device was a printed graphene channel contacted by metal electrodes and displayed a high mobility of 95 $cm^2\ V^{-1}\ s^{-1}$ and an on:off current ratio of roughly 10, which unfortunately makes it non-ideal as a transistor since a high on:off ratio is needed for a transistor to operate with low wasted power. Future graphene-based transistors were able to achieve higher mobilities but at the cost of lower on:off ratios.[164]

Parallel to graphene-based transistors are other semiconducting nanosheet network devices, most notably ones based on transition metal dichalcogenide (TMD) such as WS_2 or MoS_2. Most such printed devices display mobilities on the order of $10^{-1}\ cm^2\ V^{-1}\ s^{-1}$ and on:off current ratios on the order of 10^4.[5,279]

The main issues facing nanosheet network transistors at this time are a limited understanding of the internal workings of the networks, and the inherent issues that come with a network of discrete particles such as high junction resistances. Currently, it appears that the best way of approaching the second issue is either to aim to fabricate devices with good nanosheet-nanosheet alignment or modify the edges of nanosheets to reduce the junction resistance.[280,281,225] An example of the former is the work of Lin *et al.*[99], who fabricated high mobilities of around 10 $cm^2\ V^{-1}\ s^{-1}$ for spin-coated MoS_2 by achieving good inter-nanosheet alignments, thus reducing the junction resistance. Overcoming this junction resistance will be the next roadblock in the path to printed nanosheet network devices reaching their full potential.

Deposition Technique	Advantages	Disadvantages
Drop Casting	• Very little material waste. • Most inks can be deposited as received. • Well suited to fabricating vertical heterostructures.	• Films tend to be quite inhomogeneous. • No patterning ability.
Spin Coating	• Simple technique. • Compatible with existing industrial infrastructure. • Easy to control thickness and homogeneity of films.	• A lot of material is wasted. • High concentration inks are required.
Spray Coating	• Simple and cheap technique. • Can spray over a large area. • Can easily deposit hybrid inks.	• Extremely low resolution. • Shadow masks required to define printed area.
Inkjet Printing	• Low cost. • Low material waste. • Can easily define the printed area.	• Printing inks must have precisely controlled viscosity and surface tension. • Solvents suited to exfoliation tend to be unsuitable for printing.

Figure 3.8: An overview of the advantages and disadvantages of the various printing techniques discussed in this chapter.

There's only this one universe and only this one lifetime to try to grasp it. And while it is inconceivable that anyone can grasp more than a tiny portion of it, at least you can do that much. What a tragedy just to pass through and get nothing out of it.

Isaac Asimov

4

Materials & Methods

This chapter will outline the various techniques used to fabricate and characterise nanosheet dispersions and films throughout the rest of the thesis.

4.1 Preparation of Dispersions

Sonication

All of the liquid phase exfoliated dispersions used in this thesis were produced by tip sonication, as described in Chapter 2. Ultrasonic energy is commonly used in many scientific fields but its most relevant application to this study is its use in cleaning. Ultrasonication has been used to remove particles from surfaces by overcoming the adhesive forces keeping them in place. A Sonics Vibra-cell VCX-750 horn tip sonicator operating at 60% amplitude was used to exfoliate all dispersions used in this work. The other parameters such as exfoliation time were not fixed and will be discussed in their respective sections. Each dispersion was prepared in three steps. First the starting powder was immersed in a solvent and sonicated for a short time. This dispersion was then centrifuged for 1 hour in order, and the supernatant was discarded. This removes any soluble impurities in the starting powder. The sediment was redispersed in fresh solvent and exfoliated for a longer time, with the time taken varying depending on the

material and stabilisation method chosen.

Ultracentrifugation

All centrifugation steps in this work were performed using a Hettich Mikro 22R refrigerated centrifuge. The centrifugation rate was manually adjusted between 0.5 krpm and 18 krpm. Since the radius of the centrifuge rotor is known to have a radius of 90 mm, the relative centrifugal force (RCF) can be expressed as a function of the rotor rpm. This expresses the centrifugal force in terms of the acceleration due to gravity g, allowing the speeds from different centrifuges to be directly compared

$$RCF = \frac{\omega^2 r}{g} = 106.4 f^2 \tag{4.1}$$

where ω is the angular velocity, r is the rotor radius, and f is the rotation rate in krpm. The rotation rates used vary throughout this thesis based on the material used and the desired nanosheet size, and from this point on will discussed in terms of the RCF values for consistency. Ultracentrifugation was used in this work both as a step in the exfoliation process and to perform size selection on nanosheet dispersions after exfoliation.

4.2 Characterisation of Dispersions

UV-Vis Spectroscopy

Ultraviolet-visible spectroscopy is one of the most useful methods of characterising nanosheet dispersions. It is simple, non-destructive, and capable of analysing hundreds of billions of nanosheets at once. The output spectra then contain information on the nanosheet ensemble, rather than having to individually measure the properties of individual nanosheets.[144] This is a much faster and simpler way of collecting data on nanosheet lengths and thicknesses when compared to microscopy techniques such as AFM or TEM. As the light passes through the sample, the photons can interact with it in a variety of ways. Absorption (Abs) occurs when the photons excite an electron

within the nanosheets, which for semiconducting materials such as TMDs primarily happens for energies above the bandgap. There are also scattering (*Sca*) processes in which the photon interacts with the nanosheets and is then re-emitted in a different direction. These two processes are combined into the extinction *Ext* as

$$Ext(\lambda) = Abs(\lambda) + Sca(\lambda) \tag{4.2}$$

The same relation also holds for the respective coefficients of extinction, absorption, and scattering

$$\varepsilon(\lambda) = \alpha(\lambda) + \sigma(\lambda) \tag{4.3}$$

which have units of $\mathrm{Lg^{-1}m^{-1}}$ and the values of which are material specific. By considering *Ext* at a wavelength where the value of ε is known, the Beer-Lambert Law can be used to find the concentration of a given dispersion as follows

$$Ext = \varepsilon C l \tag{4.4}$$

where C is the concentration of dispersed material and l is the path length of light through the sample.

UV-vis spectroscopy can also be used to directly estimate the mean lengths and thicknesses of a nanosheet ink, via spectroscopic metrics. Such metrics have been developed for graphene[91] and TMD dispersions.[144,282]

A PerkinElmer Lambda 1050 dual beam spectrometer was used to characterise dispersions throughout this thesis, the schematic of which is shown in Figure 4.1. The dispersions were first diluted to a suitable optical density, such that they were semi-transparent to the human eye. They were added to a quartz cuvette with a known path length (4 mm). A second cuvette containing only solvent was also scanned, and this reference spectrum was subtracted from the main sample spectrum to decouple the solvent response from the nanomaterial response. Since the absorption and scattering contributions are combined together into the extinction spectra, it is necessary to perform a second analysis utilising an integrating sphere which is able to capture all

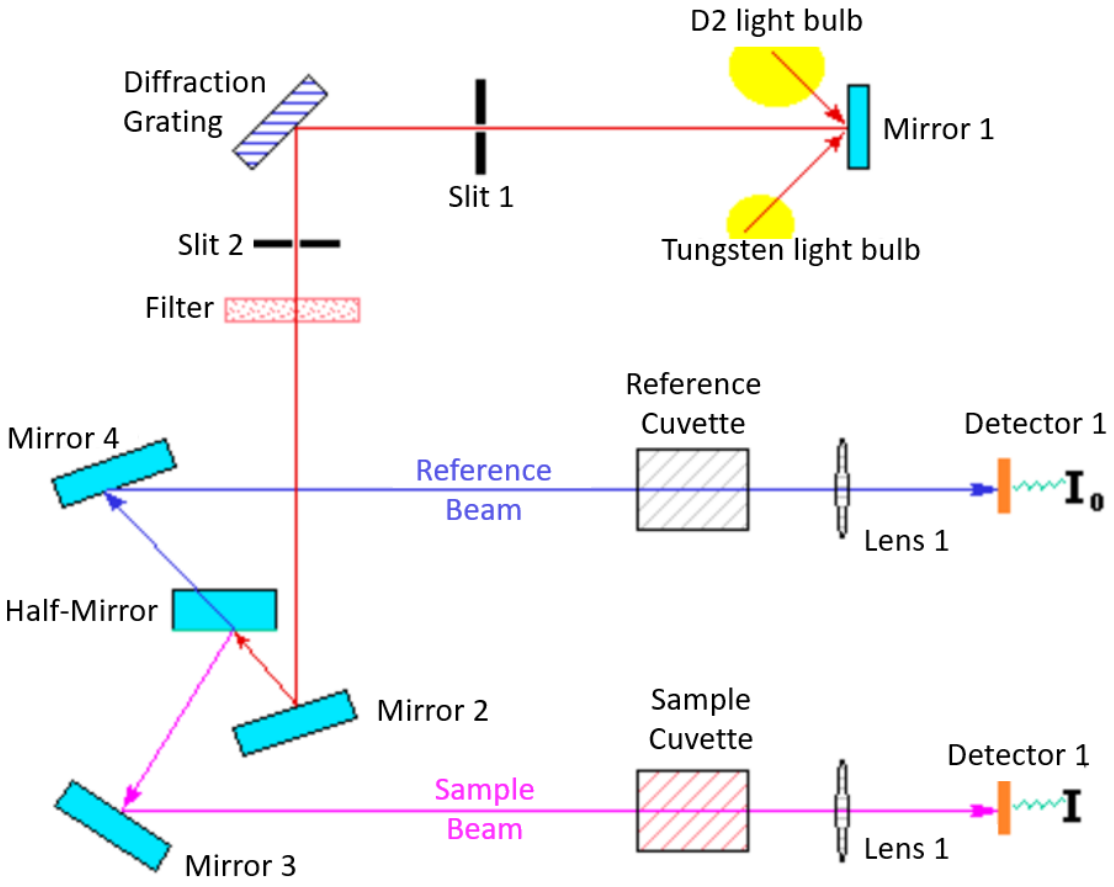

Figure 4.1: Schematic of a standard dual beam UV-vis spectrometer. Image adapted from Ref[283]

scattered light, meaning only the absorbed light is not recorded by the spectrometer. This is especially necessary when dealing with nanosheet dispersions, since the sheets are large enough to cause significant scattering.[284]

UV-vis spectroscopy was used in this work to determine the nanosheet concentration in LPE inks, as well as measuring the length and thickness of the nanosheets.

4.3 Film Formation

Spray Coating

All spray coated films were fabricated using a Harder and Steenbeck Infinity Airbrush attached to a Janome JR2300N mobile gantry. Nitrogen gas at a pressure of 4 bar was used to aerosolise the dispersions as they passed through the airbrush with ~10cm between the spray gun and the substrate, and the area being covered was defined

via software. Alumina-coated polyethylene teraphtalate (PET) from Mitsubishi Paper Mills was used as the substrate, since it is specifically made to avoid solvent wetting and provide better defined film edges. Shadow masks were used to define the length and width of the films. Following the deposition the films were annealed overnight in a vacuum oven at 80 °C. This temperature was chosen because the PET substrates used are unstable at temperatures above 110 °C,[285] and the isopropanol used as the printing solvent is suitably volatile that annealing at this temperature under vacuum would be sufficient to remove any traces remaining.

Shadow masks were used to define the deposition area, producing sixteen $1 \times 3 \times t$ mm^3 films. The thickness t was calculated via the average of multiple mechanical profilometry measurements. Gold interdigitated electrodes (IDEs) were deposited using e-beam evaporation, with the IDE area defined by shadow masks to give $L = 120\ \mu m$ and $W = 16\ mm$. Here L and W represent the length and width of the channel defined by the IDEs. Simultaneously, a glass slide was set beside the sprayed area in order to provide a separate film, the thickness of which was then measured via mechanical profilometry.

Inkjet Printing

The inkjet printing of the graphene gate electrodes in Chapter 5 was carried out using a Dimatix DMP-2831, utilising a single printhead containing 16 piezoelectric nozzles with a diameter of 21 μm. This results in droplet sizes of approximately 10 pL. Each cartridge was able to contain roughly 2 mL of ink. The individual nozzles were capable of depositing ink using a waveform based on the solvent used to define the displacement of the piezoelectric component, with each drop consisting of roughly 10 pL. The printer is capable of depositing ink over an area of roughly 30 cm × 30 cm at a time, with the full size of the platen being roughly equivalent to that of an A4 sheet of paper. Both the platen and cartridge could be heated up to 60 °C.

Each cartridge was first cleaned with a small amount of the solvent that would be used for printing, which in this case was isopropanol. A small amount of solvent was also very gently driven through the cartridge nozzles in order to investigate the

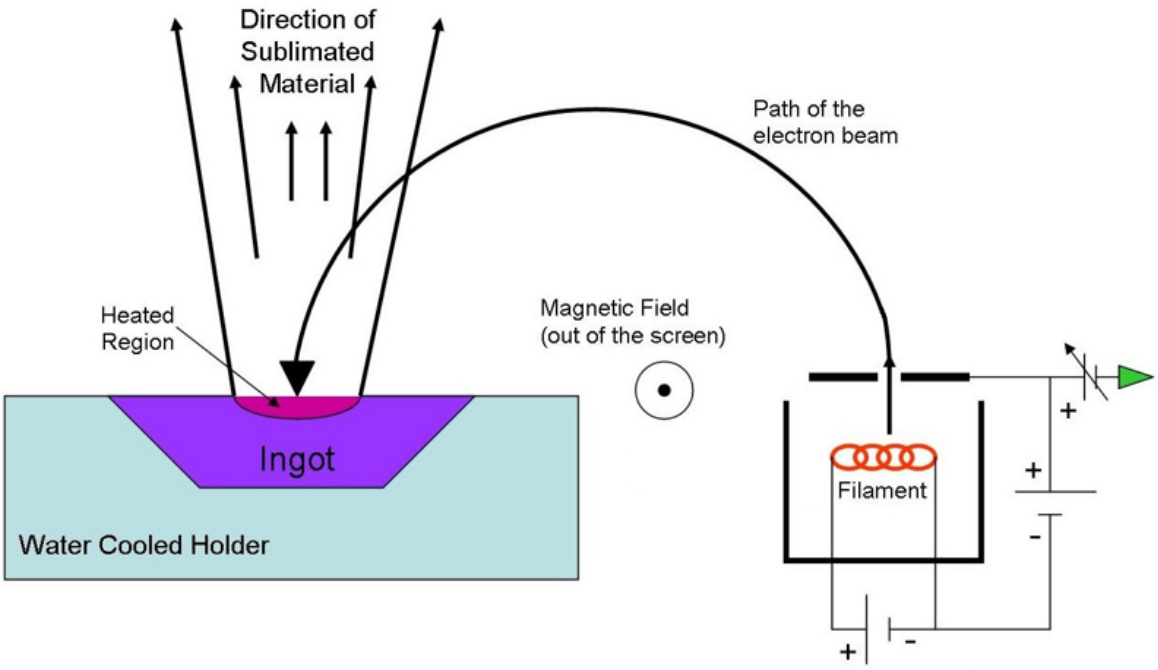

Figure 4.2: Schematic of an e-beam evaporation system. Image adapted from Ref.[286]

presence of any blocked nozzles. In the event that one or more of the nozzles was blocked, the cartridge was immersed in isopropanol and sonicated at a low intensity in order to dislodge the blockage.

The cartridge temperature was at room temperature and the platen temperature was set to 60 °C to aid evaporation of the IPA (boiling point 82 °C).[217] Alumina-coated polyethylene terephthalate (Al_2O_3-PET) purchased from Mitsubishi Paper Mills was used as the substrate. This substrate is ideal for printing purposes since it is specifically designed to prevent droplet wetting and thus provide better printing resolution.[285] The size and number of printing passes were determined via computer input, allowing for fine control of the dimensions of the printed films. The interlayer delay was set to 3 minutes in order to ensure that the maximum amount of solvent had evaporated, while also taking care not to expose the printed films to atmospheric conditions for too long. Since the printing solvent used was isopropanol, shorter delay times could be used to remove solvent. After the deposition, the samples were annealed in a vacuum oven for 12 hours at 70 °C to remove as much residual solvent as possible.

Electrode Deposition

Gold electrodes were deposited onto printed nanosheet networks using a Temescal FC2000 e-beam evaporation system. The chamber containing the samples was pumped down to high vacuum (roughly 6×10^{-6} mbar), and then rotated around a central axis in order to ensure an even coating. Electrons from an electron gun are accelerated at high energies and directed via a magnetic field into a copper crucible containing the gold, as shown in Figure 4.2. The kinetic energy of the electrons is transformed into heat, which causes the gold to melt and sublimate. The metal vapour particles coat the film, with a crystal monitor controlling the thickness and deposition rate.[287] Gold was chosen as the contact metal due to its robustness and resistance to corrosion. The precise areas of the gold electrodes were defined via shadow masks.

4.4 Characterisation of Films

Profilometry

Thickness measurements were carried out using a Bruker Dektak 9.8 µN stylus profilometer with a 10 μm tip. After ensuring that the surface was level by performing multiple thickness calculations on a blank portion of substrate, the tip was moved across a 2 mm length which included both a blank stretch of substrate and the sample being measured. This means that the step height of the film can be measured directly. The average of several such measurements at different positions along the sample is taken as the final thickness value for the film.

Raman Spectroscopy

Raman spectroscopy is an optical, non-contact, and non-destructive technique which provides a useful source of information on the composition of solid samples by analysing the interaction of monochromatic light with the internal lattice vibrations of the sample, known as phonons. When light interacts with a sample, the majority of the incoming photons will interact elastically with the material, but some will interact inelastically

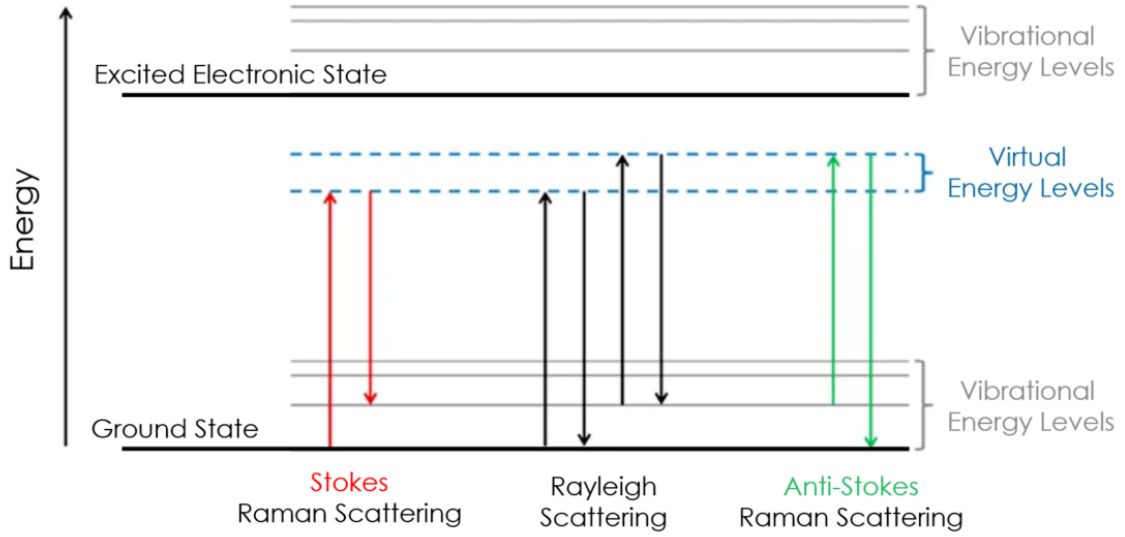

Figure 4.3: Diagram of the different types of transition that occur when light interacts with a sample. Adapted from Ref. [289]

with the phonons in the sample.[288] By modelling these phonons as harmonic oscillators, a fundamental frequency can be associated with each bond vibration.

When the incident light begins to interact inelastically with the sample, it is primarily interacting with the electron cloud of the material and as such the response from the material will be intrinsically tied to its polarisability. This causes a perturbation in the electron cloud, which serves to excite it to a virtual electronic state.[116] There are two main inelastic interactions that can then take place, both of which are shown in Figure 4.3, namely Stokes and anti-Stokes shifts. These processes operate on the same basic principle, with the key difference being whether the energy of the incident light is greater than or less than that of the photon emitted after the scattering takes place. In both cases, after the incident photon excites the electron cloud, the cloud will release a photon and transition down to a different energy state than its initial one, with the difference between the initial and final energy states defined by the vibrational energy levels, i.e. the phonon energies. In a Stokes shift, the outgoing photon will be red-shifted compared to the incident photon, with the remaining energy going towards the creation of an optical phonon. In an anti-Stokes shift this is reversed, with the incident photon absorbing energy from the material and emitting a photon blue-shifted relative to the incident photon.

The change in frequency $\Delta\nu$ is commonly expressed in units of cm^{-1}, and is described by

$$\Delta\nu = \frac{1}{\lambda_{in}} - \frac{1}{\lambda_{out}} \tag{4.5}$$

where λ_{in} and λ_{out} are the wavelengths of the incident and scattered light respectively. By plotting the intensity of scattered light as a function of $\Delta\nu$ the vibrational frequencies of the material can be found, which act as an identifying 'chemical fingerprint' for the given material. In the case of 2D materials, Raman spectra can be combined with theoretical models in order to provide information on chemical composition, doping, and the mean thickness of the nanosheets that make up the solid samples.[91,290,116]

Raman spectroscopy was performed on the printed devices under ambient conditions prior to the addition of the ionic liquid, using either a Horiba Jobin Yvon LabRAM HR800 (Chapters 5 and 6) or a WITec Alpha 300R confocal Raman microscope (Chapter 7), in both cases using a 532nm excitation laser. The Raman signals were collected by a 100× objective lens (N.A. = 0.8) and dispersed by a 600 line/mm grating. 10% laser power was used on the graphene samples and 1% laser power used on the TMD samples, to avoid damage to the TMD films. Twenty spectra were collected over a 10 μm by 10 μm area, with the average of these spectra used to characterise each device.

4.4.1 Electrical Characterisation

Electrical testing was done using a Keithely 2612A and a Janis probe station. The first set of electrical measurements was done on the sprayed films before adding any electrolyte (the "dry" state). These consisted of two-probe current-voltage (IV) measurements in order to determine the conductance and hence the conductivity of the films, since the length, width and thickness of the films were all known.

The liquid electrolyte used in this thesis was the ionic liquid 1-Ethyl-3-methylimidazolium bis (trifluoromethylsulfonyl) imide (EMIM-TFSI), which was first degassed for 12 hours under vacuum at 80 °C to remove any dissolved water. A small amount, $\approx 100\mu L$, was then pipetted onto the films such that the liquid covered the entirety of the channel and the gate electrode. Finally the samples and liquid were annealed for a further 12 hours

under vacuum at 70 °C in the Janis probe station vacuum chamber in order to remove any water that had been absorbed by the liquid during pipetting. All further electrical measurements were then conducted in the Janis vacuum chamber in the presence of the ionic liquid (the "wet" state) under vacuum.

Three-probe transistor measurements were performed on the wet state devices using the Janis probe station under high vacuum (~10^{-5} mbar) using a step size of 20 mV, a delay time of 25 ms, and a scan rate of 36 mV/s. The gate voltage was cycled from 0 to +2.5 V to −2.5 to 0 V. The source-drain voltage was fixed at 1 V throughout all gating measurements. These parameters were defined via LabView software, and were kept consistent throughout all measurements.

The transconductance g_m was calculated from the linear portion of the ON sweep for electrons, i.e. where the gate-source voltage is increasing, and from the linear portion of the OFF sweep for holes, i.e. where the gate-source voltage is decreasing. This was done in order to account for any hysteresis in the transfer curve, in particular attempting to avoid any contributions from any water remaining in the ionic liquid. This value was used to calculate the figure of merit $C_V\mu$ for the device. The average value from several different devices was then taken as the representative value for that particular set.

4.4.2 Electron Microscopy

The resolution of any microscope has a fundamental wavelength-dependent limit defined by

$$d = \frac{\lambda}{2n\ sin(\theta)} \tag{4.6}$$

where n is a positive integer, λ is the light wavelength and θ is the angle of incidence of the light. In practise this means that $d \approx 0.5\lambda$. For optical microscopy this results in a maximum resolution on the order of hundreds of nanometers. This is insufficient to image nanomaterials on the order of tens of nanometers, meaning that an alternative is necessary.

Electron microscopy is an ideal substitute for optical microscopy in this regard. By using high energy electrons in place of light the resolution can be increased significantly.

This can be seen by calculating the electrons' de Broglie wavelength

$$\lambda = \frac{h}{mv} \tag{4.7}$$

in terms of the electron energy, which is better expressed in terms of the accelerating voltage V

$$\frac{1}{2}mv^2 = eV \tag{4.8}$$

giving a final equation for the resolution of

$$\lambda = \frac{h}{\sqrt{2meV}} \tag{4.9}$$

This shows that the resolution can be improved by increasing the accelerating voltage, and this can theoretically lead to sub-Ångström resolution.[291] In practise however, this resolution will never be obtained due to unavoidable abberations within the TEM system. An example of this is chromatic abberation, which arises out of the microscope's electron source producing a narrow range of electron wavelengths rather than only one single wavelength. Since electrons of different wavelengths will be affected differently by the magnetic lenses within the microscope, this results in the formation of fringes along the edges of imaged structures. This, along with other sources of error like imperfections in the magnetic focusing lenses make obtaining this theoretical resolution extremely difficult, and in real systems 2Å resolution is likely the best that electron microscopy can achieve.[292] These electrons can, depending on the wavelength, penetrate nanomaterial samples partially or completely. They can then interact with the material in a variety of ways, as seen in Figure 4.4. Two imaging techniques were developed to obtain and analyse the information carried by these outgoing electrons, with the technique used being chosen based on whether or not the electrons are capable of penetrating through the entire sample.

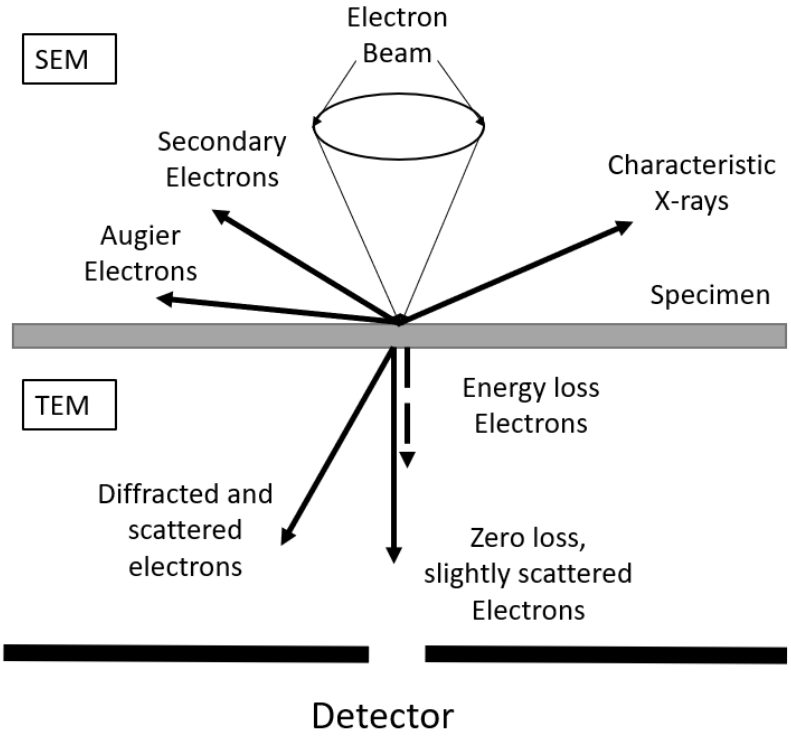

Figure 4.4: The processes involved when an electron beam interacts with a sample. Adapted from Ref.[293]

Transmission Electron Mircoscopy (TEM)

TEM imaging in this work has been carried out using a Jeol 2100 TEM operating at 200 kV. This tool uses thermionic emission from a LaB_6 crystal as the electron source and has a maximum high contrast resolution of 0.31 nm. The resulting high energy electrons can image the nanosheets with magnifications ranging from 100× to 1.2×10^5×, since the thinness of the sheets makes them electron transparent and the sub-nanometer wavelength of the electrons allows them to easily image the sheets.

As the electron beam hits and passes through the surface layers of the sample, there are a variety of electron-sample interactions that result in the emission of electrons, some of which can be seen in Figure 4.4. As the high energy electrons pass through the sample, some will interact with the constituent atoms of the sample elastically and inelastically, and be scattered away from the main beam. The degree of scattering is dependent on the atomic number of the material being analysed, as well as areas of increased thickness and grain boundaries.

A TEM can analyse materials in bright field or dark field mode, depending on what

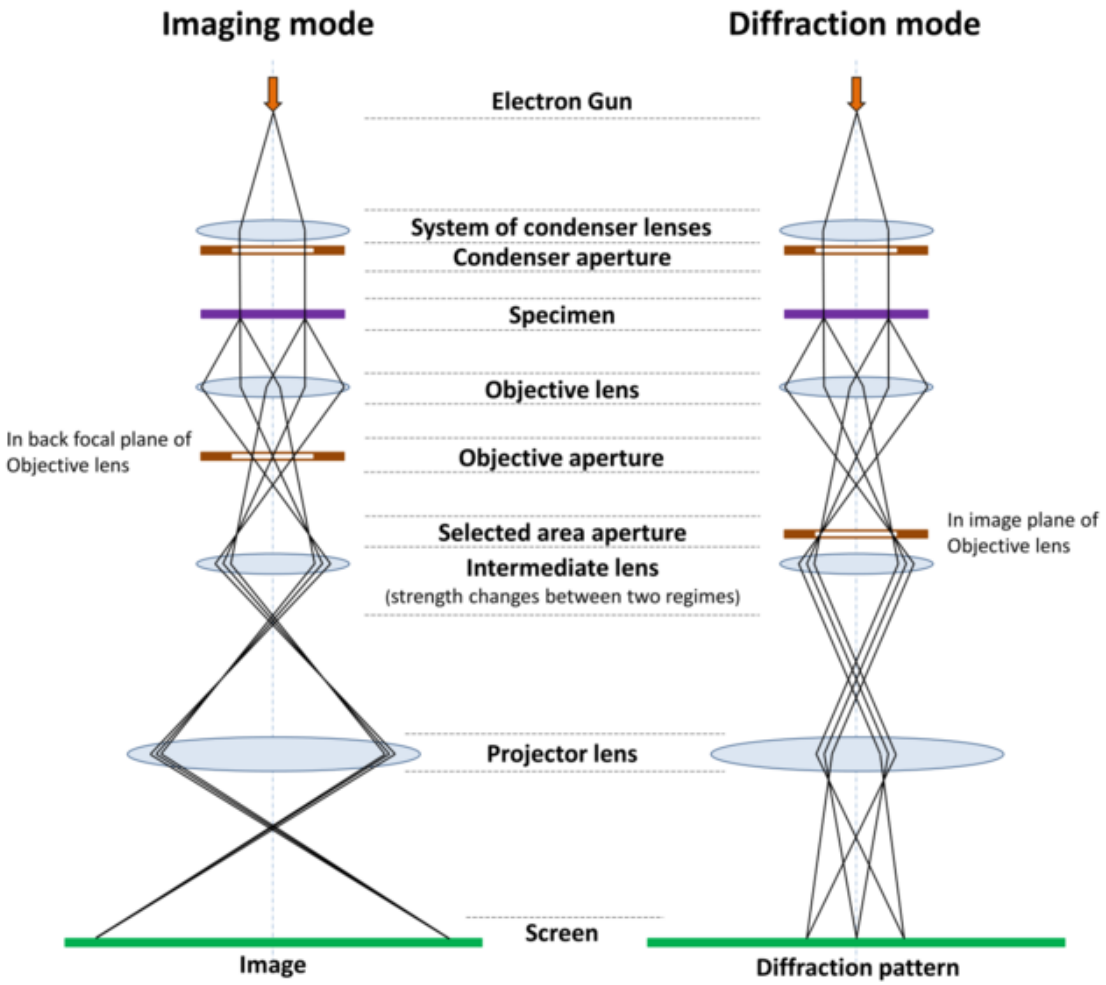

Figure 4.5: Cross-section of a TEM and the processes that take place when the electron beam interacts with the sample in bright field (left) and dark-field (right). Image from Ref[294] reproduced under CC BY-SA 4.0.

information is needed from the sample. In bright field imaging, electrons scattered via interactions with the sample are then filtered out via the objective aperture of the TEM, meaning that areas which deflect more electrons will appear darker in the resulting image. Conversely, in dark field mode these scattered electrons are included in the final image, producing a diffraction pattern dependent on the crystal structure of the sample. Schematics for the conventional imaging and diffraction modes of a TEM setup are shown in Figure 4.5, however for the purposes of this thesis only the bright-field imaging mode was used. Performing TEM on liquid phase exfoliated samples provides visual clarification that the dispersion consists of properly exfoliated nanosheets, as well as verifying that there are no unwanted non-nanosheet particles in the dispersion.

Preparing a sample for TEM analysis from a liquid phase exfoliated nanosheet ink first requires the ink to be diluted to the point that the dispersion is semi-transparent to the eye. This minimises the amount of material in a given droplet of the dispersion, enabling much more precise control over the quantity of material that is then deposited for imaging. A few drops are then pipetted onto ultrathin lacey carbon TEM grids provided by Ted Pella, Inc. placed on top of filter paper, such that any excess solvent is wicked away by the paper. The grids are then dried overnight in a vacuum oven in order to ensure that all solvent is removed. For the purposes of this work, all TEM grids were prepared using isopropanol and heated overnight at 80 °C to dry.

TEM imaging is also used to obtain a statistical analysis of the nanosheet lengths in a dispersion. This is done by taking multiple bright field images at several different points along the copper grid such that multiple nanosheets can be clearly seen on each grid. It is key that these images include all types of nanosheet present on the grid so as not to bias the resulting statistics in any way. Each individual sheet in each image is then analysed via ImageJ software in order to find the nanosheet length, which is taken to be the longest lateral dimension of the nanosheet. For an accurate measurement of the mean nanosheet length $<L>$, a large number (>150) of nanosheets should be analysed.

Scanning Electron Mircoscopy (SEM)

A Carl Zeiss Ultra Plus SEM with LaB_6 source was used throughout this thesis. This tool was operated with an accelerating voltage between 2 and 5 kV and focused onto the sample using magnetic condenser lenses. The spot size is typically on the order of a few nanometers, although this can be adjusted based on several factors, such as the accelerating voltage and the working distance.

For the purposes of imaging the sample surface, the most important of these are secondary electrons. They arise out of inelastic collisions between incoming electrons and the sample, in which valence electrons within the material are ionised. These electrons tend to have low energy, $\approx$ 50 eV,[295] meaning that only those emitted from atoms within ~20 nm of the film surface will have enough energy to escape and be

collected by the detector. As such they will provide ample information about the surface of the film, but other techniques will be necessary to image the interior. However, it also means that the secondary electrons carry detailed information on the sample topography, especially in relation to nanosheet edges, making them ideal for taking images of printed nanosheet films.

It is well known that a vital ingredient of success is not knowing that what you're attempting can't be done.

Terry Pratchett

5

WS_2-Graphene Composite Transistors

The increasing popularity of liquid phase nanomaterial dispersions has led to a similar increase in the number of studies looking into composites consisting of a mix of different nanomaterials, since two dispersions in the same solvent can easily be combined into a composite ink. Combined with the ease with which nanomaterial inks can be printed, this makes liquid phase exfoliation an ideal method for fabricating nano:nano composites without the need for any complex processing steps or time consuming techniques such as ALD.[296] It is important for clarity's sake to distinguish these nano:nano composites from the broader umbrella term of nanocomposites, which refers to any multiphase material in which one of the phases is a nanomaterial, i.e. has one or more dimensions being less than 100nm. The key distinction for nano:nano composites is that both of the component materials are nanomaterials, although the precise nature of these nanometerials is not set in stone and can range from 0D structures like buckyballs or nanoflowers to 2D nanosheets.[296,297,298]

Nano:nano composites are extremely versatile by nature, both in their potential composition and their applications. The dimensionality of the component nanomaterials is one factor that significantly influences the properties of the final composite, with a mix of different dimensionalities of nanomaterial (e.g. 1D:2D)[298] giving different properties compared to a mix of two nanomaterials of the same dimensionality (eg 2D:2D composites).[213] For example, it has been shown that the addition of carbon nanotubes

to a MoS_2 nanosheet network results in a significant increase in the overall conductivity even for very low (0.16 vol %) volume fractions of nanotubes.[298] Alternatively, one component of the composite can counter a drawback of the second component, such as when Ma *et al.* added MoS_2 nanosheets to cadmium sulfide nanoparticles.[297] The MoS_2 stabilises the CdS against photocorrosion, drastically increasing the efficiency of the resulting photocatalyst.

Many other similar studies exist showing the versatility of these nano:nano composites and the applications they are used in, ranging from strain sensors[57] and energy storage devices[299,300,301] to catalysts[302] and tribological systems.[303]

With printed nanosheet network electrochemical transistors being successfully demonstrated by Kelly *et al.* in 2017[5], the next step was to explore ways in which the performance of these devices could be improved. The transistors were heavily limited by the resistance associated with the inter-sheet junctions, with the overall film mobility being between two or three orders of magnitude lower than the mobility of a single nanosheet. The junction resistance is known to be the main factor limiting the performance of such films,[213,5] and this is known to be affected quite strongly by the morphology of the film.[99] Another potential solution to this problem, as suggested by Pathipati *et al.*,[304] is to add graphene to the mix. The graphene sheets would have significantly higher conductivity and carrier density compared to the semiconducting channel, and if added in small enough quantities might be able to improve the properties of the device by acting as small conducting islands within the semiconducting network, while still preserving the desirable switching behaviour of the semiconductor.

In this chapter we aim to investigate the properties of a porous nanosheet network (PNN) transistor as the composition of the channel is altered, moving from a purely semiconducting channel to a purely semimetallic one. In particular, we aim to investigate the network characteristics of the composite channel such as the carrier density and mobility, since prior to this, the knowledge of the properties of these nano:nano composites were limited to only basic investigations of the network conductivity.

5.1 Experimental Method

WS_2 powder purchased from Sigma Aldrich [CAS: 12138-09-9 ref: 243639] and graphite flakes purchased from Asbury Carbon [grade 3763] were exfoliated using a horn tip in HPLC N-methyl pyrrolidinone (NMP) purchased from Sigma Aldrich. 3.2 g of each material was immersed in 80 mL of NMP for an initial 40 mg/ml concentration. They were sonicated for one hour using a Sonics Vibra-cell VCX-750 ultrasonic processor at 60% amplitude, with a pulser set to 6 s on, 2 s off. The WS_2 dispersion was then centrifuged at $3218g$ in a Hettich Mikro 220R centrifuge following this initial step. The resulting sediment was collected and the supernatant discarded to remove any impurities dissolved in the solvent. The sediment was then redispersed in 80 mL of fresh NMP and exfoliated for 5 hours and 6 hours in the case of WS_2 and graphene respectively. The exfoliation conditions were the same throughout, and the dispersions were cooled using an ice bath during the exfoliation process.

Due to the inherently polydisperse nature of LPE dispersions, it was necessary to centrifuge the two dispersions to focus only on a particular range of nanosheet sizes. This was achieved using a two-step centrifugation process, in which the dispersions were centrifuged in two hour steps, first one at lower rpm and then one at higher rpm. Following the lower rpm step ($26.5g$ for WS_2, $662.5g$ for graphene), any unexfoliated material was trapped in the sediment and discarded while the supernatant was collected. They were then centrifuged at $106g$ and $3816g$ for WS_2 and graphene respectively. Given the high boiling point and known toxicity of NMP, it was necessary to transfer the dispersions into a suitable solvent for printing. A solvent exchange method[171] was used to redisperse the sediment from the higher rpm centrifuge step in isopropanol (IPA). This involved centrifuging the initial dispersion at a high rpm for two hours, so that all of the dispersed material was sedimented out of dispersion. In order to ensure that as much material as possible was collected, the rpm used for the solvent exchange was at at least twice that of the collection step in the liquid cascade centrifugation step. Once the material had sedimented, it was then redispersed in the desired replacement solvent, in this case IPA. These steps were then repeated in order to remove any trace

amounts of the initial solvent present in the dispersion.

UV-Vis spectroscopy was used to obtain concentration measurements, and the dispersions were then diluted such that the final concentrations of the WS_2 and graphene inks were approximately 1.5 mg/ml an 1 mg/ml respectively.

The inks were then mixed in specific amounts such that the mass fraction of graphene varied from 0 (pure WS_2) to 1 (pure graphene), and such that the total volume of the composite ink was between 25 and 30 mL. The composite inks were then deposited using an aerosol sprayer as described in Chapter 4. Finally, cyclic voltammetry measurements were carried out on four films ranging from 0wt% graphene to 100wt% graphene.

5.2 Results & Discussion

5.2.1 Inks and Deposition

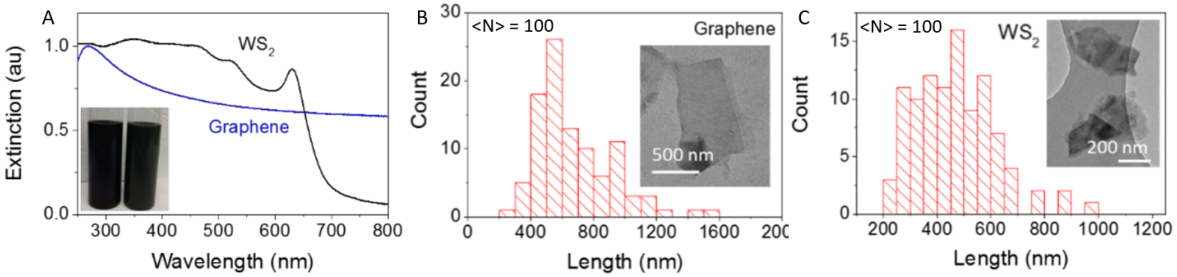

Figure 5.1: (A) Uv-Vis spectra of the graphene (blue) and WS_2 (black) inks used in this work. Inset: the two inks used. (B) Histogram for the nanosheet lengths in the graphene ink, obtained via TEM. Inset: TEM image of a graphene flake. (C) Histogram for the nanosheet lengths in the WS_2 ink, obtained via TEM. Inset: TEM image of a WS_2 flake. For both (B) and (C), the histograms represent a count of 100 nanosheets.

UV-Vis spectroscopy is a helpful way to both confirm the presence of the desired nanomaterials and provide information on the entire ensemble of nanosheets. The graphene spectrum (Figure 5.1(A), blue) shows the characteristic absorption peak at ~280nm corresponding to the Van Hove singularity, with the spectrum plateauing for longer wavelengths. The UV-Vis data also allows the mean thickness of the dispersed

graphene flakes to be estimated following the metric composed by Backes *et al.*[91]

$$< N >= 35.7 \times \frac{\varepsilon_{550}}{\varepsilon_{325}} - 14.8 \tag{5.1}$$

Where ε_{325} and ε_{550} are the values of the extinction at 325nm and 550nm respectively. Using the values obtained from Figure 5.1(A) of $\varepsilon_{325} = 0.8579$ and $\varepsilon_{550} = 0.6358$, this gives a final value for <N> of ~12 layers thick. The WS_2 spectrum (Figure 5.1(A), black) similarly shows the expected characteristic peak at ~630nm, corresponding to the A-exciton, with less pronounced peaks at shorter wavelengths corresponding to higher order excitons.[305] Similar to the graphene peak above, the A-exciton can be used to gather information about the nanosheet ensemble using this metric[152]

$$< N >= 6.35 \times 10^{-32} e^{\frac{\lambda_A}{8.51}} \tag{5.2}$$

Here, λ_A represents the wavelength associated with the A-exciton. In a WS_2 nanosheet and other TMDs, the position of the A-exciton is known to depend on the thickness of the sheet in question.[152,144,282] Since the position of the A-exciton always corresponds to a local minimum in the second derivative of the extinction spectrum, it is easy to determine the associated wavelength, which in this case was 630nm. This gives a mean thickness value of 9 layers. Since the thickness dependent bandgap of WS_2 is only a factor for $N \leq 6$,[47,54] therefore we can reasonably assume that these nanosheets, or the vast majority thereof, are of a uniform bandgap. This removes the possibility of inhomogeneities in the WS_2 bandgap. Adjacent nanosheets having different bandgaps means that an electron travelling from one to the other will need to overcome a potential barrier in order to do so, as well as the van der Waals gap associated with any nanosheet-nanosheet junction. This will manifest as an increase in the resistance associated with the junction, which will adversely affect the overall network performance. While it is not possible to definitively state that there are no nanosheets of $<N> < 6$ present in the networks due to the inherent polydisperse nature of LPE dispersions, we assume that any such nanosheets are in minute enough quantities that they will not be able to adversely impact the performance of the overall network.

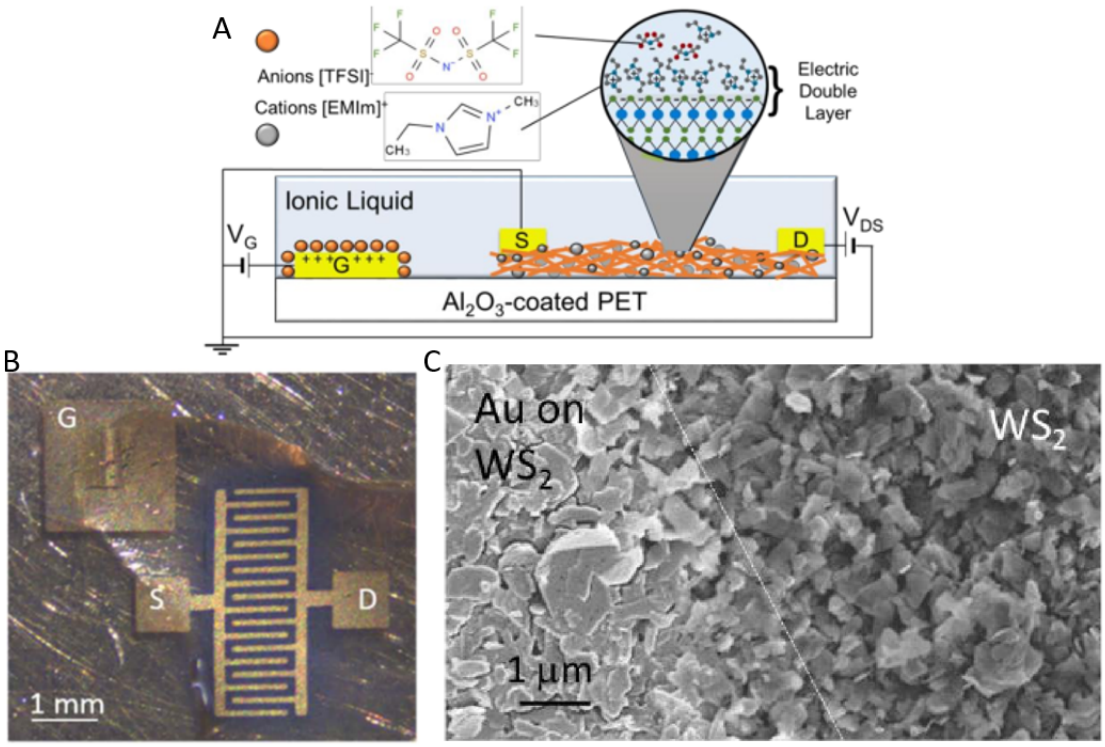

Figure 5.2: (A) A schematic of an electrolytically-gated transistor, showing the ions within the ionic liquid. The zoomed in area represents a close-up of the electrical double layer that forms during gating. (B) An image of a single transistor after the addition of the ionic liquid. The source, drain, and gate electrodes are labelled. (C) An SEM image of the same device, looking at the area where the gold was deposited on top of the nanosheet network.

In order to obtain values for the mean nanosheet length ($<L>$) of the two dispersions, statistical TEM analysis was performed on both dispersions. The length was defined as the longest lateral dimension of the nanosheets. The results of this analysis can be seen in Figures 5.1(B) and (C), providing values of $<L>$ of 470 nm and 680 nm for WS_2 and graphene respectively after >100 measurements. Individual flakes can be seen in the insets in Figures 5.1(B) and (C), confirming that the dispersions consist of properly exfoliated 2D nanosheets.

Since both inks are dispersed in the same solvent (isopropanol), this allows them to be very easily mixed into 2D:2D composite inks with tightly controlled mass fractions of graphene (M_f)

$$M_f = \frac{M_{Gr}}{M_{Gr} + M_{WS_2}} \tag{5.3}$$

ranging from pure WS_2 inks ($M_f = 0$) to pure graphene inks ($M_f = 1$). These inks were

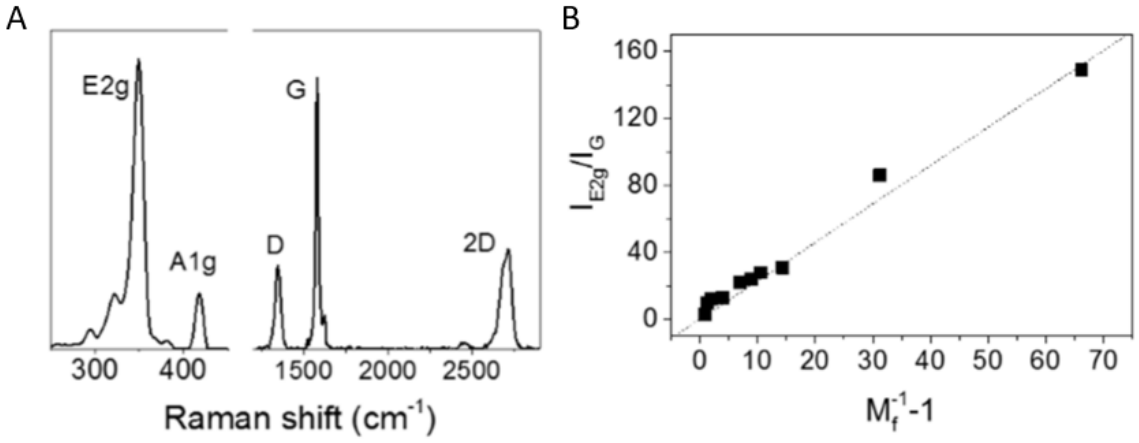

Figure 5.3: (A) Raman spectrum of a composite film with $\mathcal{M}_f = 0.5$. The graphene signal has been multiplied by 2.5. (B) Plot of the ratio of the intensities of WS_2 E_{2g} to graphene G peaks against ($\mathcal{M}_f{}^{-1}$ 1), where $\mathcal{M}_f$ is the graphene mass fraction.

then used to make sets of electrochemical transistor devices, a schematic of which can be seen in Figure 5.2(A), with a picture of the same device seen in Figure 5.2(B). The ionic liquid can be seen covering the channel and gate electrode in Figure 5.2(B). Figure 5.2(C) shows an SEM image of the nanosheet film at the electrode:channel interface, with the gold visible on top of the nanosheet network. It can be seen that the gold conforms to the surface of the network, ensuring good contact and working to lower the contact resistance associated with the electrode:channel interface. The SEM also gives an indication of the film morphology, with the nanosheets being randomly aligned within the network. The random alignment of the rigid sheets is what gives rise to the large internal free volume that is expected of porous nanosheet networks.[298,5]

Figure 5.2(A) shows the principle of operation of these electrolytically gated devices. When the gate electrode is biased against the source, ions are drawn from within the ionic liquid to the electrode:liquid interface. The oppositely charged ions within the liquid are then driven into to the channel, in turn drawing more charge carriers from the source and drain electrodes to balance out the charge of the electrolyte ions. As the voltage at the gate electrode is increased, the concentration of ions at the channel:liquid interface increases, thus increasing the carrier concentration within the channel. This in turn increases the channel conductivity.

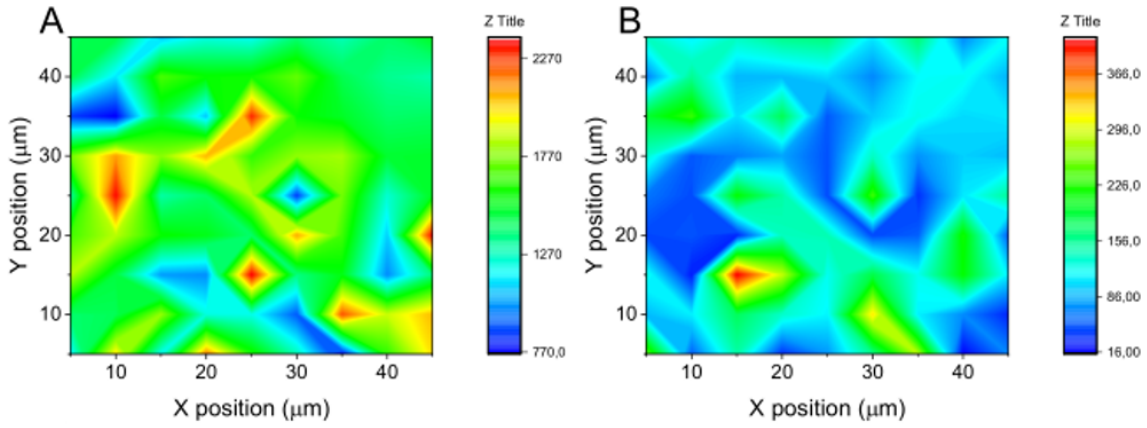

Figure 5.4: Raman maps carried out on the $M_f = 0.5$ sample, each one representing a 40 μm x 40 μm area. (A) Intensity of the WS_2 E_{2g} peak, (B) Intensity of the G peak.

As a final confirmation of the device channel composition, Raman spectroscopy was used to analyse the quality of the materials within the film, as well as providing information on the spatial distribution of the graphene and WS_2 nanosheets. A combined spectrum for the $M_f = 0.5$ ink can be seen in Figure 5.3(A), although in this graph the intensities have been adjusted so that the magnitudes of the WS_2 and graphene peaks are visually similar. This was done by multiplying the magnitude of the graphene spectrum by a factor of 2.5. The relative intensities within the graphene sub-spectrum remained the same. The low-frequency E_{2g} and A_{1g} modes correspond to WS_2, and the higher frequency D, G, and $2D$ modes correspond to graphene.[306,116] The relative intensities of the WS_2 and graphene peaks also provides information on the mass fraction of graphene, provided the film roughness and uniformity are relatively unchanged with increasing M_f, and that the total amount of material being analysed is constant. Since the film thicknesses lie all lie in the region of 500 nm to 1 μm, and Raman spectroscopy is fundamentally a surface investigation technique, this latter condition can be assumed. This is because the relative intensity of the signal coming from one material within a nano:nano composite scales linearly with the relative amount of said material under illumination, and can therefore be expressed in terms of the mass fraction of graphene M_f[307,298]

$$\frac{I_{E_{2g}}}{I_G} \propto \frac{M_{WS_2}}{M_{Gr}} = \frac{1}{M_f} - 1 \tag{5.4}$$

where $I_{E_{2g}}$ and I_G are the intensities of the WS_2 E_{2g} and graphene G modes respectively.

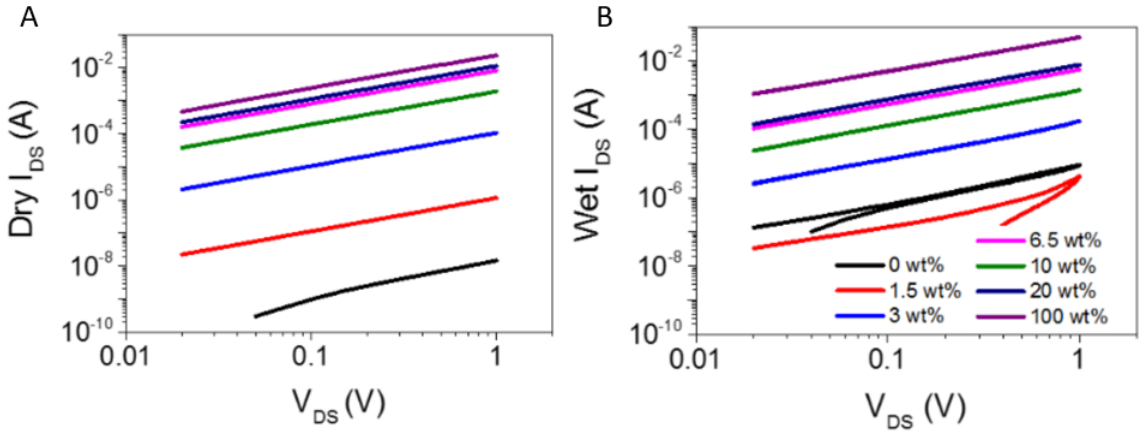

Figure 5.5: I_{DS} against V_{DS} graphs for different values of φ, for both (A) the dry state and (B) the wet state. Inset: Legend.

As seen in Figure 5.3(B) the expected linear scaling is present, showing that the film morphology is roughly similar over the range of M_f since the starting assumption in this analysis was that the film roughness and uniformity are unchanging with increasing M_f. However, as can be seen in the various Raman maps in Figure 5.4, the distribution of each of the composite materials is not uniform. Areas with higher E_{2g} signal correspond to areas with lower G signal (Figure 5.4(A)) and vice versa (Figure 5.4(B)). This kind of clumping is not uncommon in nanocomposites, but the degree of inhomogeneity seen here is not severe. It should also be noted that as a consequence of this inhomogeneity, it was necessary that the datapoints in Figure 5.3(B) be taken from the average of several Raman spectra, corresponding to a 20 µm × 20 µm area. This reduced the error arising from the graphene clumping.

5.2.2 Electrical Characterisation

While it is easier to look at the composite formation process in terms of the mass fraction of graphene, it is better to analyse the properties of the composite itself in terms of the volume fraction of graphene, since this will also take into account the film porosity P. By considering the component densities $\rho_{Gr} = 2200$ kg/m^3 and $WS_2 = 7500$ kg/m3 the volume fraction can be derived from Equation 5.3. To begin with, the volume

fraction is defined as

$$\varphi = \frac{V_{Gr}}{V_{Gr} + V_{WS_2}}(1 - P) = \frac{1 - P}{1 + \frac{V_{WS_2}}{V_{Gr}}} \tag{5.5}$$

By expressing the volumes in terms of the mass and density of the respective materials, this becomes

$$\varphi = \frac{1 - P}{1 + \frac{M_{WS_2}/\rho_{WS_2}}{M_{Gr}/\rho_{Gr}}} \tag{5.6}$$

By rewriting M_{WS_2}/M_{Gr} as $(M_{WS_2} + M_{Gr} - M_{Gr})/M_{Gr}$, Equation 5.3 can be substituted into this equation to obtain

$$\varphi = \frac{1 - P}{1 + \frac{\rho_{Gr}}{\rho_{\mathrm{WS_2}}}\left(\frac{1}{M_f} - 1\right)} \tag{5.7}$$

In this work we have taken the value of P to be 0.5, since previous works have estimated the porosity of nanosheet networks to be between 0.4 and 0.6, depending on the material used.[5,2] Since the graphene and WS_2 nanosheets are of a similar length and aspect ratio, it is assumed that the porosity P is constant with respect to volume fraction since the film morphology will be determined primarily by those factors.

Conductivity measurements were performed on the printed devices both before ("dry") and after ("wet") the addition of the ionic liquid EMIm-TFSI. The output graphs (drain-source current I_{DS} against drain-source voltage V_{DS}) for both the dry and wet states are shown in Figures 5.5(A) and Figures 5.5(B) respectively. In the dry state, the conductance shows the expected increase as φ increases, with the spread in conductances ranging from ~10^{-8} S for a pure WS_2 device to ~10^{-2} S for a pure graphene device. When comparing these curves to those exhibited by the same devices after adding the ionic liquid, the expected trend of increasing conductance with increasing graphene content is still present. It should be noted that the range of conductances over the volume fraction range has decreased, with the low-φ devices showing a larger increase from dry to wet than the high- φ devices.

A similar trend can be observed in the device transfer curves (drain-source current I_{DS} against gate-source voltage V_{GS}) in Figure 5.6 as the graphene volume fraction

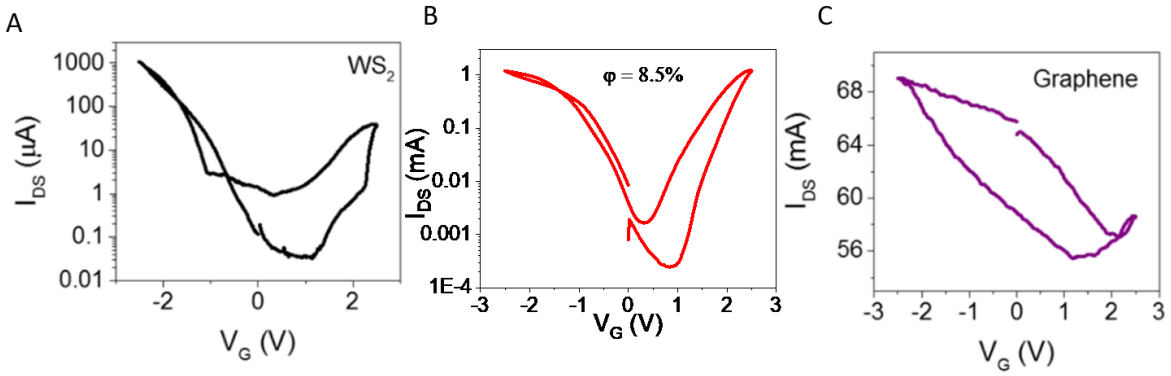

Figure 5.6: Transfer curves for (A) a pure WS_2 device, (B) a device where $\varphi = 0.085$, and (C) a pure graphene device.

increases. For the WS_2 device (Figure 5.6 (A)), the transfer curve shows a high on:off current ratio of approximately 2×10^4, with relatively low on and off currents of ~1 mA and ~0.1 μA respectively. As the graphene content increases, the composite curve seen in Figure 5.6(B) shows the same on current and a slight increase in the off current, leading to a minor decrease in the on:off ratio to 6×10^3. The graphene-only device (Figure 5.6(C)) shows very different behaviour from the previous transfer curves. The off current has increased to ~56 mA while the on current is roughly 70 mA, with a resulting on:off current of only ~1.25. It is clear that the effect of the gate voltage is massively reduced as the graphene content increases. This fits with the expected transistor behaviour, with the devices transitioning from semiconductor behaviour at low φ to conductive behaviour at high values of φ. In the case of WS_2 the carrier density of the dry channel is much lower than that of the graphene channel, and therefore the gating effect is expected to induce a much larger change in carrier density in the WS_2 devices.

All three representative transfer curves shown in Figure 5.6 also show significant hysteresis. This is an issue with electrolytically-gated devices that has been recorded in the literature,[237] and which has been attributed previously to charge trapping by water molecules near the channel, albeit in more traditional back-gated devices.[244] This can be taken as a sign that the ionic liquid is not fully dry, however the degree of hysteresis is not severe, and is in fact an improvement compared to previous nanosheet network transistors.[5]

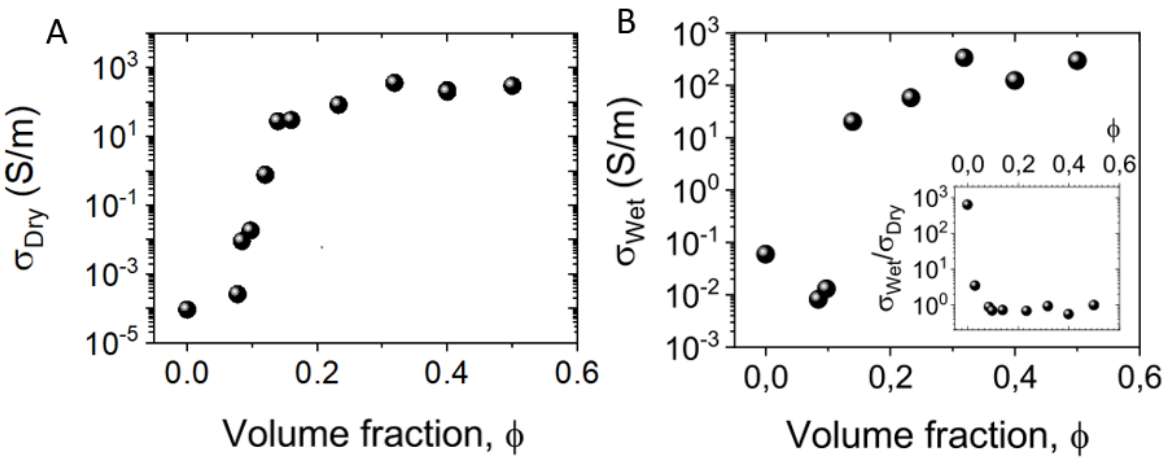

Figure 5.7: (A) Dry conductivity values as a function of volume fraction of graphene. (B) Wet conductivity values as a function of volume fraction of graphene. Inset: the ratio of wet to dry conductivity values against volume fraction.

Note that when taking transconductance measurements, all values were taken from the p-type side of the transfer curves (the side where $V_G < 0$), and therefore all mobilities and carrier densities reported are for holes. It should be noted that all three transfer curves shown do display some n-type behaviour, most prominently shown in Figure 5.6(B) where the device behaviour is fully ambipolar, with equivalent device behaviour for both n- and p-type carriers. Despite this, the majority of transfer curves analysed displayed significantly higher p-type currents than n-type currents, and thus n-type behaviour was not considered during the calculations in the rest of this chapter.

5.2.3 Percolation Behaviour

This effect can be explored in more detail by looking at the network conductivity change as the graphene content increases in Figure 5.7(A). As the volume fraction increases, the conductivity initially only slightly increases with graphene content until it hits a critical value at around $\varphi = 0.08$. Following this point, the conductivity increases sharply until it begins to level off again at $\varphi \approx 0.11$, after which it continues to increase until the maximum value at $\varphi \approx 0.3$. This matches what is predicted by percolation theory,[307] which predicts that this massive and rapid increase in conductivity occurs

after a critical value, with the trend being described using the following equation

$$\sigma = \sigma_0 \left(\varphi - \varphi_c\right)^n \tag{5.8}$$

where σ_0 is a constant related to the graphene conductivity, φ_c is the percolation threshold, and n is the percolation exponent. This equation describes the electrical behaviour of a composite consisting of one insulting component and one conductive component as the volume fraction of the conductive component increases. Applying this model to the WS_2:graphene composites, the conductivity equation must be modified to account for the starting conductivity of the WS_2

$$\sigma = \sigma_{WS_2} + \sigma_0 \left(\varphi - \varphi_c\right)^n \tag{5.9}$$

where σ_{WS_2} represents the conductivity of the WS_2 sub-network which is the insulating portion of the percolation model.

As small amounts of graphene are added to the WS_2 network, the conductivity increases slightly in the region below the percolation threshold, which is the point at which there is enough graphene within the composite to form a continuous conducting pathway from one electrode to the other. This means that the more conductive sub-network can now carry the bulk of the current as more and more graphene is added, corresponding to a rapid decrease in the network resistance. After the graphene sub-network is formed, further additions of graphene still cause an increase in conductivity, but at a much slower rate since it is already dominating the network properties by this stage. Although there is some current being carried by the WS_2 sub-network at this point, it is negligible compared to that carried by the graphene.

A similar process can be seen in both the wet conductivity in Figure 5.7(B) and the ratio between the wet and dry conductivities in Figure 5.7(B, inset). The wet conductivity shows a slight decrease following the addition of graphene, after which the conductivity increases following the same percolation curve. This initial fall in conductivity may result from experimental error, while the rest of the wet conductivity datapoints behave as expected. The similar behaviour in the ratio of wet to dry conduc-

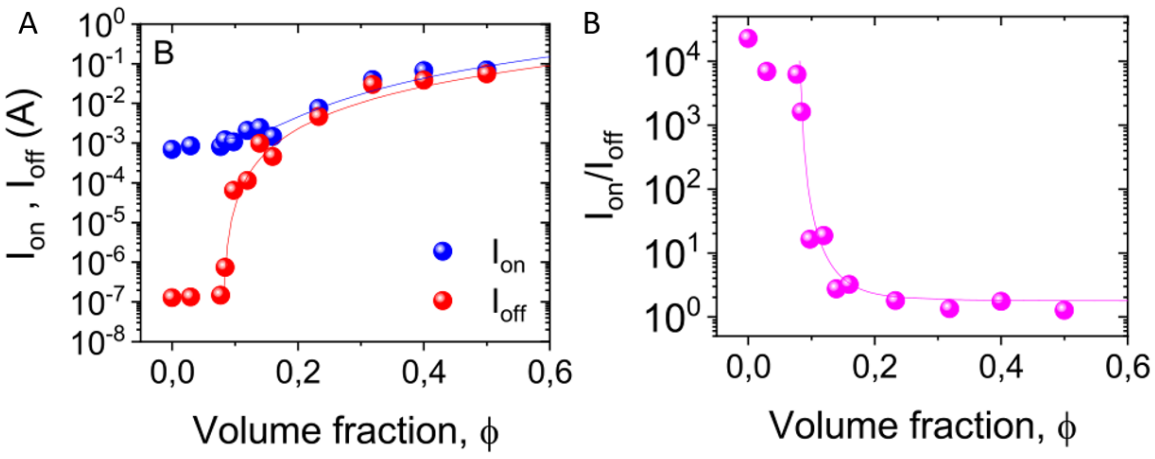

Figure 5.8: (A) The on (blue) and off (red) currents of the transistors against volume fraction of graphene. (B) The on:off current ratio against the volume fraction.

tivities also shows a clear transition between the pre-percolation networks dominated by WS_2 and the post-percolation networks dominated by graphene. For the WS_2 networks with their relatively low nanosheet carrier density, the presence of the ionic liquid causes doping, likely due to an imbalance of cations and anions at the nanosheet:liquid interfaces. This had previously been observed in other porous nanosheet network devices.[5]

Percolation theory can also be used to analyse the trend in the on and off currents, since the currents would both be expected to follow the same trend as the conductivities. Hence, the two trends seen in Figure 5.8 can be modelled using variations of Equation 5.9

$$I_{on} = I_{on,WS_2} + I_{on,Gr} 2^{n} \left(\varphi - \varphi_{c}\right)^{n} \tag{5.10}$$

for the on currents, and

$$I_{off} = I_{off,WS_2} + I_{off,Gr} 2^{n} \left(\varphi - \varphi_{c}\right)^{n} \tag{5.11}$$

for the off currents. Here I_{on} and I_{off} refer to the device on and off currents respectively, which are taken to be the maximum and minimum current values in the transfer curve respectively. The factor 2^{n} is added to account for the film porosity and ensure that the max graphene current occurs at $\varphi = 0.5$. Fitting these parameters to the on and off

current trends gives the following values: $I_{on,WS_2} = 1.3$ mA, $I_{on,Gr} = 130$ mA, $\varphi_c = 0.08$, $n = 2.6$ for the on currents, and $I_{off,WS_2} = 0.1$ μA, $I_{off,Gr} = 76$ mA, $\varphi_c = 0.08$, $n = 2.5$ for the off currents.

Since the magnitudes of the values obtained for I_{off,WS_2} and $I_{off,Gr}$ match what would be expected for a WS_2 and a graphene film respectively, and the magnitudes of I_{on,WS_2} and $I_{on,Gr}$ are similar to those obtained in the transfer curves, this shows that the on and off currents can also be predicted using percolation theory.

It also confirms the initial estimation for the percolation threshold of $\varphi_c = 0.08$. While at first glance this value seems unusually high, especially when compared to the percolation thresholds of ~0.01 observed in graphene:polymer composites[308] and 1D:2D composites,[298] it is similar to the percolation threshold that was observed in similar 2D:2D composites.[213,307] The higher percolation threshold is thus attributed to the very similar geometries of the conductive and insulating elements of the composite, since both elements are 2D rather than one being 2D and one being 1D or 0D.

Following on from this, it should also be possible to express the on:off current ratio in terms of percolation theory by combining Equations 5.10 and 5.11

$$\frac{I_{on}}{I_{off}} = \frac{I_{on,WS_2} + I_{on,Gr} 2^n \left(\varphi - \varphi_c\right)}{I_{off,WS_2} + I_{off,Gr} 2^n \left(\varphi - \varphi_c\right)} \tag{5.12}$$

Fitting this equation to the on:off current ratio as a function of φ using the values for the constants obtained during the previous fits and with n fixed as 2.5, it can be seen in Figure 5.8 that this equation fits the data and shows the same difference in behaviour between the pre-percolation threshold and post-percolation threshold regimes. This also gives estimations for the on:off ratios of both pure WS_2 and pure graphene devices as $\left(I_{on}/I_{off}\right)_{WS_2} = 1.3 \times 10^4$ and $\left(I_{on}/I_{off}\right)_{Gr} = 1.7$, both of which are consistent with the observed on:off ratios.

When analysing these printed nanosheet network transistors, it is crucial that a suitable parameter be found that can represent the overall performance of the device. Some such parameters that are often seen in the literature are the transconductance g_m, the on:off current ratio, and the product of the volumetric capacitance and network

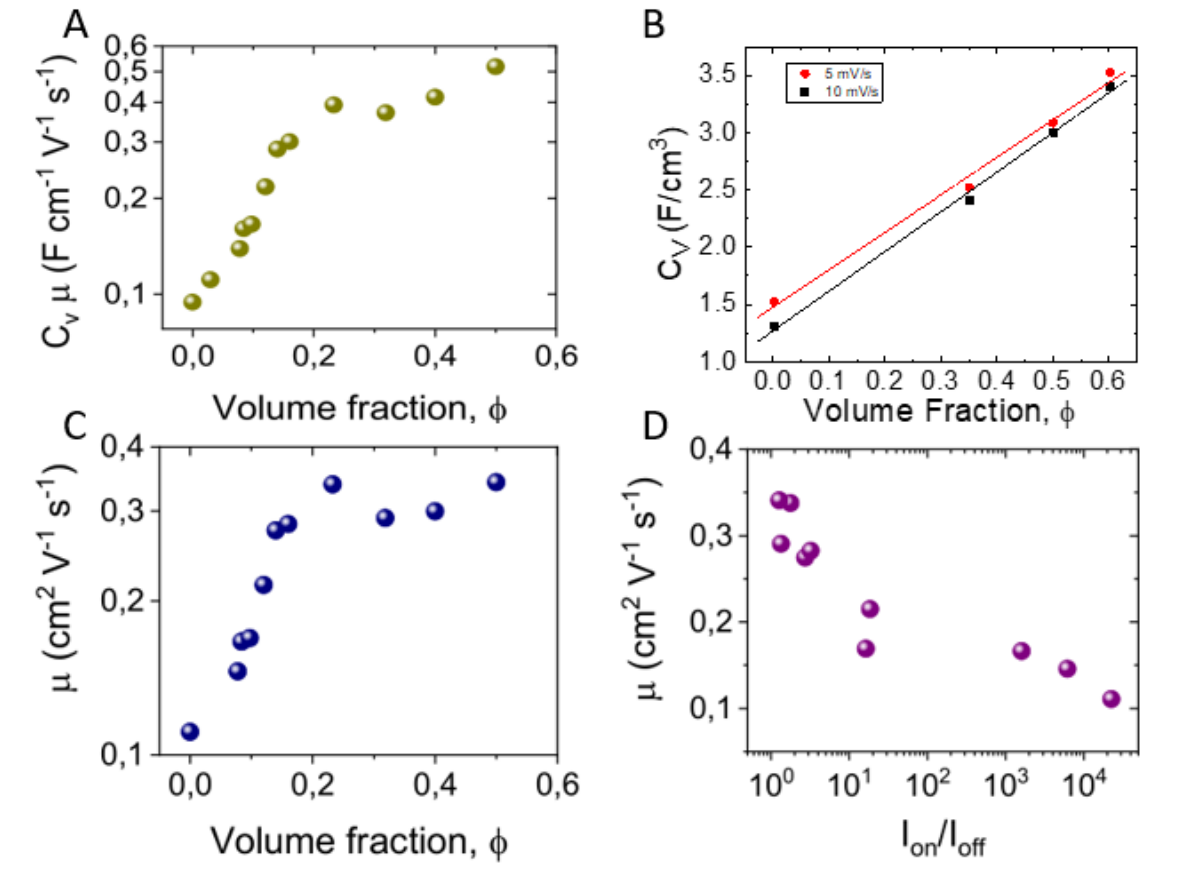

Figure 5.9: (A) A plot of the figure of merit C_V μ against volume fraction. (B) A plot of C_V against volume fraction for scan rates of 5mV/s and 10 mV/s. (C) Network mobility against volume fraction. (D) Mobility against on:off ratio.

mobility $C_V\mu$.[5] Of these three, $C_V\mu$ is the most useful since it does not depend on any of the device's physical dimensions, but instead on the inherent properties of the network. The figure of merit is calculated from the slope of the transfer curves using a rearranged form of Equation 3.30

$$C_V\,\mu = \frac{g_m L}{V_{DS}\,wt} = \left(\frac{\delta I_{DS}}{\delta V_{GS}}\right)_{Max} \frac{L}{V_{DS}\,wt} \tag{5.13}$$

where L, w, and t are the channel length, width, and thickness respectively. This allows the figure of merit as a function of φ to be plotted in Figure 5.9(A). The figure of merit shows only a slight increase with increasing graphene volume fraction, but the shape of the curve seems once again to be consistent with percolation theory, suggesting that the network mobility can also be divided into two distinct regimes. In order to correctly confirm this, it is first necessary to decouple the two terms contained within the figure

of merit, since it is not necessarily the case that the volumetric capacitance is constant with respect to volume fraction.

From analysing the cyclic voltammograms for electrochemical devices with four different values of φ ranging from $\varphi = 0$ to $\varphi = 0.5$, the value of C_V as a function of φ was found, and can be seen in Figure 5.9(B). This suggests a linear increase in C_V with increasing φ, which was then used to extrapolate C_V values for all other volume fractions. This variation in C_V with increasing graphene content is to be expected since it has been shown that the volumetric capacitance depends on the dielectric constant ($\varepsilon_{r,Gr} = 6.9$[309], $\varepsilon_{r,WS_2} = 4.13$[310]) as well as the mean thickness of the nanosheets.[235] The network mobility μ can be seen in Figure 5.9(C) plotted against φ, and it can be seen that it shows two distinct regimes. Starting at 0.11 $cm^2V^{-1}s^{-1}$ for a pure WS_2 network, the mobility increases more or less linearly with increasing graphene content until it reaches a plateau for $\varphi \geq$ ~0.2, after which it is more or less constant at 0.35 $cm^2V^{-1}s^{-1}$. This is consistent with the percolation behaviour observed in the other device parameters, since the increase in mobility starts in earnest at the percolation threshold of $\varphi = 0.08$ and begins to plateau at roughly the same value of φ as the other parameters.

This confirms that as well as the conductivity, the changes in the switching behaviour of the transistors as φ increases are governed by percolation theory. More specifically, it allows the properties of the composite network to be decoupled into the properties of the WS_2 and graphene sub-networks. Pre-percolation, the WS_2 sub-network dominates the overall behaviour, as seen by the excellent switching behaviour and high on:off current ratios observed in the devices with φ below the percolation threshold. After this point the graphene sub-network becomes fully established and begins to carry current, and it begins to dominate the device behaviour. This leads to high on and off currents and improved carrier mobility, but the on:off current ratio falls off rapidly until it is on the order of ~2. While the WS_2 sub-network is still contributing to the overall network behaviour even after percolation, as can be seen by the continuing increases in the on and off currents with increasing φ, its contribution to the network mobility is effectively zero since the mobility becomes constant for $\varphi >$ ~0.25.

The mobility observed for the WS_2 devices is broadly in line with previously observed mobilities for WS_2-based transistors,[5] but the graphene networks exhibit significantly lower mobilities than would be expected for an inkjet-printed nanosheet network device.[163,164] One likely explanation for this is the difference in morphology between the sprayed networks and the inkjet printed networks in Refs.[163,164] In an inkjet printed film, there is control over the positioning and spacing of the droplets, which allows some degree of control over how the droplets build up into a complete film, unlike the entirely random deposition that comes with a sprayed network. This in turn could lead to significantly higher junction resistances associated with sprayed films when compared to inkjet printed films, due to improved alignment between sheets. Edge-edge or edge-basal plane junctions are expected to have much higher resistances associated with them than basal plane-basal plane ones. The importance of network morphology can clearly be seen in the work of Lin *et al.*,[99] where they fabricated highly aligned MoS_2 networks which showed high network mobilities on the order of 5 $cm^2V^{-1}s^{-1}$, barely less than one tenth of the expected mobility of a single flake.[5] Likewise the works of Secor *et al.*[223] and Barwich *et al.*[225] shows the degree to which the porosity (and thus the morphology) can impact the conductivity of a network.

The increase in mobility observed for these WS_2:graphene composites is not significant, since it changes by only a factor of three when going from pure WS_2 to pure graphene. This is in sharp contrast to the behaviour exhibited by the conductivity, which increases by a factor of 10^8. Considering the significant difference in nanosheet mobilities when comparing WS_2 flakes to graphene (~50 $cm^2V^{-1}s^{-1}$ for WS_2[5], ~2000 $cm^2V^{-1}s^{-1}$ for multilayer graphene[311]), this shows that the small change observed in these networks does not arise from changes induced within the nanosheets themselves. The network mobility has two main components to it: one from the intrasheet transport and one from the intersheet transport. By considering the network as a combination of these contributions in series, the network mobility can be expressed as

$$\mu = \frac{\mu_{NS}}{\left(1 + \frac{\mu_{NS}}{\mu_J}\right)} \tag{5.14}$$

where μ_J is the contribution from intersheet transport and μ_{NS} is the contribution from the individual sheets. This is similar to what was derived in Equation 3.15, except the second term in the denominator of Equation 3.15 has been neglected.

Since the smaller quantity will dominate the overall network mobility, and the recorded values of μ are significantly lower than the nanosheet mobility values, the contribution from the indidivual sheets can be neglected and $\mu \approx \mu_J$. Hence the observed change in network mobility arises from changes in the resistances at WS_2—WS_2, WS_2—graphene, and graphene—graphene junctions, which in turn suggests that the resistance associated with a WS_2-WS_2 junction is roughly three times higher than that of a graphene-graphene junction.

The network properties being dominated by the junction resistance is further supported by the similarly low value of the dry conductivity of the sprayed graphene films of 300 Sm^{-1}, which is siginifcantly lower than values for printed graphene found in other works.[312,313] Given that the Raman spectrum showed no significant presence of defects, it is likely that this drop in conductivity is a property of the network rather than a property of the graphene flakes themselves.

While the addition of graphene to a WS_2 electrochemical transistor has successfully improved the network conductivity and mobility, it is essential to also consider how it affects the other properties of the device. An ideal transistor would show high carrier mobility but also high on:off current ratio, meaning it is important to consider the effect of the graphene on this property as well. A graph of network mobility against on:off ratio is plotted in Figure 5.9(D), and it can clearly be seen that the two properties are negatively correlated and that adjusting φ to increase one causes a decrease in the other. This trend continues even for devices near the percolation threshold, since the devices with $\varphi \approx 0.1$ still shows a decrease in the on:off ratio from 10^4 to 10^3 with a corresponding mobility increase of ~100%. However this mobility increase is quite small when taken against the accompanying decrease in the on:off ratio, which would suggest that the addition of small amounts of graphene to a TMD network is not a feasible route to improving the device performance.

Despite this unfortunate result, it is still possible to use this to further explore

the properties of the composite both before and after the addition of the ionic liquid. Although previous works have investigated the change in conductivity in a 2D nanosheet network with the addition of a conducting element[307,213], this is where such investigations tend to stop. At this point it is useful to note that a previous work[213] looking into 2D:2D MoS_2:graphene composites theorised that the increase in the network performance was due to both an improvement in the network carrier density and a simultaneous increase in the network mobility. The carrier density increase arises as a result of the naturally higher carrier density of graphene compared to WS_2, whereas the network mobility increase arises from the idea that as the carriers move through the network, they will move faster through the graphene sheets and thus the overall drift velocity increases and thus mobility will increase. Both quantities should also see an increase below the percolation threshold, although such an increase would naturally be significantly smaller than above the threshold.

To that end, the carrier density can be extracted from the existing mobility and conductivity data, since it is known that

$$\sigma = n_h e \mu_h + n_e e \mu_e \tag{5.15}$$

where σ is the conductivity, e is the charge of an electron, n_e and n_h are the carrier densities for electrons and holes respectively, and μ_e and μ_h are the electron and hole mobilities. Since the device behaviour suggests that the composites are dominated by p-type behaviour, we approximate that the conductivity term due to holes can be neglected such that $\sigma = n_h e \mu_h$. In order to properly compare the mobility with the dry conductivity however, it is necessary to assume that the overall network mobility is unaffected by the addition of the ionic liquid. This is supported by the work of Uesugi *et al.*,[240] who suggest that adding ionic liquid to a graphene nanosheet primarily affects the sheet via doping and a corresponding increase in the carrier density. Furthermore, the contribution to the network behaviour from the junction resistance is almost certain to dominate any changes to the network mobility arising from improving the mobility of individual nanosheets, as detailed above. Hence, the network mobilities shown in

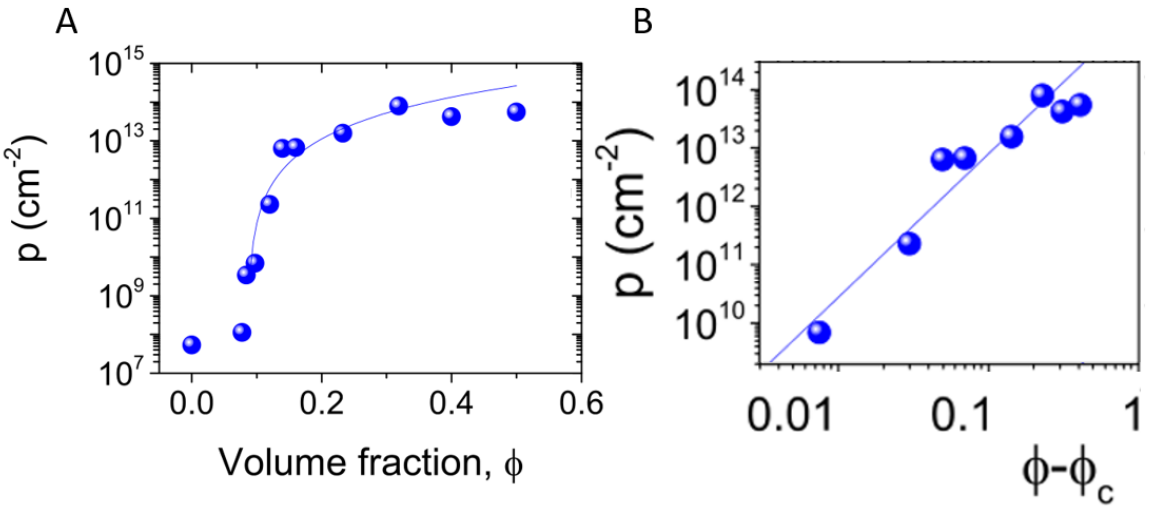

Figure 5.10: (A) A plot of the areal carrier density as derived from the dry conductivity data against volume fraction. (B) A log-log plot of areal carrier density against volume fraction. The blue lines represent fits to percolation theory.

Figure 5.9, measured in the wet state, can be assumed to be representative of the network in the dry state.

A plot of the dry areal carrier density against volume fraction can be seen in Figure 5.10(A), with the same data on a log scale in Figure 5.10(B). The data has been fitted to a curve (blue line) predicted by percolation theory

$$p = p_0 \left(\varphi - \varphi_c\right)^n \tag{5.16}$$

where p is the hole density and p_0, φ, and φ_c are analogous to the parameters used in Equation 5.9. Note that the carrier density values have been adjusted to account for the network porosity and the nanosheet thickness. This was done in order to consider the carrier density in relation to the internal surface area of the network by multiplying the volumetric carrier density by a factor $t/(1-P)$. It can be seen that the carrier density follows percolation theory, with the fitting constants coming out as $p_0 = 2.3 \times 10^{15}$ cm^{-2}, $\varphi_c = 0.09$, and $n = 2.46$. Both the φ_c and n values are similar to the values obtained previously, suggesting that the carrier density and conductivity are being affected by the addition of graphene in the same way and via the same processes. In addition, it is worth noting that the value of p_0 is very similar to the carrier density values for

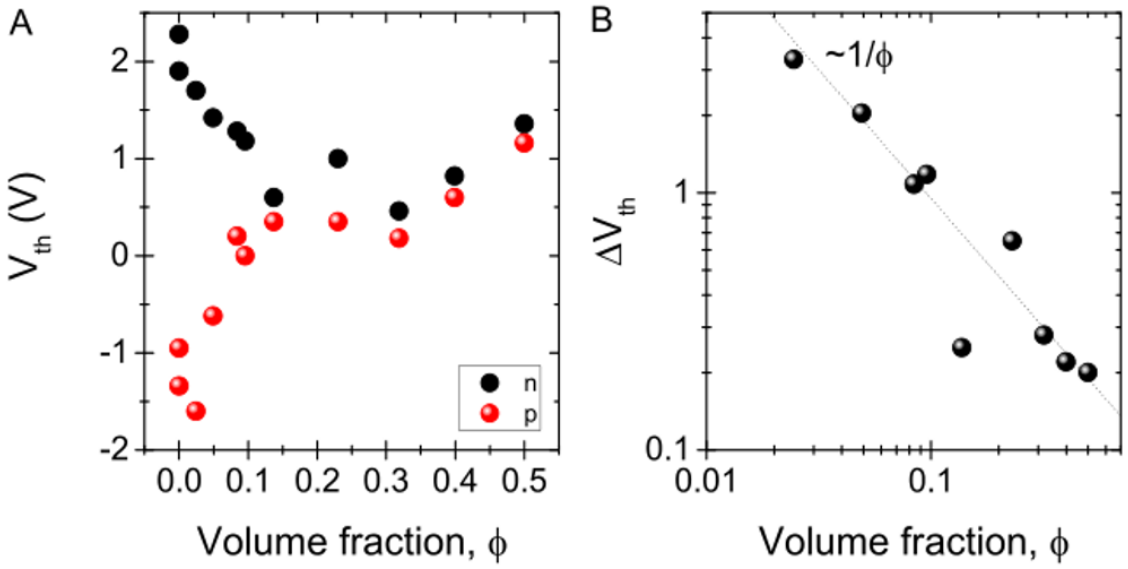

Figure 5.11: (A) The threshold voltages for n- and p-type carriers plotted against φ. (B) The difference in the n- and p-type carriers plotted against φon a log-log plot. The dotted line represents a fit to φ^{-1}.

graphene reported in the literature.[314,315] This raises the possibility that the percolation scaling of the carrier density is more significant than that of the conductivity, since the constant σ_0 is wholly unrepresentative of the final network, being a factor of 30 larger than the conductivity of the graphene network due to the impact of nanosheet junctions. This suggests that the constant p_0 represents a fundamental property of the individual nanosheets rather than the overall network, which could be an interesting avenue of research in the future.

5.2.4 Threshold Voltages

Looking back at the nanocomposite transfer curves, it is possible to probe further the changing properties of the nanosheet network with increasing volume fraction by investigating the threshold voltage, which is tied in to the operating voltages of the transistors. For electrolytically-gated transistors, it is expected that these voltages would be lower than an equivalent dielectric-gated device, due to the higher capacitance that comes with the ionic liquid.[239] These values are calculated from the device transfer curves by taking the line obtained from Equation 3.30 (used to calculate the mobility) until it

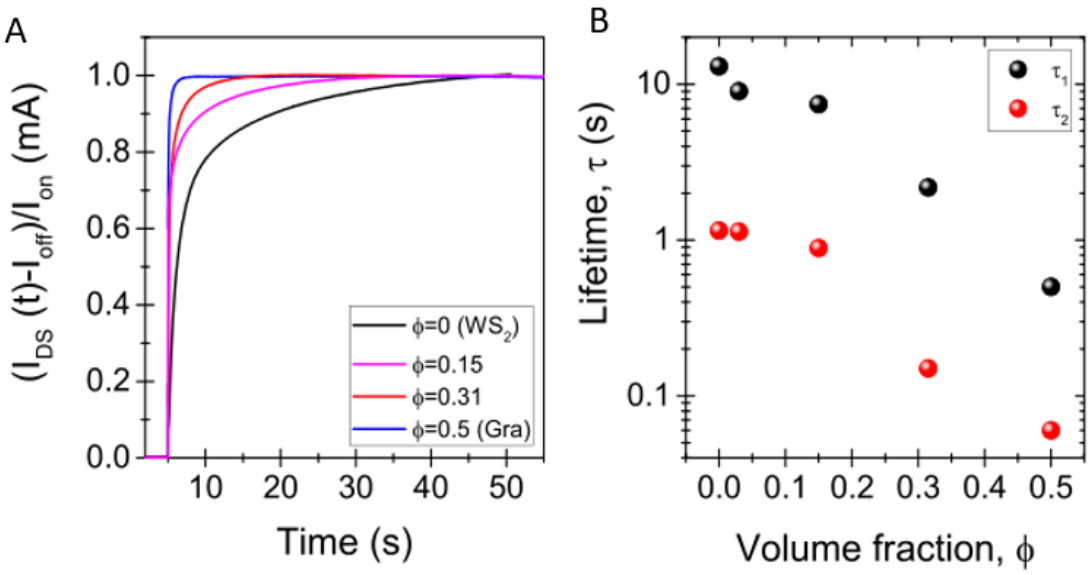

Figure 5.12: (A) The normalised response of a subset of devices in response to a step potential of $V_G = -2.5$ V. (B) The two time constants obtained from a bi-exponential fit of the curves in (C).

reaches the x-axis, resulting in the values shown in Figure 5.11(A). Both the n- and p-type threshold voltages decrease rapidly with increasing φ. The difference between these two threshold voltages, ΔV_{th}, is plotted against φ in Figure 5.11(B). It also exhibits a clear inverse correlation with φ, with the dashed line representing the equation $\Delta V_{th} \propto \varphi^{-1}$. The difference in the threshold voltages in an electrolytically-gated device has been linked to the bandgap of the semiconducting channel,[316,317] although the values of ΔV_{th} obtained here for $\varphi = 0$ are considerably higher than the bandgap of WS_2 (3 eV against ~2 eV for the direct bandgap of WS_2[318]). While it is possible that some of this discrepancy can be explained by an excitonic binding energy of ~0.5 eV[319,320], it is more likely that this discrepancy is a result of significant errors in the threshold voltage measurements due to the hysteresis that comes with electrochemical transistors.[237] Despite this however, the fact that ΔV_{th} scales with φ^{-1} does suggest that it can be interpreted as an effective bandgap that approaches zero for a pure-graphene device, which would fit with previous observations.[321]

5.2.5 Temporal Analysis

The final analysis of the nanocomposite transistors involved measuring their response to an input signal to model their temporal characteristics. A step function of $V_G = -2.5$ V was applied for a small subset of volume fractions, with the subsequent current profiles adjusted to account for the different network conductivities, which are plotted in Figure 5.12(A). The response is quite slow for a pure WS_2 network, becoming faster the more graphene is added to the network. This slow response results from the non-negligible time taken for both the ions within the ionic liquid and the charge carriers within the channel to respond to the gate voltage. As the graphene content increases and the network conductivity rises, the time taken for the current to rise to its maximum value decreases. By fitting the current graphs to a bi-exponential curve, two lifetimes (τ_1 and τ_2) can be extracted. These lifetimes are shown in Figure 5.12(B). Both lifetimes exhibit a similar dependence on the graphene volume fraction above the percolation threshold, suggesting that the network conductivity determines the change in lifetimes. They correspond to the two processes involved in the formation of the electric double layer at the channel:liquid interface, one tightly packed inner layer of ions and one more diffuse outer layer.[242] The long range outer interaction, represented by τ_1, is relatively weak as the surface charge is strongly screened by the compact layer of ions at the nanosheet surface resulting in a delayed interaction with the diffuse layer.

5.3 Conclusion

This chapter demonstrates the evolution of electrolytically-gated nanosheet network transistor properties as they moved from a pure semiconductor channel to a pure semi-metal channel by the addition of increasing amounts of graphene to the channel. Following percolation theory, the conductivity, mobility, and carrier density were all found to increase as more graphene was added, with a percolation threshold of 0.08 volume fraction. In addition, the volume fraction dependence of the on- and off-currents are also described well by percolation theory. The on:off current ratio showed a significant decrease with increasing graphene content, suggesting that the switching

behaviour shown by these electrochemical transistors is almost entirely due to the WS_2 sub-network.

Unfortunately it also showed that this was not a practical pathway to improving the performance of such devices, since any improvement in the conductivity and mobility is inversely correlated with the on:off current ratio. This was due to the overwhelming impact of the nanosheet-nanosheet junction resistance dominating the properties of the channel, and although some enhancement of the carrier mobility was observed it was not enough to suggest that adding graphene to a semiconducting nanosheet network is a feasible path to optimisation. This suggests that the way forward is to lower the junction resistance, whether this is by controlling the film morphology or by chemically modifying the nanosheet edges to improve sheet-to-sheet contact. Finding a way to overcome this obstacle is likely going to be the key to bringing nanosheet network transistors up to the same level as modern organic devices.

Wisdom comes from experience. Experience is often a result of lack of wisdom.

Terry Pratchett

6

Tuning of Transistor Properties via Changes in Gate Volume

Now that electrolytically gated nanosheet network transistors have been demonstrated, it becomes necessary to properly investigate the fabrication methods to make sure that the optimum conditions for making these devices are in place. While ionic liquid based devices have been successfully made, it is not yet clear whether these devices are being fabricated in such a way as to maximise their potential. In particular, there are some characteristics of electrolytically gated nanosheet network devices that require further investigation in order to make sure that they are not adversely affecting the transistor performance.

The high capacitances associated with the use of electrolytically gated transistors serves as a way of obtaining high transconductance values and on-currents, both of which are important for device performance. These properties arise out of the high capacitances associated with the ionic liquid, with both the gate electrode:liquid and channel:liquid interfaces showing similarly large capacitances. This is a key difference to note, since the equations used to model the transistor behaviour refer only to the capacitance at the channel:electrolyte interface, relying on the assumption that the effect of the gate:electrolyte capacitance is negligible.

It is important therefore to determine exactly what the conditions are where this

assumption can be said to hold up and to investigate what happens to the nanosheet network properties in the case where this is no longer true. In particular, this will have implications relating to the fabrication of future nanosheet network-based transistors and the conditions that must be met for these devices to operate at their full potential.

6.1 Experimental Method

Tungsten diselenide (Alfa Aesar, CAS: 12067-46-8) inks were produced via liquid phase exfoliation. The powders were dispersed in 80 mL of NMP at an initial concentration of 40 mg/mL and exfoliated for one hour using a Sonics Vibra-cell VCX-750 ultrasonic processor at 60% amplitude, with a pulser set to 6s on, 2s off. The resulting dipsersion was then centrifuged in a Hettich Mikro 220R centrifuge at $3218g$ for one hour, with the supernatant from this step being discarded. The sediment was then redispersed in 80 mL of fresh NMP and exfoliated for 5 hours using the same settings. Graphene inks were also prepared via liquid phase exfoliation using the same method and parameters as above except that the centrifugation step was done at $1303g$, and the final exfoliation step took 6 hours.

Following exfoliation, the inks were size-selected using liquid cascade centrifugation. The first centrifugation step was performed for two hours at $26.6g$ and $665g$ for WSe_2 and graphene respectively, with the resulting sediment being discarded. The second centrifugation step was performed for two hours at $106.4g$ and $3830g$ for WSe_2 and graphene respectively, with the supernatant discarded. The sediment trapped between these two speeds was then redispersed in IPA, since IPA is more suited to printing than NMP.

UV-Vis spectroscopy was used to obtain concentration measurements, and the dispersions were then diluted such that the final concentrations of the WSe_2 and graphene inks were approximately 1 mg/ml and 0.5 mg/ml respectively. Statistics on the mean length of the size selected sheets were obtained via TEM imaging as described in Chapter 4.

The graphene gate electrodes were printed as described in Chapter 4 using a Di-

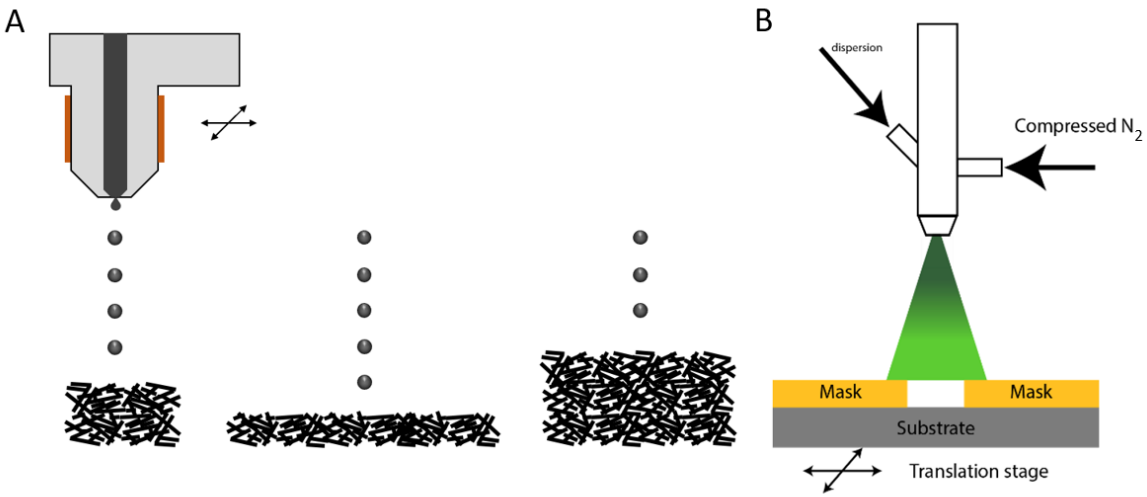

Figure 6.1: (A) A schematic of the inkjet printing of the graphene nanosheet network for the gate electrode. The area and thickness of the gate were both varied. (B) Schematic of the aerosol sprayer and the deposition process involved.

matix DMP-2831, in order that the precise dimensions of the gate could be precisely controlled as seen in Figure 6.1(A). Critically, it also allowed for both the gate area and gate thickness to be varied independently by changing the number of print passes, in order to allow for the effects of gate area, volume and thickness to be decoupled.

The deposition of the WSe_2 channel was carried out using an aerosol spray gun as seen in Figure 6.1(B), with ~10 cm between the spray gun and the substrate and the N_2 backpressure kept constant at 4 bar. Shadow masks were used to define the dimensions of the channel, and by controlling the volume of ink sprayed per set of devices the thickness was kept roughly constant at ~1.5 μm. The gold source and drain electrodes were deposited via e-beam evaporation, with shadow masks defining the channel length and width as 120 μm and 16 mm respectively.

Raman spectroscopy was performed on the printed films under ambient conditions using a Horiba Jobin Yvon LabRAM HR800 with a 532 nm excitation laser as described in Chapter 4. This was primarily used to investigate the printed nanosheet films to confirm their composition.

SEM images of the deposited nanosheet films were obtained using a Zeiss Ultra Plus scanning electron microscope, using an accelerating voltage of 2–3 kV and a 30

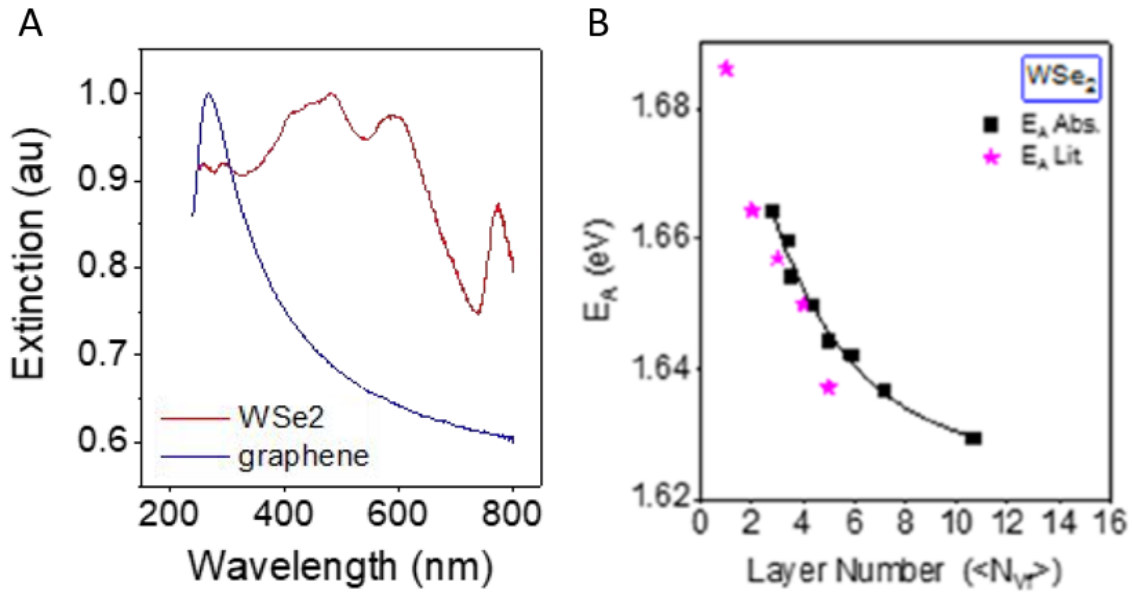

Figure 6.2: (A) UV-Vis spectroscopy of the WSe_2 (red) and graphene (blue) inks, normalised to the highest peak. (B) Relation between the A-exciton energy and number of layers for WSe_2 nanosheets. Reproduced from Ref.[282]

μm aperture at a distance of 3–5 mm.

A Keithley 2612A was used to perform all electrical measurements as described in Chapter 4. The initial electrical testing was carried out in ambient conditions with no ionic liquid present, i.e. the "dry" state. All further electrical measurements were performed after an ionic liquid, 1-ethyl-3-methylimidazolium bis (trifluoromethylsulfonyl) imide (EMIm-TFSI), was added to the devices such that all of the gate electrode and channel were covered. These are the "wet" state measurements. The volume of liquid used necessarily varied with gate volume, but in general as little liquid as possible was used. The volumes varied roughly from ~50 μL to 600 μL. The wet state measurements were performed under high vacuum following an overnight annealing under vacuum at 70 °C.

6.2 Results & Discussion

6.2.1 Inks and Deposition

The results from the initial characterisation of the dispersions can be seen in Figure 6.2. The UV-Vis spectroscopy in Figure 6.2(A) shows the WSe_2 (red) and graphene (blue) spectra, both of which show the features expected of their respective materials. For WSe_2 these features are the A- and B-exciton peaks visible in the spectrum at around 770 nm and 600 nm respectively,[54,322,323] while for graphene the characteristic Van Hove singularity is visible at around 300 nm with a plateau at longer wavelengths, in keeping with previous observations.[91] The UV-vis also provides information on the mean thicknesses of the dispersed flakes, and as in Chapter 5 the equation for graphene is as follows[91]

$$< N >= 35.7 \times \frac{\varepsilon_{550}}{\varepsilon_{325}} - 14.8 \tag{6.1}$$

where by inputting the values from the spectra, the thickness can be estimated at <N> = 12 layers for graphene.

A similar calculation can be used to estimate the <N> value for the WSe_2 dispersion. It has been previously observed that for a TMD nanosheet, the position of the A-exciton peak is dependent on the number of monolayers within the flake, with the exciton wavelengths of thicker flakes being red-shifted compared to the wavelengths of thinner flakes.[152,144] In the case of WSe_2, it is useful to consider the UV-vis metric developed by Synnatschke *et al.*[282] which plots the changes in the A-exciton energy E_A as a function of the layer number of WSe_2. The relevant graph is reproduced in Figure 6.2(B). Unfortunately, the UV-vis spectrum obtained for WSe_2 in Figure 6.2(A) shows an A-exciton peak at approximately 775 nm, which corresponds to a value for E_A of 1.6 eV, significantly smaller than the values of E_A recorded in Figure 6.2(B). The reason for this discrepancy is due to the non-negligible contribution from scattering interactions in the UV-vis data in Figure 6.2(A), which Synnatschke *et al.* note will lead to red-shifting of the exciton peak in the extinction spectrum compared to the absorption spectrum. This unfortunately means that a UV-vis based metric for the

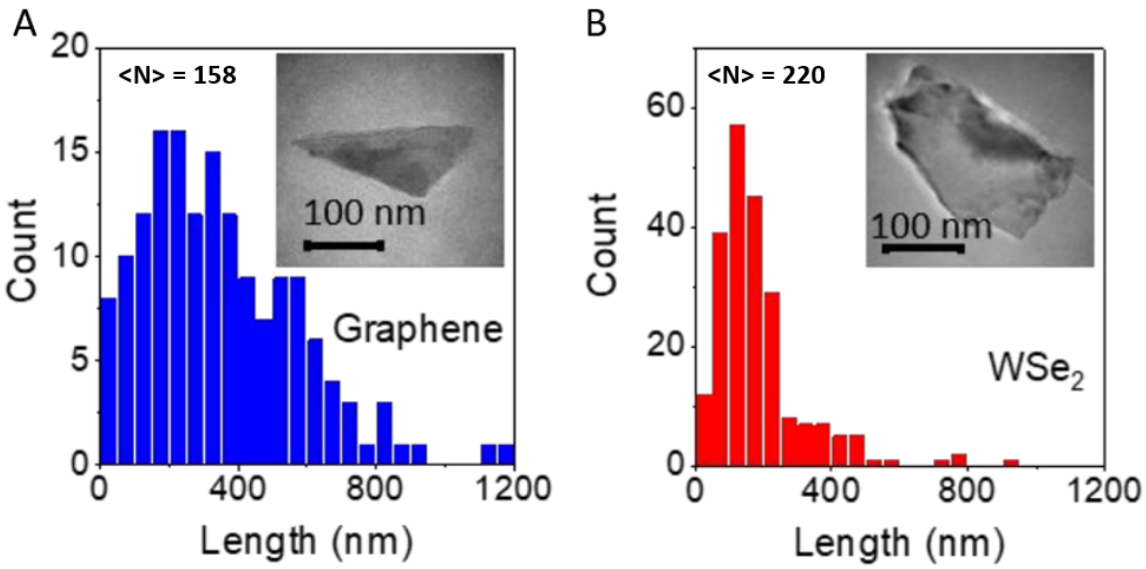

Figure 6.3: (A) TEM histogram of measured nanosheet lengths and image of a representative nanosheet (inset) for the graphene ink. (B) TEM histogram of measured nanosheet lengths and image of a representative nanosheet (inset) for the WSe_2 ink.

length of the WSe_2 nanosheets cannot be used in this instance.

Previous works have estimated that the point at which the bandgap of a WSe_2 nanosheet begins to exhibit a dependence on the nanosheet thickness is approximately 6 layers.[54] From Figure 6.2(B), this would correspond to an A-exciton energy of 1.64 eV and a wavelength of ~756 nm. This is almost 20 nm smaller than the peak observed in Figure 6.2(A), and so it can be safely assumed that all of the WSe_2 nanosheets used in this work exhibit the bulk bandgap of 1.2 eV, avoiding the possibility of having unwanted variations in the bandgaps of adjacent WSe_2 nanosheets.

Statistical TEM analysis was carried out on the graphene and WSe_2 dispersions, and the histograms associated with the nanosheet lengths can be seen in Figures 6.3(A) and (B) for graphene and WSe_2 respectively. This provides values for the mean nanosheet length <L> of 360 ± 20 nm for graphene and 185 ± 9 nm for WSe_2. Using the fact that NMP-exfoliated WSe_2 has been previously observed to have an aspect ratio of ~25,[5] and the fact that LPE dispersions tend to have a constant aspect ratio which depends heavily on the material,[112] this provides an estimate for the mean number of layers per WSe_2 nanosheet of 7.4 layers, which is larger than the thickness-dependent bandgap cutoff point of 6 layers.[47]

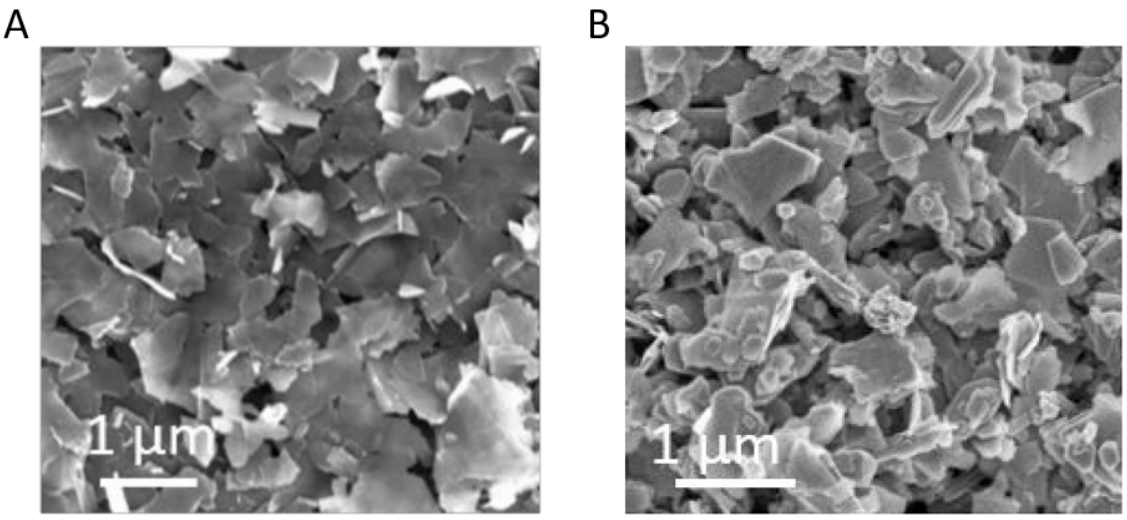

Figure 6.4: SEM images of (A) a printed graphene nanosheet network and (B) a sprayed WSe_2 network.

The insets in Figures 6.3(B) and (C) show two representative graphene and WSe_2 nanosheets captured via TEM, showing the quasi-2D nature of the sheets that make up the dispersions. More crucially the TEM failed to detect any non-planar objects, suggesting that the inks are free from contamination.

Following the device fabrication, SEM images were obtained for the graphene and WSe_2 networks, which can be seen in Figures 6.4(A) and (B) respectively. Both show the key features expected of printed nanosheet networks, namely the film porosity and the random alignment of the loosely packed flakes. The polydisperse nature of the inks can also be seen since the size of the flakes varies, often significantly. While some of the flakes naturally align in-plane, there is also a significant amount of edge-edge junctions visible in both SEM images which arise as a result of the low aspect ratio and high rigidity of the nanosheets. The porosity of the films in Figures 6.4(A) and (B) are visually in line with SEM images of inkjet printed and sprayed nanosheet films from other works[213,5], which suggests that the film porosities can be estimated to be between 40% and 60%. This porosity is crucial in allowing the liquid electrolyte to permeate the entirety of the nanosheet films.[237]

The last of the initial analyses of the printed films was carried out via Raman spectroscopy, which allows non-destructive insights into the properties of the nanosheets. The graphene spectrum in Figure 6.5(A) shows the characteristic G peak at 1580 cm^{-1},

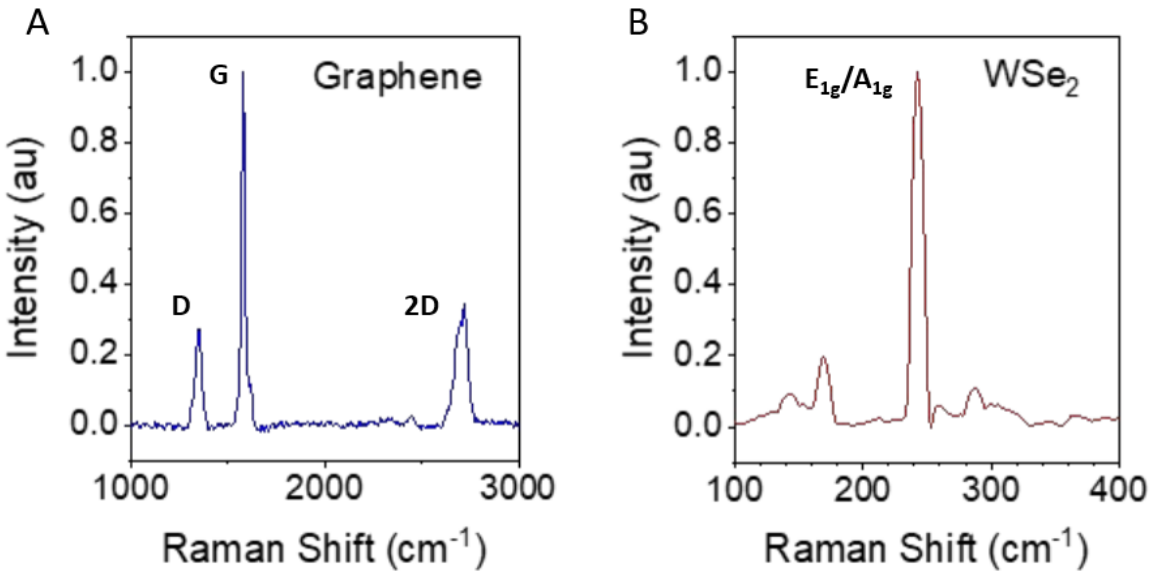

Figure 6.5: Raman spectroscopy of (A) a graphene gate and (B) a WSe_2 channel. The spectra have been normalised to the value of the highest peak.

with the D and 2D peaks also visible at 1351 cm^{-1} and 2717 cm^{-1} respectively. The D/G intensity ratio is known to provide information as to the level of defects in a graphene nanosheet,[116,324] and for this sample the D/G ratio is equal to 0.27, indicating that the graphene is relatively free of basal plane defects. Since the D/G ratio will always include a contribution from edge defects, which are unavoidable in LPE samples, the D/G ratio would be expected to be non-zero.[325] Likewise the WSe_2 spectrum in Figure 6.5(B) shows the characteristic 250 cm^1 peak corresponding to the degenerate E_{1_g} and A_{1_g} modes.[326]

The nanomaterial inks were used to print arrays of nanosheet network transistors, with each set containing four devices. Each device consisted of a sprayed WSe_2 film with dimensions of 3 mm × 1 mm × 1.5 μm, with the gold source and drain electrodes deposited by e-beam deposition such that the channel length and width were 120 μm and 16 mm respectively. Although printed graphene source and drain electrodes have been used in other works,[327] using e-beam deposited electrodes ensures good contact with the channel. It also avoids any potential changes in the device characteristics as a result of this change, since it is better to focus on changing one thing at a time from Chapter 5 rather than change multiple aspects of the devices at a time. Each transistor then had a graphene side gate electrode deposited via inkjet printing a distance of 0.5

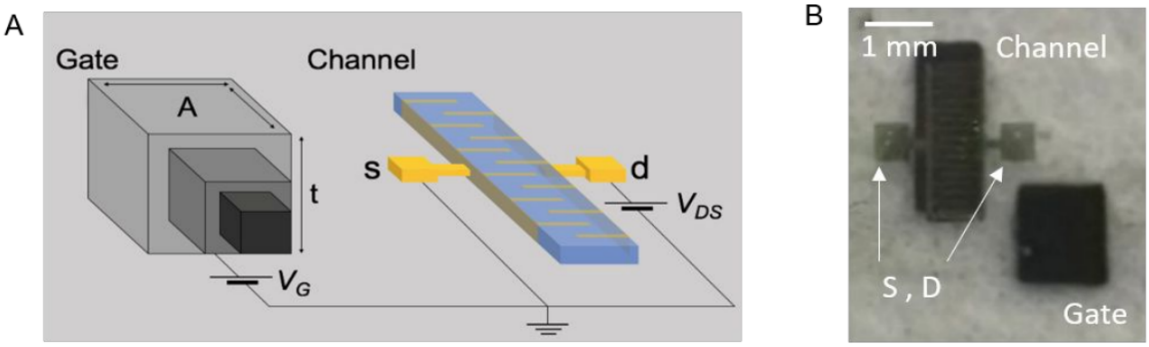

Figure 6.6: (A) Schematic of an electrochemical transistor used in this experiment. The volume of the gate electrode was varied while the channel volume was kept approximately constant throughout, with any differences arising from slight variations in device thickness. (B) A picture of one such device showing the sprayed WSe_2 channel, printed graphene gate, and evaporated gold source and drain electrodes.

mm away from the channel. The dimensions and thickness of the gate electrode were independently varied, from 0.1 mm^2 to 450 mm^2 for the gate area and from 0.5 μm to 2 μm for the thickness. This gave a range of gate volumes that encompassed several orders of magnitude, allowing for its effect to be investigated in detail. It also allowed the gate thickness and area to be decoupled, in the event that either had an effect on the device performance aside from simply A schematic of a finished device can be seen in Figure 6.6(A), with a photograph of the same device in Figure 6.6(B).

6.2.2 Initial Characterisation

A graph of representative dry output curves for a selection of gate volume to channel volume ratios is seen in Figure 6.7(A), with each IV curve normalised to the device thickness to allow for an easy visual comparison. Since the channel length and width are constant throughout the experiment, this figure can provide information about the channel conductivities at a glance. Immediately it can be seen that the dry IV curves do not seem to exhibit any systematic dependence on the gate:channel volume ratio, which indicates that the fabrication method, and more specifically the inkjet printing of the gates, does not have any knock-on effects on the channel. For example, the black and cyan curves overlay each other, despite corresponding to gate:channel volume ratios of 583 and 0.73 respectively. This is further confirmed by plotting the

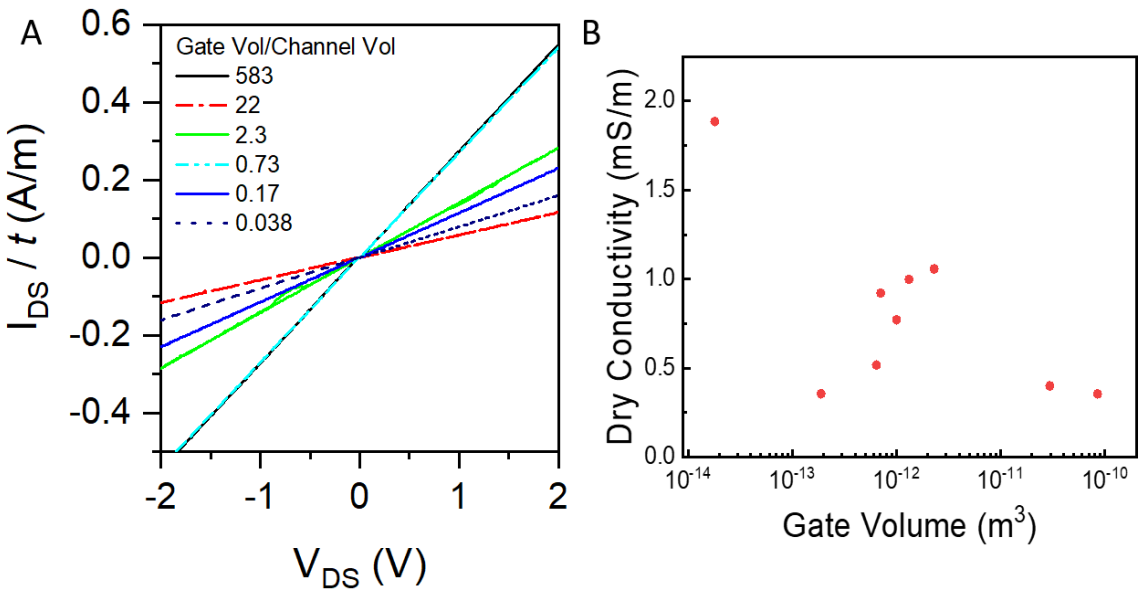

Figure 6.7: (A) Output dry IV curves for a range of gate volume:channel volume ratios, normalised with respect to device thickness, *t*. (B) Dry conductivities plotted against gate volume.

dry conductivities against the gate:volume channel ratio, as can be seen in Figure 6.7(B). Although this data appears to show a slight linear increase in conductivity with increasing gate:channel volume ratio, performing a statistical analysis on the data indicates that the F-value for the fit is only 2.97, corresponding to a 12.9% chance that a random datapoint will have a larger F-value, i.e. will not be explicable by random noise. This means that the slope of the fitted line can not be said to be significantly different from zero at the $\alpha < 0.05$ level, meaning it cannot be assumed that the trend is due to a causative effect and not the impact of random noise. The apparent trend visible in Figure 6.7(B) is also being significantly driven by the outlier at $V_g \approxeq 10^{-14}$ m^3, further reducing the confidence with which any trend can be deduced from this data. Further investigations would be required before any definitive conclusions could be confidently drawn.

Likewise, the representative wet output curves are shown in Figure 6.8(A), for similar (but not identical) gate:channel volume ratios as in Figure 6.7(A), and again normalised with respect to the channel thickness in each case. Different gate:volume ratios were used in Figures 6.7(A) and 6.8(A) such that as many sets of devices as possible contributed to the two figures. Due to the nonlinear nature of these IV curves, it is much harder to discern whether the wet conductivities show the same non-dependence

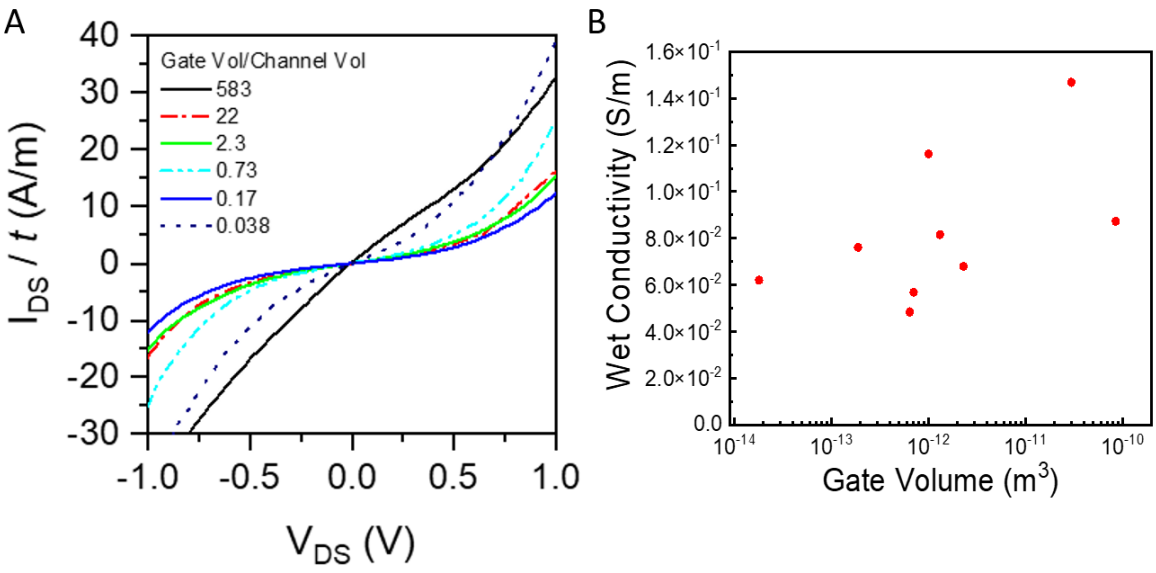

Figure 6.8: (A) Output wet IV curves for a range of gate volume:channel volume ratios, normalised with respect to device thickness The red line is the line of best fit.

on the gate:channel volume ratio as the dry conductivities do. This non-linearity in the wet state has been previously observed, and is attributed to ions being drawn to the channel-liquid interface from the electrolyte with increasing source-drain voltage, even at zero gate voltage, thus increasing the network carrier density.[5,89] Once again, it is prudent to investigate the wet conductivities as a function of the gate:channel volume ratio and see if a linear fit can be used to describe the trend with gate volume. While this data, shown in Figure 6.8(B), also suggests a slight nonzero trend with increasing gate:channel volume ratio. However, once again the results of a statistical analysis of the data indicates that there is enough of a probability that this trend is a result of random experimental noise that it cannot be assumed that the observed trend is significant. This suggests that the presence of increasing amounts of graphene has no effect on the channel in the case of zero gate voltage.

The transfer curves (I_{DS} against V_{GS}) for a selection of gate:channel volume ratios are plotted in Figure 6.9(A), with the current normalised with respect to channel thickness in order to make comparing the devices more straightforward, and to account for differences in thickness between sets of devices. It can clearly be seen that there is a significant difference in the transfer curves between devices with high gate:channel volume ratios and devices with low gate:channel volume ratios, with an increase in

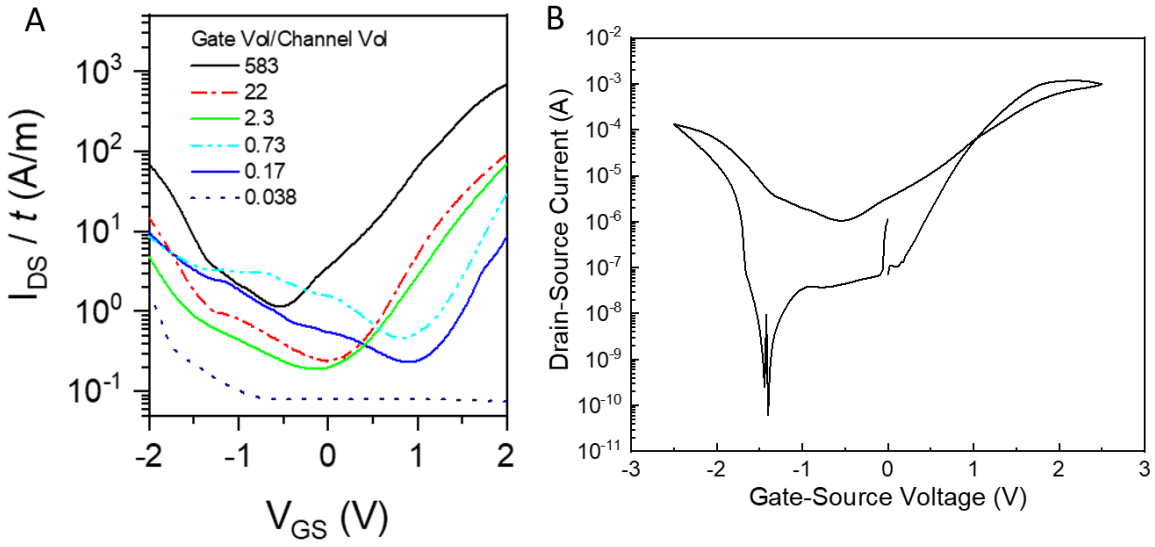

Figure 6.9: (A) Transfer IV curves for a range of gate volume:channel volume ratios, normalised with respect to device thickness, t. (B) A single transfer curve for V_G = 300 mm^2 without normalisation.

the gate volume corresponding to higher drain-source currents. With one exception (the $\nu_G/\nu_{Ch} = 0.038$ device), all devices investigated showed effective switching for both holes and electrons, matching the expected ambipolar behaviour of WSe_2.[328] It is not clear why this device set did not show any n-type behaviour, but since this is the set with the lowest gate volume it is possible that this is a result of the low gate volume. A representative transfer curve can be seen in Figure 6.9(B), with switching behaviour visible for both electrons and holes. In a standard liquid-electrolyte transistor, the mechanism behind the change in the channel conductivity is well described in the literature.[238,5] The gate voltage draws ions to the gate:electrolyte interface, with the counterions being drawn to the channel:electrolyte interface, with an electrical double layer (EDL) forming in both cases.[236] At the channel:electrolyte interface, more carriers are in turn drawn in from the source and drain electrodes to complete the EDL at the channel. The increase in the channel conductivity as the transistor is switched ON arises from charge carriers being drawn in from the source and drain electrodes to balance out the charge of the electrolyte ions gathering near the channel.

6.2.3 Modelling the Gate Volume Dependence

In order to understand the changes in the device behaviour with increasing gate volume, it is necessary to go back and look at the equation that describes the source-drain current in a transistor (adapted from Equation 3.29 by rearranging for I_{DS})

$$I_{DS} = \frac{WtC_V}{L}\mu V_{DS}\left(V_{GS} - V_T\right) \tag{6.2}$$

where I_{DS} is the source-drain current; V_{DS}, V_{GS}, and V_T are the source-drain, gate-source, and threshold voltages respectively; L, W, and t are the channel length, width and thickness; and C_V and μ are the volumetric capacitance and mobility of the channel. Of the assumptions used to derive this equation, the relevant one to this discussion is that the capacitance of the full gate-electrolyte-channel system is accurately described only by the capacitance at the channel:electrolyte interface. As described previously the figure of merit commonly proposed for these devices is $C_V\mu$, and by rewriting C_V in terms of the channel volume (since it is assumed that this capacitance refers only to the channel:electrolyte capacitance) the following can be obtained

$$I_{DS} = \frac{Wt\ V_{DS}}{L}\left(\frac{C\mu}{\nu_{Ch}}\right)\left(V_{GS} - V_T\right) \tag{6.3}$$

where ν_{Ch} is the channel volume. While $C\mu/\nu_{Ch}$ can be directly obtained from the slope of the transfer curve, the mobility value in this quantity can not always be taken to be representative of the network mobility unless certain conditions are fulfilled. Aside from the assumptions discussed in Chapter 3, the device capacitance must be investigated in more detail.

A common way to model the gate-electrolyte-channel system in an electrolytically-gated transistor is as two capacitors arranged in series, which in turn means that the overall capacitance is dominated by the smaller of the two capacitances[238]

$$C_T{}^{-1} = C_{Ch}{}^{-1} + C_G{}^{-1} \tag{6.4}$$

where C_{Ch} and C_G are the channel:electrolyte and gate:electrolyte capacitances respec-

tively. By assuming that the volumetric capacitances of channel and gate remain unchanged with respect to the channel and gate dimensions, this can be rewritten as

$$C_T{}^{-1} = (C_{V,Ch}\ \nu_{Ch})^{-1} + (C_{V,G}\ \nu_G)^{-1} \tag{6.5}$$

where $C_{V,Ch}$ and $C_{V,G}$ are the volumetric capacitances of the channel and gate respectively. This is where the large capacitances associated with electrolytically gated transistors becomes an issue, especially because in this work the gate and channel are both made of porous nanosheet networks. The resulting large internal area of the gate electrode can lead to high capacitances,[235] such that it is no longer reasonable to assume that $C_{Ch} \ll C_G$ and that $C/\nu_{Ch} \approx C_{V,Ch}$ is no longer valid.

In the case that the gate capacitance is equivalent to or smaller than the channel capacitance, it is important to modify the source-drain current equation to account for this. In the scenario where the assumption of $C_{Ch} \ll C_G$ holds, then no changes are necessary and the relevant equation is the same as Equation 6.3 above, where $C = C_{V,Ch}\ \nu_{Ch}$. Similarly in situations where $C_{Ch} \approx C_G$, then the total capacitance of the system can be approximated as $C = C_{Ch}/2 = C_G/2$, with the resulting source-drain current behaviour described by

$$I_{DS} = \frac{Wt\ V_{DS}}{2L}\left(\frac{C\ \mu}{\nu_{Ch}}\right)(V_{GS} - V_T) \tag{6.6}$$

where $C = C_{V,Ch}(\nu_{Ch}/2)$.

The final and most important case is where $C_{Ch} > C_G$, in which case the total capacitance is given by

$$I_{DS} = \frac{W\ V_{DS}}{L}\left(\frac{\mu}{\nu_{Ch}}\right)(C_{V,G}\ t_G\ \nu_G)\,(V_{GS} - V_T) \tag{6.7}$$

where the key difference is that the value t in the previous equations has been replaced with t_G, the thickness of the graphene gate electrode. This is because during the derivation of Equation 3.29 the capacitance was originally describing the areal capacitance of the oxide:semiconductor interface, with the thickness value arising from the fact that

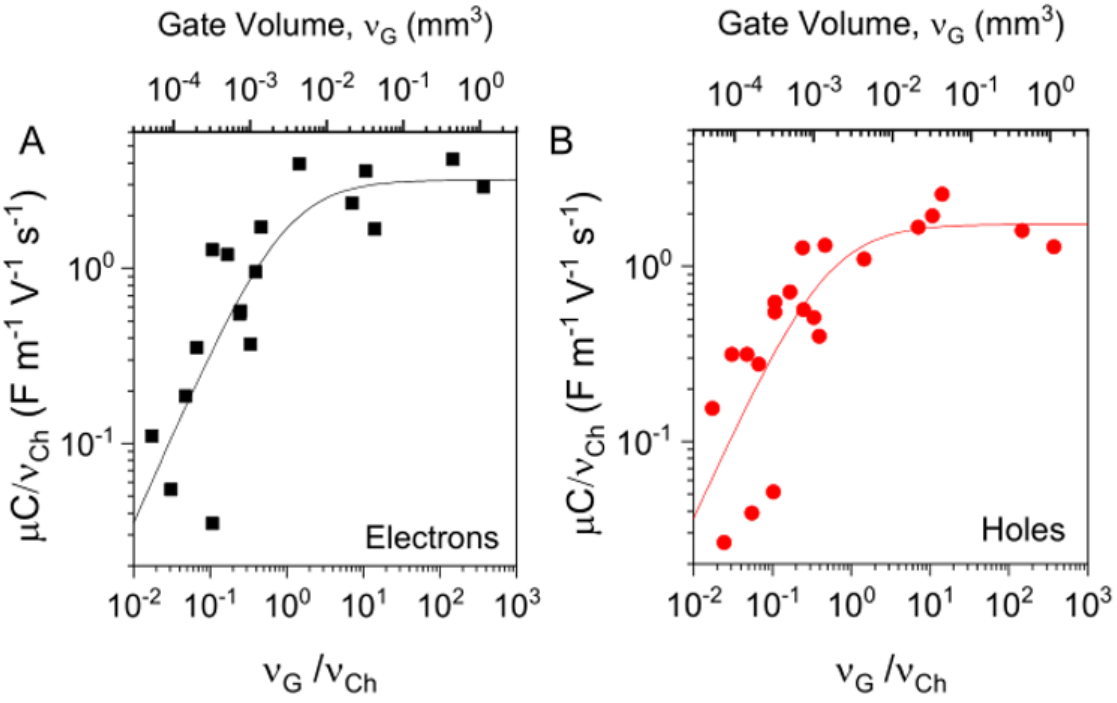

Figure 6.10: Plot of the transistor figure of merit $C\,\mu/\nu_{Ch}$ against the gate:channel volume ratio for (A) electrons and (B) holes. The solid lines represent the trend predicted by Equation 6.8. The gate volume is also given on the top of the graph.

the entire volume of porous nanosheet films contribute to the switching process. This normally gives $C_{ox} = C_{V,Ch}\ t$, but since the gate capacitance is now the dominating contribution to the system capacitance it is the gate thickness t_G that must be taken into account. Hence, C becomes $C_{V,G}\nu_G$.

This means that the figure of merit $C\,\mu/\nu_{Ch}$ obtained from the transconductance must be modified to account for all three of these regimes by replacing C with a suitable replacement

$$\frac{C\,\mu}{\nu_{Ch}} = \frac{\mu\ C_{V,Ch}}{1 + (\nu_{ch}/\nu_G)\,(C_{V,Ch}/C_{V,G})} \tag{6.8}$$

which rewrites the figure of merit to account for the gate volume. This allows the figure of merit to be plotted against the gate:channel volume ratio ν_G/ν_{Ch}, the graph of which is shown in Figure 6.10(A) and (B) for both electrons and holes respectively. The solid lines represent fits to Equation 6.8, and it can be seen that the data follows the predicted trend, with the values of $C\,\mu/\nu_{Ch}$ rising constantly with increasing gate volume for $\nu_G/\nu_{Ch} \lessapprox$~0.5, with the data then levelling off until it reaches a plateau at

around $\nu_G/\nu_{Ch} \approx 2$. This shows that the gate volume only begins to affect the overall device performance after a certain threshold has been reached.

By fitting the data in Figure 6.10 to Equation 6.8, values of $\mu C_{V,Ch}$ can be extracted for both electrons and holes. Since $C_{V,Ch}$ is a constant relating to the geometry of the sheets within the channel, it is unaffected by the changes in gate volume. Using the value of $C_{V,Ch} = 1.3$ F cm^{-3} previously reported for WSe_2,[5] this gives mobility values of $\mu_e = (2.5 \pm 1) \times 10^{-2}$ cm^2 V^{-1} s^{-1} and $\mu_h = (1.3 \pm 0.4) \times 10^{-2}$ cm^2 V^{-1} s^{-1}. These values are comparable to similar nanosheet networks printed using both WS_2 and WSe_2, with previous works reporting WSe_2 mobility values of 8×10^{-2} cm^2 V^{-1} s^{-1},[5] and WS_2 mobility values of 10^{-2} cm^2 V^{-1} s^{-1}.[279] The fitted values are also quite similar to the mobility values of 10^{-1} cm^2 V^{-1} s^{-1} obtained for WS_2 networks in Chapter 5. The similarities between the different types of nanosheet reinforces the idea that the flake-to-flake junctions remain the dominant factor in limiting the network mobility.

The fits to Equation 6.8 also provide an estimate for the ratio of the volumetric capacitances: $C_{V,Ch}/C_{V,G} = 0.9 \pm 0.5$ and 0.5 ± 0.25 respectively for electrons and holes. This can further be broken down by considering the formula relating the volumetric capacitance to the internal surface area of the network

$$C_V = \frac{\varepsilon_r \varepsilon_0 A_{int}}{\lambda \nu} \tag{6.9}$$

and the formula for the volumetric capacitance of a porous nanosheet network[235]

$$C_V = \frac{2\varepsilon_r \varepsilon_0 (1 - P)}{\lambda < N > d_0} \tag{6.10}$$

where λ is the thickness of the electrical double layer, A_{int}/ν is the internal surface area per unit volume, P is the network porosity, $< N >$ is the mean number of layers per nanosheet, and d_0 is the monolayer thickness. Fitting the data in Figures 6.10(A) and (B) give values of $C_{V,Ch}/C_{V,G}$ close to unity, which implies that the values of A_{int}/ν are roughly equivalent for both the graphene and WSe_2 networks, presuming that the values of λ are similar for gate and channel.

This also provides another method for estimating the relative porosities of the gate

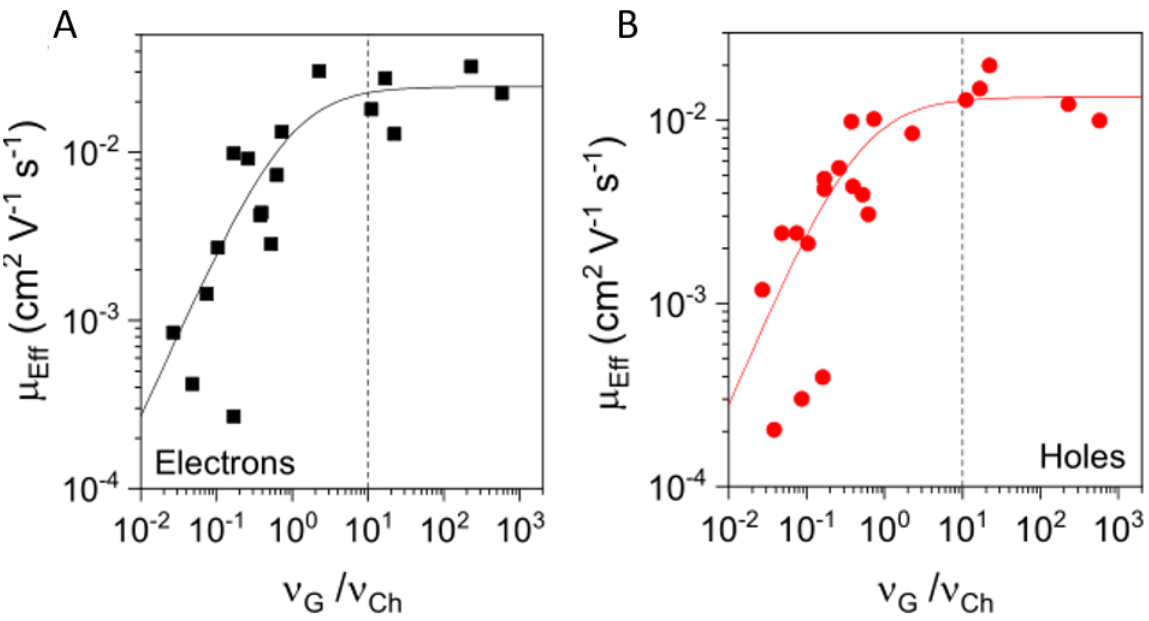

Figure 6.11: Plot of the effective mobility against the gate:channel volume ratio for (A) electrons and (B) holes. The solid lines represent the trend predicted by Equation 6.8.

and channel networks. Since $< N >$ is similar for both graphene and WSe_2, the ratio $C_{V,Ch}/C_{V,G}$ can be approximated as

$$\frac{C_{V,Ch}}{C_{V,G}} \approx \frac{(1-P_{Ch})d_{Gra}}{1-P_G)d_{\mathrm{WSe_2}}} \tag{6.11}$$

where d_{Gra} and d_{WSe_2} are equal to 0.35 Åand 0.6 Årespectively. By taking the value of $C_{V,Ch}/C_{V,G} = 0.7$ as the average of the electron and hole values and rearranging to separate the porosities, this yields $P_{ch} \approx 1.2P_G - 0.2$. Using the estimate of $P_G = 0.6$ this gives $P_{Ch} \approx 0.5$, in which case both porosity values lie within the range of 0.4 and 0.6 predicted for nanosheet networks.[5]

While analysing the figure of merit is an ideal starting point, it is better to decouple the volumetric capacitance from the mobility so that the device mobility can be analysed independently. However, in this case it is important to recognise that the values extracted from Equation 6.2 do not represent the actual network mobility unless the gate volume is large enough relative to the channel volume. Hence, it is useful to define

the effective mobility μ_{Eff} as follows

$$\mu_{Eff} = \frac{C\,\mu}{\nu_{Ch}} = \frac{\mu}{1 + (\nu_{ch}/\nu_G)\,(C_{V,Ch}/C_{V,G})} \tag{6.12}$$

By taking the previously reported value of $C_{V,Ch} = 1.3$ F cm^{-3},[5] μ_{Eff} can be plotted against ν_G/ν_{Ch} as seen in Figure 6.11. By fitting this data to Equation 6.12 and by using $C_{V,Ch} = 1.3$ Fcm^{-3} and $C_{V,G} = 0.7$ as the values for the volumetric capacitances, it is clear that the effective mobility is independent of gate volume for $\nu_G/\nu_{Ch} > 10$. This is consistent with the rule of thumb suggested by Jonathan Rivnay *et al.*[238] that the gate capacitance in an electrolytically-gated transistor should be at least 10 times that of the channel capacitance. In other words, the effective mobility is only a reliable estimation of the actual network mobility when the gate capacitance is above this threshold.

6.2.4 Further Analysis

It is also important to consider the impact of gate volume on other aspects of the device performance, namely the on:off current ratio and the maximum on-current, since both are important to consider when looking at the overall device performance. As seen in Figure 6.12, both of these quantities show an increase with increasing gate volume with no clear saturation at higher gate volumes. As the gate volume increases, the amount of ions being drawn to the gate electrode by a given applied voltage will likewise increase, assuming that the concentration of ions at the gate:electrolyte interface remains constant. This means that an equal number of counter-ions will be drawn to the channel:electrolyte interface, and therefore that more charge carriers will be drawn into the channel for a larger gate volume than for a smaller one. Hence, higher on-currents (and therefore transconductances) and on:off current ratios will be observed as the gate volume increases. This effect was previously observed by A.T. Wong *et al.*[329] in a study focusing on the area of the gate electrode. It is therefore clear that unless the gate volume is sufficiently large, roughly 10× that of the channel, the entirety of the nanosheet network transistor performance will be adversely affected.

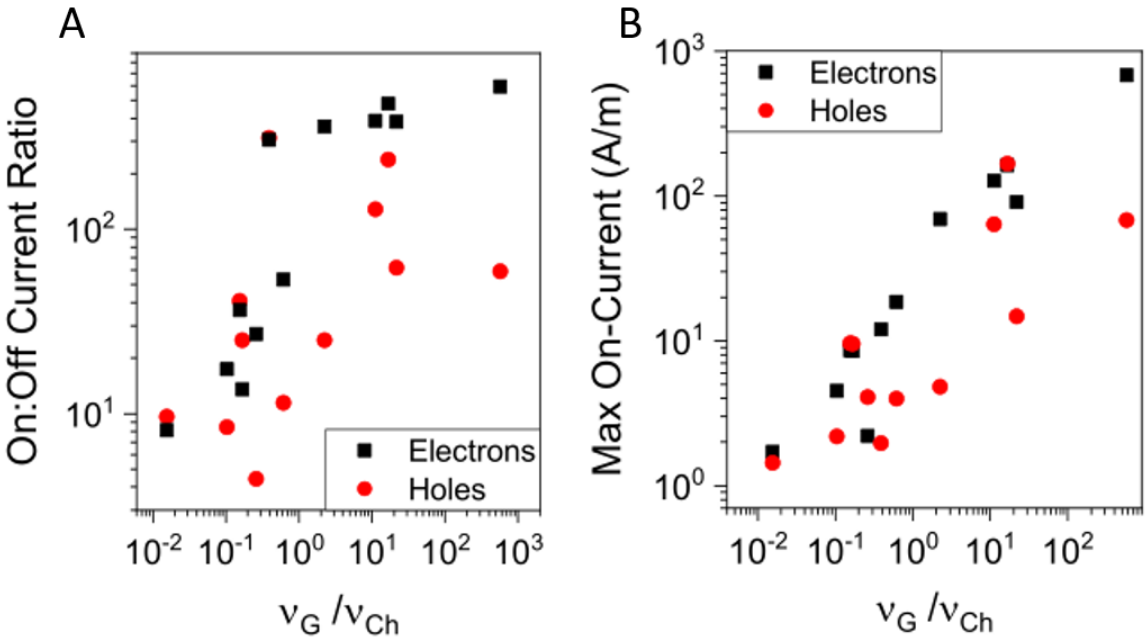

Figure 6.12: (A) The on:off current ratio for both electrons and holes plotted against gate:channel volume ratio. (B) The on current for both electrons and holes plotted against the gate:channel volume ratio. The on current has been normalised with respect to device thickness.

6.3 Conclusion

This chapter shows that in a nanosheet network electrolytically-gated transistor, the balance between the channel and gate volumes must be carefully managed in order to ensure that the device is able to perform properly, with the optimal rule of thumb being that the gate volume should be 10 times that of the channel volume. When this condition is not fulfilled, the gate capacitance will begin to affect the total device capacitance, leading to detrimental effects on the device mobility, on:off current, and transconductance. While this does also allow the effective device mobility to be tuned away from the true network mobility, this will come at an unavoidable cost. Likewise, while in such circumstances it is theoretically possible to estimate the network mobility μ from the effective mobility via Equation 6.12, even if the all other variables in Equation 6.12 are known this is not practical due to the additional negative effects of low gate volume on device performance.

Printed nanosheet network gate electrodes here have an advantage over their solid electrode counterparts, since their porous nature means that it is the gate volume rather

than the gate area that determines the gate capacitance. This means that, unlike in the case of a solid electrode, the gate capacitance can be increased simply by increasing the thickness of the gate electrode. This is a key realisation for future all-printed nanosheet network devices, and means that the gate electrode thickness will be an important factor when fabricating such devices.

Although this chapter has outlined new conditions that must be met for new nanosheet network transistors going forward, it is clear that much work remains to be done. The relatively low network mobilities obtained for these devices even at high gate volumes shows that the sprayed semiconductor channels remain unoptimised, with the most likely culprit being the high inter-sheet junction resistance. It is clear that this will have to be overcome in some way in order to further optimise these devices.

I refuse to answer that question on the grounds
that I don't know the answer.

Douglas Adams

7

The Effect of Flake Geometry on the Performance of Nanosheet Network Transistors

Up until this point the electrical behaviour of nanosheet networks has been something of a black box, with the precise details of what determines the conductivity of a network largely unknown. While it is clear that the network morphology has a large part to play in this, this is a broad term that likely has multiple factors contributing to it and impacting it in ways that are not yet known. One thing that is heavily suggested by previous works, including the prior two chapters in this thesis, is that the nanosheet-nanosheet junction resistance is a major factor in determining the electrical properties of a nanosheet network.[5,89,330] In order to precisely estimate this value and determine the impact that it has on network behaviour, it is clear that the electrical properties of these nanosheet networks needs to be investigated in more detail. Ideally, this will also shed some light on the conduction processes taking place within the network.

In this chapter we investigate the internal workings of a series of nanosheet network transistors by fabricating devices with different mean nanosheet lengths, and investigating the changes in the device properties that take place as a result. In particular,

any changes with respect to nanosheet length will have to be related to the conduction taking place within the network.

7.1 Experimental Method

Tungsten disulfide (Alfa Aesar; CAS: 12067-46-8) and molybdenum diselenide (Alfa Aesar; CAS: 12058-18-3) inks were fabricated using liquid phase exfoliation. In each case, the starting powder was first dispersed in 80 mL of deionised (DI) water at a starting concentration of 35 mg/mL. They were then sonicated for one hour using a Sonics Vibra-cell VCX-750 ultrasonic processor at 60% amplitude, with a pulser set to 6s on, 2s off. Next, the dispersion was centrifuged for one hour at 2555g in order to remove any soluble impurities, with the resulting supernatant discarded. The sediment was then redispersed in a 2 mg/mL solution of sodium cholate (SC) in DI water and sonicated for eight hours, with the pulser set to 4s on, 4s off.

Following exfoliation, both dispersions were size selected using liquid cascade centrifugation (LCC). The dispersions were first centrifuged for two hours at 26.6g in order to remove any unexfoliated material. Successive centrifugation runs were performed on each dispersion at higher speeds for two hours, with each run using the supernatant from the previous run. The speeds used were, in order: 106.4g, 239.4g, 665g, 957.6g, 1702.4g, 3218.6g, 10640g. In addition, the material collected at 106.4g was then redispersed in more SC solution and centrifuged for a further 30 minutes to sediment out the very largest flakes, because this step collected enough material to allow it to be separated into two samples. The sediment from this step was redispersed and recorded as XL(L), with the supernatant from this step recorded as the XL(S) sample.

This gave a total of nine dispersions with different mean flake lengths and thicknesses. The sediments from each centrifugation step were then transferred into isopropanol via a solvent exchange method as previously described in Chapter 4.[171] This involved centrifuging for two hours at a speed that is at least twice the rpm of the centrifuge run used to collect the initial sediment. For this step 3830.4g was used to sediment the first six samples, and 27240g was used to sediment the final three. This

was repeated a second time in order to ensure that as much of the SC was removed as possible.

The switch to a water/cholate based dispersion was primarily motivated by the need to obtain much smaller and thinner flakes for this experiment than in the previous chapters in this thesis. Surfactant-based stabilisation methods tend to give smaller and thinner nanosheets than a equivalent solvent-based method for the same nanomaterial concentration and exfoliation time.[144] Since LCC techniques tend to give diminishing masses of material as the size of the trapped nanosheets decreases, starting off with a larger proportion of smaller thinner flakes was necessary in order to obtain enough mass to fabricate devices. UV-vis spectroscopy was used to obtain concentration measurements for each WS_2 dispersion, using the fact that the extinction coefficient of WS_2 is length-independent, equal to 4770 L $g^{-1}m^{-1}$ at $\lambda = 235$ nm.[152]

Mass filtration was used to obtain concentration measurements for the $MoSe_2$ dispersions owing to inconsistencies between the concentration values predicted by the UV-vis spectra and those given via this method, and as such the mass filtration method was taken to be the most accurate. This was accomplished by pipetting a known volume of ink onto an alumina membrane, and vacuum filtering the ink through the membrane. The membrane was then dried overnight in a vacuum oven. By comparing the mass of the membrane before and after the filtration process a value was found for the concentration of each ink. Further statistics on the mean length $<L>$ of the nanosheet ensembles were found via TEM imaging. A JEOL JEM-2100 LaB_6 transmission electron microscope was used to image the nanosheets and estimate the mean length of the nanosheets within each dispersion. When analysing the images, the longest axis of each nanosheet was taken to be the length.

The inks were diluted to a concentration of 1 mg/mL and sprayed using an aerosol spray gun as shown in Figure 7.1(A), with shadow masks used to define the deposited area. Simultaneously, a glass slide was set beside the sprayed area in order to provide a separate film, the thickness of which was then measured via mechanical profilometry. E-beam evaporation was used to deposit the gold source, drain, and gate electrodes, with the dimensions defined by the shadow mask shown in Figure 7.1(B). This gives a

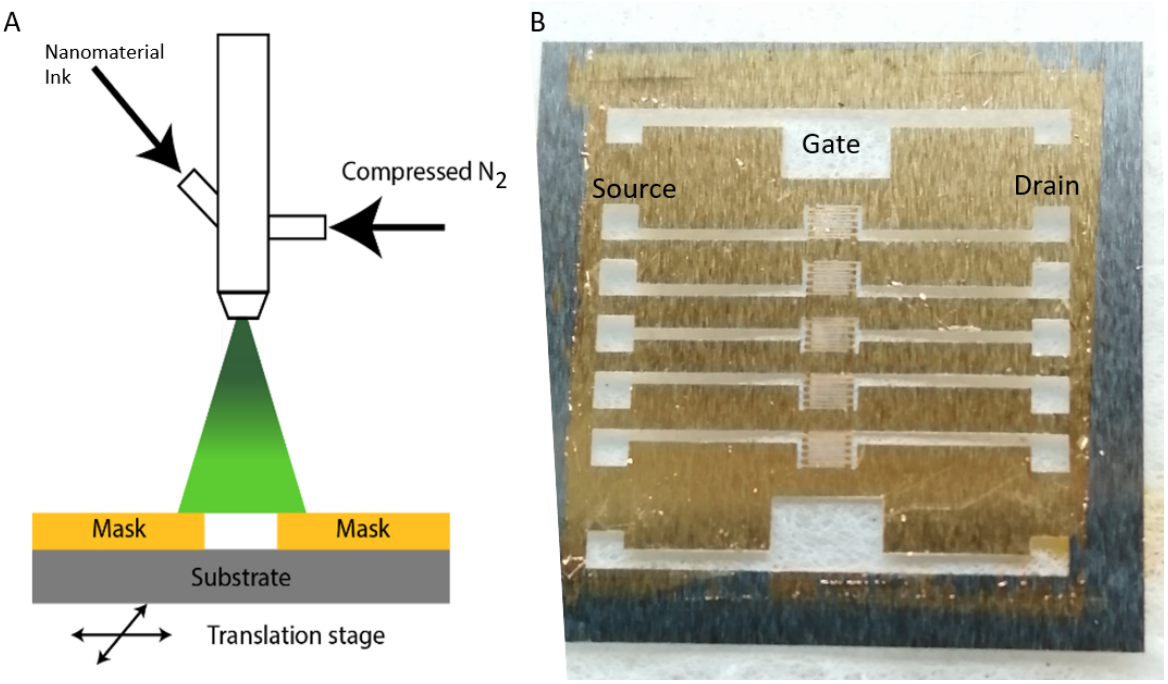

Figure 7.1: (A) Schematic of the aerosol sprayer used to deposit the semiconducting channels. (B) Photograph of the new shadow mask used to define the areas of the source and drain electrodes. The channel length and width were 50 µm and 9 mm respectively.

channel length of 50 µm and a channel width of 9 mm. Note that although an inkjet printed gate electrode was successfully used in the previous chapter, the decision was made to switch back to an e-beam deposited gate in order to reduce the number of steps in the fabrication process.

Raman spectroscopy was performed on the printed devices prior to the addition of ionic liquid using a WITec Alpha 300R confocal Raman microscope and a 532 nm excitation laser. The Raman signals were collected by a 100× objective lens (N.A. = 0.95) and dispersed by a 1800 line/mm grating. 1% laser power was used for all samples, to avoid any damage to the films caused by the beam. Ten spectra were collected at different positions for each sample, and were averaged to obtain a representative Raman spectrum. SEM images of the deposited nanosheet films were obtained using a Zeiss Ultra Plus scanning electron microscope, using an accelerating voltage of 2–3 kV and a 30 μm aperture at a distance of 3–5 mm.

A Keithley 2612A was used to perform all electrical measurements as previously described in Chapter 4. Once again it is critical to emphasise the two sets of measurements performed, one before and one after the addition of the ionic liquid to the device.

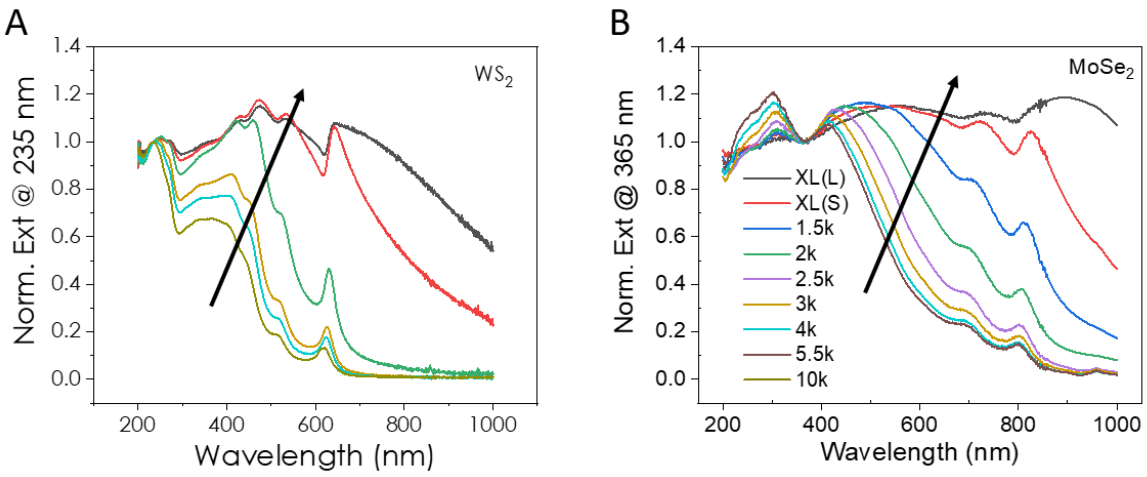

Figure 7.2: (A) UV-vis spectra for WS_2 inks with different mean nanosheet lengths, normalised to the value at 235 nm. The arrow indicates the direction of increasing nanosheet size. (B) UV-vis spectra for $MoSe_2$ inks with different mean nanosheet lengths, normalised to the value at 365 nm. The arrow indicates the direction of increasing nanosheet size. The legend is the same for both graphs.

These are the "dry" and "wet" state measurements respectively, and this distinction will play a key role in interpreting the data in this chapter.

7.2 Results & Discussion

7.2.1 Inks & Deposition

The UV-vis spectra obtained from the size-selected dispersions are shown in Figure 7.2. Figure 7.2(A) shows the WS_2 spectra for nine different mean sizes of nanosheet. All of these spectra display the expected characteristics of a WS_2 dispersion, namely the A-exciton located at approximately 650 nm and higher energy B and C excitons visible at lower wavelengths.[305] As the rpm of the centrifuging step increases, the A-exciton peak becomes blue-shifted, which has been confirmed to be a sign of decreasing nanosheet size in LPE dispersions.[152,282] It should be noted that the spectra for larger sized nanosheet dispersions do not taper to zero extinction at higher wavelengths. This is due to an increased contribution from scattering processes as the nanosheet sizes increase.[331]

A similar analysis can be performed on the $MoSe_2$ spectra shown in Figure 7.2(B).

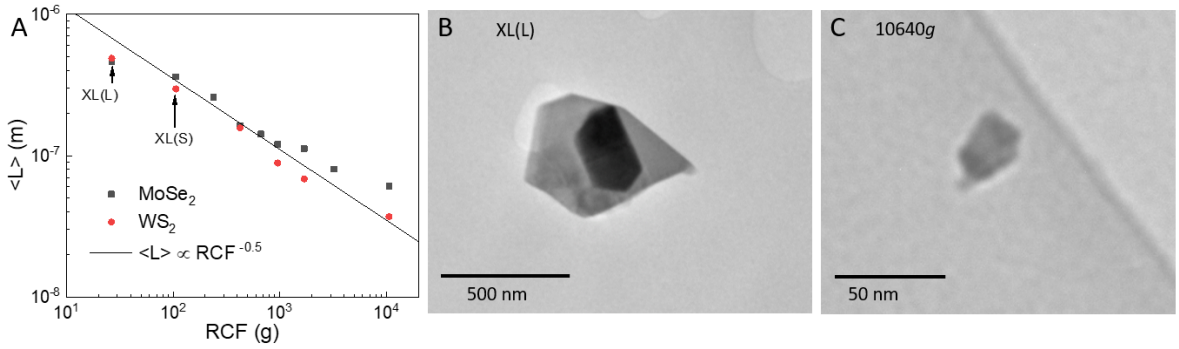

Figure 7.3: Mean nanosheet lengths for $MoSe_2$ (black) and WS_2 (red) inks plotted against the upper centrifugal force used during the liquid cascade centrifugation step. The solid line represents a slope of -0.5. (B) A representative WS_2 nanosheet from the XL(L) ink. (C) A representative WS_2 nanosheet from the 10640*g* (10K) ink.

Like WS_2, the $MoSe_2$ spectra show characteristic peaks corresponding to the A-exciton between 800 nm and 900 nm, with the corresponding wavelength increasing for larger, thicker nanosheets.[282,332] Both sets of spectra showed the expected decrease in nanosheet length with increasing centrifuge speed, consistent with what is expected considering previous work on cascade centrifugation.[152,282]

In order to obtain accurate values for the mean nanosheet length $<L>$, TEM measurements are the preferable option due to the more precise nature of such measurements. This allows the values of <L> to be plotted as a function of the upper relative centrifugal force (RCF) used to size select the nanosheets. The results of this are shown in Figure 7.3. The <L> values of both materials show a power law trend with respect to the RCF values of $< L > \propto \ (RCF)^{-0.5}$, represented in Figure 7.3 by the solid line. This is consistent with previous observations for size-selected LPE dispersions.[152,112,333] Even though the 106.4*g* sample containing the largest nanosheets was centrifuged a second time to separate the XL(S) and XL(L) samples, both of them still fall near the expected $< L > \propto \ (RCF)^{-0.5}$ trendline when the maximum RCF is taken as 26.6*g* and 106.4*g* respectively. This indicates that the change in centrifuging parameters used for this particular step is successfully able to separate the initial 106.4*g* sediment into two meaningfully distinct samples.

Two representative WS_2 nanosheets are shown in Figures 7.3(B) and (C), respectively chosen from the inks with the largest and smallest sized flakes. Both inks exclu-

sively showed two-dimensional structures indicating that the nanosheets are properly exfoliated. In addition, the inks showed no signs of additional non-2D materials that would suggest contamination.

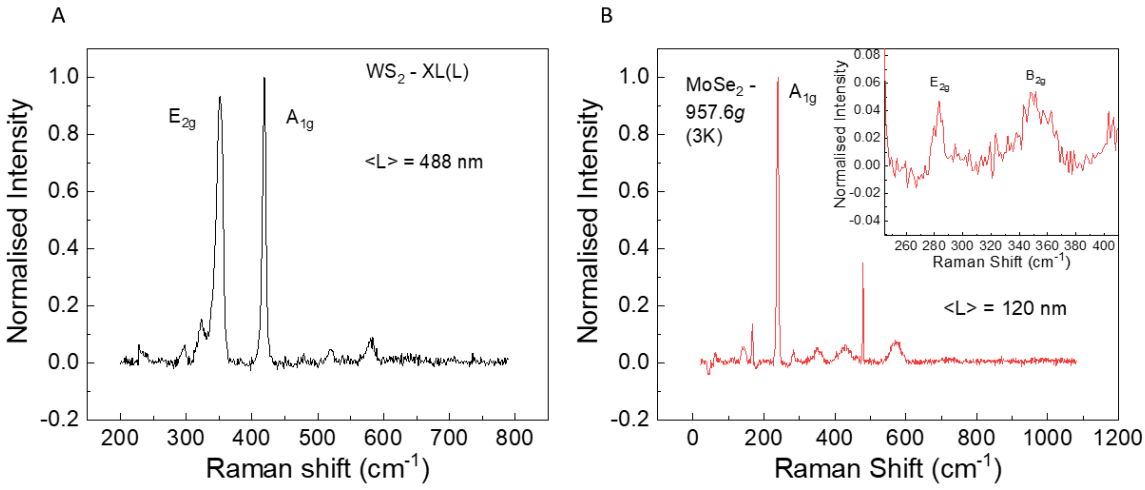

Figure 7.4: Raman spectra for (A) the XL(L) WSe_2 sample and (B) the 957.6g $MoSe_2$ sample. The inset of (B) is a close up on the E_{2g} and B_{2g} $MoSe_2$ Raman peaks.

After the size selected inks were deposited onto PET substrate, Raman spectroscopy was performed on the printed films and the spectra are shown in Figure 7.4. Figure 7.4(A) shows a representative WS_2 spectrum for the XL(L) sample, which displays the characteristic peaks at 351 cm^{-1} and 419 cm^{-1} which correspond to the E_{2_g} and A_{1_g} Raman modes respectively.[306] Figure 7.4(B) similarly shows a representative $MoSe_2$ Raman spectrum for the 957.6g or 3K sample. The peak at 239 cm^{-1} corresponds to the A_{1_g} mode of $MoSe_2$,[334] while the peak at 480 cm^{-1} is attributed to a signal from the Al_2O_3-PET since it was also present in the scans performed on a blank piece of substrate. The $MoSe_2$ spectrum is also noteworthy since it shows the E_{2g} and B_{2g} modes at 280 cm^{-1} and 350 cm^{-1} respectively, shown in Figure 7.4(B, inset). Tonndorf *et al.* note that these modes only appear for $MoSe_2$ flakes with five or fewer layers.[334] This particular film was formed from the 957.6g film and was the first film to clearly display these peaks. Therefore, it follows that the samples with the four smallest $<L>$ values have a mixture of different bandgaps present in the films, since the commonly accepted cutoff point for thickness dependent bandgaps in TMDs is 6 layers.[47,54]

Representative SEM images obtained for two sprayed $MoSe_2$ films are shown in

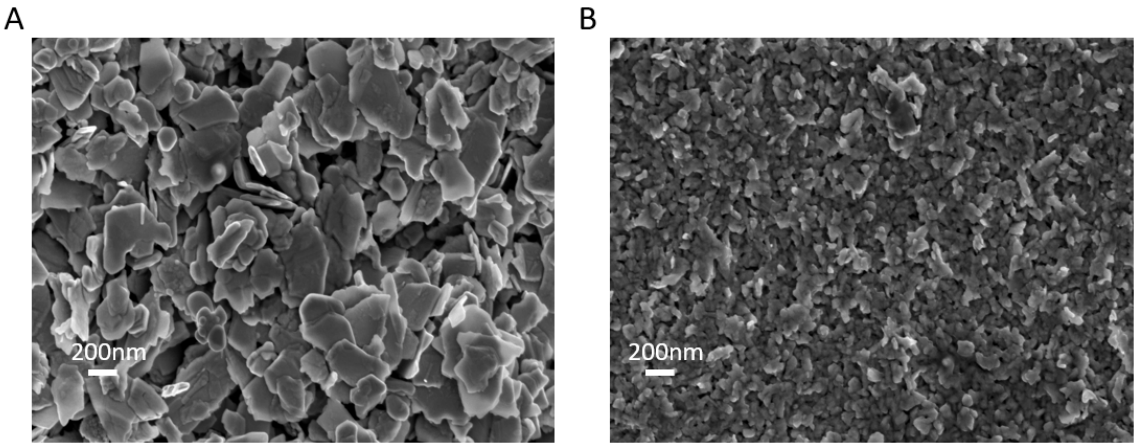

Figure 7.5: SEM images of sprayed $MoSe_2$ films. (A) Film sprayed using the ink with the largest nanosheets. (B) Film sprayed using the ink with the smallest nanosheets. The magnification and scale are the same for both images.

Figure 7.5. Figure 7.5(A) shows a film sprayed using the XL(L) ink with a mean nanosheet length of 462 nm, while Figure 7.5(B) shows a film sprayed using the $10640g$ ink which has a mean nanosheet length of 61 nm. This change in nanosheet size can clearly be seen by comparing the two images since the same magnification was used to capture both images. Crucially, both films display the pores and random flake alignment that is expected of a sprayed nanosheet network. It should be noted that some small (<100 nm) nanosheets can also be seen in Figure 7.5(A), which suggests that these small sheets are present in all of the size selected inks. This is not unexpected when dealing with LPE inks due to their polydisperse nature, and the most likely reason for their presence is small sheets being dragged down by larger ones into the sediment during the centrifugation process.

7.2.2 Modelling the Network Conductivity

The initial current-voltage output curves for the WS_2 devices, before the addition of ionic liquid, are shown in Figure 7.6(A). This data clearly shows a decrease in the device conductances as the centrifuge trapping speed increases and the nanosheet size is reduced. It can also be seen from this graph that the change in the conductances appears to cover at least one order of magnitude, which can be directly linked to the

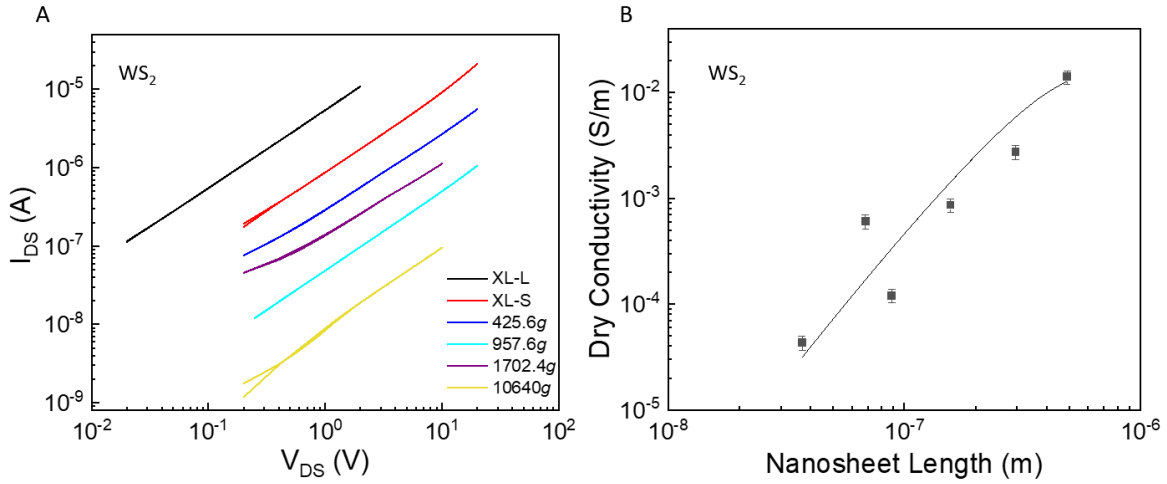

Figure 7.6: (A) Current-voltage graphs for sprayed WS_2 transistors before the addition of ionic liquid. (B) The dry conductivity plotted against <L> for WS_2 before the addition of ionic liquid. The solid line represents a fit to Equation 3.19.

conductivities due to the fact that the device thicknesses all lie between 1 - 2 µm. This is shown much more clearly in Figure 7.6(B), which plots the dry conductivity as a function of the mean nanosheet length, which clearly shows a fall in the network conductivity as the nanosheet length decreases.

Now that a trend of σ_{Net} against $<L>$ has been established, this can be used to calculate the network properties. This is done by using the model that relates the properties of a nanosheet network to the properties of the individual flakes, previously derived in Chapter 3.3. This equation is shown again below

$$\sigma_{Net} \approx \frac{\mu_{NS} n_{NS} e (1 - P)}{\left(1 + 2R_J n_{NS} e \mu_{NS} l_{NS} / k\right)\left(1 + \frac{2k}{n_{NS} l_{NS}^3}\right)}$$

where σ_{Net} is the network conductivity, μ_{NS} is the nanosheet mobility, n_{NS} is the nanosheet carrier density, e is the charge of an electron, R_J is the inter-sheet junction resistance, k is the nanosheet aspect ratio, and l_{NS} is the nanosheet length.

Since there are multiple unknown parameters within this equation, it is not feasible to fit it to the data in Figure 7.6(B) without setting some initial conditions. To begin with, P can be fixed at 0.5, since this has previously been observed to be true for sprayed nanosheet films.[5] The work of Kelly *et al.* can also be used to provide an

estimate for the WS_2 nanosheet mobility $\mu_{NS} \approx 50 \times 10^{-4}$ m^2 V^{-1} s^{-1}, and the nanosheet aspect ratio $k = 30$. This leaves only the junction resistance R_J and carrier density n_{NS} as independent variables.

Fitting Equation 3.19 to the data in Figure 7.6(B) gives the solid line shown in Figure 7.6(B), which shows good agreement with the data, and gives values for the junction resistance and carrier density of 0.37 GΩ and 3.4×10^{20} m^{-3}. These values are consistent with previous publications, since WS_2 networks have previously shown junction resistance values on the order of 1 GΩ.[279,226] While the junction resistance is significantly larger than the estimates of 10 kΩ previously observed for CVD-grown graphene,[335] this in itself is not unexpected. Analyses on nanotube networks indicate that junction resistances between metallic nanotubes are lower than those between semiconducting nanotubes,[336] and it would come as no surprise that the same might apply to 2D:2D junctions.

Similarly, the WS_2 carrier density data in Chapter 5 (Figure 5.10) also showed a dry carrier density of ~10^{20} m^{-3},[89] which indicates that the model's predictions line up with previous results. One oddity that must be pointed out is that the conductivity for the XL(L) and XL(S) samples are significantly higher than the expected conductivity for bulk WS_2 of ~10^{-4} S m^{-1}.[89] It is likely that the switch from solvent- to surfactant-based stabilisation has impacted the conductivity, due to the presence of adsorbed surfactants doping the nanosheets. Surfactant-based stabilisation methods have been observed to dope the nanosheets in previous studies which would explain the abnormally high conductivity results.

The current-voltage plots taken in the wet state, after annealing under vacuum in the presence of the ionic liquid, are shown in Figure 7.7(A). This data has been normalised with respect to device thickness in order to make the trend in conductances more visible to the eye. It is clear that the trend in the wet conductance values covers a significantly smaller range than the dry values, and this is shown more clearly in Figure 7.7(B), which plots the wet conductivity values against the nanosheet length. A key difference between the dry and wet data which becomes apparent here is that the trend in the wet conductivity data is going in the opposite direction to the dry

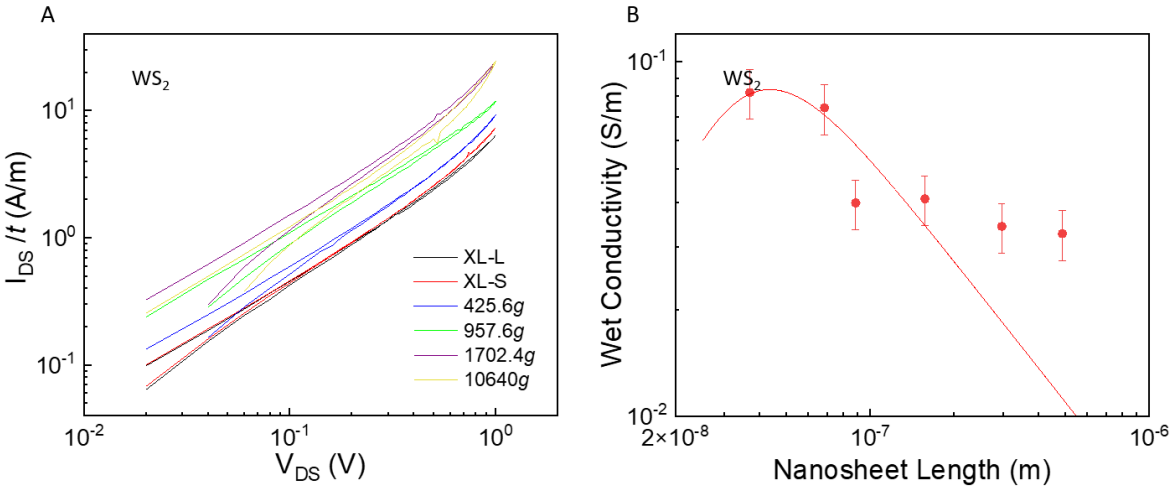

Figure 7.7: (A) Current-voltage graphs for sprayed WS_2 devices after annealing in the presence of ionic liquid. The curves have been normalised with respect to device thickness for visual clarity. (B) Wet conductivity values as a function of nanosheet length. The solid line represents a fit to Equation 3.19.

conductivity data as the nanosheet size increases.

This data can also be fitted to Equation 3.19, and the result of this fit appears as the red line in Figure 7.7(B). The data largely agrees with the fit up to $< L > \approx 200$ nm after which the data begins to deviate from the model, with the two largest sizes giving higher conductivity values than predicted. It should be noted that these two samples also gave higher than expected conductivities for the dry conductivity data. Despite this, it is noteworthy that the fit is capable of broadly describing the trend with increasing nanosheet length, especially since it is the opposite trend to that observed for the dry conductivity data.

The fit in Figure 7.7(B) was performed in the same manner as for the dry conductivity data, with the nanosheet mobility and aspect ratio kept the same. Note that this assumed that the nanosheet mobility is unchanged by the ionic liquid, an assumption that has been utilised throughout this thesis and is supported by the work of Uesugi *et al.*.[240] Hence, by fixing $\mu_{NS} = 50 \times 10^{-4}$ m^2 V^{-1} s^{-1} and $k = 30$ and fitting to Equation 3.19, this gives $R_J = 1.37$ GΩ and $n_{NS} = 1.44 \times 10^{24}$ m^{-3}. The increase by a factor of 4 in the junction resistance is unexpected, but can likely be attributed to the fact that the model is currently best suited only to general trends. The increase in the carrier density is roughly 10^4 which is expected since the ionic liquid is known to

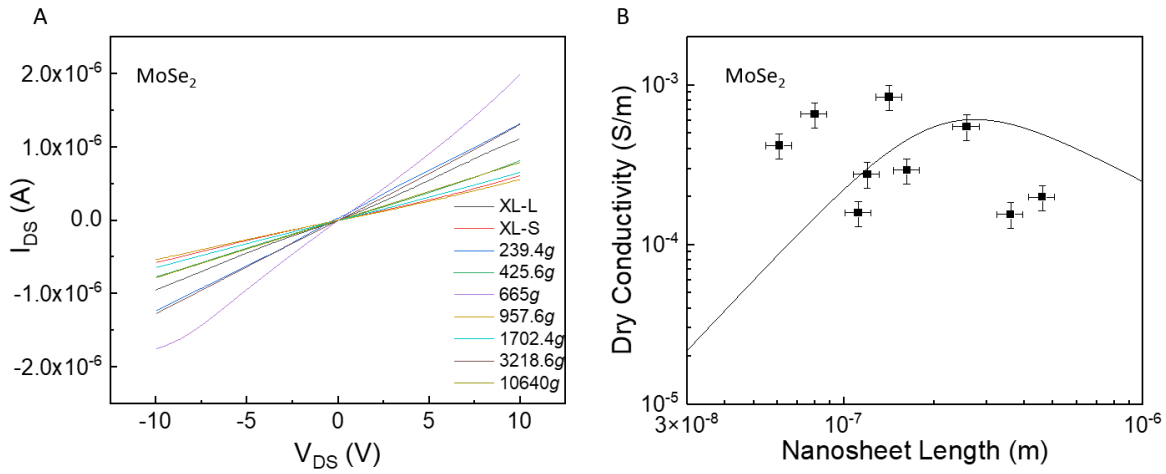

Figure 7.8: (A) Current-voltage graphs for sprayed $MoSe_2$ transistors before the addition of ionic liquid. (B) The dry conductivity plotted against <L> for $MoSe_2$ before the addition of ionic liquid. The solid line represents a fit to Equation 3.19.

affect these nanosheet networks via doping.[5,330] Crucially, the model's predictions are in agreement with the expected parameters of WS_2 in both the doped and un-doped cases. More specifically, the model predicts that the network carrier density is the main driver of whether the network conductivity increases or decreases with nanosheet length, with the switch in direction happening when the carrier density is increased above a certain threshold. This is reflected in the fitting results, with a carrier density of 3.4×10^{20} m^{-3} showing a conductivity increase with $<L>$ and a carrier density of 1.44×10^{24} m^{-3} showing a decrease with $<L>$.

This same process can be applied to the $MoSe_2$ films, beginning with the measurements performed in the dry state. The output curves from this are shown in Figure 7.8(A). It is immediately clear that the change with respect to nanosheet length does not cover the same range as for the WS_2 films, since the difference between the highest and lowest conductances is roughly a factor of four. This is shown more explicitly in Figure 7.8(B), which plots the device dry conductivity against nanosheet length. Due to the amount of scatter present in this data, it is difficult to discern any trend in the data. It is not clear at present where this scatter has come from or why it is so severe, although the scatter appears to be centered around the expected conductivity of 10^{-3} S m^{-1} for $MoSe_2$ nanosheet networks.[5]

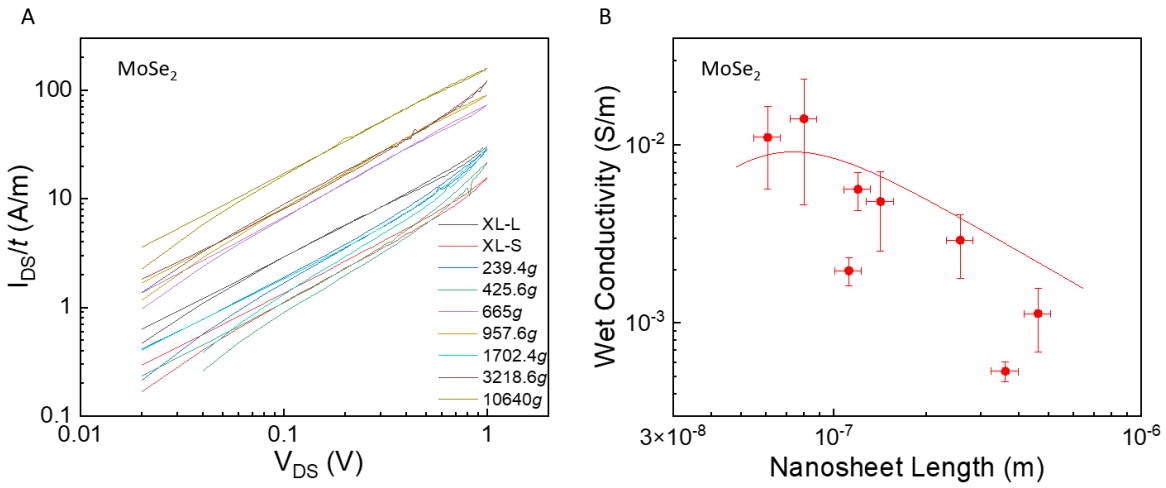

Figure 7.9: (A) Current-voltage graphs for sprayed $MoSe_2$ devices after annealing in the presence of ionic liquid. The curves have been normalised with respect to device thickness to make the trend more apparent. (B) Wet conductivity values as a function of nanosheet length. The solid line represents a fit to Equation 3.19.

Fitting this conductivity data to Equation 3.19 results in the black line in Figure 7.8(B), which despite being the line of best fit is unable to account for most of the variations between different samples. As with the WS_2 samples it is necessary to fix the values of the nanosheet mobility and aspect ratio at 50×10^{-4} $m^2V^{-1}s^{-1}$ and 30 respectively. Hence, the junction resistance and nanosheet carrier density were found to be 30 GΩ and 5.8×10^{21} m^{-3} respectively. While the model is clearly unable to account for the large degree of scatter present in the initial data, the trend remains promising since the model is able to provide a reasonable estimate for n_{NS}, since ~10^{21} m^{-3} is what would be expected of an undoped $MoSe_2$ film.[226] While the junction resistance is significantly larger than those obtained for the WS_2 films, this could be a result of the high amount of scatter in the $MoSe_2$ data or a sign that the model requires improvement. Future measurements will be able to reduce this scatter and thus provide a better opportunity to test the validity of the model.

Despite the scatter present in the dry conductivity data, the wet conductivity data is likely to provide further insights in to the network behaviour due to the doping caused by the presence of the ionic liquid. The output current-voltage curves for these wet networks are shown in Figure 7.9(A), normalised with respect to channel thickness. It is interesting to note that some of the output curves show nonlinear behaviour, which can

be attributed to ions being drawn in from the ionic liquid even at zero gate voltage and has been observed in previous works discussing electrolytically gated transistors.[5,330] As the ions in the ionic liquid reach the nanosheet surface, any imbalance in the binding energies of positive and negative ions will result in different concentrations of both being present at the nanosheet surfaces, in turn leading to doping of the network which is exacerbated as the source-drain voltage is increased. The wet conductivity values are shown in Figure 7.9(B), and show a general downward trend with increasing nanosheet length similar to the WS_2 wet conductivity data.

Fitting this data to Equation 3.19 results in the solid red curve in Figure 7.9(B). By fixing $\mu_{NS} = 50 \times 10^{-4} \mathrm{m^2 V^{-1} s^{-1}}$ and $k = 30$, this gives $R_J = 7.4$ GΩ and $n_{NS} = 3 \times 10^{23}$ $\mathrm{m^{-3}}$. This value for the junction resistance is closer to what was obtained for the WS_2 network, although it remains orders of magnitude higher than previous estimations for R_J in $MoSe_2$ nanosheets.[226] Despite the fact that the method used for the $MoSe_2$ sample discussed in Ref[226] (taken from Ref[5]) also used spray coated $MoSe_2$ films on an Al_2O_3-PET substrate, this is likely a sign that the model used in Ref[226] was a previous iteration of the one derived in Chapter 3.3. The carrier density value on the other hand is near to what was expected of an ionic-liquid doped network, being roughly a factor of four smaller than for the WS_2 network. While the model is able to account for the general trend in conductivity of the doped $MoSe_2$ nanosheet networks, further measurements are needed to test its validity in the case of undoped $MoSe_2$ networks.

7.2.3 Length Dependent Transistor Behaviour

Despite the focus given to the network conductivities up to this point, it would be remiss to neglect the effect of the nanosheet geometry on the switching behaviour of the nanosheet network transistors, particularly with a view to improving the overall device mobility. Analysing the changes in device performance alongside the nanosheet size can provide additional information on the network behaviour as it is gated, as well as finding out if there is an ideal nanosheet length value for future devices.

A set of representative transfer curves is shown in Figure 7.10 for both WS_2 (A)

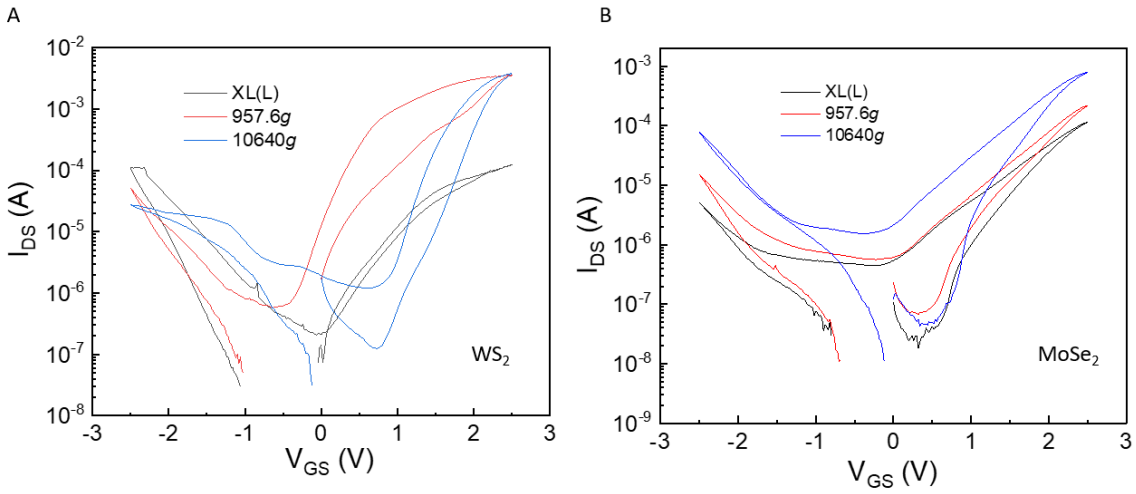

Figure 7.10: Representative transfer curves for (A) WS_2 devices and (B) $MoSe_2$ devices. Each shows a transfer curve from the XL(L), 975.6*g*, and 10640*g* samples.

and $MoSe_2$ (B) devices. In both cases, the transfer curves chosen include the largest size nanosheets, the smallest size, and a third intermediate size. From looking at the WS_2 data, the n-type on-current shows a significant increase of more than an order of magnitude moving from the XL(L) (black) sample to the 957.6g (red) sample, followed by no change between it and the 10640g (blue) sample. Looking at the p-type on-currents, the opposite trend can be seen in which the on-current decreases as the nanosheet size decreases. It is useful to note that the polarity of the WS_2 curve in this chapter is the opposite to what was observed in Chapter 5. This is attributed to the exfoliation method, as Higgins *et al.*[279] previously noted that solvent stabilised nanosheets produced n-type behaviour, in contrast to NMP-stabilised nanosheets which produced p-type behaviour. In contrast, the $MoSe_2$ transfer curves all display the n- and p-type on-currents increasing with decreasing nanosheet size.

At this point it is key to note that it is not possible to move from the transfer curves to the mobility via the transconductance equation (Equation 3.30) using values of C_V taken from the work of Kelly *et al.*, as was done in the previous chapters. The reason for this is that, as noted by Gholamvand *et al.*,[235] the volumetric capacitance of a nanosheet network is proportionate to $1/ < N >$ where $<N>$ is the mean number of layers per nanosheet. Since the ratio of $< L > / < N >$ for the WS_2 and $MoSe_2$ dispersions are expected to be the same independent of the size selection parameters,[112]

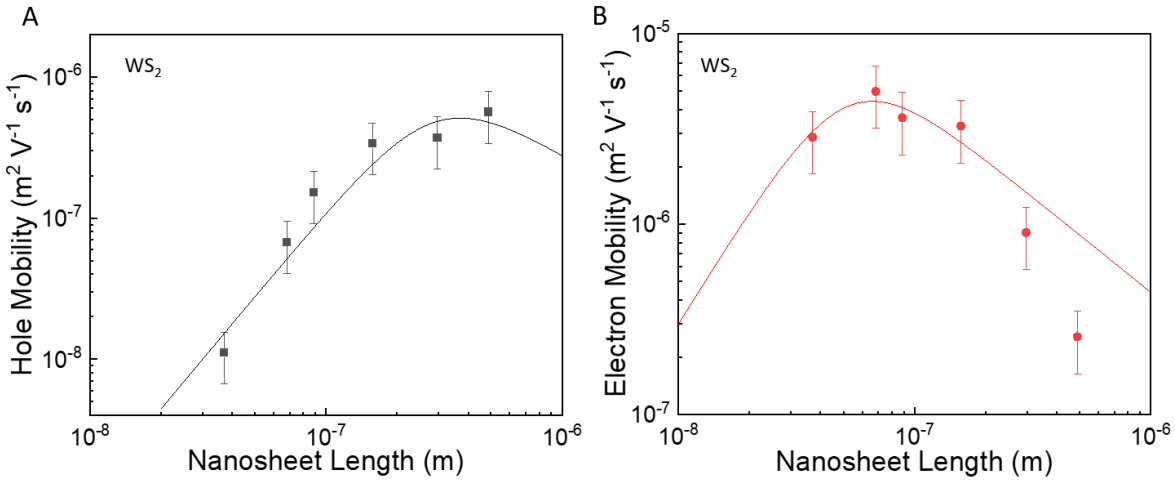

Figure 7.11: Length-dependent mobility data for (A) holes and (B) electrons in WS_2 networks. The solid lines represent fits to Equation 3.18.

this allows the values of C_V to be extrapolated from the data in Ref[5] by assuming that $C_V < L >$ is constant with respect to $<L>$ for each material, allowing the mobility to be directly calculated.

The p- and n-type mobilities for the WS_2 devices are shown in Figure 7.11(A) and (B) respectively. Both show a clear trend as the nanosheet length increases, with the p-type mobility increasing and the n-type mobility showing a peak at $<L> \approx$ 60 nm. The solid lines in Figure 7.11(A) and (B) represent fits to Equation 3.18 (reproduced below)

$$\mu_{Net} \approx \frac{\mu_{NS}}{\left(1 + 2R_J n_{NS} e \mu_{NS} l_{NS}/k\right)\left(1 + \frac{2k}{n_{NS} l_{NS}^3}\right)}$$

Similar to the conductivity data, by fixing $\mu_{NS} = 50 \times 10^{-4}$ m^2 V^{-1} s^{-1} and $k = 30$ this allows the junction resistance and carrier density to be derived from the fit. For the p-type mobility, this gives $R_J = 140$ GΩ and $n_{NS} = 3.51 \times 10^{21}$ m^{-3}. This junction resistance is much higher than expected, given the value of R_J obtained for the wet conductivity of 1.37 GΩ, which combined with a carrier density value of 10^{21} m^{-3} suggests that holes are the minority carriers for these networks since the junction resistance for holes is roughly a factor of 100 higher than that obtained for the wet conductivity. In contrast, the n-type mobility fit gives $R_J = 0.52$ GΩ and $n_{NS} = 4.15 \times 10^{23}$ m^{-3}, which suggests that the majority carriers in these WS_2 network

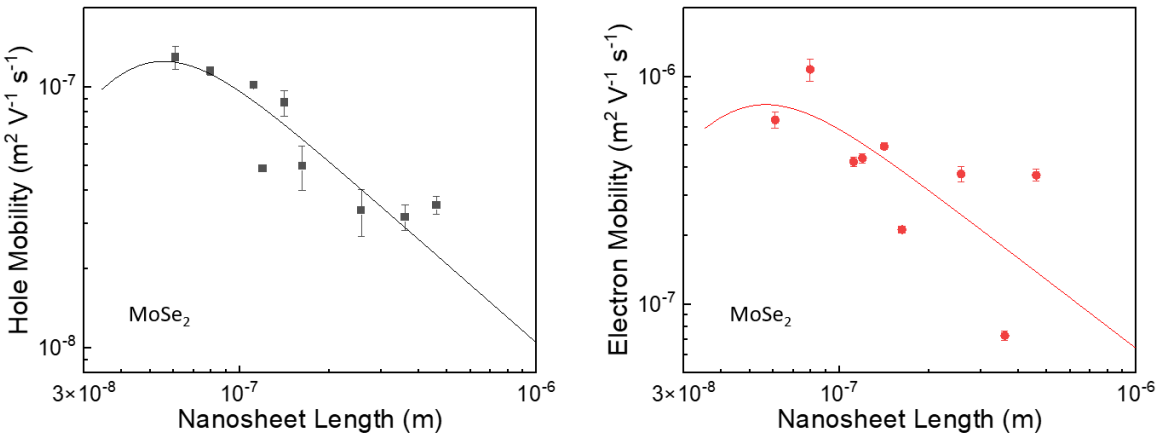

Figure 7.12: Length-dependent mobility data for (A) holes and (B) electrons in $MoSe_2$ networks. The solid lines represent fits to Equation 3.18.

devices are electrons. This is consistent with the prior observations of Higgins *et al.* for cholate-stabilised WS_2.[279] Finally, a value was obtained for the value of $<L>$ for which the device mobility was at its highest, which amounted to a value of μ_e 4.96 $\times 10^{-2}$ cm^2 V^{-1} s^{-1} at $<L> = 69$ nm.

A similar analysis can be performed on the $MoSe_2$ data, with the hole and electron mobility respectively shown in Figure 7.12(A) and (B). It can be seen that both sets of data show the same trend: a peak in mobility values near $< L > \approx 50$ nm followed by a decrease in mobility with increasing nanosheet length, with the electron mobility roughly 10 times higher than the hole mobility. By fitting this data to Equation 3.18, this gives $R_J = 12.9$ GΩ and $n_{NS} = 6.97 \times 10^{23}$ m^{-3} for holes, and $R_J = 2.22$ GΩ and $n_{NS} = 6.6 \times 10^{23}$ m^{-3} for electrons. The two carrier densities being roughly equal and the junction resistance being 10 times higher for holes than for electrons supports the trend seen in Figure 7.10(B), in which the on-currents for electrons were always roughly 10 times larger than for holes. Lastly, as with the WS_2 a value for <L> was found at which the device mobility was at its highest. In this case, the maximum mobility value was μ_e 1.07 $\times 10^{-2}$ cm^2 V^{-1} s^{-1} at $<L> = 80$ nm.

7.3 Conclusion

By using size-selected inks to change the size of the individual nanosheets, clear trends in dry conductivity, wet conductivity, and mobility were observed for both WS_2 and $MoSe_2$ networks. More importantly, the direction of the trend was observed to change between the dry and wet conductivity as the networks were doped, with the dry data showing an increase in conductivity with nanosheet size and the wet data showing the opposite. Crucially, these trends appear counter to the expected intuitive behaviour of showing a consistent trend with respect to nanosheet size.

While the model proposed in Chapter 3 is by no means conclusive, it is able to make predictions that match the data obtained for both the WS_2 and $MoSe_2$ transistors as the nanosheet length is changed. More specifically, it predicts that as the carrier density is increased, the direction of the trend changes from increasing with $<L>$ to decreasing with $<L>$. This shows the potential of this model to provide valuable insight into the inner workings of these nanosheet networks, something that is crucial to developing further means to improve their performance. The model was also able to provide estimates for the inter-sheet junction resistance and the sheet carrier density. While the data from the WS_2 set remains suspect due to a high initial conductivity, this is most likely a sign of the model still being in its early stages of development. The estimates for the junction resistance were 0.37 GΩ from the dry conductivity data, 1.37 GΩ from the wet conductivity data, and for holes and electrons respectively from the mobility data. Likewise the carrier density was estimated to be 3.4×10^{20} m^{-3} for dry networks, 1.44×10^{24} m^{-3} for wet networks. These values match with the expected increase in the carrier density as ionic liquid is added to the network.

In the case of the $MoSe_2$ devices, the high degree of scatter present in the dry conductivity is a sign that further investigation is needed to make the fitting values obtained from this data more reliable. Currently, the dry conductivity data does not show a clear trend, although fitting the data to the model gives the a peak near $<L>$ = 150 nm. The wet conductivity shows a clearer trend that decreases with increasing nanosheet size. Applying the model to these datasets gives a junction resistance of 30

GΩ and carrier density of 5.8×10^{21} m^{-3} for the dry conductivity, and a junction resistance of 7.4 GΩ and carrier density of 3×10^{23} m^{-3} for the wet conductivity.

Importantly, the model was also able to account for the behaviour of the networks while being electrolytically gated, showing that it can be used to evaluate networks with high carrier densities. For WS_2, this gave carrier densities of 4.15×10^{23} m^{-3} for electrons and 10^{21} m^{-3} for holes, with corresponding junction resistances of 0.52 GΩ and 140 GΩ. Likewise, applying the model to the $MoSe_2$ mobility gives carrier densities of 6.97×10^{23} m^{-3} for holes and 6.6×10^{23} m^{-3} for electrons, with corresponding junction resistances of 12.9 GΩ and 2.22 GΩ. This supports the n-type behaviour observed in the WS_2 transfer curves, and the more ambipolar behaviour observed for the $MoSe_2$ devices.

Finally, this model shows potential to determine the optimal value of <L> for a given material to maximise the network mobility, something that will hopefully prove useful in future optimisation of printed nanosheet network transistors. Both the WS_2 and $MoSe_2$ networks showed maximum network mobilities at <L>~80 nm, suggesting an optimum flake size for future nanosheet network transistors. Since the model used to make these predictions also makes no assumptions as to the method in which the nanosheets were prepared other than a constant aspect ratio, it is also likely that this model can be further utilised to characterise the behaviour of nanosheets produced via such methods as electrochemical exfoliation, thus further increasing its utility. While it is also the case that the model makes multiple approximations to reach this stage, accounting for said approximations would only further increase the accuracy of the model's predictions and thus its ability to describe the electrical characteristics of a nanosheet network.

Information is not knowledge, knowledge is not wisdom, and wisdom is not foresight. Each grows out of the other, and we need them all.

Arthur C. Clarke

8

Conclusion & Future Work

Although electrolytically-gated nanosheet network transistors show great potential in printed device applications, it is clear that there remains a good deal of necessary work to fully realise this potential. In their current state these printed transistors are heavily limited by the junction resistances, which are in turn influenced by the film morphology. This work hopes to illuminate pathways for future research into these networks by providing some insight into their inner workings, as well as outlining the requirements for future transistor applications derived from them.

Following the successful demonstration by Kelly *et al.* of an electrochemical nanosheet-network transistor, it was clear that despite the good switching behaviour observed for such devices, the mobility obtained for such devices was orders of magnitude below that of a single nanosheet. In this work a potential solution to this issue was investigated, namely the addition of small quantities of highly conducting nanosheets to boost the overall network properties while maintaining the switching behaviour needed for transistor applications. A series of transistors with nano-nano composite films of graphene and WS_2 nanosheets were studied, with particular focus on the changes in conductivity, mobility, and on:off ratio as the amount of graphene was increased from 0 volume fraction (WS_2 only film) to 0.5 volume fraction (graphene only film). The conductivity and mobility were found to scale following percolation theory with a percolation threshold of 0.08, which means that above this value the graphene nanosheets are able to form a conducting sub-network within the composite that carries the brunt of the current.

This has a large adverse impact on the on:off ratio, which decreased from 2×10^4 for a WS_2 only network to ~10^1 above the percolation threshold. Unfortunately this decrease is far too severe to be worth the relatively small increase in device mobility, since adding the amount of graphene needed to cause a twofold increase in network mobility results in a fall in the on:off ratio of a factor of 10^3. Unfortunately this means that tuning the device properties by adding a conductive filler is not a feasible route to improving device performance.

A key step towards future applications for printed nanosheet network transistors is to be able to fabricate as many elements as possible out of printed nanosheet networks. To this end, it was key to investigate the impact that switching from a planar gold gate electrode to a porous graphene gate electrode would have on the device performance. In particular it was important to determine whether changes in the gate geometry would impact the device performance, since this would set a baseline for future all-printed nanosheet network transistors. To address this, WSe_2-channel transistors were fabricated with printed graphene gate electrodes, with the volume of the gate electrode varied from ~10^{-4} mm^3 to ~1 mm^3. As the gate volume decreased, the gate capacitance began to dominate the overall device capacitance and began to negatively impact the performance. For gate:channel volume ratios below ~10, the gate volume was able to negatively affect the overall device, with the network mobility decreasing rapidly for gate:volume ratios of < 1. In addition to the mobility, the transistor on:off ratio and magnitude of the on-currents also decreased once the gate capacitance began to influence the device behaviour.

While it is well-documented at this point that nanosheet networks are limited by the inter-sheet junction resistances, work to characterise the inner workings of these networks is limited. A model to describe the conductivity and mobility of a nanosheet network in terms of the properties of the individual nanosheets and the inter-sheet resistance was derived by the Coleman group and was applied to a series of WS_2 and $MoSe_2$ nanosheet network transistors with varying mean nanosheet size. The model was capable of describing both the undoped and doped conductivity, as well as the n- and p-type mobility. This demonstrates the utility of such a model, as well as illuminating

some of the inner workings of these nanosheet networks.

8.1 Future Work

One of the most important avenues of future research will be addressing the impact of network morphology on these devices, both in terms of characterising the precise nature of said impact and in developing means to control the film morphology.

A potential work-around to the problem of junction-limited devices has been found by Lin *et al.*,[99] by manufacturing nanosheet network transistors via spin-coating of electrochemically exfoliated nanosheets, although this method is not without its drawbacks. First and foremost is the lack of scalability that comes with electrochemical exfoliation, and the amount of time necessary to exfoliate enough material to create a suitable spin-coated device. In contrast, LPE-based inks are easily capable of producing large quantities of material but are currently unable to reproduce the high aspect ratio nanosheets created via electrochemical exfoliation. Finding a suitable middle ground where large quantities of high aspect ratio nanosheets can be produced in large quantities is ideal for further improving the performance of printed transistors.

A potential workaround to this issue is to produce tiled networks of nanosheets, which are closely packed low-porosity networks, via layer-by-layer deposition techniques. These networks are able to achieve similar high-mobility networks that are able to severely reduce the impact of inter-sheet junctions, via the formation of "fish scale" structures which produce both good nanosheet alignment and high sheet-to-sheet overlap.[337] This has considerable potential for optoelectronic applications, as demonstrated by Neilson *et al.* who achieved MoS_2-based FET mobilities and on:off ratios comparable to CVD-grown films.[338]

In addition, there are two techniques which promise the ability to gain further insight into the inner workings of printed nanosheet networks. The first is FIB-SEM tomography, which involves sequential FIB and SEM steps performed on a printed film to build up a full 3D image of the nanosheet network, allowing simultaneous investigation of pore structure and nanosheet alignment, both of which are key to

developing an understanding of the morphology. The second is impedance spectroscopy, expanding on the methodology used by Kelly *et al.* to analyse printed hBN capacitors.[2] This gives insight into the behaviour of such networks over a range of frequencies which will in turn provide insight into junction resistances and inter-sheet capacitances, by treating the nanosheet networks in a similar manner to that of the model derived in Chapter 3.2. Preliminary work in this area has already been carried out by Nalawade *et al.* for BiOCl printed nanosheet network capacitors, where impedance spectroscopy was used to probe the equivalent circuit of the device while simultaneously confirming the absence of pinholes in the dielectric.[339]

Another issue facing electrochemical transistors is the lengthy annealing process necessary to prepare the liquid electrolyte for device operation. While this is necessary to maintain the stability of the ionic liquid and suitably widen the electrochemical window, it limits the potential of the devices since they must be kept away from moisture. Investigating ways to encapsulate these devices while maintaining their performance will be necessary, building on previous efforts to encapsulate other electrochemical devices.[340]

One final issue facing ionic liquid gated transistors is the slow switching speed displayed by the devices made during this thesis, which were on the order of seconds. In order for these devices to become viable for commercial use, it is clear that this issue must be overcome. Since the device geometries in this work involve a side gate located a distance on the order of millimetres from the channel, the time taken for the ions to diffuse from gate to channel will impact the switching speed.

Chapter & Material	Figure(s) of Merit	Key Results
Chapter 5 WS_2 & graphene	• Figure of merit C_V µ varies with graphene loading level. • Percolation threshold found to be at φ= 0.08. • Trend in C_V µagainst φ is well described by percolation theory.	• For pure WS_2 device, µ= 0.1 cm^2 V^{-1} s^{-1} and on:off ratio = 10^4. • For pure graphene device, µ= 0.35 cm^2 V^{-1} s^{-1} and on:off ratio = 1.3.
Chapter 6 WSe_2	• Figure of merit C_V µ affected by graphene gate volume. • Below a certain gate volume threshold C_V µ depends on gate volume. • This threshold is when the gate volume:channel volume ratio is equal to 10.	• Above V_G/V_{Ch} = 10, µ≈ 10^{-2} cm^2 V^{-1} s^{-1}. • Below V_G/V_{Ch} = 10, µ decreases with gate volume to as low as 10^{-4} cm^2 V^{-1} s^{-1}.
Chapter 7 WS_2 & $MoSe_2$	• Conductivity and mobility both scale with mean nanosheet length. • Addition of ionic liquid causes the direction of the trend in conductivity to switch direction. • This is due to the increase in carrier density that comes with the addition of ionic liquid. • The model derived in Chapter 3.2 is able to both account for and predict this change in direction.	• For WS_2, the maximum mobility value was μ_e 4.96 $\times 10^{-2}$ cm^2 V^{-1} s^{-1} at $<L>$ = 69 nm. • For $MoSe_2$, the maximum mobility value was μ_e 1.07 $\times 10^{-2}$ cm^2 V^{-1} s^{-1} at $<L>$ = 80 nm.

Figure 8.1: A summary of the various devices produced throughout this thesis, as well as some of the key results obtained.

References

[1] Taoran Le, Vasileios Lakafosis, Ziyin Lin, C. P. Wong, and M. M. Tentzeris. Inkjet-printed graphene-based wireless gas sensor modules. In *Proceedings - Electronic Components and Technology Conference*, 2012.

[2] Adam G. Kelly, David Finn, Andrew Harvey, Toby Hallam, and Jonathan N. Coleman. All-printed capacitors from graphene-BN-graphene nanosheet heterostructures. *Applied Physics Letters*, 109(2):023107, jul 2016.

[3] Hattan Abuzaid, Nicholas X Williams, and Aaron D Franklin. How good are 2D transistors? an application-specific benchmarking study. *Applied Physics Letters*, 118(3):030501, 2021.

[4] Andrea C Ferrari, Francesco Bonaccorso, Vladimir Fal'Ko, Konstantin S Novoselov, Stephan Roche, Peter Bøggild, Stefano Borini, Frank HL Koppens, Vincenzo Palermo, Nicola Pugno, et al. Science and technology roadmap for graphene, related two-dimensional crystals, and hybrid systems. *Nanoscale*, 7(11):4598–4810, 2015.

[5] Adam G. Kelly, Toby Hallam, Claudia Backes, Andrew Harvey, Amir Sajad Esmaeily, Ian Godwin, João Coelho, Valeria Nicolosi, Jannika Lauth, Aditya Kulkarni, Sachin Kinge, Laurens D.A. Siebbeles, Georg S. Duesberg, and Jonathan N. Coleman. All-printed thin-film transistors from networks of liquid-exfoliated nanosheets. *Science*, 2017.

[6] M Reibold, P Paufler, AA Levin, W Kochmann, N Pätzke, and DC Meyer. Carbon nanotubes in an ancient damascus sabre. *Nature*, 444(7117):286–286, 2006.

[7] Richard P Feynman. There's plenty of room at the bottom. *Resonance*, 16(9):890–905, 2011.

[8] Michael Faraday. X. the bakerian lecture.—experimental relations of gold (and other metals) to light. *Philosophical Transactions of the Royal Society of London*, (147):145–181, 1857.

[9] Harold W Kroto, James R Heath, Sean C O'Brien, Robert F Curl, and Richard E Smalley. C_{60}: buckminsterfullerene. *Nature*, 318(6042):162–163, 1985.

[10] Sumio Iijima. Helical microtubules of graphitic carbon. *nature*, 354(6348):56–58, 1991.

[11] K. S. Novoselov, A. K. Geim, S. V. Morozov, D. Jiang, Y. Zhang, S. V. Dubonos, I. V. Grigorieva, and A. A. Firsov. Electric field in atomically thin carbon films. *Science*, 306(5696):666–669, October 2004.

[12] Kunfeng Chen, Shuyan Song, Fei Liu, and Dongfeng Xue. Structural design of graphene for use in electrochemical energy storage devices. *Chemical Society Reviews*, 44(17):6230–6257, 2015.

[13] Conor S Boland, Umar Khan, Gavin Ryan, Sebastian Barwich, Romina Charifou, Andrew Harvey, Claudia Backes, Zheling Li, Mauro S Ferreira, Matthias E Möbius, et al. Sensitive electromechanical sensors using viscoelastic graphene-polymer nanocomposites. *Science*, 354(6317):1257–1260, 2016.

[14] Zhaoyang Lin, Yu Huang, and Xiangfeng Duan. Van der waals thin-film electronics. *Nature Electronics*, 2(9):378–388, 2019.

[15] P. R. Wallace. The band theory of graphite. *Physical Review*, 71:622–634, May 1947.

[16] Brodie Benjamin Collins. On the atomic weight of graphene. *Philosophical Transactions of the Royal Society*, pages 149249–259, 1859.

[17] Roscoe G. Dickinson and Linus Pauling. The crystal structure of molybdenite. *Journal of the American Chemical Society*, 45(6):1466–1471, Jun 1923.

[18] E. Lifshitz L. Landau. Statistical physics part i, 1980.

[19] J. A. Venables and G. D. T. Spiller. *Nucleation and Growth of Thin Films*, pages 341–404. Springer US, Boston, MA, 1983.

[20] Jannik C. Meyer, A. K. Geim, M. I. Katsnelson, K. S. Novoselov, T. J. Booth, and S. Roth. The structure of suspended graphene sheets. *Nature*, 446(7131):60–63, Mar 2007.

[21] A. K. Geim and K. S. Novoselov. The rise of graphene. *Nature Materials*, 6(3):183–191, March 2007.

[22] Dexter Johnson. Europe has invested €1 billion into graphene - but for what?, 2019. Accessed on 2/6/21.

[23] Rubén Mas-Ballesté, Cristina Gómez-Navarro, Julio Gómez-Herrero, and Félix Zamora. 2D materials: to Graphene and Beyond. *Nanoscale*, 3(1):20–30, 2011.

[24] F. Bonaccorso, Z. Sun, T. Hasan, and A. C. Ferrari. Graphene photonics and optoelectronics. *Nature Photonics*, 4(9):611–622, Sep 2010.

[25] Alexander A. Balandin, Suchismita Ghosh, Wenzhong Bao, Irene Calizo, Desalegne Teweldebrhan, Feng Miao, and Chun Ning Lau. Superior thermal conductivity of single-layer graphene. *Nano Letters*, 8(3):902–907, 2008.

[26] Scarpa F., Adhikari S., and Srikantha Phani A. Effective elastic mechanical properties of single layer graphene sheets. *Nanotechnology*, 20(6):065709, 2009.

[27] Ashtami Jayakumar, Anju Surendranath, and PV Mohanan. 2D materials for next generation healthcare applications. *International Journal of Pharmaceutics*, 551(1-2):309–321, 2018.

[28] Alessandro Silvestri, Alejandro Criado, and Maurizio Prato. Concluding remarks: Chemistry of 2-dimensional materials: beyond graphene. *Faraday Discuss.*, pages 383–395, 2021.

[29] Zhaoming Kang, Muhammad Arif Khan, Yanmei Gong, Rida Javed, Yuan Xu, Daixin Ye, Hongbin Zhao, and Jiujun Zhang. Recent progress of mxenes and mxene-based nanomaterials for the electrocatalytic hydrogen evolution reaction. *Journal of Material Chemistry A*, 9:6089–6108, 2021.

[30] Zengle Cao, Fengrui Hu, Chunfeng Zhang, Shining N. Zhu, Min Xiao, and Xiaoyong Wang. Optical studies of semiconductor perovskite nanocrystals for classical optoelectronic applications and quantum information technologies: a review. *Advanced Photonics*, 2(5):1 – 15, 2020.

[31] Encai Ou, Yanyan Xie, Chang Peng, Yawei Song, Hua Peng, Yuanqin Xiong, and Weijian Xu. High concentration and stable few-layer graphene dispersions prepared by the exfoliation of graphite in different organic solvents. *RSC Advances*, 3(24):9490–9499, 2013.

[32] Ujjal Kumar Sur. Graphene: a rising star on the horizon of materials science. *International Journal of Electrochemistry*, 2012, 2012.

[33] Vinod K. Sangwan and Mark C. Hersam. Electronic Transport in Two-Dimensional Materials. *Annual Review of Physical Chemistry*, 69(1):299–325, apr 2018.

[34] A. H. Castro Neto, F. Guinea, N. M. R. Peres, K. S. Novoselov, and A. K. Geim. The electronic properties of graphene. *Reviews of Modern Physics*, 81:109–162, Jan 2009.

[35] K. S. Novoselov, A. K. Geim, S. V. Morozov, D. Jiang, Y. Zhang, S. V. Dubonos, I. V. Grigorieva, and A. A. Firsov. Electric field effect in atomically thin carbon films. *Science*, 306(5696):666–669, 2004.

[36] V. E. Calado, Shou-En Zhu, S. Goswami, Q. Xu, K. Watanabe, T. Taniguchi, G. C. A. M. Janssen, and L. M. K. Vandersypen. Ballistic transport in graphene grown by chemical vapor deposition. *Applied Physics Letters*, 104(2):023103, 2014.

[37] Michael S. Fuhrer, Chun Ning Lau, and Allan H. MacDonald. Graphene: Materially better carbon. *MRS Bulletin*, 35(4):289–295, Apr 2010.

[38] Xiaowu Tang, G. Murali, Hyungjin Lee, Seongmin Park, Seongeun Lee, Sun Moo Oh, Jihoon Lee, Tae Yun Ko, Chong Min Koo, Yong Jin Jeong, Tae Kyu An, Insik In, and Se Hyun Kim. Engineering aggregation-resistant mxene nanosheets as highly conductive and stable inks for all-printed electronics. *Advanced Functional Materials*, 31(29):2010897, 2021.

[39] Roscoe G. Dickinson and Linus Pauling. The crystal structure of molybdenite. *Journal of the American Chemical Society*, 45(6):1466–1471, Jun 1923.

[40] J.A. Wilson and A.D. Yoffe. The transition metal dichalcogenides discussion and interpretation of the observed optical, electrical and structural properties. *Advances in Physics*, 18(73):193–335, 1969.

[41] R. F. Frindt. Single crystals of MoS_2 several molecular layers thick. *Journal of Applied Physics*, 37(4):1928–1929, 1966.

[42] R. F. Frindt. Optical absorption of a few unit-cell layers of MoS_2. *Physical Review*, 140:A536–A539, Oct 1965.

[43] MA Py and RR Haering. Structural destabilization induced by lithium intercalation in mos2 and related compounds. *Canadian Journal of Physics*, 61(1):76–84, 1983.

[44] Per Joensen, RF Frindt, and S Roy Morrison. Single-layer mos2. *Materials research bulletin*, 21(4):457–461, 1986.

[45] K. S. Novoselov, D. Jiang, F. Schedin, T. J. Booth, V. V. Khotkevich, S. V. Morozov, and A. K. Geim. Two-dimensional atomic crystals. *Proceedings of the National Academy of Sciences*, 102(30):10451–10453, 2005.

[46] Tianshu Li and Giulia Galli. Electronic properties of mos2 nanoparticles. *The Journal of Physical Chemistry C*, 111(44):16192–16196, 2007.

[47] Kin Fai Mak, Changgu Lee, James Hone, Jie Shan, and Tony F. Heinz. Atomically Thin MoS_2: A New Direct-Gap Semiconductor. *Physical Review Letters*, 105(13):136805, sep 2010.

[48] Sihan Zhao, Takato Hotta, Takashi Koretsune, Kenji Watanabe, Takashi Taniguchi, Katsuaki Sugawara, Takashi Takahashi, Hisanori Shinohara, and Ryo Kitaura. Two-dimensional metallic NbS_2: growth, optical identification and transport properties. *2D Materials*, 3(2):025027, may 2016.

[49] P K Das, D Di Sante, F Cilento, C Bigi, D Kopic, D Soranzio, A Sterzi, J A Krieger, I Vobornik, J Fujii, T Okuda, V N Strocov, M B H Breese, F Parmigiani, G Rossi, S Picozzi, R Thomale, G Sangiovanni, R J Cava, and G Panaccione. Electronic properties of candidate type-II weyl semimetal WTe_2. a review perspective. *Electronic Structure*, 1(1):014003, mar 2019.

[50] Manish Chhowalla, Hyeon Suk Shin, Goki Eda, Lain-Jong Li, Kian Ping Loh, and Hua Zhang. The chemistry of two-dimensional layered transition metal dichalcogenide nanosheets. *Nature Chemistry*, 5(4):263–275, Apr 2013.

[51] Youngki Yoon, Kartik Ganapathi, and Sayeef Salahuddin. How good can monolayer MoS_2 transistors be? *Nano Letters*, 11(9):3768–3773, Sep 2011.

[52] B. Radisavljevic, A. Radenovic, J. Brivio, V. Giacometti, and A. Kis. Single-layer MoS_2 transistors. *Nature Nanotechnology*, 6(3):147–150, Mar 2011.

[53] Hailong Zhou, Chen Wang, Jonathan C. Shaw, Rui Cheng, Yu Chen, Xiaoqing Huang, Yuan Liu, Nathan O. Weiss, Zhaoyang Lin, Yu Huang, and Xiangfeng Duan. Large area growth and electrical properties of p-type WSe_2 atomic layers. *Nano Letters*, 15(1):709–713, Jan 2015.

[54] Weijie Zhao, Zohreh Ghorannevis, Leiqiang Chu, Minglin Toh, Christian Kloc, Ping-Heng Tan, and Goki Eda. Evolution of Electronic Structure in Atomically Thin Sheets of WS_2 and WSe_2. *ACS Nano*, 7(1):791–797, jan 2013.

[55] Zhipei Sun, Amos Martinez, and Feng Wang. Optical modulators with 2D layered materials. *Nature Photonics*, 10(4):227–238, Apr 2016.

[56] Qu Yue, Jun Kang, Zhengzheng Shao, Xueao Zhang, Shengli Chang, Guang Wang, Shiqiao Qin, and Jingbo Li. Mechanical and electronic properties of monolayer MoS_2 under elastic strain. *Physics Letters A*, 376(12):1166–1170, Feb 2012.

[57] Sonia Biccai, Conor S. Boland, Daniel P. Odriscoll, Andrew Harvey, Cian Gabbett, Domhnall R. O Suilleabhain, Aideen J. Griffin, Zheling Li, Robert J. Young, and Jonathan N. Coleman. Negative Gauge Factor Piezoresistive Composites Based on Polymers Filled with MoS_2 Nanosheets. *ACS Nano*, 2019.

[58] J.A. Wilson and A.D. Yoffe. The transition metal dichalcogenides discussion and interpretation of the observed optical, electrical and structural properties. *Advances in Physics*, 18(73):193–335, 1969.

[59] Claudia Ruppert, Ozgur Burak Aslan, and Tony F. Heinz. Optical properties and band gap of single- and few-layer $MoTe_2$ crystals. *Nano Letters*, 14(11):6231–6236, Nov 2014.

[60] Sohail Ahmad and Sugata Mukherjee. A comparative study of electronic properties of bulk MoS_2 and its monolayer using dft technique: application of mechanical strain on MoS_2 monolayer, 2014.

[61] Andrea Splendiani, Liang Sun, Yuanbo Zhang, Tianshu Li, Jonghwan Kim, Chi-Yung Chim, Giulia Galli, and Feng Wang. Emerging photoluminescence in monolayer MoS_2. *Nano Letters*, 10(4):1271–1275, Apr 2010.

[62] Th. Finteis, M. Hengsberger, Th. Straub, K. Fauth, R. Claessen, P. Auer, P. Steiner, S. Hüfner, P. Blaha, M. Vögt, M. Lux-Steiner, and E. Bucher. Occupied and unoccupied electronic band structure of WSe_2. *Physical Review B*, 55:10400–10411, Apr 1997.

[63] Shivani Sharma, Shubham Bhagat, Jasvir Singh, Manzoor Ahmad, and Sandeep Sharma. Temperature dependent photoluminescence from WS_2 nanostructures. *Journal of Materials Science: Materials in Electronics*, 29(23):20064–20070, Dec 2018.

[64] Gianluca Fiori, Francesco Bonaccorso, Giuseppe Iannaccone, Tomás Palacios, Daniel Neumaier, Alan Seabaugh, Sanjay K. Banerjee, and Luigi Colombo. Electronics based on two-dimensional materials. *Nature Nanotechnology*, 9(10):768–779, Oct 2014.

[65] Jinhua Hong, Zhixin Hu, Matt Probert, Kun Li, Danhui Lv, Xinan Yang, Lin Gu, Nannan Mao, Qingliang Feng, Liming Xie, Jin Zhang, Dianzhong Wu, Zhiyong Zhang, Chuanhong Jin, Wei Ji, Xixiang Zhang, Jun Yuan, and Ze Zhang. Exploring atomic defects in molybdenum disulphide monolayers. *Nature Communications*, 6(1):6293, Feb 2015.

[66] Kristen Kaasbjerg, Kristian S. Thygesen, and Karsten W. Jacobsen. Phonon-limited mobility in *n*-type single-layer MoS_2 from first principles. *Physical Review B*, 85:115317, Mar 2012.

[67] Britton W. H. Baugher, Hugh O. H. Churchill, Yafang Yang, and Pablo Jarillo-Herrero. Intrinsic electronic transport properties of high-quality monolayer and bilayer MoS_2. *Nano Letters*, 13(9):4212–4216, Sep 2013.

[68] Saptarshi Das, Hong-Yan Chen, Ashish Verma Penumatcha, and Joerg Appenzeller. High performance multilayer MoS_2 transistors with scandium contacts. *Nano Letters*, 13(1):100–105, Jan 2013.

[69] A. S. Bhalla, R. Guo, and R. Roy. The perovskite structure – a review of its role in ceramic science and technology. *Material Research Innovations*, 4(1):3–26, Nov 2000.

[70] Pengchen Zhu and Jia Zhu. Low-dimensional metal halide perovskites and related optoelectronic applications. *InfoMat*, 2(2):341–378, 2020.

[71] Xuhai Liu, Dejian Yu, Xiufeng Song, and Haibo Zeng. Metal halide perovskites: Synthesis, ion migration, and application in field-effect transistors. *Small*, 14(36):1801460, 2018.

[72] Challa Vijaya Kumar and Ajith Pattammattel. Introduction to graphene, 2017.

[73] M. Topsakal, E. Aktürk, and S. Ciraci. First-principles study of two- and one-dimensional honeycomb structures of boron nitride. *Physical Review B*, 79:115442, Mar 2009.

[74] Amir Pakdel, Yoshio Bando, and Dmitri Golberg. Nano boron nitride flatland. *Chemical Society Reviews*, 43:934–959, 2014.

[75] Noa Marom, Jonathan Bernstein, Jonathan Garel, Alexandre Tkatchenko, Ernesto Joselevich, Leeor Kronik, and Oded Hod. Stacking and registry effects in layered materials: The case of hexagonal boron nitride. *Physical Review Letters*, 105:046801, July 2010.

[76] Kailiang Zhang, Yulin Feng, Fang Wang, Zhengchun Yang, and John Wang. Two dimensional hexagonal boron nitride (2D-hBN): synthesis, properties and applications. *Journal of Materials Chemistry C*, 5:11992–12022, 2017.

[77] C. Dean, A.F. Young, L. Wang, I. Meric, G.-H. Lee, K. Watanabe, T. Taniguchi, K. Shepard, P. Kim, and J. Hone. Graphene based heterostructures. *Solid State Communications*, 152(15):1275–1282, 2012. Exploring Graphene, Recent Research Advances.

[78] C. R. Dean, A. F. Young, I. Meric, C. Lee, L. Wang, S. Sorgenfrei, K. Watanabe, T. Taniguchi, P. Kim, K. L. Shepard, and J. Hone. Boron nitride substrates for high-quality graphene electronics. *Nature Nanotechnology*, 5(10):722–726, Oct 2010.

[79] A. V. Kretinin, Y. Cao, J. S. Tu, G. L. Yu, R. Jalil, K. S. Novoselov, S. J. Haigh, A. Gholinia, A. Mishchenko, M. Lozada, T. Georgiou, C. R. Woods, F. Withers, P. Blake, G. Eda, A. Wirsig, C. Hucho, K. Watanabe, T. Taniguchi, A. K. Geim, and R. V. Gorbachev. Electronic properties of graphene encapsulated with different two-dimensional atomic crystals. *Nano Letters*, 14(6):3270–3276, Jun 2014.

[80] Alexander S. Mayorov, Roman V. Gorbachev, Sergey V. Morozov, Liam Britnell, Rashid Jalil, Leonid A. Ponomarenko, Peter Blake, Kostya S. Novoselov, Kenji Watanabe, Takashi Taniguchi, and A. K. Geim. Micrometer-scale ballistic transport in encapsulated graphene at room temperature. *Nano Letters*, 11(6):2396–2399, Jun 2011.

[81] Rostislav A. Doganov, Steven P. Koenig, Yuting Yeo, Kenji Watanabe, Takashi Taniguchi, and Barbaros Özyilmaz. Transport properties of ultrathin black phosphorus on hexagonal boron nitride. *Applied Physics Letters*, 106(8):083505, 2015.

[82] R. F. Frindt. Single crystals of MoS_2 several molecular layers thick. *Journal of Applied Physics*, 37(4):1928–1929, 1966.

[83] Vardan Galstyan, Manohar P. Bhandari, Veronica Sberveglieri, Giorgio Sberveglieri, and Elisabetta Comini. Metal oxide nanostructures in food applications: Quality control and packaging. *Chemosensors*, 6(2), 2018.

[84] Van Luan Nguyen, David J. Perello, Seunghun Lee, Chang Tai Nai, Bong Gyu Shin, Joong-Gyu Kim, Ho Yeol Park, Hu Young Jeong, Jiong Zhao, Quoc An Vu, Sang Hyub Lee, Kian Ping Loh, Se-Young Jeong, and Young Hee Lee. Wafer-scale single-crystalline ab-stacked bilayer graphene. *Advanced Materials*, 28(37):8177–8183, 2016.

[85] Yonghun Kim, Ah Ra Kim, Guoqing Zhao, Sun Young Choi, Soo Cheol Kang, Sung Kwan Lim, Kang Eun Lee, Jucheol Park, Byoung Hun Lee, Myung Gwan Hahm, Dong-Ho Kim, Jungheum Yun, Kyu Hwan Lee, and Byungjin Cho. Wafer-scale integration of highly uniform and scalable MoS_2 transistors. *ACS Applied Materials & Interfaces*, 9(42):37146–37153, Oct 2017.

[86] Masihhur R. Laskar, Lu Ma, Santhakumar Kannappan, Pil Sung Park, Sriram Krishnamoorthy, Digbijoy N. Nath, Wu Lu, Yiying Wu, and Siddharth Rajan. Large area single crystal (0001) oriented MoS_2. *Applied Physics Letters*, 102(25):252108, 2013.

[87] Guohua Hu, Joohoon Kang, Leonard W.T. Ng, Xiaoxi Zhu, Richard C.T. Howe, Christopher G. Jones, Mark C. Hersam, and Tawfique Hasan. Functional inks and printing of two-dimensional materials, 2018.

[88] Y.F. Zhang, M.N. Gamo, C.Y. Xiao, and T. Ando. Liquid phase synthesis of carbon nanotubes. *Physica B: Condensed Matter*, 323(1):293–295, 2002. Proceedings of the Tsukuba Symposium on Carbon Nanotube in Commemoration of the 10th Anniversary of its Discovery.

[89] Domhnall O'Suilleabhain, Victor Vega-Mayoral, Adam G. Kelly, Andrew Harvey, and Jonathan N. Coleman. Percolation Effects in Electrolytically Gated WS_2 /Graphene Nano:Nano Composites. *ACS Applied Materials & Interfaces*, 11(8):8545–8555, feb 2019.

[90] F. Withers, H. Yang, L. Britnell, A. P. Rooney, E. Lewis, A. Felten, C. R. Woods, V. Sanchez Romaguera, T. Georgiou, A. Eckmann, Y. J. Kim, S. G. Yeates, S. J. Haigh, A. K. Geim, K. S. Novoselov, and C. Casiraghi. Heterostructures produced from nanosheet-based inks. *Nano Letters*, 14(7):3987–3992, Jul 2014.

[91] Claudia Backes, Keith R. Paton, Damien Hanlon, Shengjun Yuan, Mikhail I. Katsnelson, James Houston, Ronan J. Smith, David McCloskey, John F. Donegan, and Jonathan N. Coleman. Spectroscopic metrics allow in situ measurement of mean size and thickness of liquid-exfoliated few-layer graphene nanosheets. *Nanoscale*, 8(7):4311–4323, 2016.

[92] W Rüdorff. Graphite intercalation compounds. In *Advances in Inorganic Chemistry and Radiochemistry*, volume 1, pages 223–266. Elsevier, 1959.

[93] RB Somoano, V Hadek, and A Rembaum. Alkali metal intercalates of molybdenum disulfide. *The Journal of Chemical Physics*, 58(2):697–701, 1973.

[94] Valeria Nicolosi, Manish Chhowalla, Mercouri G. Kanatzidis, Michael S. Strano, and Jonathan N. Coleman. Liquid exfoliation of layered materials. *Science*, 340(6139), 2013.

[95] Kai Huang, Géraud Delport, Lucile Orcin-Chaix, Carlos Drummond, Jean-Sebastien Lauret, and Alain Penicaud. Single layer nano graphene platelets derived from graphite nanofibres. *Nanoscale*, 8:8810–8818, 2016.

[96] Francesco Bonaccorso, Antonio Lombardo, Tawfique Hasan, Zhipei Sun, Luigi Colombo, and Andrea C. Ferrari. Production and processing of graphene and 2D crystals. *Materials Today*, 15(12):564–589, 2012.

[97] Yao Li, Karel-Alexander N. Duerloo, Kerry Wauson, and Evan J. Reed. Structural semiconductor-to-semimetal phase transition in two-dimensional materials induced by electrostatic gating. *Nature Communications*, 7(1):10671, Feb 2016.

[98] M Kan, JY Wang, XW Li, SH Zhang, YW Li, Y Kawazoe, Q Sun, and P Jena. Structures and phase transition of a mos2 monolayer. *The Journal of Physical Chemistry C*, 118(3):1515–1522, 2014.

[99] Zhaoyang Lin, Yuanyue Liu, Udayabagya Halim, Mengning Ding, Yuanyue Liu, Yiliu Wang, Chuancheng Jia, Peng Chen, Xidong Duan, Chen Wang, Frank Song, Mufan Li, Chengzhang Wan, Yu Huang, and Xiangfeng Duan. Solution-processable 2D semiconductors for high-performance large-area electronics. *Nature*, 562(7726):254–258, oct 2018.

[100] Fan Yang, Kuaishe Wang, Ping Hu, Xiaoyu Wang, Tian Chang, Zhenyu Chen, Jie Deng, Pengfa Feng, and Alex A Volinsky. Detonation exfoliated mechanism of graphene-like mos2 prepared by the intercalation-detonation method and promising exfoliation for 2d materials. *Applied Surface Science*, 525:145867, 2020.

[101] Yenny Hernandez, Valeria Nicolosi, Mustafa Lotya, Fiona M. Blighe, Zhenyu Sun, Sukanta De, I. T. McGovern, Brendan Holland, Michele Byrne, Yurii K. Gun'Ko, John J. Boland, Peter Niraj, Georg Duesberg, Satheesh Krishnamurthy, Robbie Goodhue, John Hutchison, Vittorio Scardaci, Andrea C. Ferrari, and Jonathan N. Coleman. High-yield production of graphene by liquid-phase exfoliation of graphite. *Nature Nanotechnology*, 3(9):563–568, Sep 2008.

[102] Peter Blake, Paul D Brimicombe, Rahul R Nair, Tim J Booth, Da Jiang, Fred Schedin, Leonid A Ponomarenko, Sergey V Morozov, Helen F Gleeson, Ernie W Hill, et al. Graphene-based liquid crystal device. *Nano Letters*, 8(6):1704–1708, 2008.

[103] John B. Boland, Andrew Harvey, Ruiyuan Tian, Damien Hanlon, Victor Vega-Mayoral, Beata Szydlowska, Aideen Griffin, Tanja Stimpel-Lindner, Sonia Jaskaniec, Valeria Nicolosi, Georg Duesberg, and Jonathan N. Coleman. Liquid phase exfoliation of MoO_2 nanosheets for lithium ion battery applications. *Nanoscale Advances*, 1:1560–1570, 2019.

[104] Andrew Harvey, John B. Boland, Ian Godwin, Adam G. Kelly, Beata M. Szydłowska, Ghulam Murtaza, Andrew Thomas, David J. Lewis, Paul O'Brien, and Jonathan N. Coleman. Exploring the versatility of liquid phase exfoliation: producing 2D nanosheets from talcum powder, cat litter and beach sand. *2D Materials*, 4(2):025054, mar 2017.

[105] Samanta Witomska, Tim Leydecker, Artur Ciesielski, and Paolo Samorì. Production and patterning of liquid phase–exfoliated 2D sheets for applications in optoelectronics. *Advanced Functional Materials*, 29(22):1901126, 2019.

[106] Edward B. Flint and Kenneth S. Suslick. The temperature of cavitation. *Science*, 253(5026):1397–1399, 1991.

[107] Zheling Li, Robert J. Young, Claudia Backes, Wen Zhao, Xun Zhang, Alexander A. Zhukov, Evan Tillotson, Aidan P. Conlan, Feng Ding, Sarah J. Haigh, Kostya S. Novoselov, and Jonathan N. Coleman. Mechanisms of liquid-phase exfoliation for the production of graphene. *ACS Nano*, 14(9):10976–10985, Sep 2020.

[108] María Victoria Bracamonte, Gabriela Inés Lacconi, Silvia Elena Urreta, and Luis Eduardo Francisco Foa Torres. On the nature of defects in liquid-phase exfoliated graphene. *The Journal of Physical Chemistry C*, 118(28):15455–15459, Jul 2014.

[109] Theodosis Skaltsas, Xiaoxing Ke, Carla Bittencourt, and Nikos Tagmatarchis. Ultrasonication induces oxygenated species and defects onto exfoliated graphene. *The Journal of Physical Chemistry C*, 117(44):23272–23278, Nov 2013.

[110] Han Ma, Zhigang Shen, and Shuang Ben. Understanding the exfoliation and dispersion of MoS_2 nanosheets in pure water. *Journal of Colloid and Interface Science*, 517:204–212, 2018.

[111] Dmitry V. Kosynkin, Amanda L. Higginbotham, Alexander Sinitskii, Jay R. Lomeda, Ayrat Dimiev, B. Katherine Price, and James M. Tour. Longitudinal unzipping of carbon nanotubes to form graphene nanoribbons. *Nature*, 458(7240):872–876, Apr 2009.

[112] Claudia Backes, Davide Campi, Beata M. Szydlowska, Kevin Synnatschke, Ezgi Ojala, Farnia Rashvand, Andrew Harvey, Aideen Griffin, Zdenek Sofer, Nicola Marzari, Jonathan N. Coleman, and David D. O'Regan. Equipartition of energy defines the size–thickness relationship in liquid-exfoliated nanosheets. *ACS Nano*, 13(6):7050–7061, Jun 2019.

[113] Steffen Ott, Nadja Wolff, Farnia Rashvand, Vaishnavi J. Rao, Jana Zaumseil, and Claudia Backes. Impact of the MoS_2 starting material on the dispersion quality and quantity after liquid phase exfoliation. *Chemistry of Materials*, 31(20):8424–8431, Oct 2019.

[114] Jonathan N. Coleman, Mustafa Lotya, Arlene O'Neill, Shane D. Bergin, Paul J. King, Umar Khan, Karen Young, Alexandre Gaucher, Sukanta De, Ronan J. Smith, Igor V. Shvets, Sunil K. Arora, George Stanton, Hye-Young Kim, Kangho Lee, Gyu Tae Kim, Georg S. Duesberg, Toby Hallam, John J. Boland, Jing Jing Wang, John F. Donegan, Jaime C. Grunlan, Gregory Moriarty, Aleksey Shmeliov, Rebecca J. Nicholls, James M. Perkins, Eleanor M. Grieveson, Koenraad Theuwissen, David W. McComb, Peter D. Nellist, and Valeria Nicolosi. Two-dimensional nanosheets produced by liquid exfoliation of layered materials. *Science*, 331(6017):568–571, 2011.

[115] Jonathan N. Coleman. Liquid Exfoliation of Defect-Free Graphene. *Accounts of Chemical Research*, 46(1):14–22, jan 2013.

[116] A. C. Ferrari, J. C. Meyer, V. Scardaci, C. Casiraghi, M. Lazzeri, F. Mauri, S. Piscanec, D. Jiang, K. S. Novoselov, S. Roth, and A. K. Geim. Raman spectrum of graphene and graphene layers. *Physical Review Letters*, 97:187401, Oct 2006.

[117] Shane D. Bergin, Zhenyu Sun, David Rickard, Philip V. Streich, James P. Hamilton, and Jonathan N. Coleman. Multicomponent solubility parameters for single-walled carbon nanotube−solvent mixtures. *ACS Nano*, 3(8):2340–2350, Aug 2009.

[118] Shane D. Bergin, Valeria Nicolosi, Philip V. Streich, Silvia Giordani, Zhenyu Sun, Alan H. Windle, Peter Ryan, N. Peter P. Niraj, Zhi-Tao T. Wang, Leslie Carpenter, Werner J. Blau, John J. Boland, James P. Hamilton, and Jonathan N. Coleman. Towards solutions of single-walled carbon nanotubes in common solvents. *Advanced Materials*, 20(10):1876–1881, 2008.

[119] Jonathan N. Coleman. Liquid-phase exfoliation of nanotubes and graphene. *Advanced Functional Materials*, 19(23):3680–3695, 2009.

[120] J. Marguerite Hughes, Damian Aherne, and Jonathan N. Coleman. Generalizing solubility parameter theory to apply to one- and two-dimensional solutes and to incorporate dipolar interactions. *Journal of Applied Polymer Science*, 127(6):4483–4491, 2013.

[121] Michael Rubinstein. Polymer physics—the ugly duckling story: Will polymer physics ever become a part of "proper" physics? *Journal of Polymer Science Part B: Polymer Physics*, 48(24):2548–2551, 2010.

[122] F. H. MacDougall. Solubility of Non-electrolytes. by Joel H. Hildebrand. *The Journal of Physical Chemistry*, 40(5):700–700, May 1936.

[123] C. M. Hansen. Three dimensional solubility parameter and solvent diffusion coefficient. importance in surface coating formulation. *Doctoral Dissertation*, 1967.

[124] Damien Hanlon, Claudia Backes, Evie Doherty, Clotilde S Cucinotta, Nina C Berner, Conor Boland, Kangho Lee, Andrew Harvey, Peter Lynch, Zahra Gholamvand, et al. Liquid exfoliation of solvent-stabilized few-layer black phosphorus for applications beyond electronics. *Nature Communications*, 6(1):1–11, 2015.

[125] Haiyan Sun Alberto Ansaldo Vittorio Pellegrini Andrea Capasso, AE Del Rio Castillo and Francesco Bonaccorso. Ink-jet printing of graphene for flexible electronics: An environmentally-friendly approach. *Solid State Communications*, 224:53–63, 2015.

[126] Kai-Ge Zhou, Nan-Nan Mao, Hang-Xing Wang, Yong Peng, and Hao-Li Zhang. A mixed-solvent strategy for efficient exfoliation of inorganic graphene analogues. *Angewandte Chemie International Edition*, 50(46):10839–10842, 2011.

[127] Udayabagya Halim, Chu Ran Zheng, Yu Chen, Zhaoyang Lin, Shan Jiang, Rui Cheng, Yu Huang, and Xiangfeng Duan. A rational design of cosolvent exfoliation of layered materials by directly probing liquid–solid interaction. *Nature Communications*, 4(1):2213, Jul 2013.

[128] Arlene O'Neill, Umar Khan, Peter N. Nirmalraj, John Boland, and Jonathan N. Coleman. Graphene dispersion and exfoliation in low boiling point solvents. *The Journal of Physical Chemistry C*, 115(13):5422–5428, Apr 2011.

[129] Sean P. Ogilvie, Matthew J. Large, Giuseppe Fratta, Manuela Meloni, Ruben Canton-Vitoria, Nikos Tagmatarchis, Florian Massuyeau, Christopher P. Ewels, Alice A. K. King, and Alan B. Dalton. Considerations for spectroscopy of liquid-exfoliated 2D materials: emerging photoluminescence of N-methyl-2-pyrrolidone. *Scientific Reports*, 7(1):16706, Dec 2017.

[130] Hin Chun Yau, Mustafa K. Bayazit, Joachim H. G. Steinke, and Milo S. P. Shaffer. Sonochemical degradation of n-methylpyrrolidone and its influence on single walled carbon nanotube dispersion. *Chemical Communications*, 51:16621–16624, 2015.

[131] Dimitrios Tasis, Kostas Papagelis, Panagiotis Spiliopoulos, and Costas Galiotis. Efficient exfoliation of graphene sheets in binary solvents. *Materials Letters*, 94:47–50, 2013.

[132] Sebastian Barwich, Umar Khan, and Jonathan N. Coleman. A technique to pretreat graphite which allows the rapid dispersion of defect-free graphene in solvents at high concentration. *The Journal of Physical Chemistry C*, 117(37):19212–19218, Sep 2013.

[133] Ibrahim Sadek Khattab, Farzana Bandarkar, Mohammad Amin Abolghassemi Fakhree, and Abolghasem Jouyban. Density, viscosity, and surface tension of water+ethanol mixtures from 293 to 323k. *Korean Journal of Chemical Engineering*, 29(6):812–817, Jun 2012.

[134] Francesco Bonaccorso, Antonino Bartolotta, Jonathan N. Coleman, and Claudia Backes. 2D-Crystal-Based Functional Inks. *Advanced Materials*, 28(29):6136–6166, aug 2016.

[135] Aideen Griffin, Katharina Nisi, Joshua Pepper, Andrew Harvey, Beata M. Szydłowska, Jonathan N. Coleman, and Claudia Backes. Effect of surfactant choice and concentration on the dimensions and yield of liquid-phase-exfoliated nanosheets. *Chemistry of Materials*, 32(7):2852–2862, Apr 2020.

[136] W. Wenseleers, I.I. Vlasov, E. Goovaerts, E.D. Obraztsova, A.S. Lobach, and A. Bouwen. Efficient isolation and solubilization of pristine single-walled nanotubes in bile salt micelles. *Advanced Functional Materials*, 14(11):1105–1112, 2004.

[137] F. Bonaccorso, T. Hasan, P. H. Tan, C. Sciascia, G. Privitera, G. Di Marco, P. G. Gucciardi, and A. C. Ferrari. Density gradient ultracentrifugation of nanotubes: Interplay of bundling and surfactants encapsulation. *The Journal of Physical Chemistry C*, 114(41):17267–17285, Oct 2010.

[138] Shangchao Lin and Daniel Blankschtein. Role of the bile salt surfactant sodium cholate in enhancing the aqueous dispersion stability of single-walled carbon nanotubes: A molecular dynamics simulation study. *The Journal of Physical Chemistry B*, 114(47):15616–15625, Dec 2010.

[139] M.J. Rosen and J.T. Kunjappu. *Surfactants and interfacial phenomena*. John Wiley & Sons, 2012.

[140] B Derjaguin and L Landau. Theory of the stability of strongly charged lyophobic sols and of the adhesion of strongly charged particles in solutions of electrolytes. *Progress in Surface Science*, 43(1):30–59, 1993.

[141] E. J. W. Verwey. Theory of the stability of lyophobic colloids. *The Journal of Physical and Colloid Chemistry*, 51(3):631–636, Mar 1947.

[142] Hugo C Hamaker. The london—van der waals attraction between spherical particles. *Physica*, 4(10):1058–1072, 1937.

[143] Mats Larsson, Adrian Hill, and John Duffy. Suspension stability; why particle size, zeta potential and rheology are important. *Annual Transactions of the Nordic Rheology Society*, 20(2012):6, 2012.

[144] Claudia Backes, Ronan J. Smith, Niall McEvoy, Nina C. Berner, David McCloskey, Hannah C. Nerl, Arlene O'Neill, Paul J. King, Tom Higgins, Damien Hanlon, Nils Scheuschner, Janina Maultzsch, Lothar Houben, Georg S. Duesberg, John F. Donegan, Valeria Nicolosi, and Jonathan N. Coleman. Edge and confinement effects allow in situ measurement of size and thickness of liquid-exfoliated nanosheets. *Nature Communications*, 5(1):4576, Aug 2014.

[145] H Zecha. Stabilization of colloidal dispersions by polymer adsorption. von tatsuo sato and richard ruch. surfactant science series. new york/basel: Marcel dekker inc. 1980. 155 s., 46 abb., 302 lit. sfr. 58.—. *Acta Polymerica*, 32(9):582–582, 1981.

[146] Victor Vega-Mayoral, Claudia Backes, Damien Hanlon, Umar Khan, Zahra Gholamvand, Maria O'Brien, Georg S. Duesberg, Christoph Gadermaier, and Jonathan N. Coleman. Photoluminescence from liquid-exfoliated WS_2 monomers in poly(vinyl alcohol) polymer composites. *Advanced Functional Materials*, 26(7):1028–1039, 2016.

[147] Peter May, Umar Khan, Arlene O'Neill, and Jonathan N Coleman. Approaching the theoretical limit for reinforcing polymers with graphene. *Journal of Materials Chemistry*, 22(4):1278–1282, 2012.

[148] Thomas F Jaramillo, Kristina P Jørgensen, Jacob Bonde, Jane H Nielsen, Sebastian Horch, and Ib Chorkendorff. Identification of active edge sites for electrochemical H_2 evolution from MoS_2 nanocatalysts. *Science*, 317(5834):100–102, 2007.

[149] Alexander A Green and Mark C Hersam. Ultracentrifugation of single-walled nanotubes. *Materials Today*, 10(12):59–60, 2007.

[150] Xiao Zhang, Zhuangchai Lai, Chaoliang Tan, and Hua Zhang. Solution-processed two-dimensional MoS_2 nanosheets: preparation, hybridization, and applications. *Angewandte Chemie International Edition*, 55(31):8816–8838, 2016.

[151] Theodor Svedberg, Kai Oluf Pedersen, et al. The ultracentrifuge. *The Ultracentrifuge.*, 1940.

[152] Claudia Backes, Beata M. Szydłowska, Andrew Harvey, Shengjun Yuan, Victor Vega-Mayoral, Ben R. Davies, Pei-liang Zhao, Damien Hanlon, Elton J. G. Santos, Mikhail I. Katsnelson, Werner J. Blau, Christoph Gadermaier, and Jonathan N. Coleman. Production of Highly Monolayer Enriched Dispersions of Liquid-Exfoliated Nanosheets by Liquid Cascade Centrifugation. *ACS Nano*, 10(1):1589–1601, jan 2016.

[153] Yi-Zhou Zhang, Yang Wang, Tao Cheng, Lan-Qian Yao, Xiangchun Li, Wen-Yong Lai, and Wei Huang. Printed supercapacitors: materials, printing and applications. *Chemical Society Reviews*, 48:3229–3264, 2019.

[154] Daryl McManus, Sandra Vranic, Freddie Withers, Veronica Sanchez-Romaguera, Massimo Macucci, Huafeng Yang, Roberto Sorrentino, Khaled Parvez, Seok-Kyun Son, Giuseppe Iannaccone, Kostas Kostarelos, Gianluca Fiori, and Cinzia Casiraghi. Water-based and biocompatible 2D crystal inks for all-inkjet-printed heterostructures. *Nature Nanotechnology*, 12(4):343–350, apr 2017.

[155] Daryl McManus, Andrea Dal Santo, PB Selvasundaram, Ralph Krupke, A LiBassi, and Cinzia Casiraghi. Photocurrent study of all-printed photodetectors on paper made of different transition metal dichalcogenide nanosheets. *Flexible and Printed Electronics*, 3(3):034005, 2018.

[156] Global Forecast Report. Printed electronics market. Accessed on 1/9/2021.

[157] Raghu Das Dr Matthew Dyson and Dr Richard Collins. Materials for printed/flexible electronics 2021-2031: Technologies, applications, market forecasts. Accessed on 4/9/21.

[158] Yotsarayuth Seekaew, Shongpun Lokavee, Ditsayut Phokharatkul, Anurat Wisitsoraat, Teerakiat Kerdcharoen, and Chatchawal Wongchoosuk. Low-cost and flexible printed graphene–pedot:pss gas sensor for ammonia detection. *Organic Electronics*, 15(11):2971–2981, 2014.

[159] Xinlei Ma, Zhuang Xie, Zhanhai Yang, Guangquan Zeng, Mianqi Xue, and Xueji Zhang. Inkjet printed 2D SnS_2 nanosheets for ammonia gas sensor. *Materials Research Express*, 6(1):015025, 2018.

[160] David Dodoo-Arhin, Richard C.T. Howe, Guohua Hu, Yinghe Zhang, Pritesh Hiralal, Abdulhakeem Bello, Gehan Amaratunga, and Tawfique Hasan. Inkjet-printed graphene electrodes for dye-sensitized solar cells. *Carbon*, 105:33–41, Aug 2016.

[161] Ravindra Ketan Mehta and Anupama Bhat Kaul. Black phosphorus-molybdenum disulfide hetero-junctions formed with ink-jet printing for potential solar cell applications with indium-tin-oxide. *Crystals*, 11(5), 2021.

[162] Jiantong Li, Fei Ye, Sam Vaziri, Mamoun Muhammed, Max C. Lemme, and Mikael Östling. Efficient inkjet printing of graphene. *Advanced Materials*, 25(29):3985–3992, 2013.

[163] Felice Torrisi, Tawfique Hasan, Weiping Wu, Zhipei Sun, Antonio Lombardo, Tero S. Kulmala, Gen-Wen Hsieh, Sungjune Jung, Francesco Bonaccorso, Philip J Paul, Daping Chu, and Andrea C Ferrari. Inkjet-Printed Graphene Electronics. *ACS Nano*, 6(4):2992–3006, apr 2012.

[164] Tian Carey, Stefania Cacovich, Giorgio Divitini, Jiesheng Ren, Aida Mansouri, Jong M. Kim, Chaoxia Wang, Caterina Ducati, Roman Sordan, and Felice Torrisi. Fully inkjet-printed two-dimensional material field-effect heterojunctions for wearable and textile electronics. *Nature Communications*, 8(1):1202, dec 2017.

[165] Alexander Y Malkin and Avraam I Isayev. *Rheology: concepts, methods, and applications*. Elsevier, 2017.

[166] Jungho Park and Jooho Moon. Control of colloidal particle deposit patterns within picoliter droplets ejected by ink-jet printing. *Langmuir*, 22(8):3506–3513, 2006.

[167] J Baker, D Deganello, DT Gethin, and TM Watson. Flexographic printing of graphene nanoplatelet ink to replace platinum as counter electrode catalyst in flexible dye sensitised solar cell. *Materials Research Innovations*, 18(2):86–90, 2014.

[168] Ulrich Bröckel, Willi Meier, and Gerhard Wagner. *Product design and engineering: formulation of gels and pastes*. John Wiley & Sons, 2013.

[169] Nandy Putra, Wilfried Roetzel, and Sarit K Das. Natural convection of nano-fluids. *Heat and Mass Transfer*, 39(8):775–784, 2003.

[170] S Mueller, EW Llewellin, and HM Mader. The rheology of suspensions of solid particles. *Proceedings of the Royal Society A: Mathematical, Physical and Engineering Sciences*, 466(2116):1201–1228, 2010.

[171] Xiaoyan Zhang, Anthony C Coleman, Nathalie Katsonis, Wesley R Browne, Bart J Van Wees, and Ben L Feringa. Dispersion of graphene in ethanol using a simple solvent exchange method. *Chemical Communications*, 46(40):7539–7541, 2010.

[172] Kim Tremel and Sabine Ludwigs. Morphology of P_3HT in thin films in relation to optical and electrical properties. *P_3HT revisited–from molecular scale to solar cell devices*, pages 39–82, 2014.

[173] Andrew Carlson, Audrey M Bowen, Yonggang Huang, Ralph G Nuzzo, and John A Rogers. Transfer printing techniques for materials assembly and micro/nanodevice fabrication. *Advanced Materials*, 24(39):5284–5318, 2012.

[174] S Logothetidis. Polymeric substrates and encapsulation for flexible electronics: bonding structure, surface modification and functional nanolayer growth. *Reviews on Advanced Materials Science*, 10(5):387–397, 2005.

[175] Stergios Logothetidis. Flexible organic electronic devices: Materials, process and applications. *Materials Science and Engineering: B*, 152(1-3):96–104, 2008.

[176] Dracula Technologies. Thin film processing methods. Accessed on 24/9/21.

[177] Stefano Cinti and Fabiana Arduini. Graphene-based screen-printed electrochemical (bio) sensors and their applications: Efforts and criticisms. *Biosensors and Bioelectronics*, 89:107–122, 2017.

[178] Prerona Gogoi, Arun Chattopadhyay, and Partho Sarathi Gooh Pattader. Toward controlling evaporative deposition: Effects of substrate, solvent, and solute. *The Journal of Physical Chemistry B*, 124(50):11530–11539, 2020.

[179] Robert D Deegan, Olgica Bakajin, Todd F Dupont, Greb Huber, Sidney R Nagel, and Thomas A Witten. Capillary flow as the cause of ring stains from dried liquid drops. *Nature*, 389(6653):827–829, 1997.

[180] Hua Hu and Ronald G Larson. Marangoni effect reverses coffee-ring depositions. *The Journal of Physical Chemistry B*, 110(14):7090–7094, 2006.

[181] M Mikolajek, A Friedrich, W Bauer, and JR Binder. Requirements to ceramic suspensions for inkjet printing. In *Ceram. Forum Int*, volume 92, page E25, 2015.

[182] Ian M Hutchings and Graham D Martin. *Inkjet technology for digital fabrication*. John Wiley & Sons, 2012.

[183] DS Eom, J Chang, Y-W Song, JA Lim, JT Han, H Kim, and K Cho. Coffee-ring structure from dried graphene derivative solutions: a facile one-step fabrication route for all graphene-based transistors. *The Journal of Physical Chemistry C*, 118(46):27081–27090, 2014.

[184] Pei He and Brian Derby. Controlling coffee ring formation during drying of inkjet printed 2D inks. *Advanced Materials Interfaces*, 4(22):1700944, 2017.

[185] Karam Nashwan Al-Milaji and Hong Zhao. Probing the colloidal particle dynamics in drying sessile droplets. *Langmuir*, 35(6):2209–2220, 2019.

[186] Shaobo Xie, Oana M Istrate, Peter May, Sebastian Barwich, Alan P Bell, Umar Khan, and Jonathan N Coleman. Boron nitride nanosheets as barrier enhancing fillers in melt processed composites. *Nanoscale*, 7(10):4443–4450, 2015.

[187] Berend-Jan de Gans and Ulrich S Schubert. Inkjet printing of well-defined polymer dots and arrays. *Langmuir*, 20(18):7789–7793, 2004.

[188] Suhao Wang, Michael Kappl, Ingo Liebewirth, Maren Müller, Katrin Kirchhoff, Wojciech Pisula, and Klaus Müllen. Organic field-effect transistors based on highly ordered single polymer fibers. *Advanced Materials*, 24(3):417–420, 2012.

[189] Peter J Diemer, Christopher R Lyle, Yaochuan Mei, Christopher Sutton, Marcia M Payne, John E Anthony, Veaceslav Coropceanu, Jean-Luc Brédas, and Oana D Jurchescu. Vibration-assisted crystallization improves organic/dielectric interface in organic thin-film transistors. *Advanced Materials*, 25(48):6956–6962, 2013.

[190] Javeed Mahmood, Eun Kwang Lee, Minbok Jung, Dongbin Shin, In-Yup Jeon, Sun-Min Jung, Hyun-Jung Choi, Jeong-Min Seo, Seo-Yoon Bae, So-Dam Sohn, et al. Nitrogenated holey two-dimensional structures. *Nature Communications*, 6(1):1–7, 2015.

[191] Jusef Hassoun, Francesco Bonaccorso, Marco Agostini, Marco Angelucci, Maria Grazia Betti, Roberto Cingolani, Mauro Gemmi, Carlo Mariani, Stefania Panero, Vittorio Pellegrini, et al. An advanced lithium-ion battery based on a graphene anode and a lithium iron phosphate cathode. *Nano Letters*, 14(8):4901–4906, 2014.

[192] K Norrman, A Ghanbari-Siahkali, and NB Larsen. 6 studies of spin-coated polymer films. *Annual Reports Section C (Physical Chemistry)*, 101:174–201, 2005.

[193] David Levy and Marcos Zayat. *The Sol-Gel Handbook, 3 Volume Set: Synthesis, Characterization, and Applications*, volume 2. John Wiley & Sons, 2015.

[194] Zhimin Zhu, Joyce Lowes, John Berron, Brian Smith, and Dan Sullivan. Spin-coating defect theory and experiments. *ECS Transactions*, 60(1):293, 2014.

[195] Chih-Ta Wang and Shi-Chern Yen. Theoretical analysis of film uniformity in spinning processes. *Chemical Engineering Science*, 50(6):989–999, 1995.

[196] Edward D Cohen and Edgar B Gutoff. *Modern coating and drying technology.* University of Texas Press, 1992.

[197] DFS Petri. Characterization of spin-coated polymer films. *Journal of the Brazilian Chemical Society*, 13(5):695–699, 2002.

[198] Niranjan Sahu, B Parija, and S Panigrahi. Fundamental understanding and modeling of spin coating process: A review. *Indian Journal of Physics*, 83(4):493–502, 2009.

[199] Sheng Yang, Ke Zhang, Antonio Gaetano Ricciardulli, Panpan Zhang, Zhongquan Liao, Martin R Lohe, Ehrenfried Zschech, Paul WM Blom, Wojciech Pisula, Klaus Müllen, et al. A delamination strategy for thinly layered defect-free high-mobility black phosphorus flakes. *Angewandte Chemie*, 130(17):4767–4771, 2018.

[200] Yifan Zheng, Shuguang Li, Wei Shi, and Junsheng Yu. Spray-coated nanoscale conductive patterns based on in situ sintered silver nanoparticle inks. *Nanoscale Research Letters*, 9(1):145, Mar 2014.

[201] Rose A Ryntz and Philip V Yaneff. *Coatings of polymers and plastics*, volume 21. CRC Press, 2003.

[202] Núria Ferrer-Anglada, Martti Kaempgen, Viera Skákalová, Ursula Dettlaf-Weglikowska, and Siegmar Roth. Synthesis and characterization of carbon nanotube-conducting polymer thin films. *Diamond and Related Materials*, 13(2):256–260, 2004.

[203] Oleg V Salata. Tools of nanotechnology: Electrospray. *Current Nanoscience*, 1(1):25–33, 2005.

[204] Claudio Girotto, Barry P Rand, Jan Genoe, and Paul Heremans. Exploring spray coating as a deposition technique for the fabrication of solution-processed solar cells. *Solar Energy Materials and Solar Cells*, 93(4):454–458, 2009.

[205] K Xerxes Steirer, Matthew O Reese, Benjamin L Rupert, Nikos Kopidakis, Dana C Olson, Reuben T Collins, and David S Ginley. Ultrasonic spray deposition for production of organic solar cells. *Solar Energy Materials and Solar Cells*, 93(4):447–453, 2009.

[206] Vittorio Scardaci, Richard Coull, Philip E Lyons, David Rickard, and Jonathan N Coleman. Spray deposition of highly transparent, low-resistance networks of silver nanowires over large areas. *Small*, 7(18):2621–2628, 2011.

[207] H Shi and C Kleinstreuer. Simulation and analysis of high-speed droplet spray dynamics, 2007.

[208] Xiaoying Shen, Chih-Ming Ho, and Tak-Sing Wong. Minimal size of coffee ring structure. *The Journal of Physical Chemistry B*, 114(16):5269–5274, 2010.

[209] Gobinath Velu Kaliyannan, Senthil Velmurugan Palanisamy, Manivasakan Palanisamy, Moganapriya Chinnasamy, Sankaranarayanan Somasundaram, Nithyavathy Nagarajan, and Rajasekar Rathanasamy. Utilization of 2D gahnite nanosheets as highly conductive, transparent and light trapping front contact for silicon solar cells. *Applied Nanoscience*, 9(7):1427–1437, 2019.

[210] Mainak Majumder, Clint Rendall, Michelle Li, Natnael Behabtu, J Alexander Eukel, Robert H Hauge, Howard K Schmidt, and Matteo Pasquali. Insights into the physics of spray coating of swnt films. *Chemical Engineering Science*, 65(6):2000–2008, 2010.

[211] Brian Derby. Inkjet printing of functional and structural materials: Fluid property requirements, feature stability, and resolution. *Annual Review of Materials Research*, 40(1):395–414, 2010.

[212] Alan Faulkner and Wenmiao Shu. Biological cell printing technologies. *Nanotechnology Perceptions*, 8, 2012.

[213] Adam G. Kelly, Conor Murphy, Victor Vega-Mayoral, Andrew Harvey, Amir Sajad Esmaeily, Toby Hallam, David McCloskey, and Jonathan N. Coleman. Tuneable photoconductivity and mobility enhancement in printed MoS 2 /graphene composites. *2D Materials*, 4(4):041006, sep 2017.

[214] Hsien-Hsueh Lee, Kan-Sen Chou, and Kuo-Cheng Huang. Inkjet printing of nanosized silver colloids. *Nanotechnology*, 16(10):2436–2441, 2005.

[215] Brian Derby and Nuno Reis. Inkjet printing of highly loaded particulate suspensions. *MRS Bulletin*, 28(11):815–818, Nov 2003.

[216] Daehwan Jang, Dongjo Kim, and Jooho Moon. Influence of fluid physical properties on ink-jet printability. *Langmuir*, 25(5):2629–2635, Mar 2009.

[217] Isopropyl alcohol solvent properties. Accessed on 30/9/2021.

[218] Pyungho Shin, Jaeyong Sung, and Myeong Ho Lee. Control of droplet formation for low viscosity fluid by double waveforms applied to a piezoelectric inkjet nozzle. *Microelectronics Reliability*, 51(4):797–804, 2011.

[219] Jiazhen Sun, Minxuan Kuang, and Yanlin Song. Control and application of "coffee ring" effect in inkjet printing. *Progress in Chemistry*, 27(8):979, 2015.

[220] Congbiao Jiang, Zhiming Zhong, Baiquan Liu, Zhiwei He, Jianhua Zou, Lei Wang, Jian Wang, JunBiao Peng, and Yong Cao. Coffee-ring-free quantum dot thin film using inkjet printing from a mixed-solvent system on modified zno transport layer for light-emitting devices. *ACS Applied Materials & Interfaces*, 8(39):26162–26168, 2016.

[221] Mikio Tamura and Michio Kurata. On the viscosity of binary mixture of liquids. *Bulletin of the Chemical Society of Japan*, 25(1):32–38, 1952.

[222] Matthew J Large, Sean P Ogilvie, Aline Amorim Graf, Peter J Lynch, Marcus A O'Mara, Thomas Waters, Izabela Jurewicz, Jonathan P Salvage, and Alan B Dalton. Large-scale surfactant exfoliation of graphene and conductivity-optimized graphite enabling wireless connectivity. *Advanced Materials Technologies*, 5(7):2000284, 2020.

[223] Ethan B Secor, Manuel H Dos Santos, Shay G Wallace, Nathan P Bradshaw, and Mark C Hersam. Tailoring the porosity and microstructure of printed graphene electrodes via polymer phase inversion. *The Journal of Physical Chemistry C*, 122(25):13745–13750, 2018.

[224] Manal MYA Alsaif, Adam F Chrimes, Torben Daeneke, Sivacarendran Balendhran, Darin O Bellisario, Youngwoo Son, Matthew R Field, Wei Zhang, Hussein Nili, Emily P Nguyen, et al. High-performance field effect transistors using electronic inks of 2D molybdenum oxide nanoflakes. *Advanced Functional Materials*, 26(1):91–100, 2016.

[225] Sebastian Barwich, João Medeiros de Araújo, Aran Rafferty, Claudia Gomes da Rocha, Mauro S. Ferreira, and Jonathan N. Coleman. On the relationship between morphology and conductivity in nanosheet networks. *Carbon*, 171:306–319, Jan 2021.

[226] Adam G Kelly, Domhnall O'Suilleabhain, Cian Gabbett, and Jonathan N Coleman. The electrical conductivity of solution-processed nanosheet networks. *Nature Reviews Materials*, pages 1–18, 2021.

[227] Matthew P Garrett, Ilia N Ivanov, Rosario A Gerhardt, Alex A Puretzky, and David B Geohegan. Separation of junction and bundle resistance in single wall carbon nanotube percolation networks by impedance spectroscopy. *Applied Physics Letters*, 97(16):163105, 2010.

[228] Yuki Kuwahara, Fumiyuki Nihey, Shigekazu Ohmori, and Takeshi Saito. Length dependent performance of single-wall carbon nanotube thin film transistors. *Carbon*, 91:370–377, 2015.

[229] GE Moore. Electronics 38, 114 (1965).

[230] Jim Handy. How many transistors have ever shipped?, 2014. Accessed on 30/9/2021.

[231] Hassan Mujtaba. Amd 2nd gen epyc rome processors feature a gargantuan 39.54 billion transistors. Accessed on 1/10/21.

[232] Joel Hruska. Cerebras systems unveils 1.2 trillion transistor wafer-scale processor for ai. Accessed on 30/9/21.

[233] Cyril Buttay. Lateral mosfet diagram. CC BY-SA 3.0 <http://creativecommons.org/licenses/by-sa/3.0/>, via Wikimedia Commons.

[234] Simon M Sze, Yiming Li, and Kwok K Ng. *Physics of semiconductor devices*. John wiley & sons, 2021.

[235] Zahra Gholamvand, David McAteer, Andrew Harvey, Claudia Backes, and Jonathan N. Coleman. Electrochemical Applications of Two-Dimensional Nanosheets: The Effect of Nanosheet Length and Thickness. *Chemistry of Materials*, 28(8):2641–2651, apr 2016.

[236] Maxim V. Fedorov and Alexei A. Kornyshev. Towards understanding the structure and capacitance of electrical double layer in ionic liquids. *Electrochimica Acta*, 53(23):6835–6840, oct 2008.

[237] Se Hyun Kim, Kihyon Hong, Wei Xie, Keun Hyung Lee, Sipei Zhang, Timothy P. Lodge, and C. Daniel Frisbie. Electrolyte-gated transistors for organic and printed electronics, 2013.

[238] Jonathan Rivnay, Sahika Inal, Alberto Salleo, Róisín M. Owens, Magnus Berggren, and George G. Malliaras. Organic electrochemical transistors. *Nature Reviews Materials*, 3(2):17086, feb 2018.

[239] Takuya Fujimoto and Kunio Awaga. Electric-double-layer field-effect transistors with ionic liquids. *Physical Chemistry Chemical Physics*, 15(23):8983, 2013.

[240] Eri Uesugi, Hidenori Goto, Ritsuko Eguchi, Akihiko Fujiwara, and Yoshihiro Kubozono. Electric double-layer capacitance between an ionic liquid and few-layer graphene. *Scientific Reports*, 3(1):1595, dec 2013.

[241] S.A. Gajar and M.W. Geis. An ionic liquid-channel field-effect transistor. *IEEE Transactions on Electron Devices*, 39(11):2649–2650, 1992.

[242] M. A. Gebbie, M. Valtiner, X. Banquy, E. T. Fox, W. A. Henderson, and J. N. Israelachvili. Ionic liquids behave as dilute electrolyte solutions. *Proceedings of the National Academy of Sciences*, 110(24):9674–9679, jun 2013.

[243] Daniel A Bernards and George G Malliaras. Steady-state and transient behavior of organic electrochemical transistors. *Advanced Functional Materials*, 17(17):3538–3544, 2007.

[244] Woong Kim, Ali Javey, Ophir Vermesh, Qian Wang, Yiming Li, and Hongjie Dai. Hysteresis caused by water molecules in carbon nanotube field-effect transistors. *Nano Letters*, 2003.

[245] Sung Hun Jin, Ahmad E. Islam, Tae-il Kim, Ji-hun Kim, Muhammad A. Alam, and John A. Rogers. Sources of Hysteresis in Carbon Nanotube Field-Effect Transistors and Their Elimination Via Methylsiloxane Encapsulants and Optimized Growth Procedures. *Advanced Functional Materials*, 22(11):2276–2284, jun 2012.

[246] Uwe Schröder, Jay D Wadhawan, Richard G Compton, Frank Marken, Paulo AZ Suarez, Crestina S Consorti, Roberto F de Souza, and Jaïrton Dupont. Water-induced accelerated ion diffusion: voltammetric studies in 1-methyl-3-[2, 6-(s)-dimethylocten-2-yl] imidazolium tetrafluoroborate, 1-butyl-3-methylimidazolium tetrafluoroborate and hexafluorophosphate ionic liquids. *New Journal of Chemistry*, 24(12):1009–1015, 2000.

[247] Hiroyuki Ohno. *Electrochemical aspects of ionic liquids*. John Wiley & Sons, 2005.

[248] Maan Hayyan, Farouq S. Mjalli, Mohd Ali Hashim, Inas M. AlNashef, and Tan Xue Mei. Investigating the electrochemical windows of ionic liquids. *Journal of Industrial and Engineering Chemistry*, 2013.

[249] Emma I Rogers, Biljana Sljukic, Christopher Hardacre, and Richard G Compton. Electrochemistry in room-temperature ionic liquids: potential windows at mercury electrodes. *Journal of Chemical & Engineering Data*, 54(7):2049–2053, 2009.

[250] Aoife M. O'Mahony, Debbie S. Silvester, Leigh Aldous, Christopher Hardacre, and Richard G. Compton. Effect of Water on the Electrochemical Window and Potential Limits of Room-Temperature Ionic Liquids. *Journal of Chemical & Engineering Data*, 53(12):2884–2891, dec 2008.

[251] Jing Li, Jie Tang, Jinshi Yuan, Kun Zhang, Qingguo Shao, Yige Sun, and Lu-Chang Qin. Interactions between Graphene and Ionic Liquid Electrolyte in Supercapacitors. *Electrochimica Acta*, 197:84–91, apr 2016.

[252] Dion Khodagholy, Jonathan Rivnay, Michele Sessolo, Moshe Gurfinkel, Pierre Leleux, Leslie H Jimison, Eleni Stavrinidou, Thierry Herve, Sébastien Sanaur, Róisín M Owens, et al. High transconductance organic electrochemical transistors. *Nature Communications*, 4(1):1–6, 2013.

[253] Shigehiko Sasa, Masashi Ozaki, Kazuto Koike, Mitsuaki Yano, and Masataka Inoue. High-performance ZnO / znmgo field-effect transistors using a hetero-metal-insulator-semiconductor structure. *Applied Physics Letters*, 89(5):053502, 2006.

[254] A Tsumura, H Koezuka, and TJAPL Ando. Macromolecular electronic device: Field-effect transistor with a polythiophene thin film. *Applied Physics Letters*, 49(18):1210–1212, 1986.

[255] Yogesh Yadav, Sajal Kumar Ghosh, and Samarendra Pratap Singh. High-performance organic field-effect transistors gated by imidazolium-based ionic liquids. *ACS Applied Electronic Materials*, 3(3):1496–1504, 2021.

[256] Huihuang Yang, Guocheng Zhang, Jie Zhu, Weixin He, Shuqiong Lan, Lei Liao, Huipeng Chen, and Tailiang Guo. Improving charge mobility of polymer transistors by judicious choice of the molecular weight of insulating polymer additive. *The Journal of Physical Chemistry C*, 120(31):17282–17289, 2016.

[257] Brijesh Kumar, Brajesh Kumar Kaushik, and Yuvraj Singh Negi. Organic thin film transistors: Structures, models, materials, fabrication, and applications: A review. *Polymer Reviews*, 54(1):33–111, 2014.

[258] Jongwan Choi, Heeseok Song, Nakjoong Kim, and Felix Sunjoo Kim. Development of *n*-type polymer semiconductors for organic field-effect transistors. *Semiconductor Science and Technology*, 30(6):064002, 2015.

[259] Hagen Klauk. Organic thin-film transistors. *Chemical Society Reviews*, 39(7):2643–2666, 2010.

[260] John E Northrup and Michael L Chabinyc. Gap states in organic semiconductors: Hydrogen-and oxygen-induced states in pentacene. *Physical Review B*, 68(4):041202, 2003.

[261] Phaedon Avouris, Marcus Freitag, and Vasili Perebeinos. Carbon-nanotube photonics and optoelectronics. *Nature Photonics*, 2(6):341–350, Jun 2008.

[262] Aaron D Franklin. Nanomaterials in transistors: From high-performance to thin-film applications. *Science*, 349(6249), 2015.

[263] Francesca Scuratti, Jorge Mario Salazar-Rios, Alessandro Luzio, Sebastian Kowalski, Sybille Allard, Stefan Jung, Ullrich Scherf, Maria Antonietta Loi, and Mario Caironi. Charge transport in high-mobility field-effect transistors based on inkjet printed random networks of polymer wrapped single-walled carbon nanotubes. *Advanced Functional Materials*, 31(5):2006895, 2021.

[264] Saunab Ghosh, Sergei M Bachilo, and R Bruce Weisman. Advanced sorting of single-walled carbon nanotubes by nonlinear density-gradient ultracentrifugation. *Nature Nanotechnology*, 5(6):443–450, 2010.

[265] C Kocabas, N Pimparkar, O Yesilyurt, SJ Kang, Muhammad A Alam, and JA Rogers. Experimental and theoretical studies of transport through large scale, partially aligned arrays of single-walled carbon nanotubes in thin film type transistors. *Nano Letters*, 7(5):1195–1202, 2007.

[266] Ming Zheng. Sorting carbon nanotubes. *Single-Walled Carbon Nanotubes*, pages 129–164, 2019.

[267] Chenliang Li, Jing Guo, Chaoying Wang, Decai Ma, and Baolai Wang. Design of mxene contacts for high-performance WS_2 transistors. *Applied Surface Science*, 527:146701, 2020.

[268] Alessia Di Vito, Alessandro Pecchia, Matthias Auf der Maur, and Aldo Di Carlo. Nonlinear work function tuning of lead-halide perovskites by mxenes with mixed terminations. *Advanced Functional Materials*, 30(47):1909028, 2020.

[269] Yi-Zhou Zhang, Yang Wang, Qiu Jiang, Jehad K El-Demellawi, Hyunho Kim, and Husam N Alshareef. Mxene printing and patterned coating for device applications. *Advanced Materials*, 32(21):1908486, 2020.

[270] Bouchaib Zazoum, Abdel Bachri, and Jamal Nayfeh. Functional 2D mxene inks for wearable electronics. *Materials*, 14(21), 2021.

[271] Mohammad Khazaei, Masao Arai, Taizo Sasaki, Chan-Yeup Chung, Natarajan S Venkataramanan, Mehdi Estili, Yoshio Sakka, and Yoshiyuki Kawazoe. Novel electronic and magnetic properties of two-dimensional transition metal carbides and nitrides. *Advanced Functional Materials*, 23(17):2185–2192, 2013.

[272] Philipp Maisch, Kai Cheong Tam, DongJu Jang, Marc Steinberger, Fu Yang, Christoph J Brabec, and Hans-Joachim Egelhaaf. Inkjet printed organic and perovskite photovoltaics—review and perspectives. *Organic Flexible Electronics*, pages 305–333, 2021.

[273] Zhanhua Wei, Haining Chen, Keyou Yan, and Shihe Yang. Inkjet printing and instant chemical transformation of a $CH_3NH_3PbI_3$/nanocarbon electrode and interface for planar perovskite solar cells. *Angewandte Chemie*, 126(48):13455–13459, 2014.

[274] Alexandre Gheno, Yong Huang, Johann Bouclé, Bernard Ratier, Alain Rolland, Jacky Even, and Sylvain Vedraine. Toward highly efficient inkjet-printed perovskite solar cells fully processed under ambient conditions and at low temperature. *Solar RRL*, 2(11):1800191, 2018.

[275] Huihui Zhu, Eun-Sol Shin, Ao Liu, Dongseob Ji, Yong Xu, and Yong-Young Noh. Printable semiconductors for backplane tfts of flexible oled displays. *Advanced Functional Materials*, 30(20):1904588, 2020.

[276] Yuxiang Wu, Juan Li, Jian Xu, Yangyang Du, Like Huang, Jian Ni, Hongkun Cai, and Jianjun Zhang. Organic–inorganic hybrid $CH_3NH_3PbI_3$ perovskite materials as channels in thin-film field-effect transistors. *RSC Advances*, 6:16243–16249, 2016.

[277] Bert Conings, Jeroen Drijkoningen, Nicolas Gauquelin, Aslihan Babayigit, Jan D'Haen, Lien D'Olieslaeger, Anitha Ethirajan, Jo Verbeeck, Jean Manca, Edoardo Mosconi, et al. Intrinsic thermal instability of methylammonium lead trihalide perovskite. *Advanced Energy Materials*, 5(15):1500477, 2015.

[278] Guohua Hu, Tom Albrow-Owen, Xinxin Jin, Ayaz Ali, Yuwei Hu, Richard C.T. Howe, Khurram Shehzad, Zongyin Yang, Xuekun Zhu, Robert I. Woodward, Tien Chun Wu, Henri Jussila, Jiang Bin Wu, Peng Peng, Ping Heng Tan, Zhipei Sun, Edmund J.R. Kelleher, Meng Zhang, Yang Xu, and Tawfique Hasan. Black phosphorus ink formulation for inkjet printing of optoelectronics and photonics. *Nature Communications*, 2017.

[279] Thomas M. Higgins, Sean Finn, Maik Matthiesen, Sebastian Grieger, Kevin Synnatschke, Maximilian Brohmann, Marcel Rother, Claudia Backes, and Jana Zaumseil. Electrolyte-Gated *n*-Type Transistors Produced from Aqueous Inks of WS_2 Nanosheets. *Advanced Functional Materials*, 2019.

[280] Simone Bertolazzi, Marco Gobbi, Yuda Zhao, Claudia Backes, and Paolo Samori. Molecular chemistry approaches for tuning the properties of two-dimensional transition metal dichalcogenides. *Chemical Society Reviews*, 47(17):6845–6888, 2018.

[281] Alexander Yu Polyakov, Lena Yadgarov, Ronit Popovitz-Biro, Vasily A Lebedev, Iddo Pinkas, Rita Rosentsveig, Yishay Feldman, Anastasia E Goldt, Eugene A Goodilin, and Reshef Tenne. Decoration of WS_2 nanotubes and fullerene-like MoS_2 with gold nanoparticles. *The Journal of Physical Chemistry C*, 118(4):2161–2169, 2014.

[282] Kevin Synnatschke, Patrick Arthur Cieslik, Andrew Harvey, Andres Castellanos-Gomez, Tian Tian, Chih-Jen Shih, Alexey Chernikov, Elton J. G. Santos, Jonathan N. Coleman, and Claudia Backes. Length- and thickness-dependent optical response of liquid-exfoliated transition metal dichalcogenides. *Chemistry of Materials*, 31(24):10049–10062, Dec 2019.

[283] Michigan State University. Uv-visible spectroscopy. Accessed on 01/01/2022.

[284] Arlene O'Neill, Umar Khan, and Jonathan N. Coleman. Preparation of High Concentration Dispersions of Exfoliated MoS_2 with Increased Flake Size. *Chemistry of Materials*, 24(12):2414–2421, jun 2012.

[285] F. Bodino, G. Baud, M. Benmalek, J. P. Besse, H. M. Dunlop, and M. Jacquet. Alumina coating on polyethylene terephthalate. *Thin Solid Films*, 241(1-2):21–24, 1994.

[286] Jatosado. E-beam evaporation. CC BY-SA 3.0, https://commons.wikimedia.org/w/index.php?curid=20296340.

[287] Temescal fc2000 user manual. Accessed on 17/9/2021.

[288] Chandrasekhara Venkata Raman and Kariamanikkam Srinivasa Krishnan. A new type of secondary radiation. *Nature*, 121(3048):501–502, 1928.

[289] Katherine JI Ember, Marieke A Hoeve, Sarah L McAughtrie, Mads S Bergholt, Benjamin J Dwyer, Molly M Stevens, Karen Faulds, Stuart J Forbes, and Colin J Campbell. Raman spectroscopy and regenerative medicine: a review. *NPJ Regenerative medicine*, 2(1):1–10, 2017.

[290] John B Boland, Ruiyuan Tian, Andrew Harvey, Victor Vega-Mayoral, Aideen Griffin, Dominik V Horvath, Cian Gabbett, Madeleine Breshears, Joshua Pepper, Yanguang Li, et al. Liquid phase exfoliation of ges nanosheets in ambient conditions for lithium ion battery applications. *2D Materials*, 7(3):035015, 2020.

[291] Michael A O'Keefe, Lawrence F Allard, and Douglas A Blom. HRTEM imaging of atoms at sub-Ångström resolution. *Journal of Electron Microscopy*, 54(3):169–180, 2005.

[292] David J Smith. Ultimate resolution in the electron microscope? *Materials Today*, 11:30–38, 2008.

[293] J. N. Coleman. Trinity college dublin PY4P04 nanoscience course notes. Accessed on 17/9/2021.

[294] Eric Kvaalen. Schematic view of imaging and diffraction modes in tem. CC BY-SA 4.0 via Wikimedia Commons. Accessed on 30/5/2022.

[295] BJ Inkson. Scanning electron microscopy (sem) and transmission electron microscopy (tem) for materials characterization. In *Materials characterization using nondestructive evaluation (NDE) methods*, pages 17–43. Elsevier, 2016.

[296] Taejin Choi, Soo Hyeon Kim, Chang Wan Lee, Hangil Kim, Sang-Kyung Choi, Soo-Hyun Kim, Eunkyoung Kim, Jusang Park, and Hyungjun Kim. Synthesis of carbon nanotube–nickel nanocomposites using atomic layer deposition for high-performance non-enzymatic glucose sensing. *Biosensors and Bioelectronics*, 63:325–330, 2015.

[297] Fukun Ma, Yongzhong Wu, Yongliang Shao, Yueyao Zhong, Jiaxin Lv, and Xiaopeng Hao. 0D/2D nanocomposite visible light photocatalyst for highly stable and efficient hydrogen generation via recrystallization of cds on mos2 nanosheets. *Nano Energy*, 27:466–474, 2016.

[298] Cian Gabbett, Conor S Boland, Andrew Harvey, Victor Vega-Mayoral, Robert J Young, and Jonathan N Coleman. The effect of network formation on the mechanical properties of 1D:2D nano:nano composites. *Chemistry of Materials*, 30(15):5245–5255, 2018.

[299] Kun Chang and Weixiang Chen. l-cysteine-assisted synthesis of layered mos2/graphene composites with excellent electrochemical performances for lithium ion batteries. *ACS Nano*, 5(6):4720–4728, Jun 2011.

[300] Su Zhang, Lingxiang Zhu, Huaihe Song, Xiaohong Chen, and Jisheng Zhou. Enhanced electrochemical performance of mno nanowire/graphene composite during cycling as the anode material for lithium-ion batteries. *Nano Energy*, 10:172–180, 2014.

[301] Haimei Liu and Wensheng Yang. Ultralong single crystalline V_2O_5 nanowire/graphene composite fabricated by a facile green approach and its lithium storage behavior. *Energy & Environmental Science*, 4:4000–4008, 2011.

[302] Shengjie Peng, Linlin Li, Xiaopeng Han, Wenping Sun, Madhavi Srinivasan, Subodh G Mhaisalkar, Fangyi Cheng, Qingyu Yan, Jun Chen, and Seeram Ramakrishna. Cobalt sulfide nanosheet/graphene/carbon nanotube nanocomposites as flexible electrodes for hydrogen evolution. *Angewandte Chemie*, 126(46):12802–12807, 2014.

[303] Chunying Min, Yuzi Yang, Hongyu Liang, Zengbao He, Jinfeng Zhu, and Qiuying Li. Covalently bonded 2D/0D g-C_3N_4/MoS_2 nanocomposites for enhanced tribological properties in oil. *ChemistrySelect*, 6(7):1661–1668, 2021.

[304] Srinivasa Rao Pathipati, Egon Pavlica, Andrea Schlierf, Mirella El Gemayel, Paolo Samori, Vincenzo Palermo, and Gvido Bratina. Graphene-induced enhancement of n-type mobility in perylenediimide thin films. *The Journal of Physical Chemistry C*, 118(43):24819–24826, 2014.

[305] Victor Vega-Mayoral, Daniele Vella, Tetiana Borzda, Matej Prijatelj, Iacopo Tempra, Eva A. A. Pogna, Stefano Dal Conte, Peter Topolovsek, Natasa Vujicic, Giulio Cerullo, Dragan Mihailovic, and Christoph Gadermaier. Exciton and charge carrier dynamics in few-layer WS_2. *Nanoscale*, 8:5428–5434, 2016.

[306] M Thripuranthaka, Ranjit V Kashid, Chandra Sekhar Rout, and Dattatray J Late. Temperature dependent raman spectroscopy of chemically derived few layer mos2 and ws2 nanosheets. *Applied Physics Letters*, 104(8):081911, 2014.

[307] Graeme Cunningham, Mustafa Lotya, Niall McEvoy, Georg S. Duesberg, Paul van der Schoot, and Jonathan N. Coleman. Percolation scaling in composites of exfoliated MoS_2 filled with nanotubes and graphene. *Nanoscale*, 4(20):6260, 2012.

[308] Sasha Stankovich, Dmitriy A Dikin, Geoffrey HB Dommett, Kevin M Kohlhaas, Eric J Zimney, Eric A Stach, Richard D Piner, SonBinh T Nguyen, and Rodney S Ruoff. Graphene-based composite materials. *Nature*, 442(7100):282–286, 2006.

[309] Jingtian Fang, William G. Vandenberghe, and Massimo V. Fischetti. Microscopic dielectric permittivities of graphene nanoribbons and graphene. *Physical Review B*, 94:045318, Jul 2016.

[310] Zhishuo Huang, Wenxu Zhang, and Wanli Zhang. Computational search for two-dimensional MX_2 semiconductors with possible high electron mobility at room temperature. *Materials*, 9(9), 2016.

[311] Kosuke Nagashio, Tomonori Nishimura, Koji Kita, and Akira Toriumi. Mobility variations in mono-and multi-layer graphene films. *Applied physics express*, 2(2):025003, 2009.

[312] Ethan B. Secor, Pradyumna L. Prabhumirashi, Kanan Puntambekar, Michael L. Geier, and Mark C. Hersam. Inkjet printing of high conductivity, flexible graphene patterns. *Journal of Physical Chemistry Letters*, 4(8):1347–1351, 2013.

[313] Sukanta De and Jonathan N Coleman. Are there fundamental limitations on the sheet resistance and transmittance of thin graphene films? *ACS Nano*, 4(5):2713–2720, 2010.

[314] Alexandre Pachoud, Manu Jaiswal, Priscilla Kailian Ang, Kian Ping Loh, and Barbaros Oezyilmaz. Graphene transport at high carrier densities using a polymer electrolyte gate. *EPL (Europhysics Letters)*, 92(2):27001, 2010.

[315] Tian Fang, Aniruddha Konar, Huili Xing, and Debdeep Jena. Carrier statistics and quantum capacitance of graphene sheets and ribbons. *Applied Physics Letters*, 91(9):092109, 2007.

[316] Daniele Braga, Ignacio Gutiérrez Lezama, Helmuth Berger, and Alberto F. Morpurgo. Quantitative Determination of the Band Gap of WS_2 with Ambipolar Ionic Liquid-Gated Transistors. *Nano Letters*, 12(10):5218–5223, oct 2012.

[317] Ignacio Gutiérrez-Lezama, Bojja Aditya Reddy, Nicolas Ubrig, and Alberto F Morpurgo. Electroluminescence from indirect band gap semiconductor res2. *2D Materials*, 3(4):045016, 2016.

[318] Alexey Chernikov, Timothy C Berkelbach, Heather M Hill, Albert Rigosi, Yilei Li, Ozgur Burak Aslan, David R Reichman, Mark S Hybertsen, and Tony F Heinz. Exciton binding energy and nonhydrogenic rydberg series in monolayer WS_2. *Physical Review Letters*, 113(7):076802, 2014.

[319] Bairen Zhu, Xi Chen, and Xiaodong Cui. Exciton binding energy of monolayer WS_2. *Scientific Reports*, 5(1):1–5, 2015.

[320] Heather M Hill, Albert F Rigosi, Cyrielle Roquelet, Alexey Chernikov, Timothy C Berkelbach, David R Reichman, Mark S Hybertsen, Louis E Brus, and Tony F Heinz. Observation of excitonic rydberg states in monolayer MoS_2 and WS_2 by photoluminescence excitation spectroscopy. *Nano Letters*, 15(5):2992–2997, 2015.

[321] F. Schwierz. Graphene transistors. *Nature Nanotechnology*, 5(July):487, 2010.

[322] Elena del Corro, Humberto Terrones, Ana Elias, Cristiano Fantini, Simin Feng, Minh An Nguyen, Thomas E. Mallouk, Mauricio Terrones, and Marcos A. Pimenta. Excited excitonic states in 1L, 2L, 3L, and bulk WSe_2 observed by resonant raman spectroscopy. *ACS Nano*, 8(9):9629–9635, 2014. PMID: 25162682.

[323] Soohyung Park, Niklas Mutz, Thorsten Schultz, Sylke Blumstengel, Ali Han, Areej Aljarb, Lain-Jong Li, Emil J W List-Kratochvil, Patrick Amsalem, and Norbert Koch. Direct determination of monolayer MoS_2 and WSe_2 exciton binding energies on insulating and metallic substrates. *2D Materials*, 5(2):025003, jan 2018.

[324] L.M. Malard, M.A. Pimenta, G. Dresselhaus, and M.S. Dresselhaus. Raman spectroscopy in graphene. *Physics Reports*, 473(5-6):51–87, apr 2009.

[325] Yoshihiko Arao, Yoshinori Mizuno, Kunihiro Araki, and Masatoshi Kubouchi. Mass production of high-aspect-ratio few-layer-graphene by high-speed laminar flow. *Carbon*, 102:330–338, 2016.

[326] Wei Shi, Miao Ling Lin, Qing Hai Tan, Xiao Fen Qiao, Jun Zhang, and Ping Heng Tan. Raman and photoluminescence spectra of two-dimensional nanocrystallites of monolayer WS_2 and WSe_2. *2D Materials*, 2016.

[327] Jong Su Kim, Beom Joon Kim, Young Jin Choi, Moo Hyung Lee, Moon Sung Kang, and Jeong Ho Cho. An organic vertical field-effect transistor with underside-doped graphene electrodes. *Advanced Materials*, 28(24):4803–4810, 2016.

[328] Zegao Wang, Qiang Li, Yuanfu Chen, Bianxiao Cui, Yanrong Li, Flemming Besenbacher, and Mingdong Dong. The ambipolar transport behavior of WSe_2 transistors and its analogue circuits. *NPG Asia Materials*, 2018.

[329] A. T. Wong, J. H. Noh, P. R. Pudasaini, B. Wolf, N. Balke, A. Herklotz, Y. Sharma, A. V. Haglund, S. Dai, D. Mandrus, P. D. Rack, and T. Z. Ward. Impact of gate geometry on ionic liquid gated ionotronic systems. *APL Materials*, 2017.

[330] Domhnall O'Suilleabhain, Adam G. Kelly, Ruiyuan Tian, Cian Gabbett, Dominik Horvath, and Jonathan N. Coleman. Effect of the gate volume on the

performance of printed nanosheet network-based transistors. *ACS Applied Electronic Materials*, 2(7):2164–2170, Jul 2020.

[331] Andrew Harvey, Claudia Backes, John B Boland, Xiaoyun He, Aideen Griffin, Beata Szydlowska, Cian Gabbett, John F Donegan, and Jonathan N Coleman. Non-resonant light scattering in dispersions of 2d nanosheets. *Nature communications*, 9(1):1–11, 2018.

[332] Ashish Arora, Karol Nogajewski, Maciej Molas, Maciej Koperski, and Marek Potemski. Exciton band structure in layered $MoSe_2$: from a monolayer to the bulk limit. *Nanoscale*, 7(48):20769–20775, 2015.

[333] TJ Nacken, C Damm, J Walter, A Rüger, and W Peukert. Delamination of graphite in a high pressure homogenizer. *Rsc Advances*, 5(71):57328–57338, 2015.

[334] Philipp Tonndorf, Robert Schmidt, Philipp Böttger, Xiao Zhang, Janna Börner, Andreas Liebig, Manfred Albrecht, Christian Kloc, Ovidiu Gordan, Dietrich R. T. Zahn, Steffen Michaelis de Vasconcellos, and Rudolf Bratschitsch. Photoluminescence emission and raman response of monolayer MoS_2, $MoSe_2$, and WSe_2. *Optics Express*, 21(4):4908–4916, Feb 2013.

[335] Peter N Nirmalraj, Tarek Lutz, Shishir Kumar, Georg S Duesberg, and John J Boland. Nanoscale mapping of electrical resistivity and connectivity in graphene strips and networks. *Nano letters*, 11(1):16–22, 2011.

[336] Simone Colasanti, Vijay Deep Bhatt, Ahmed Abdelhalim, and Paolo Lugli. 3-d percolative model-based multiscale simulation of randomly aligned networks of carbon nanotubes. *IEEE Transactions on Electron Devices*, 63(3):1346–1351, 2016.

[337] Xinming Li, Tingting Yang, Yao Yang, Jia Zhu, Li Li, Fakhr E. Alam, Xiao Li, Kunlin Wang, Huanyu Cheng, Cheng-Te Lin, Ying Fang, and Hongwei Zhu. Large-area ultrathin graphene films by single-step marangoni self-assembly for highly sensitive strain sensing application. *Advanced Functional Materials*, 26(9):1322–1329, 2016.

[338] Joseph Neilson, Michael P. Avery, and Brian Derby. Tiled monolayer films of 2D molybdenum disulfide nanoflakes assembled at liquid/liquid interfaces. *ACS Applied Materials & Interfaces*, 12(22):25125–25134, Jun 2020.

[339] Yashaswi Nalawade, Joshua Pepper, Andrew Harvey, Aideen Griffin, David Caffrey, Adam G. Kelly, and Jonathan N. Coleman. All-printed dielectric capacitors from high-permittivity, liquid-exfoliated biocl nanosheets. *ACS Applied Electronic Materials*, 2(10):3233–3241, Oct 2020.

[340] Amir Asadpoordarvish, Andreas Sandström, and Ludvig Edman. A flexible encapsulation structure for ambient-air operation of light-emitting electrochemical cells. *Advanced Engineering Materials*, 18(1):105–110, 2016.